CHAPTER -1

INTRODUCTION

It is desirable to minimize the introduction of harmful gases and by-products into the environment. There is also need to minimize the content of harmful component of the effluent gas before released into the atmosphere. This minimization should be carried out in an efficient and inexpensive manner to protect vegetation and grazing animals and there of human health. People are exposed to airborne fluorides because of air pollution caused by aluminium smelting, coal burning and nuclear power plants, glass etching, petroleum refining, plastic manufacturing, phosphatic fertilizer production, silicon chip manufacturing and uranium enrichment facilities. Exposure to fluoride gas either in the form of direct contact with the skin or inhalation leads to serious health hazards even at very low concentrations. The strict restriction from the Ministry of Environment and Forest, Govt. of India on the emissions of harmful fluoride containing gases into the atmosphere has increased the need of impurity free effluent gas. Thus, all the industries which emit such fluoride containing gases should adopt modern abatement techniques to reduce their emissions in order to meet the government regulations. That is why gaseous fluoride treatment needs much attention.

The most recent abatement technique for fluoride includes the fluidized bed method which uses fluidized bed reactor (FBR). The FBR has many advantages over other reactors. Proper design of FBR can treat industrial gaseous effluents properly. The method and degree of contact varies from reactor to reactor thereby varying their efficiencies. Efficiency of a reactor depends upon the extent of conversion of the reactants which in turn depends upon many factors. Thus extents of gas-solid contact affect the reaction kinetics in turn the efficiency of the reactor. Therefore attempt has been made to study the bed dynamics of FBR in detail so that it can treat any industrial gaseous effluent containing gaseous pollutants efficiently.

1.1 Advantages and Disadvantages of Fluidized Bed Reactor

Fluidization is one of the most important fluid-solid contacting processes. The demand for fluidization process is increasing day by day because of several advantages [Shah (1979), Fan (1989), Page et al. (1992)]. A fluidized bed reactor (FBR) in many ways is better than other conventional reactors. Some of the advantages of fluidized bed reactors are as follows.

- FBR has ability to maintain a uniform temperature and eliminates hot spots.
- With FBR significantly lower pressure drops are achieved thus pumping costs are reduced.
- There is no moving part, and hence a fluidized bed reactor is not a mechanically agitated reactor. For this reason, maintenance costs are low.
- Catalyst may be withdrawn, reactivated and added to fluidized beds continuously without affecting the hydrodynamic performance of the reactor. New improved catalyst can replace older catalysts with minimal effort.
- Bed plugging and channelling are minimized due to the movement of solids.
- Low investments are required for the same feed and product specifications.
- More efficient contacting of fluid and solid than any other catalytic reactors.

1.2 Application of Fluidized Bed Reactor

FBR has extensive industrial applications due to above mentioned advantages. It is suitable for accomplishing heat-sensitive or exothermic or endothermic reactions. It is used in nuclear power plants, chemical, biochemical and metallurgical industries. It is extensively used in petroleum industry for fluid bed catalytic cracking [Yang (2003)] and produces gasoline along with other fuels and many other chemicals. Various other reactions like hydrogenation, oxidation and many more reactions are also carried out in FBR [Fan (1989), Wild and Poncin (1996)].

1.3 Computational Fluid Dynamics

Computational fluid dynamics (CFD) is one of the modern tools that use numerical methods and algorithms to analyze and solve problems that involve fluid flows. Due to a combination of increased computer efficacy, advanced numerical methods and numerical simulation techniques, CFD becomes a reality and offers an effective mean of quantifying the physical and chemical processes in the fluidized bed reactors under various operating conditions within a virtual environment. The results of accurate simulations can help to optimize the system design and operation and understand the dynamic processes inside the reactors. Researchers have been using CFD to simulate and analyze the performance of various equipments such as fluidized beds, fixed beds, combustion furnaces, firing boilers, rotating cones and rotary kilns etc. CFD programs predict not only fluid flow behavior, but also heat and mass transfer, chemical reactions (e.g. devolatilization, combustion), phase changes (e.g. vapour in drying, melting, slagging), and mechanical movements (e.g. rotating cone reactor). Compared to the experimental data, CFD model results are capable of predicting qualitative information and in many cases accurate quantitative information.

1.4 Objectives of the Present Research Work

Before using the FBR it is essential to know how efficient it is, whether proper fluidization can be achieved within the FBR or not. Again it is also essential to check whether the selected FBR can be used as a generalized reactor for treatment of gaseous pollutants or not. The FBR has been selected for the treatment of industrial gaseous effluents containing fluorides. Thus the objectives for the present work can be summarized as follows.

1.4.1 General objective

The present work is carried out in two parts.

Part – 1: Treatment of gaseous effluents collected from Aluminium industry.

To check the reduction in the concentration of gaseous pollutant, fluorides.

Part – 2: CFD simulation for validation of FBR.

To carry out CFD simulation for validation of experimental results.

1.4.2 Specific objectives

For part – 1:

- To carry out several experiments for studying the hydrodynamics of FBR.
- To allow the reactions to take place among effluent gas and bed materials within FBR under different operating conditions.
- To characterize the bed materials before and after the experiment with / without use of industrial effluent gas.

For part – 2:

- To carry out CFD simulation for hydrodynamic studies for two-phase fluidized bed with different bed materials.
    - Single sized particles
    - Binary mixture of particles
- To compare the experimentally observed hydrodynamics of FBR with those obtained from CFD simulations.
- To carry out CFD simulation for studying the temperature effect on bed dynamics of the FBR with the binary mixture as bed materials.

1.5 Thesis Summary

The present work has been reported in the form of a thesis. This thesis comprises of six chapters viz. Introduction, Literature Survey, Experimentation, Result and Discussion, CFD simulation and Conclusion and Future scope of the work.

- *Chapter 1* describes the introduction to the present study with the advantages of fluidized bed reactor (FBR) and computational fluid dynamics. The objectives of the present work are also discussed in this chapter.

- *Chapter 2* discusses different research works already carried out in the areas of fluidized bed reactor and FBR modeling using CFD. This chapter also describes the computational models in details with the numerical methodology adopted in the CFD simulation. Governing equations of CFD are also mentioned in this chapter.
- *Chapter 3* discusses about the experimental set up with its components used during the experimental investigation. Experimental procedures, scope of the experiment are also discussed here in this section.
- *Chapter 4* lists the results of various hydrodynamic studies obtained from experimental investigations. Results of different characterization analysis carried out for different bed materials before and after the experiments are also discussed in this chapter.
- *Chapter 5* describes the CFD simulated results obtained from bed hydrodynamics of FBR using 2D and 3D models. Various simulation results obtained for bed hydrodynamics of fluidized bed reactor under different system parameters and CFD parameters with single and binary mixtures of particles are also reported in this chapter.
- *Chapter 6* describes the overall conclusions obtained from experimental and simulation studies. Future recommendations based on the present research outcomes are also suggested in this chapter. The major findings of the work are also summarized in this chapter.

CHAPTER - 2

LITERATURE SURVEY

2.1 INTRODUCTION

The fluorides coming out from process industries need to be treated before venting to the atmosphere. Many methods have been developed by the researchers for the treatment of gaseous effluents containing fluorides. Different methods being used by different researchers [Arno (2004), Cady (1935), Tonnies et al. (2000, 1998)] for abatement of fluorides are

- Dilution Treatment
- Dry Abatement
- Thermal Abatement
- Conventional Treatment
- Wet Abatement
- Point-Of-Use Method
- Adsorption method
- Fluidized Bed Method

2.1.1 Fluidized Bed Method

Fluidized bed method is one of several methods being used for treatment of gaseous effluents containing fluorides. Researchers have used bag filters for the abetment of fluorides [Alary et al. (1982)]. Jia et al. (2013) have used fluidized bed method to treat wastewater for abatement of fluorides. Holmes et al. (1967) describes the abatement of fluoride using a fluidized bed of activated alumina particles. High fluoride removal efficiency (>99%) was easily achieved at a reaction temperature between 300 to 400°C. The flow rate was limited to 1.25 to 1.65 minimum fluidization velocities. Other methods of fluoride disposal are found in the report by Netzer (1977). By the use of zirconium alloys it was possible to abate NF_3 in fluidized beds by contacting the alloys with NF_3 [Iwata and Hatakeyama (1995)]. A process of destroying fluoride species selected from the gas mixture (groups consisting of fluorine, chlorine, trifluoride and mixture containing fluorine species) by contacting the gas with a fluidized bed of metal particles is capable of reacting with fluoride species [Hsiung and Withers (1999)]. It is observed that the study of abetment of fluorides at higher temperatures

inside a FBR is very much limited. Thus in this work attention is given to study the abetment of fluorides under fluidizing conditions.

In the fluidized bed method gaseous fluorides are reduced to solid fluorides. The industrial gaseous effluent containing fluorides is allowed to pass through the fluidized bed of metal particles. Such metal particles are capable of reacting with gaseous fluorides where the metal particles have particle sizes essentially no greater than approximately 300 microns. The process can also be conducted in parallel connected switching fluidized beds wherein the beds are switched based upon achieving a predetermined bed height expansion. Bed expansion depends on the reaction of the metal particles with such fluorides [Hsiung and Withers (1999)].

Fluidized bed reactors are widely used in the industries due to their superior heat and mass transfer ability. This is because of relatively larger particle-fluid contact compared to other types of reactors. Therefore fluidized beds are suitable for catalytic / non-catalytic reactions especially for exothermic reactions [Kunii and Levenspiel (1991)]. Fluidized-bed reactors are used in a wide range of applications in various industrial operations including chemical, mechanical, petroleum, mineral, food and pharmaceutical industries. Therefore FBRs have been the focus of much research.

2.2 Physical Model of Fluidized Bed Reactor

A fluidized bed reactor (FBR) is a type of reactor that can be used to carry out a variety of multiphase chemical reactions at heterogeneous / homogenous condition (**Fig.-2.1**). In this type of reactor, a fluid (gas or liquid) is passed through a bed of granular solid materials (usually a catalyst) at high enough velocities to suspend the solids. The solid substrate materials in the fluidized bed reactor are typically supported by a porous plate distributor. The fluid is then forced through the distributor up through the solid material. As the fluid velocity is increased, a stage comes where the force exerted by the fluid on the solids is

enough to balance the weight of the solid materials. This stage is known as incipient fluidization which occurs at the minimum fluidization velocity. Once this minimum velocity is surpassed, the bed materials begin to expand and swirl around much like an agitated tank or boiling pot of water. The reactor is now a fluidized bed. Depending on the operating conditions and properties of solid phase various flow regimes are observed in this reactor. The particles typically are in size range of 10 – 300 microns. While designing a fluidized bed reactor, the catalyst life is also to be taken into account. Objective of the present work is to check the adoptability of the FBR for treatment of fluorides and other gaseous pollutants which are released to the atmosphere from several industries.

2.3 Design Aspects of Gas-Solid Fluidized Bed Reactor

Considerable progress has been made with respect to understanding of the phenomenon of gas-solid fluidization. The successful design and operation of a gas-solid fluidized bed system depends on the ability to accurately predict the fundamental properties of the system. Therefore it is necessary to predict important aspects with respect to bed dynamics for efficient design of a FBR. Most often, to achieve the desired efficiency of FBR basic factors like the effects of various operating parameters on the hydrodynamics may be required to analyze. For the given fluid and solid properties, the operating gas superficial velocity must then be set and the reactor size should be determined based upon the expected bed expansion and hold-ups of solid and gas phases. Sometimes some operating conditions may vary over a wide range for which reactors with different dimensions might be required. But it is not always possible either technically or economically to fabricate reactors with different dimensions. Therefore it is required to check the suitable / optimum range of conditions by means of any software. Thus CFD is found to be suitable method for validating the experimentally observed data over a wide range of operating conditions. Some of the aspects used to describe proper fluidization phenomena within the reactor are described below.

- Bed Pressure Drop (Δp)
- Minimum Fluidization Velocity (U_{mf})
- Bed Expansion Ratio (R)
- Bed Fluctuation Ratio (r)
- Fluidization Index (FI)

All these terms constitute the bed hydrodynamics which are interrelated and describe the fluidization process both qualitatively and quantitatively. Thus it is essential to study the hydrodynamics of FBR for proper design and modeling. These aspects of FBR have been studied both computationally and experimentally in the present work for knowing the bed hydrodynamics. Different system parameters have been varied to analyze their effects on bed hydrodynamics.

2.3.1 Bed Pressure drop

Bed Pressure drop measures the drag in combination with the buoyancy and phase holdups. Therefore it is important to analyze bed pressure drop which will indicate about the quality of fluidization. At low flow rates of fluid the bed behaves like a packed bed, where the pressure drop is approximately proportional to gas velocity without any change in the bed height. With further increase in velocity, the bed materials start moving and the fluidization begins. Once the bed is fluidized, the pressure drop across the bed remains constant, but bed height continues to increase with increasing flow of fluid [Kunii and Levenspiel, (1991)].

2.3.2 Minimum Fluidization Velocity

Minimum fluidization velocity is the superficial velocity at which the bed starts to fluidize which is the key point to give information regarding fluidization process. The minimum fluidization velocity (U_{mf}) is the point of transition between a fixed bed regime and a bubbling regime in a fluidized bed. Minimum fluidization velocity is one of the most important normalized parameters for characterizing the hydrodynamics in a fluidized bed (Ramos et al., 2002). Usually, the minimum fluidization velocity is obtained experimentally and several techniques are also reported in the literature to find the minimum fluidization

velocity for a multiphase flow system. Gupta and Sathiyamoorthy (1999) have reported three different methods to measure U_{mf}. These are (i) the pressure drop method, (ii) the voidage method and (iii) the heat transfer method. Out of these methods pressure drop method is widely used because of simplicity.

Zhou et al. (2008) have used the pressure drop method to compare the minimum fluidization velocities obtained by using fluidize of different geometry i.e. conical and a cylindrical fluidized bed. The comparison among the experimental results and the theoretical values of U_{mf} obtained by using Ergun equation as well as other reported models has shown very good agreement thereby justifying pressure drop method to be accurate. The minimum fluidization velocity depends on the many factors such as material properties, the bed geometry and the fluid properties [Hilal et al. (2001)]. The minimum fluidization velocity of fine particles has been determined by Cardoso et al. (2008). Effect of bed geometry on U_{mf} has further been verified by Singh and Roy (2005). Zhiping et al. (2007) have studied variations in the minimum fluidization velocities for different materials like quartz, sand and glass beads under different pressures (0.5, 1.0, 1.5 and 2.0 MPa). The minimum fluidization velocity has been observed to decrease with the increasing pressure. Again the minimum fluidization velocity has also been found to be greater for larger particles than for smaller ones.

2.3.3 Bed Expansion Ratio (R)

Bed Expansion Ratio (R) is used to describe the characteristics of bed during fluidization condition. This is quantitatively defined as the ratio of average expanded bed height of a fluidized bed to the initial static bed height at any particular flow rate of the fluidizing medium above the minimum fluidization. Average expanded bed height is the arithmetic mean of highest and lowest levels attained by top surface of the fluidized bed.

$$\mathbf{R} = \left(\frac{\mathbf{H_{avg}}}{\mathbf{H_{static}}}\right) = \left(\frac{\mathbf{H_{max}} + \mathbf{H_{min}}}{\mathbf{2 * Hs}}\right) \quad (2.1)$$

Where H_{avg} is the average expanded bed height, H_s is the initial static bed height, H_{max} is maximum expanded bed height and H_{min} is the minimum expanded bed height. Sau et al. (2010) have studied the bed expansion for tapered fluidized bed using spherical and non-spherical particles.

2.3.4 Bed Fluctuation Ratio

The term bed fluctuation ratio is also used to describe the characteristics of the bed during fluidization process. This is defined as the ratio of the highest and lowest levels attained by the top surface of the bed at any particular flow rate of fluid above minimum fluidization. It is denoted by "**r**".

$$\mathbf{r} = \left(\frac{\mathbf{H_{max}}}{\mathbf{H_{min}}}\right) \quad (2.2)$$

A lower value of fluctuation ratio is indicative of improved fluidization quality with less fluctuation of the top surface of the bed in the fluidized condition. Many researchers have studied bed expansion / fluctuation for single / binary mixtures of regular / irregular particles in cylindrical beds. Effects of stirrers on bed dynamics are also studied with respect to bed expansion / fluctuation ratio [Singh and Roy (2006), Sahoo (2011) and Kumar and Roy (2007)].

2.3.5 Fluidization Index

Fluidization index is the ratio of pressure drop across the bed to the weight of the bed material per unit area of cross-section of the column.

$$\mathbf{F.I.} = \left[\frac{\Delta \mathbf{P}}{\left(\mathbf{W}/\mathbf{A}\right)}\right] \quad (2.3)$$

Fluidization index varies in between 0 and 1. Fluidization index of 1 indicates ideal or proper fluidization and 0 indicates poor fluidization or static condition. Fluidization index measures the degree of uniform expansion during fluidization condition [Singh and Roy (2005)]. The

higher the ratio, the bed holds more gas between the minimum fluidization and bubbling point.

2.4 Previous Works on Hydrodynamics of Two Phase Fluidized Bed Reactor

Wang et al. (1998) have observed plugging, channeling, disruption and agglomeration in the fluidization of fine particles (size range of 0.01-18.1 μm and density range of 101~8600 kg/m^3). Laszuk et al. (2008) have used rotational mixer for uniform fluidization of fine material (particle size ≤ 50 μm) where the hydraulic resistance of the bed has been measured as a function of its height and the rotational speed of the mixer during the fluidization process. Kusakabe et al. (1989) have used submicron size of fine particles under reduced pressures where only the upper part of the bed is observed to fluidize and the rest was quiescent for which the minimum fluidization velocity was determined for a shallow bed.

Avidan and Yerushalmi (1982) investigated bed expansion of fine powders with two different high aspect ratios i.e. expanded top bed and a circulating system. Xu and Zhu[a] (2006) investigated the effects of vibration on fluidization of fine particles (4.8 – 216 μm size in average) and concluded that the fluidization quality is enhanced under mechanical vibration leading to larger bed pressure drops at low superficial gas velocities U_{mf}. Mawatari et al. (2005) studied vibro-fluidization using fine cohesive particles by decreasing and increasing gas velocity. Jaraiz et al. (1992) estimated the inter particle cohesive forces from pressure drop versus bed expansion data using packed vibrated beds of very fine particles. Valverde et al. (2009) investigated the behavior of a fluidized bed of fine magnetite particles, with the help of a cross flow magnetic field. Russo et al. (1995) have carried out fluidization using non-fluent catalyst particles where acoustic field is generated with a loud speaker. Stable fluidization is obtained with the application of the magnetic field and acoustic field where the bed expansion is observed to increase with higher gas velocities.

2.5 Computational Fluid Dynamics

In the field of fluidization, in particular, the use of CFD has pushed the frontiers of fundamental understanding of fluid–solid interactions and has enabled the correct theoretical prediction of various macroscopic phenomena encountered in fluidized beds. Fluid (gas and liquid) flows are governed by partial differential equations (PDE) which represent conservation laws for the mass, momentum and energy. Computational Fluid Dynamics (CFD) is used to replace such PDE systems by a set of algebraic equations which can be solved using digital computers. The basic principle behind CFD modeling method is that the simulated flow region is divided into small cells. Differential equations of mass, momentum and energy balance are discretized and represented in terms of the variables at any predetermined position within the cell or at the center of cell [John and Anderson (1995)]. These equations are solved iteratively until the solution reaches the desired accuracy (ANSYS Fluent 13.0).

2.6 Problem Statement

Computational Fluid Dynamics (CFD) simulation is an economical and effective tool to study and investigate the bed dynamics and thermal flow inside a fluidized bed reactor. As described in the objective, the purpose of this study is to investigate the hydrodynamic behaviour of a two-phase (i.e. gas-solid) fluidized bed numerically. It is a multiphase problem between gases and solid particles where both gas phase (primary phase) and solid phases (secondary phase) are solved by using Eulerian method. The flow inside the domain is unsteady, two dimensional, incompressible, and turbulent where Gravitational force is also considered. The hydrodynamic behaviours required to be studied numerically are the bed pressure drop, minimum fluidization velocity and bed expansion / fluctuation. In the present work two geometries for the physical unit have been considered. First, a two dimensional (2D) geometry is simulated with CFD tools to check the findings with the laboratory data.

Then a three dimensional (3D) geometry is considered to see the variations in the hydrodynamic behaviours against the laboratory data.

2.7 Selection of an appropriate computational model

Two-phase fluidization involves gas and solid phases. Hence choosing an appropriate multiphase model for computational study plays an important role in the simulation result. There are different multiphase models available in commercial software, ANSY'S FLUENT. The details of various models and numerical schemes used in the present work are discussed below. Currently, two approaches being used for the numerical calculation of multiphase flow are

(i) The Eulerian-Lagrangian approach

(ii) The Euler-Euler approach.

In the Euler-Euler approach, different phases are treated mathematically as interpenetrating continua. Since the volume of one phase cannot be occupied by the other phase the concept of phasic volume fraction is introduced. These volume fractions are assumed to be continuous function of space and time whose sum is equal to one. Conservation equations for each phase are derived to obtain a set of equations which have similar structure for all the phases. These equations are closed by providing constitutive relations that are obtained from empirical informations or by application of kinetic theory in the case of granular flow [Kumar et al. (2009)]. The Euler-Euler approach is suitable for volume averaged information on any hydrodynamic property for its simplicity [Pain et al. (2001), Gera (1998)].

There are three different Euler-Euler multiphase models available. These are as follows.

- The volume of fluid (VOF) model
- The Mixture model
- The Eulerian model

The Eulerian model is the most complex of the multiphase models in ANSYS FLUENT. It solves a set of momentum and continuity equations for each phase. Through the pressure and interphase exchange coefficients, couplings are achieved. The manner in which this coupling is handled depends upon the type of phases involved. Granular (fluid-solid) flows are handled differently than non-regular (fluid-fluid) flows. For granular flows, the properties are obtained from the kinetic theory applications. Momentum exchange between the phases is also dependent upon the type of mixture being modeled.

In the present work, an Eulerian granular multiphase model is adopted where gas and solid phases are all treated as continua, interpenetrating and interacting with each other everywhere in the computational domain [Anderson and Jackson (1967)]. With the Eulerian multiphase model, the number of secondary phase is limited only by memory requirement and convergence behaviour. Eulerian multiphase model does not distinguish between fluid-fluid and fluid-solid (granular) multiphase flows. A granular phase is simple in application which involves at least one phase that has been designated as a granular phase. The pressure field is assumed to be shared by all the three phases, in proportion to their volume fractions. Shear and bulk viscosities for solid phase are obtained by applying kinetic theory of granular flows.

2.8 Conservation equations

The motion of each phase is governed by respective mass, momentum and energy conservation equations [ANSYS FLUENT, Theory Guide (2009)].

2.8.1 Conservation of mass:

Mass conservation equations are written as

For gas phase, $$\frac{\partial}{\partial t}\left(\varepsilon_g \rho_g\right) + \nabla.\left(\varepsilon_g \rho_g \vec{u}_g\right) = 0 \quad (2.4)$$

For solid phase, $$\frac{\partial}{\partial t}\left(\varepsilon_s \rho_s\right) + \nabla.\left(\varepsilon_s \rho_s \vec{u}_s\right) = 0 \quad (2.5)$$

Where ρ is the density of the phase, ε is the volume fraction and $\vec{u}$ is the velocity of the phase. s, g are subscripts for solid and gas phases respectively. The volume fraction of the two phases satisfies the following condition:

$$\varepsilon_g + \varepsilon_s = 1 \tag{2.6}$$

2.8.2 Conservation of momentum

Newton's second law of motion states that the change in momentum equals the sum of forces on the domain. The conservation of momentum equation for the gas phase is written as follows

$$\frac{\partial}{\partial t}\left(\rho_g \varepsilon_g \vec{u}_g\right) + \nabla.\left(\rho_g \varepsilon_g \vec{u}_g \vec{u}_g\right) = -\varepsilon_g \nabla p + \nabla.\bar{\bar{\tau}}_g + \rho_g \varepsilon_g \vec{g} + \vec{F}_{i,g} \tag{2.7}$$

The conservation of momentum for the solid phase is given below

$$\frac{\partial}{\partial t}\left(\rho_s \varepsilon_s \vec{u}_s\right) + \nabla.\left(\rho_s \varepsilon_s \vec{u}_s \vec{u}_s\right) = -\varepsilon_s \nabla p - \nabla p_s + \nabla.\bar{\bar{\tau}}_s + \rho_s \varepsilon_s \vec{g} + \vec{F}_{i,s} \tag{2.8}$$

Where p_s is the *s* solid pressure, $\vec{g}$ is the acceleration due to gravity,

The terms $\bar{\bar{\tau}}_g$ and $\bar{\bar{\tau}}_s$ are the stress-strain tensors for gas and solid phases respectively. They are expressed as follows.

$$\bar{\bar{\tau}}_g = \varepsilon_g \mu_g\left(\nabla \vec{u}_g + \nabla \vec{u}_g^T\right) + \varepsilon_g\left(\lambda_g - \frac{2}{3}\mu_g\right)\nabla \vec{u}_g \bar{\bar{I}} \tag{2.9}$$

$$\bar{\bar{\tau}}_s = \varepsilon_s \mu_s\left(\nabla \vec{u}_s + \nabla \vec{u}_s^T\right) + \varepsilon_s\left(\lambda_s - \frac{2}{3}\mu_s\right)\nabla \vec{u}_s \bar{\bar{I}} \tag{2.10}$$

Here $\bar{\bar{I}}$ is unity tensor (dimensionless).

2.8.3 Conservation of Energy

Equations for conservation of energy are written as

For solid phase,

$$\rho_s C_{ps}\frac{\partial \varepsilon_s T_s}{\partial t} + \rho_s C_{ps}\frac{\partial}{\partial x}\left(\varepsilon_s \vec{u}_s T_s\right) + \rho_s C_{ps}\frac{\partial}{\partial y}\left(\varepsilon_s \vec{u}_s T_s\right) = \frac{\partial}{\partial x}\left(\varepsilon_s k_s \frac{\partial T_s}{\partial x}\right) + \frac{\partial}{\partial y}\left(\varepsilon_s k_s \frac{\partial T_s}{\partial y}\right) + h_v\left(T_g - T_s\right) + \varepsilon_s \dot{q} \tag{2.11}$$

For gas phase,

$$\rho_g C_{pg} \frac{\partial \varepsilon_g T_g}{\partial t} + \rho_g C_{pg} \frac{\partial}{\partial x}\left(\varepsilon_g \vec{u}_g T_g\right) + \rho_g C_{pg} \frac{\partial}{\partial y}\left(\varepsilon_g \vec{u}_g T_g\right) = \frac{\partial}{\partial x}\left(\varepsilon_g k_g \frac{\partial T_g}{\partial x}\right) + \frac{\partial}{\partial y}\left(\varepsilon_g k_g \frac{\partial T_g}{\partial y}\right) + h_v\left(T_s - T_g\right) \quad (2.12)$$

2.8.3.1 Thermal conductivity values (k_g and k_s)

The thermal conductivities for the gas phase and the solid phase (k_g and k_s) in the two fluids model formulation are interpreted as effective transport coefficients. It can be represented in general as:

$$k_g = k_g\ (k_{g,o}\ ,\ k_{s,o}\ ,\varepsilon_g\ ,\ \text{particle geometry}) \quad (2.13)$$

$$k_s = k_s(k_{g,o}\ ,\ k_{s,o}\ ,\varepsilon_g\ ,\ \text{particle geometry}) \quad (2.14)$$

where $k_{g,o}$, $k_{s,o}$ are microscopic coefficients.

2.8.4 Interphase Exchange Coefficient

The inter phase momentum exchange terms *Fi* are considered to be composed of a linear combination of different interaction forces between different phases such as the drag force, the lift force and the added mass force, etc., and is generally represented as

$$F_i = F_D + F_L + F_M \quad (2.15)$$

Where D, L and M subscripts are used to respect drag, lift and mass forces respectively. The effect of various interfacial forces has been discussed by Rafique et al. (2004). They have reported that the effect of added mass can be seen only when high frequency fluctuations of the slip velocity occur. They have also observed that the added mass force is much smaller than the drag force in bubbling flow. By default, Fluent does not include the added or virtual mass force. In the previous studies, lift force has been applied to a few 2D simulations of gas–liquid flows. But, it has been often omitted in 3D simulations of bubble flows. The main reason for this is the lack of understanding about the complex mechanism of lift forces in gas–liquid flows [Bunner and Tryggvason (1999)]. Also depending on the bubble size, a negative or positive lift coefficient has been used in the literature to obtain good agreement

between simulated and experimented results. Recently Sokolichin et al. (2004) have suggested that the lift force should be omitted as long as no clear experimental evidences for their direction and magnitude are available. It is also observed that negligence of lift force can still lead to good comparison between simulated and experimental data [Pan et al. (1999, 2000)]. The lift force is observed to be insignificant compared to the drag force. Hence, only the drag force is considered in the present work for inter-phase momentum exchange in CFD simulation.

The inter-phase force term is defined as

$$F_{D,gs} = K_{gs}(u_g - u_s) \tag{2.16}$$

Where K_{gs} $(= K_{sg})$ is the inter-phase momentum exchange coefficient.

In the present work, the gas phase is considered as the continuous phase and the solid phases are treated as dispersed phases. The inter phase drag force between the phases is discussed below.

2.8.4.1 Fluid-solid Exchange Coefficient

The fluid-solid exchange coefficient K_{sg} can be written in the following general form

$$K_{sg} = \frac{\varepsilon_s \rho_s f}{\tau_s} \tag{2.17}$$

Where f is defined differently for the different exchange coefficient model and τ_s, the particulate relaxation time is expressed as per following.

$$\tau_s = \frac{\rho_s d_s^2}{18\,\mu_g} \tag{2.18}$$

Where d_s is the diameter of the particles. The definition of f includes a drag function (C_D) that is based on the relative Reynolds number (Re_s). It is this drag function that differs among the exchange coefficient models.

For analysing exchange coefficient models, many researchers [Huilin et al. (2002), Enwald et al. (1996), Yang et al. (2003)] have used Gidaspow drag models; some researchers

[Hamzehei et al. (2010), Benzarti et al. (2012)] have referred Syamlal – O'Brien drag model and few more researchers [Visuri et al. (2012), Huang (2011)] have used Wen & Yu drag model. That is why these three drag models viz. Gidaspow, Syamlal – O'Brien and Wen & Yu are analysed in the present work.

With Gidaspow drag model

Exchange coefficients are different for different gas voidages. These are expressed as follows.

When $\varepsilon_g > 0.8$, $$K_{gs} = \frac{3}{4} C_D \frac{\varepsilon_s \varepsilon_g \rho_g \left|\vec{u}_g - \vec{u}_s\right|}{d_p} \varepsilon_g^{-2.65} \tag{2.19}$$

When $\varepsilon_g \leq 0.8$ $$K_{gs} = 150 \frac{\varepsilon_s (1-\varepsilon_g)\mu_g}{\varepsilon_g d_p^2} + 1.75 \frac{\rho_g \varepsilon_s \left|\vec{u}_g - \vec{u}_s\right|}{d_p} \tag{2.20}$$

where $$C_D = \frac{24}{\varepsilon_g R_{ep}} \left[1 + 0.15 (\varepsilon_g R_{ep})^{0.687}\right] \tag{2.21}$$

The particle Reynolds number is defined as follows $$R_{ep} = \frac{\rho_g d_p \left|\vec{u}_g - \vec{u}_s\right|}{\mu_g} \tag{2.22}$$

With Syamlal – O'Brien drag model

For this model the exchange coefficient is expressed as

$$K_{gs} = \frac{3}{4} \frac{\varepsilon_s \varepsilon_g \rho_g}{v_{r,s}^2 d_p} . C_D \left(\frac{R_{ep}}{v_{r,s}}\right) \left|\vec{u}_g - \vec{u}_s\right| \tag{2.23}$$

$$\text{Where } C_D = \left(0.63 + \frac{4.8}{\sqrt{R_{ep}/v_{r,s}}}\right)^2 \tag{2.24}$$

$$\text{and } v_{r,s} = 0.5 \left(A - 0.06 . Re_p + \sqrt{(0.06 . Re_p)^2 + 0.12 Re_p (2.B - A) + A^2}\right) \tag{2.25}$$

A, B values differ for different conditions as per the following.

Case – I: $A = \varepsilon_g^{4.14}$ and $B = 0.8\, \varepsilon_g^{1.28}$ for $\varepsilon_g \leq 0.85$

Case – II: $A = \varepsilon_g^{4.14}$ and $B = \varepsilon_g^{2.65}$ for $\varepsilon_g > 0.85$

With Wen and Yu drag model

The exchange coefficient is expressed as

$$K_{gs} = \frac{3}{4} C_D \frac{\varepsilon_s \varepsilon_g \rho_g \left|\vec{u}_g - \vec{u}_s\right|}{d_p} \varepsilon_g^{-2.65} \tag{2.26}$$

The drag coefficient C_D is different for different Reynold numbers. These are

(i) $C_D = \frac{24}{\varepsilon_g R_{ep}} \left[1 + 0.15\left(\varepsilon_g R_{ep}\right)^{0.687}\right]$ for $R_{ep} < 1000$ (2.27)

(ii) $C_D = 0.44$ for $R_{ep} \geq 1000$ (2.28)

2.8.4.2 Solid - Solid Exchange Coefficient

The symmetric Syamlal (1987) model is recommended for a pair of solids where the solid-solid exchange coefficient K_{ss} has the following form:

$$K_{ss} = \frac{3(1+e_{ls}) + \left(\frac{\pi}{2} + C_{fr,ls}\frac{\pi^2}{8}\right)\varepsilon_s \rho_s \varepsilon_l \rho_l (d_l + d_s)^2 g_{0,ls}}{2\pi\left(\rho_l d^3{}_l + \rho_s d^3{}_s\right)} \left|\vec{v}_s - \vec{v}_l\right| \tag{2.29}$$

Where *l* is the l^{th} fluid phase, *s* is for the s^{th} solid phase particles

e_{ls} = the restitution coefficient

$C_{fr,ls}$= the coefficient of friction between the l^{th} and s^{th} solid-phase particles ($C_{fr,ls}$= 0)

d_l= the diameter of the l^{th} solid particles

d_s = the diameter of the s^{th} solid particles

$g_{0,ls}$= the radial distribution coefficient between l^{th} and s^{th} solid particles

2.8.5 Solid Pressure

For granular flow in the compressible regime (i.e. where the solid volume fraction is less than its maximum allow value), a solid pressure is induced which is calculated independently. This is used for the pressure gradient term ($\nabla . p_s$) in the granular-phase momentum equation. Because of use of Maxwellian velocity distribution for the particles, a granular temperature is

introduced into the model which appears in the expression for the solid pressure and viscosities. The solid pressure is composed of a kinetic term and a secondary term due to particle collisions [Lun et al. (1984)].

$$p_s = \varepsilon_s \rho_s \Theta_s + 2\rho_s(1+e_{ss})\varepsilon_s^2 g_{0,ss}\Theta_s \quad (2.30)$$

Where e_{ss} = the co-efficient of restitution for particle collisions

$g_{0,ss}$ = the radial distribution function

Θ_s = the granular temperature

The granular temperature Θ_s is proportional to the kinetic energy of the fluctuating particle motion. In ANSYS FLUENT a default value of 0.9 for Θ_s is used and can be adjusted to suit the particle type. The function $g_{0,ss}$ is a distribution function that governs the transition from the "compressible" condition with $\varepsilon_s < \varepsilon_{s,max}$ (where the spacing among the solid particles continues to decrease) to incompressible condition with $\varepsilon = \varepsilon_{s,max}$ (where there is no further decrease in space). The default value for $\varepsilon_{s,max}$ is taken as 0.63.

2.8.6 Radial Distribution Function

The radial distribution function g_o is a correction factor that modifies the probability of collision between grains when the solid granular phase becomes dense [Ding and Gidaspow (1990)]. This function may also be interpreted as the non-dimensional distance between spheres and is expressed as follows.

$$g_o = \frac{s + d_p}{s} \quad (2.31)$$

where *s* = the distance between grains and d_p = the diameter of particle.

From equation (2.31) it can be observed that for a dilute solid phase when s >> d_p, $g_o \to 1$.

In the limiting case for solid phase contact, (s is zero) $g_o \to \infty$.

For one solid phase, the non-dimensional distance: $g_o = [1 - (\frac{\varepsilon_s}{\varepsilon_{s,max}})^{1/3}]^{-1}$ (2.32)

2.8.7 Solid Shear Stresses

The solid shear stresses are constituted of shear and bulk viscosities arising from particle momentum exchange resulted due to translation and collision. A frictional component of viscosity can also be included to account for the viscous-plastic transition that occurs when particle of solid phase reach the maximum solid volume fraction. The collision, kinetics and the optional frictional parts are added to give the solid shear viscosity as expressed below.

$$\mu_s = \mu_{s,col} + \mu_{s,kin} + \mu_{s,fr} \tag{2.33}$$

2.8.7.1 Collision Viscosity

The collisional part of the shear viscosity modeled by Gidaspow et al. (1992) is mentioned below.

$$\mu_{s,col} = \frac{4}{5}\varepsilon_s\rho_s d_s g_{o,ss}(1+e_{ss})\left(\frac{\Theta_s}{\pi}\right)^{1/2}\alpha_s \tag{2.34}$$

2.8.7.2 Kinetic Viscosity

The kinetic part of the shear viscosity is modeled by Syamlal and O'Brien (1989) as

$$\mu_{s,kin} = \frac{\varepsilon_s d_s \rho_s \sqrt{\Theta_s \pi}}{6(3-e_{ss})}\left[1+\frac{2}{5}(1+e_{ss})(3e_{ss}-1)\varepsilon_s g_{o,ss}\right] \tag{2.35}$$

2.8.7.3 Bulk Viscosity

The bulk viscosity accounts for the resistances of the granular particles to compression and expansion. It is expressed in the following form [Lun et al. (1984)].

$$\lambda_s = \frac{4}{3}\varepsilon_s\rho_s d_s g_{o,ss}(1+e_{ss})\left(\Theta_s/\pi\right)^{\frac{1}{2}} \tag{2.36}$$

2.8.7.4 Frictional Viscosity

In dense flow at low shear, where the secondary volume fraction for a solid phase approaches the packing limit, the stress is generated mainly due to friction between particles. In the

present work, the following expression for frictional viscosity [Schaeffer et al. (1987)] is considered.

$$\mu_{s.fr} = \frac{p_s \sin\phi}{2\sqrt{I_{2D}}} \tag{2.37}$$

where, p_s is the solids pressure, ϕ is the angle of internal friction, and I_{2D} is the second invariant of the deviatoric stress tensor.

2.8.8 Granular Temperature

The granular temperature for the s[th] solids phase is proportional to the kinetic energy resulted by random motion of particles. The transport equation derived from kinetic theory takes the following form.

$$\frac{3}{2}\left[\frac{\partial}{\partial t}(\rho_s \varepsilon_s \Theta_s) + \nabla.(\rho_s \varepsilon_s \vec{v}_s \Theta_s)\right] = \left(-p_s \bar{\bar{I}} + \bar{\bar{\tau}}_s\right) : \nabla.\vec{v}_s + \nabla.\left(K_{\Theta_s} \nabla.\Theta_s\right) - \Upsilon_{\Theta_s} + \Phi_{ls} \tag{2.38}$$

Where $\left(-p_s \bar{\bar{I}} + \bar{\bar{\tau}}_s\right) : \nabla.\vec{v}_s$ = the generation of energy by solid stress tensor

$K_{\Theta_s} \nabla.\Theta_s$ = the diffusion of energy

K_{Θ_s} = the diffusion co-efficient

Υ_{Θ_s} = the collisional dissipation of energy

Φ_{ls} = the energy exchange between the *l*[th] and s[th] solid phase particles

$K_{\Theta_s}.\nabla.\Theta_s$ describes the diffusive flux of granular energy. The diffusion coefficient for granular energy, K_{Θ_s} is given by the following expression [Syamlal and O'Brien (1989)].

$$K_{\Theta_s} = \frac{15\, d_s \rho_s \varepsilon_s \sqrt{\Theta_s \pi}}{4(41-33\eta)}\left[1 + \frac{12}{5}\eta^2(4\eta-3)\varepsilon_s g_{0,ss} + \frac{16}{15\pi}(41-33\eta)\eta\varepsilon_s g_{0,ss}\right] \tag{2.39}$$

Where $\eta = \frac{1}{2}(1+e_{ss})$

The collisional dissipation of energy, Υ_{Θ_s} represents the rate of energy dissipation within the s[th] solid phase due to collision between particles [Lun et al. (1984)]. This term is represented by the following expression.

$$\Upsilon_{\Theta_m} = \frac{12(1-e_{ss}^2)g_{0,ss}}{d_s\sqrt{\pi}} \cdot \rho_s \varepsilon_s^2 \Theta_s^{3/2} \tag{2.40}$$

The transfer of kinetic energy (resulted by the random fluctuations in particle velocity) from the s^{th} solid phase to the l^{th} fluid or solid phase is represented by ϕ_{ls} which is written as

$$\phi_{ls} = -3K_{ls}\Theta_s \tag{2.41}$$

2.8.9 Turbulence Model

To describe the effect of turbulent fluctuations in velocities in a multiphase flow, large numbers of terms are to be modeled in the momentum equations. This makes the modeling of turbulence in multiphase simulations extremely complex. There are three methods for modeling turbulence in multiphase flow.

(i) Mixture Turbulence Model

(ii) Turbulence Model for each phase

(iii)Dispersed Turbulence Model

2.8.9.1 K – ε Dispersed Model

In the present work dispersed turbulence model is applied. This model is applicable only when there is clearly one primary continuous phase and rest are dispersed dilute secondary phases. In this case, interparticle collisions are considered to be negligible and the dominant process in the random motion of the secondary phase is the influence of the primary phase turbulence. Fluctuations in the quantities of the secondary phases can therefore be defined in terms of the mean characteristics of the primary phase and the ratio of the mean particle relaxation time to eddy particle relaxation time.

(a) Turbulence in the continuous phase :

The eddy viscosity model is used to calculate average fluctuations in the quantities. The Reynolds stress tensor for continuous phase, $\overline{\overline{\tau_q}}$ is expressed in the following form.

$$\bar{\bar{\tau}}_q'' = -\frac{2}{3}\left(\rho_p k_q + \rho_q v_{tq} \cdot \nabla \cdot \vec{U}_q\right)\bar{\bar{I}} + \rho_q v_{tq}\left(\nabla \cdot \bar{\bar{U}}_q + \nabla \cdot \vec{U}_q^T\right) \tag{2.42}$$

Where, $\vec{U}_q$ is the phase-weighted velocity.

The turbulent viscosity $\mu_{t,q}$ is written in term of the turbulent kinetic energy of phase q as per the following expression.

$$\mu_{t,q} = \rho_q C_\mu \frac{k_q^2}{\varepsilon_q} \tag{2.43}$$

The characteristic time of the energetic turbulence eddies is defined as:

$$\tau_{t,p} = \frac{3}{2} C_\mu \frac{k_q}{\varepsilon_q} \tag{2.44}$$

Where, $\varepsilon_q$is the dissipation rate and C_μ is the coefficient (= 0.9 in the present case).

The length scale of the turbulent eddies is written as:

$$L_{t,q} = \sqrt{\frac{3}{2}}\, C_\mu \frac{k_q^{3/2}}{\varepsilon_q} \tag{2.45}$$

Turbulent predictions are obtained from the modified $K-\varepsilon$ model as follows:

$$\frac{\partial}{\partial t}(\varepsilon_q \rho_q k_q) + \nabla.(\varepsilon_q \rho_q \vec{U}_q k_q) = \nabla.\left(\varepsilon_q \frac{\mu_{t,q}}{\sigma_k} \nabla k_q\right) + \varepsilon_q \rho_q \varepsilon_q + \varepsilon_q \rho_q \Pi_{k_q} \tag{2.46}$$

and

$$\frac{\partial}{\partial t}(\varepsilon_q \rho_q \varepsilon_q) + \nabla.(\varepsilon_q \rho_q \vec{U}_q k_q) = \nabla.\left(\varepsilon_q \frac{\mu_{T,q}}{\sigma_\varepsilon} \nabla \varepsilon_q\right) + \varepsilon_q \frac{\varepsilon_q}{k_q}(C_{1\varepsilon} G_{kq} - C_{2\varepsilon} \rho_q \varepsilon_q) + \varepsilon_q \rho_q \Pi_{\varepsilon q} \tag{2.47}$$

Here $\Pi_{k_q}$and Π_{ε_q}represent the influence the dispersed phase on the continuous phase q, and $G_{k,q}$ is production of turbulence in kinetic energy.

The term $\Pi_{k_q}$is derived from the instantaneous equation of the continuous phase and is written in the following form:

$$\Pi_{kq} = \sum_{p=1}^{M} \frac{k_{pq}}{\alpha_q \rho_q} \left(k_{pq} - 2k_q + \vec{v}_{pq}.\vec{v}_{dr}\right) \tag{2.48}$$

M represents the number of secondary phases.

(b) Turbulence in the dispersed phase :

Time and length scale which characterize the motion are used to evaluate dispersion coefficient correlation function of the turbulent kinetic energy for each dispersed phase. The characteristic relaxation time connected with inertial effects acting on a dispersed phase p is defined as:

$$\tau_{F,pq} = \varepsilon_p \rho_q K_{pq}^{-1} \left(\frac{\rho_p}{\rho_q} + C_v \right) \tag{2.49}$$

The Lagrangian integral time scale is calculated along the particle trajectories and is observed to be affected mainly by the crossing trajectories. This is defined as

$$\tau_{t,pq} = \frac{\tau_{t,q}}{\sqrt{(1+C_\beta \xi^2)}} \tag{2.50}$$

Where $\xi = \frac{|\vec{v}_{pq}|\tau_{t,q}}{L_{t,q}}$ (2.51)

and $C_\beta = 1.8 - 1.35(\cos\theta)^2$ (2.52)

where, θ is the angle between the mean particle velocity and the mean relative velocity.

The ratio between these characteristic times is written as:

$$\eta_{pq} = \frac{\tau_{t,pq}}{\tau_{F,pq}} \tag{2.53}$$

Turbulence terms for dispersed phase, p are written as:

$$k_p = k_q \left(\frac{b^2+\eta_{pq}}{1+\eta_{pq}} \right) \tag{2.54}$$

$$k_{pq} = 2k_q \left(\frac{b+\eta_{pq}}{1+\eta_{pq}} \right) \tag{2.55}$$

$$D_{t,pq} = \frac{1}{3} k_{pq} \tau_{t,pq} \tag{2.56}$$

$$D_p = D_{t,pq} + \left(\frac{2}{3} k_p - b \frac{1}{3} k_{pq} \right) \tau_{F,pq} \tag{2.57}$$

$$b = (1 + C_v) \left(\frac{\rho_p}{\rho_q} + C_v \right) \tag{2.58}$$

$C_v = 0.5$ is the added mass coefficient.

2.9 Previous Works on CFD Simulation for Two Phase Fluidized Bed Reactor

A number of independent variables such as particle density, size, and shape can influence hydrodynamic behaviours of fluidized bed [Kunii and Levenspiel (1991), Ranade (2002), Grace and Taghipour (2004)]. Gobin et al. (2003) numerically have simulated a fluidized bed using two-phase flow method. In their work, time-dependent simulations have been performed for operating conditions of industrial and pilot plant reactor. The numerical predictions are found to be in good qualitative agreement with the observed behavior in terms of bed height, pressure drop and mean flow regimes. Goldschmidt et al. (2004) have compared a hard-sphere discrete particle model with a two-fluid model containing kinetic theory closure equations using appropriate experimental data. Their results indicate that both the CFD models predict adequate fluidization regimes, trends in bubble size and bed expansion. Whereas predicted bed expansion dynamics are observed to differ significantly from the experimental results. Behjat et al. (2008) have simulated a gas-solid fluidized bed, based on the Eulerian description of the phases and multiphase fluid dynamic model. They have considered the following assumptions.

(i) Solid particles release a constant amount of heat.

(ii) Fine polymer particles have higher activity.

(iii) Fine particles generate more heat than coarse particles.

Their results indicate that with two solid phases, particles with smaller diameters have a lower volume fraction at the bottom of the bed and a higher volume fraction at the top of the bed. In addition, it is also revealed that bed expansion is larger for a bimodal particle mixture in comparison with the mono dispersed particles.

The flow behaviours of a lab-scale fluidized bed are studied computationally [Chiesa et al. (2005)]. The influence of inter particle force is studied on flow behaviour [Rhodes et al. (2001)]. The results obtained from a 'discrete particle method' (DPM) are compared qualitatively with that of a multi fluid computational fluid dynamic (CFD) model. Experimental study on the hydrodynamics of a gas-fluidized beds have been carried out by Valverde[a,b] et al. (2003) with the effects of particle size and interparticle forces. Hydrodynamic behaviours of gas-solid fluidized bed reactor are also investigated by several researchers by using multi fluid Eulerian model where the effects of particle size and superficial gas velocity have been studied [Taghipour et al. (2005), Hamzehei et al. (2010), Sau and Biswal (2011)]. CFD simulation results have been compared with those obtained from the experiments with respect to bed expansion, gas–solid flow patterns, instantaneous and time-average local voidage profiles.

Simulations for minimum fluidization, bubbling and slugging velocities have also been carried out using four types of Geldart particles by Labview method [Shaul et al. (2012)]. Lettieri et al. (2004) have used the Eulerian-Eulerian granular kinetic model (CFX-4 code) to simulate the transition from bubbling to slugging fluidization at four fluidizing velocities. Results from simulations have been analyzed in terms of voidage profiles and bubble size which showed typical features of a slugging bed. Good agreement between the simulated and predicted transition velocity is also obtained.

The knowledge of particulate mixing and segregation, bubble formation and shear forces would be useful in the design and operation of bubbling fluidized-bed reactors [Van Wachem[a] (2001), Rasul et al (1999), Cooper and Coronella (2005)]. Huilin et al. (2003) have studied bubbling fluidized bed of the binary mixtures with multi-fluid Eularian CFD model. Their simulation results showed that hydrodynamics of gas bubbling fluidized bed are related with the distribution of particle sizes and the amount of dissipated energy in particle–particle

interactions. Van Wachem et al. (1998) verified Eulerian-Eulerian gas-solid model simulations of bubbling fluidized beds with existing correlations for bubble size or bubble velocity.

In recent years, hydrodynamics of gas–solid fluidized beds of binary mixtures have been extensively investigated by experimental and computational methods. Attention mostly has been given on the minimum fluidization velocity and the segregation / mixing behavior of binary mixtures [Chiba et al. (1979), Noda et al. (1986)]. The variables affecting the mixing/segregation behavior have been studied by many researchers [Garcia et al. (1989), Wu and Baeyens (1998), Marzocchella et al. (2000), Formisani et al. (2001)]. The segregation mechanism has also been studied [Hoffmann et al. (1993), Olivieri et al. (2004), Joseph et al. (2007)]. Direct particle–particle heat transfer is thought to be significant in a gas–solid fluidized bed. Wen and Chang (1967) seems to be the first group to investigate the particle–particle heat transfer in a gas–solid fluidized bed. It is found that the particle–particle heat transfer covered 10–35% of the global heat transfer. Delvosalle and Vanderschuren (1985) have developed an inter-particle heat transfer model due to conduction through the gas layer between hot and cold particles. Their results have indicated that the ratio of particle–particle heat transfer coefficient to gas-particle heat transfer coefficient can reach to 20–50% for particle size variation in the range of 2.25 to 0.9 mm. McKenna et al. (1999) have pointed out that heat transfer between the large and small particles within the same reactor helps to reduce the problem of overheating. However, Mansoori[a] et al. (2002) have concluded that the effect of particle–particle heat transfer is insignificant on mean particle and gas temperatures. It is further observed that heat transfer is dominated by the particle–gas convection for the condition of their study.

CFD simulation of a fluidized-bed reactor has been conducted by Fan (2006). Chemical kinetics has been focused with the effects of intraparticle heat and mass transfer

rates, polydisperse particle distributions and multiphase fluid dynamics. Kaneko et al. (1999) have analyzed numerically the temperature profiles for solid and gas phases in a fluidized bed reactor by applying a discrete element method. They estimated heat transfer from particles to the gas using Ranz–Marshall equation. They have focused on the chemical kinetics, intraparticle heat and mass transfers, poly-disperse particle distributions and multiphase fluid dynamics. Van Wachem[b] et al. (2001) have developed CFD model for fluidized beds containing a mixture of two particles. Bed expansion of a binary mixture of different particle sizes is observed to be much higher than that of a system of mono-sized particles.

Many researchers have focused on the effect of temperature on minimum fluidization velocity and voidage [Xu and Zhu[b] (2006), Formisani et al. (1998, 2002), Guo et al. (2003), Subramani et al (2007)]. Geldart & Kapoor (1967) have studied the effect of temperature on the minimum bubbling velocity and bubble diameter for Group-A particles. Kai & Furusaki (1985) have found the same trend for the bubble size in the fluidization of the FCC and alumina particles in the temperature range of 280-400 K. Hatate et al. (1988) have reported a rise in the bubble size by increasing temperature from ambient to 600 K in fluidization of Group-B particles whose trend is different from that of Geldart-A particles.

The collisions of particles may actually occur when there is a gas film separating adjacent particles. The restitution coefficient (e) characterizes the energy dissipated during particle collisions [Du et al. (2006), Huilin et al. (2003, 2007)]. This is certainly a factor to be considered. However, Gidaspow and Lu (1998) have suggested an "effective restitution coefficient" nearly equal to 1. In the studies of literatures [Roy and Dudukovic (2001), Cheng and Zhu (2005), and Lettieri et al. (2006)], it is observed that the granular flow model has been applied to liquid-solid fluidized beds where coefficient of restitution has been considered to be less than one (implying inelastic collisions). They have also considered no explicit condition indicating that this approach is independent of collisions. In the first two

cases, good agreement is claimed between predicted and experimental results. Whereas the CFD model in the third case failed to predict a high superficial velocity flow transition. Two dimensional multi fluids Eulerian CFD model with closure laws has also been applied to study the effect of the restitution coefficient on the hydrodynamics of dense gas phase fluidized beds [Goldschmidt et al. (2001)]. Li and Kuipers (2007) have studied the effect of restitution and friction coefficients on formation, growth and coalescence of bubbles in a discrete model. Coroneo et al. (2011) have investigated the behaviour of solid particles for different gas velocities (0.10, 0.12, 0.14 m/s) at different restitution coefficients (0.60, 0.70, 0.80, 0.90, 0.99). Tagliaferri et al. (2013) have also studied the effect of restitution coefficient and integration methods for bidisperse mixtures (i.e. equal density and different size) in a fluidized bed. Taghipour et al. (2005) have considered the effect of particle-particle interactions to obtain realistic simulations using a fundamental hydrodynamics model. It is observed that the restitution coefficient values do not affect significantly neither with solid volume fraction nor with axial particle velocity [Neri and Gidaspow (2000), McKeen and Pugsley (2003)] thereby indicating that restitution coefficient plays a minor role in the fluidization of fine particles.

The Specularity coefficient measures the fraction of collisions which transfers the momentum to wall. A small value of specularity coefficient i.e. the free-slip boundary condition gives less friction [He and Simonin (1993), Benyahia (2005)]. Mansoori[b] et al. (2002) have carried out simulations for gas-solid turbulent upward flow in a vertical pipe using k-ε turbulence modeling and Eulerian-Lagrangian approach. Particle-particle and particle-wall collisions are simulated based on deterministic approach. The influence of particle collisions on the particle concentration, mean temperature and fluctuating velocities is also investigated. The profiles of particle concentration, mean velocity and temperature are

seen to be flat with consideration of interparticle collisions. It is also demonstrated that the effect of interparticle collisions has a dramatic influence on the particle fluctuation velocity.

Lettieri et al. (2000, 2001) have reported a case, where interparticle forces can be dominant. They studied the fluidization of fresh and used FCC catalysts at temperatures up to 650ºC. The large deviation between calculated and measured pressure drops for FCC and doped silica catalysts at 200ºC shows that the interparticle forces become important at this temperature. Effect of temperature on solids mixing and phase dynamics for Group-A and B particles have already been previously studied in the temperature range of 25-400ºC [Cui et al. (2003), Cui and Chaouki (2004), Radmanesh et al. (2005)].

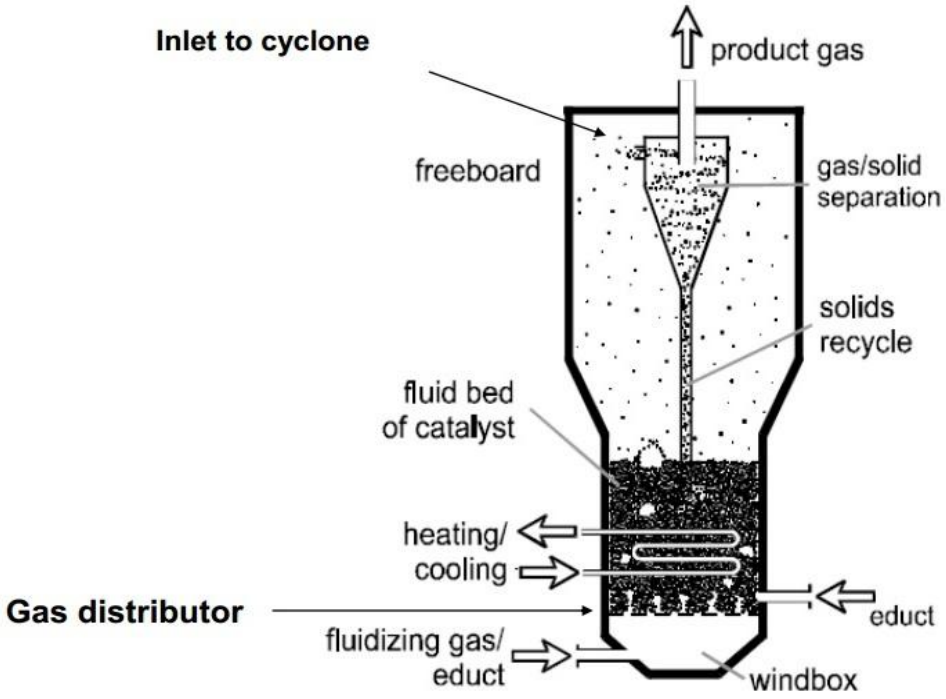

Fig.-2.1: Components of fluidized bed reactor

CHAPTER -3

EXPERIMENTATION

From the literature it is known that metal particle is required to convert gaseous fluoride to solid metal fluorides. Waste material produced from Aluminium industry (Red Mud) is found to have many metals whose composition is shown in **Table – 3.1** [Chaddha et al. (2007), Reddy and Chandra (2014)]. That is why Red Mud is selected as bed material for fluidization. Several experiments have been carried out to study bed hydrodynamics and reactions using a fluidized bed reactor. Different sized solid particles with different densities have been used as bed materials in the fluidized bed reactor (FBR).

3.1. BED HYDRODYNAMICS

Hydrodynamic studies for FBR have been carried out by varying different system parameters viz. static bed height, particle size and superficial air velocity. Schematic diagram and laboratory view of the experimental set up are shown in **Fig. – 3.1** and **Fig. – 3.2** respectively.

3.1.1 Components of Experimental Set-Up for Hydrodynamics

Different components of the experimental set-up are as follows :

a). Air Compressor:

It is a multistage air compressor with a capacity of 25 kgf/cm^2.

b). Air Accumulator / Receiver:

It is a horizontal cylindrical vessel used for storing the compressed air from compressor. There is one G.I. pipe inlet to the accumulator and one by-pass line from one end of the vessel. The exit line is also a G.I. pipe taken from the central part of the vessel. The purpose of using the air accumulator in the line is to dampen the pressure fluctuations. The operating pressure in the vessel is kept at 20 psig.

c). Pressure Gauge:

A pressure gauge in the required range (1-50 psig) is fitted in the line for measuring the working pressure. The pressure gauge is fitted with the air accumulator / receiver.

d). Silica Gel Tower:

A silica gel tower is used for absorbing moisture content from the supplied air which is provided in the line immediately after the air receiver to arrest the moisture carried by air from the receiver / air accumulator.

e). Valves:

A globe valve of ½ inch (1.27 cm) ID is also provided in the by-pass line for sudden release of line pressure. A gate valve of 1/2 inch (1.27 cm) ID is also provided in the line just before Rotameter to control the rate of flow of air to the fluidizing bed.

f). Rotameter:

A Rotameter (0-10 lpm) is used in the line for measuring the rate of flow air which is used as the fluidizing medium.

g). Air Calming Section:

The conical bottom part of the set up is known as the Calming section. This part is an important component of the experimental set-up. The cone is made of ordinary G.I. sheet. The inside hollow space of the calming section (i.e. cone) is filled with spherical glass beads of size 5 mm for uniform distribution of air. Its dimensions are as follows.

Large end diameter = Same as column diameter (12 cm)

Small end diameter = Same as outlet pipe diameter (3 cm)

Height / Length = 30 cm

Cone angle = about 30^{o}

h). Air Distributor:

A filter cloth placed over the calming section is used as the air distributor for fluidization process. Opening of this filter cloth are of 40 microns in diameter.

i). Fluidizer:

A cylindrical column of 12 cm inside diameter and 70 cm height is used as the fluidizer and is made up of transparent Perspex material. Bottom end of fluidizer is fixed to the flanged conical bottom. Top end is kept open. Two pressure tapings are provided for noting the bed pressure drop.

j). Flanges:

Flange joint is used to attach the bottom / calming section to cylindrical column. Details of flange are as follows.

Flange thickness = 2 cm

No. of bolts = 4

Bolt Size = ¼" (0.635 cm)

Gasket material : Asbestos

Gasket thickness = 0.5 cm

Gasket width = 2 cm

k). Manometer Panel Board:

A U-tube manometer is used to measure the bed pressure drop. Mercury is used as the manometric fluid for single sized particle system while carbon tetra chloride is used for binary mixtures during the fluidization process.

3.1.2 Experimental Procedure

The calming section is packed with spherical glass beads of 5 mm in size for uniform distribution of fluid to avoid channelling. Filter cloth is tightly attached to the column with the help of a gasket so that there is no leakage of air. The column is loaded with fine particles

upto certain heights. The column is also covered with a filter cloth at the top to prevent the entrainment of the particles. Air is supplied from the bottom of the column to the bed through the distributor at the ambient conditions. A Rotameter and a U-tube manometer are connected to the fluidizer for measuring the flow rate of air and bed pressure drop respectively. The bed pressure drop and expanded bed heights (maximum and minimum heights within which the bed fluctuates) are noted against each air flow rate.

The same procedure is repeated for different static bed heights and different particle sizes / densities of bed materials. The variations of different system parameters are discussed in scope of the experiment for single sized and binary mixtures of particles in **Table – 3.2** and **Table – 3.3** respectively. The bed dynamics (i.e. bed expansion / fluctuation ratio and fluidization index) are calculated by using eq^{n} 2.1, 2.2 and 2.3 respectively for knowing the fluidization characteristics of bed materials.

3.2 REACTION ASPECTS

Solid particles with different sizes / densities have been used as bed materials in the FBR for studying the abatement of fluorides at high temperature. Schematic diagram and laboratory view of experimental set up for reaction studies are shown in **Fig. – 3.3** and **Fig. – 3.4** respectively.

3.2.1 Components of High Temperature Fluidized Bed Reactor

Different components of the FBR are as follows:

a). Air Blower:

An air blower of the specification 2850 RPM, 180 Watts, 230 Volts, 50 Hz Amps and Temperature rise of 3-82.5^{0}C (276 – 355.5K) is used to fluidize the bed material.

b). Reactor Column:

FBR used in the laboratory is a cylindrical vessel with conical ends. The removable bolt joint between the cone and the reactor shell is provided with iron heat gasket to prevent

leakage. Reactor is made up of Stainless Steel 316 grade material and is able to withstand pressures upto 5 atm.

The dimensions of the reactor shell are: Length = 70 cm

Internal Diameter = 12 cm

Wall thickness = 1 cm

The dimensions of conical end: Large end diameter = 12 cm

Small end diameter = 2.55 cm

Height / Length = 10 cm

Cone angle = 30^{o}

Thickness = 1 cm

c). Heaters:

A ceramic heater surrounds FBR (upto 11.5 cm from bottom of column). This is capable of heating upto a maximum temperature of 500^{0}C and a tubular heater is provided just after the air blower in the setup as shown in **Fig. – 3.3**. This tubular heater uses Nichrome wire to heat the tube and is capable of heating air upto a maximum temperature of 100^{0}C. The dimension of tubular heater is as follows.

Length = 30.5 cm

Internal diameter = 3.81 cm

Thickness = 1 cm

Thickness of Nichrome wire = 0.12 cm

d). Gas distributor:

The large end of the cone is fitted with wire meshes of size approximately 40 microns. The wire mesh acts as the gas distributor to fluidize the bed materials.

e). Air Valves:

The reactor is also provided with two ½ inch (1.27 cm) gate valves and one ½ inch (1.27 cm) globe valve. The globe valve is used to maintain the steady air flow rate from the air blower. The gate valves are used either to allow the air to circulate or to stop at certain points.

3.2.2 Experimental Procedure for Fluidized Bed Reaction

A wired mesh with pores of approx. 40 microns is placed in between the lower flange of the reactor and the conical bottom to prevent the backflow of bed materials. This is tightly attached to the column with the help of a gasket, so that there is no leakage of air. Then the material is loaded in the reactor column. Air is passed through the bed by an air blower. The ceramic heater as well as the tubular heater is switched on for getting maximum temperature of bed material inside the reactor.

Characteristics of Red Mud fluidized at different temperature are studied in first stage of experiment for which about 1 kg of Red Mud (77 microns) is fluidized by air. The bed material is heated to maximum temperature (500^0C). Then the characteristics of Red Mud at different temperatures is analysed by different characterizing techniques. In the second stage of experiment, same amount of Red Mud is fluidized by the mixture air and effluent gas (collected from Aluminium industry). The air is supplied by the blower and the Effluent gas is supplied from the stainless steel sampling cylinder. This Effluent gas is supplied as a secondary medium. The bed material is allowed to fluidize at a temperature of 250°C and a residence time of 30 minutes is given for proper mixing of secondary medium with the bed materials. Then the samples of bed materials are collected for characterization.

In the third stage of experiment, 900 grams of Red Mud (77 microns) and 100 grams (83 microns) of Aluminium powder are used as bed materials. This binary mixture of bed materials is fluidized with the mixture of air and Effluent gas at 250^0C with a residence time

of 30 minutes. Aluminium powder size is taken as 83 microns slightly larger than Red Mud size for which this acts as lubricant to fine Red Mud and enhances quality of fluidization implying catalytic action. The characteristics of the binary mixtures of Red Mud and Aluminium powder are also analyzed before and after experiments with different characterization techniques.

To further compare the experimental results obtained with Red Mud another bed material (Sand) is selected for investigation. In the fourth stage of experiment, 1000 grams of Sand (77 microns) is fluidized by the mixture of air and effluent gas. The Sand particles are allowed to fluidize at same conditions i.e. temperature of 250°C and residence time of 30 minutes. Then the bed material samples are collected for analysis which indicates the non-catalytic condition.

The different characterizing techniques i.e. X-Ray Diffraction (XRD), Fourier Transform Infrared Spectroscopy (FTIR), Thermo Gravimetric Analysis (TGA), Differential Thermal Analysis (DTA), Field Emission Scanning Electron Microscopy (FESEM), Energy Dispersive X-ray Spectroscopy (EDX), Inductively Coupled Plasma Mass Spectrometry (ICP-MS), Particle Size Analysis (PSA) and Brunauer – Emmett – Teller (BET) analysis are used in the present work and listed in **Table - 3.4**.

The XRD pattern of the material and the material composition are analyzed using PHILIPS X'Pert X-Ray diffractometer with a Cu Kα radiation source in a 2θ range of 10^0 to 70^0 at spanning range of 3° min^{-1}. The FT-IR spectra of the samples are obtained by using Perkin Elmer FT-IR Spectrometer (Spectrum RX-I). The range is taken between 4000 - 400 cm^{-1}. Each of the samples is mixed with anhydrous Potassium Bromide (KBr) and is then pressed at 10 tons/cm^2 pressure to make translucent tablets required for recording of FT-IR spectra.

The TGA and DTA analysis are carried out using SHIMADZU DTG - 60H. In this analysis 17.361 mg of the sample is used at room temperature. The sample is heated in an alumina crucible from 28°C to 500°C at a heating rate of 10°C min^{-1} in N_2 atmosphere where the gas flow rate is maintained at 35 ml min^{-1}. FESEM and EDX analysis are used to study the surface morphology and elemental composition of the samples respectively using NOVA NANO SEM 450. ICP-MS analysis is carried out at NML Jamshedpur to find the elemental composition of the samples. The particle sizes of the samples are measured using MALVERN MASTERSIZER (Hydro 2000MU and Range: 0.02µ to 2000µ). The surface area of the samples is also measured by BET apparatus (QUANTACHROME AUTOSORB-1) using liquid Nitrogen.

Table - 3.1: Typical composition of Red Mud

Composition	Weight %
Fe_2O_3	30-60
Al_2O_3	10-20
SiO_2	3-50
Na_2O	2-10
CaO	2-8
TiO_2	25

Table – 3.2: Scope of experiment for single sized fine particles

SL.NO.	Bed Materials	Static Bed Height (H_s), cm	Particle Size (d_p), µm	Particle Density (ρ_s), kg/m^3
1	Red Mud	8	77	1300
2	Red Mud	10	77	1300
3	Red Mud	12	77	1300
4	Red Mud	14	77	1300
5	Red Mud	10	58	1300
6	Red Mud	10	98	1300
7	Red Mud	10	116	1300
8	Aluminium	10	77	1100
9	Sand	10	77	1500

Table – 3.3: Scope of experiment for binary mixture of fine particles

SL.NO.	Bed Materials	Weight. Ratio (w_1:w_2), %	Average Particle Size ($d_{p,avg}$), µm *	Average Particle Density ($\rho_{s,\ avg}$), kg/m^3 *
1	Red Mud + Aluminium	95 : 05	77.3	1290
2	Red Mud + Aluminium	90 : 10	77.6	1280
3	Red Mud + Aluminium	85 : 15	77.9	1270
4	Red Mud + Aluminium	80 : 20	78.2	1260
5	Red Mud + Aluminium	90 : 10	75.1	1280
6	Red Mud + Aluminium	90 : 10	76.2	1280
7	Red Mud + Aluminium	90 : 10	79.1	1280

***Formula:** $d_{p,\ avg} = w_1 d_{p1} + w_2\ d_{p2}$

$\rho_{s,\ avg} = w_1 \rho_{s1} + w_2\ \rho_{s2}$

Table - 3.4: List of apparatus used for characterisation of samples

Sl. No.	Analysis	Equipment	Range
1	XRD Analysis	PHILIPS X'Pert X-Ray diffractometer	2θ range of 10^0 to 70^0 (spanning range of 3° min^{-1})
2	TGA Analysis	SHIMADZU DTG	28°C to 500°C (N_2 atmosphere)
3	Differential Scanning Calorimetry	SHIMADZU DTG	28°C to 500°C (N_2 atmosphere)
4	Particle Size	MALVERN MASTERSIZER (Hydro 2000MU)	0.02µ to 2000µ
5	FESEM	NOVA NANO SEM 450	-
6	Energy Dispersive X-Ray	NOVA NANO SEM 450	-
7	FT-IR spectra	Perkin Elmer FT-IR Spectrometer (Spectrum RX-I)	4000-400 cm^{-1}
8	Surface Area	BET (QUANTACHROME AUTOSORB-1)	-

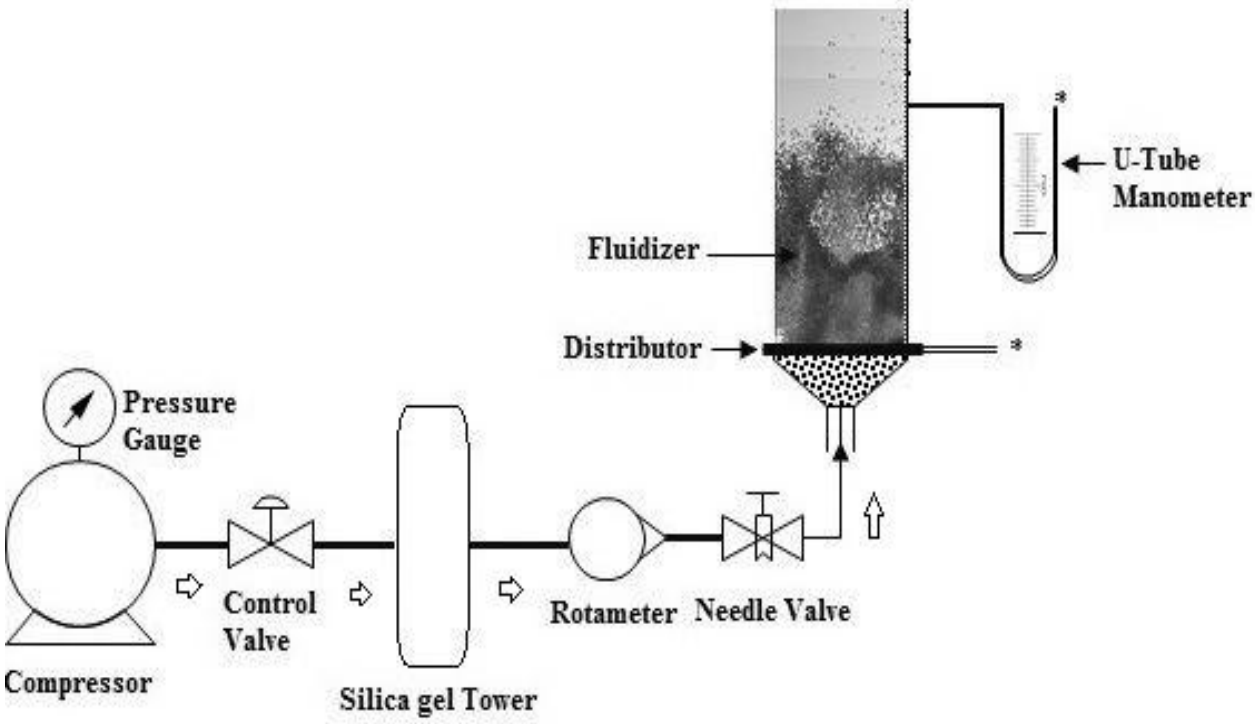

Fig. – 3.1: Schematic view of the experimental set-up for studies on hydrodynamics

Fig. – 3.2: Laboratory view of the experimental set-up for studies on hydrodynamics

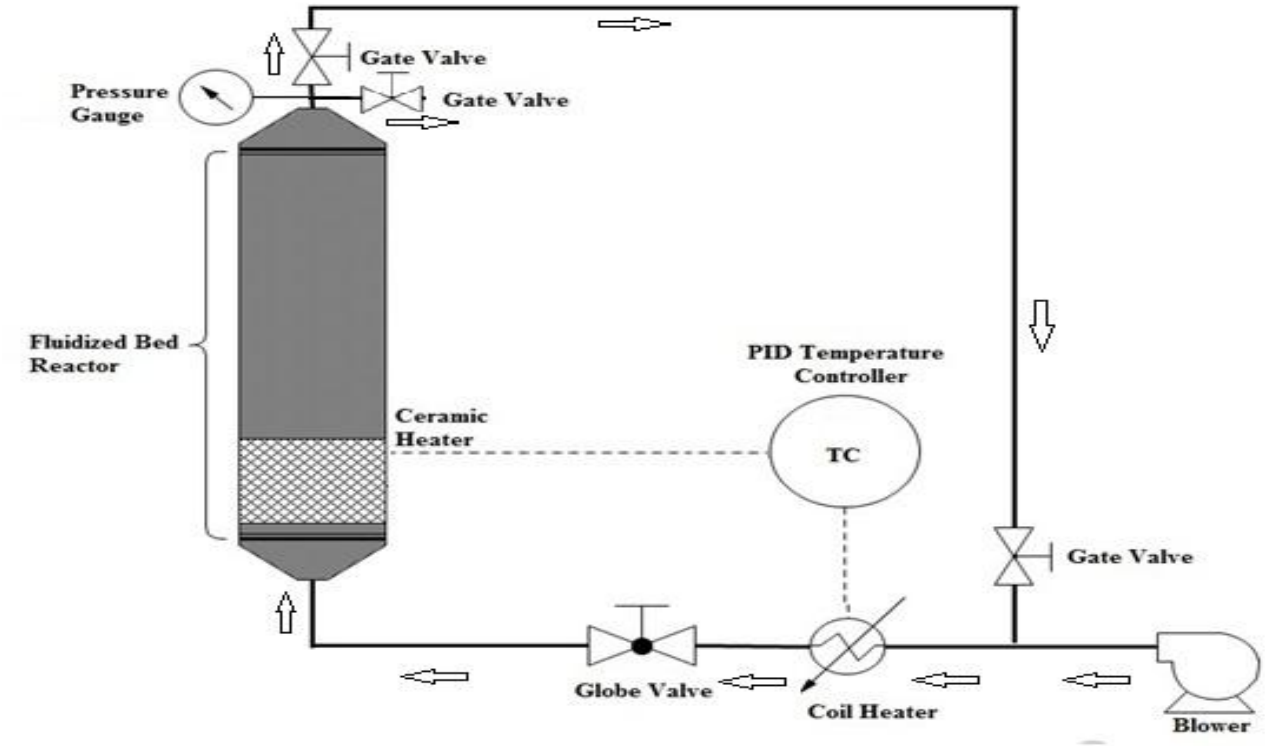

Fig. – 3.3: Schematic view of the experimental set-up for studies on reaction

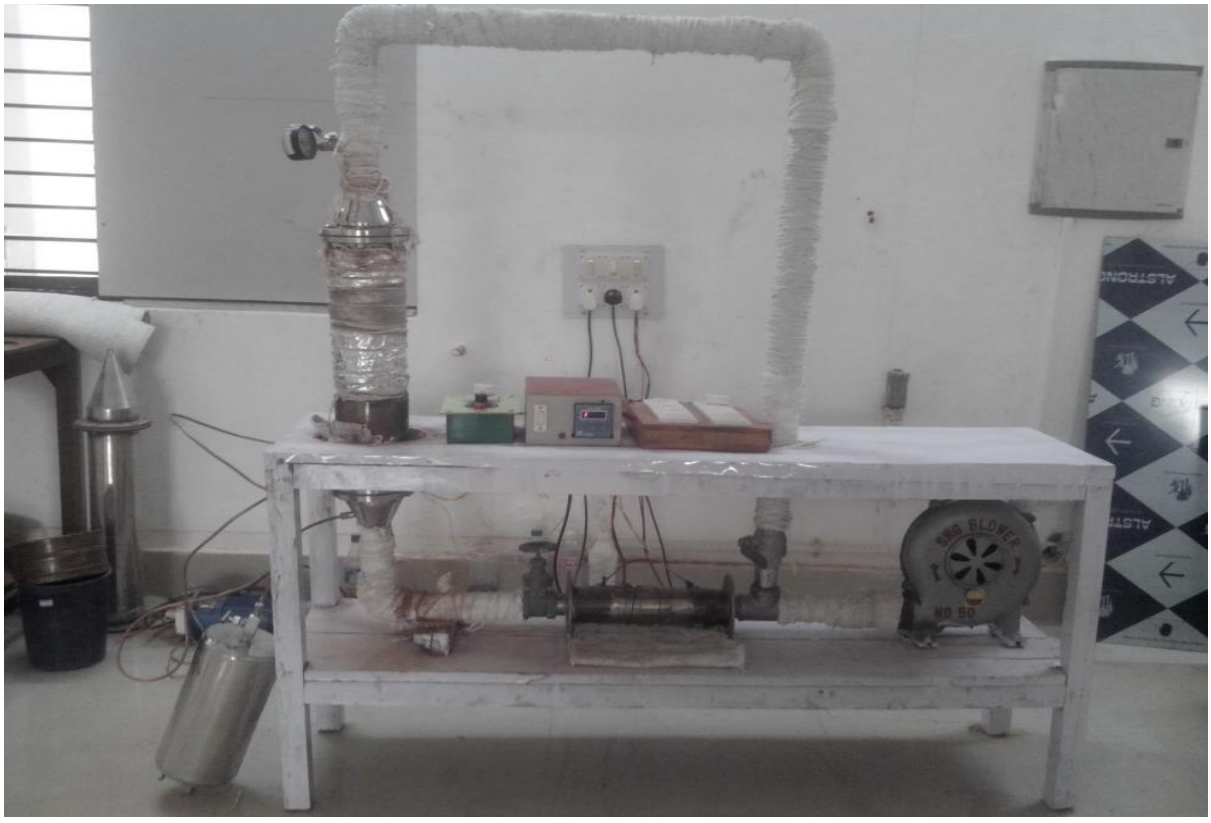

Fig. – 3.4: Laboratory view of the experimental set-up for studies on reaction

CHAPTER - 4

RESULTS AND DISCUSSION

4.0 HYDRODYNAMIC STUDIES

The hydrodynamic studies of the fluidized bed reactor have been carried out by analyzing the bed dynamics for single and binary mixtures of fine particles. The bed dynamics analyzed in this work are

- Bed Pressure Drop (Δp)
- Bed Expansion Ratio (R)
- Fluidization Index (FI)
- Minimum Fluidization Velocity (U_{mf})
- Bed Fluctuation Ratio (r)

4.1 SINGLE SIZED FINE PARTICLES

4.1.1 Effect of Particle Size, Static bed Height and Particle Density

The hydrodynamic studies of fluidized bed are carried out using single sized fine particles with different static bed heights (i.e. 8, 10, 12 and 14 cm). The minimum fluidization velocity, bed pressure drop, bed expansion and / or fluctuation ratio and fluidization index are analysed. The same procedure is repeated for different particle sizes and densities of bed materials.

4.1.1.1 Pressure Drop and Minimum Fluidization Velocity

The plots of bed pressure drop against fluidization velocity for fine particle systems are shown in **Fig. - 4.1**. **Fig. – 4.1 (a)** compares the pressure drop profile against fluidization velocity for different particle sizes. Similarly **Fig. – 4.1 (b)** and **(c)** compare the pressure drop profiles against fluidization velocity for different static bed heights and different bed materials respectively. It is observed that bed pressure drop increases with the increase in superficial velocity (U_o) for all the cases i.e. for different particle sizes, static bed heights and densities of bed materials. The bed pressure drop gradually increases with increase in superficial gas velocity upto a certain limit, after which it remains constant indicating the initiation of fluidization process. Again it is observed from **Fig. – 4.1 (a)** that the bed pressure

drop decreases with increase in particle size. This may be due to the presence of more voids in turn more number of air bubbles with large sized particles which causes free flow of particles. Thus the bed pressure drop reduces with increasing particle sizes.

Fig. - 4.1 (b) reveals that the bed pressure drop increases with increase in static bed heights. This may be due to more weight of bed materials with increased bed height needs more force to fluidize. The minimum fluidization velocity of Red Mud particles is observed to be 0.010 m/s for different sizes of particles as well as different static bed heights of fluidized bed. The reason for this may be that particle size difference is not much (i.e. in the range of 20 microns) and bed height as such does not affect the minimum fluidization velocity [Sau et al. (2007), Gunn and Hilal (1997), Cranfield and Geldart (1974)]. It is seen from **Fig. – 4.1 (c)** that the pressure drop increases with increase in density. This is obvious as increased weight of materials requires more force to fluidize. Lighter materials fluidize first for which Aluminium powder shows lower pressure drop and Sand shows higher pressure drop.

4.1.1.2 Bed Expansion Ratio (R)

The bed expansion ratio for different system parameters viz. particle sizes, static bed heights and bed materials are shown in **Fig. – 4.2**. **Fig. – 4.2 (a), 4.2 (b)** and **4.2 (c)** show the comparisons of bed expansion ratios (R) against superficial air velocity for different particle sizes, static bed heights and bed materials respectively. It is observed that the bed expansion ratio increases with the increase in superficial gas velocity (U_o) for all the cases. This may be due to the fact that when superficial gas velocity exceeds minimum fluidisation velocity more drag force is exerted and this causes the movement of materials thereby increasing the bed expansion. It is further observed that bed expansion decreases with increase in particle size, density and static bed heights. The reason may be due to fact that bigger size of particles, greater static bed heights or denser materials require more force to fluidize. As a result larger

sized, greater height and denser bed materials expand less. Therefore the bed expansion ratio (R) is observed to decrease in all the cases.

From **Fig. - 4.2 (c)** it is seen that Red Mud shows more expansion than that lighter (Aluminium) particles. Reason may be irregular shape and rough surface of Aluminium particles might be breaking the bubbles frequently thereby causing less bed expansion than smooth Red Mud particles.

4.1.1.3 Bed Fluctuation Ratio (r)

The bed fluctuation ratios for different system parameters of fine particles are shown in **Fig. – 4.3**. **Fig. – 4.3 (a), (b)** and **(c)** show the comparisons of bed fluctuation ratios against superficial air velocity for different particle sizes, static bed heights and particle densities respectively. It is observed that with increase in superficial gas velocity (U_o) the bed fluctuation ratios increase in all cases. This may be due to the formation of more gas bubbles with increased superficial gas velocity beyond minimum fluidization. From **Fig. – 4.3 (a)** and **(b)** it is observed that fluctuation ratio (r) decreases with increase in particle sizes and static bed heights. The reason remains same as for bed expansion ratio, i.e. larger size or greater weight of bed materials expand less. Alternately formation of large bubbles decreases in turn breakage of bubbles decreases. Thus fluctuation ratios decrease. From **Fig. – 4.3 (c)** it is observed that Red Mud shows less fluctuation than Sand and Aluminium particles. Although Aluminium particle is lighter than Red Mud it does not expand much but fluctuates more. The reason may be surface roughness and irregularities for which fluctuation might be more within a limited range of height of the bed. Smooth particles i.e. Red Mud shows least bed fluctuation because of less bubble breakage for which difference between H_{min} and H_{max} might be very less. Otherwise it can be said that minimum expanded bed height (H_{min}) does not decrease more for Aluminium particles than the other materials for which bed fluctuation becomes more.

4.1.1.4 Fluidization Index

The fluidization index observed for different conditions are plotted against superficial air velocity in **Fig. – 4.4**. **Fig. – 4.4 (a), 4.4 (b)** and **4.4 (c)** compares the fluidization index for different particle sizes, static bed heights and density of particles respectively. It is observed that the fluidization index increases with the increase in superficial gas velocity. Fluidization index gives an idea of the degree of the uniformity in bed expansion. A high value of fluidization index implies that bed can hold more gas between the minimum fluidization and bubbling point or proper fluidization is achieved. A low value of fluidization index implies that less gas is hold between the minimum fluidization and bubbling point or improper fluidization is achieved. The reason may be due to the more and less number of bubble formations for proper and improper fluidization respectively.

Again **Fig. – 4.4 (a)** shows fluidization index decreases with increase in particle size. This is because of the fact that pressure drop decreases with increased particle size when bed weight remains same. From **Fig. – 4.4 (b),** it is observed that fluidization index decreases with increase in static bed height. It is known that more force is required to cause fluidization of more material. That means pressure drop increases with static bed height. Again bed weight also increases with increase in static bed height. As both pressure drop and weight of bed increase, it is difficult to decide which factor affects much. But from common sense it can be said that at any particular velocity less material will exhibit better fluidization which is evident here. Thus fluidization index is higher when $\Delta P/W$ increases. Fluidization index decreases when $\Delta P/W$ decreases as cross-sectional area remains constant. Thus fluidization index may increase / decrease with decrease / increase in weight of bed materials respectively.

It is seen from **Fig. – 4.4 (c)** that Aluminium powder shows lower fluidization index than Sand and Red Mud. It is also observed that rough / lighter particles have less pressure

drop. This implies that Aluminium powders show poor fluidization as bed weight and cross-sectional area remains constant. Smooth particles (Red Mud) with constant weight having higher pressure drop indicates higher fluidization index than others. This may be because of higher cohesive forces among Red Mud particles.

4.2 BINARY MIXTURE OF FINE PARTICLES

4.2.1 Effect of Particle Size and Density

The hydrodynamic behaviours of the fluidized bed with respect to bed pressure drop, expansion ratio, fluctuation ratio and fluidization index are carried out for binary mixtures of Red Mud and Aluminium particles. In this case, different sizes of Aluminium particles are mixed with 77 microns of Red Mud to study the effect of particle size. Again Red Mud and Aluminium particles (83 microns) are mixed in different proportions as per the scope of the experiment (**Table – 3.2**) to study the effect of particle density.

4.2.1.1 Pressure Drop and Minimum Fluidization Velocity

The variation in bed pressure drop against fluidization velocity for different particle sizes and densities of binary mixtures are shown in **Fig. - 4.5**. It is observed that bed pressure drop increases with the increase in superficial velocity (U_o) for both, i.e. different particle sizes and different densities. The bed pressure drop gradually increases with increase in superficial gas velocity upto a certain limit after which it remains constant once the entire bed starts fluidizing. From **Fig. – 4.5 (a)**, it is seen the bed pressure drop decreases with increase in average particle size of binary mixtures. This may be due to the presence of more void spaces in turn more number of air bubbles in large sized particle mixtures. From **Fig. – 4.5 (b)** it is observed that the bed pressure drop increases with increase in particles density of binary mixtures. This may be due to the greater weight of bed materials which needs more force to be fluidized properly. The minimum fluidization velocity for binary mixtures is

found to be 0.014 and 0.015 m/s for different particle density and particle size mixture of Red Mud–Aluminium particles respectively.

4.2.1.2 Bed Expansion Ratio(R)

The bed expansion ratios against superficial air velocity for binary mixtures of Red Mud–Aluminium particles with different sizes and densities are shown in **Fig. – 4.6 (a)** and **(b)** respectively. It is observed that the bed expansion ratio increases with the increase in average particle size and density of the binary mixtures. This may be due to the fact that when superficial gas velocity exceeds minimum fluidisation velocity more number of gas bubbles form which in turn increases the bed expansion. From **Fig. – 4.6 (a)** it is seen that bed expansion decreases with decrease of average particle size of binary mixture. This may be due to the fact that average particle size changes for different sizes of Aluminium particles. As 90 percentage of Red Mud (77μ) is mixed with 10 percentages of different sizes of Aluminium particles to make different binary mixture, Red Mud is not responsible for the bed behaviour. Higher average particle size mixture contains larger particles (98μ) of Aluminium which causes to have more void spaces in turn more bubbles thereby resulting in more bed expansion. Therefore bed expansion is observed to be more for smaller size particles.

From **Fig. – 4.6 (b)** it is seen that denser bed mixture expands less. Reason is obvious. As the bed weights more because of higher percentages of Red Mud which is denser than Aluminium particles, less bed expansion is observed with denser bed mixture. Thus bed expansion decreases with increased density of bed materials.

4.2.1.3 Bed Fluctuation Ratio (r)

The bed fluctuation ratio against superficial air velocity for different particle sizes and densities of binary mixtures of Red Mud–Aluminium are shown in **Fig. – 4.7**. It is observed that bed fluctuation ratio increases with the increase in superficial air velocity for different

particle sizes and densities of bed mixtures. This may be due to formation of more gas bubbles with the increased velocity beyond the minimum fluidization condition. **Fig. – 4.7 (a)** compares the bed fluctuations for different particle sizes. It is observed that larger size show higher bed fluctuation which decreases with decrease in average particle size. Reason for this may be higher bed expansion with larger size particles. Again larger size of Aluminium particles present in bed mixtures (having larger average particle size) might be breaking the bubbles frequently thereby causing higher bed fluctuations. **Fig. – 4.7 (b)** compares the bed fluctuations for different densities of bed materials. It is observed that bed fluctuations increase with increase in densities of bed materials. From **Fig. – 4.6 (b)**, it is seen that the bed expansions are almost close to each other for different densities of bed materials. From eq^{n} 2.1 and 2.2 it is understood that if maximum expanded bed height (H_{max}) increases or minimum expanded bed height (H_{min}) decreases bed fluctuation increases. With increased bed density (because of more percentage of Red Mud in the bed mixture) minimum expanded bed height (H_{min}) might have decreased causing more bed fluctuations. As Red Mud is more cohesive in nature and more percentage of Red Mud in bed mixture makes it more difficult to fluidize. Thus H_{min} decreases resulting higher fluctuations with increased densities.

4.2.1.4 Fluidization Index

The fluidization index versus superficial air velocity for binary mixtures of Red Mud-Aluminium particles are shown in **Fig. – 4.8. Fig. – 4.8 (a)** and **(b)** compare the fluidization index for different sizes and densities of bed materials respectively. From **Fig. – 4.8 (a)** it is observed that fluidization index increases with decrease in particle size. The reason is that at any flow rate smaller sized particles will need more force to fluidize because of less void space. As a result pressure drop increases in turn fluidization index increases because for constant bed weight and constant cross-sectional area, fluidization index is directly proportional to pressure drop. **Fig. – 4.8 (b)** indicates that fluidization index increases with

decrease in density of bed materials. Reason is that pressure drop increases for denser particles during fluidization process. At any flow rate lighter particles will fluidize better than denser particles. Thus when average density of particles increases due to higher percentages of Red Mud fluidization index decreases because of more cohesive force among Red Mud particles.

4.3 CHARACTERIZATION OF BED MATERIALS

Bed materials such as Red Mud, Red Mud-Aluminium mixture and Sand are fluidized in a high temperature fluidized bed reactor. Initially Red Mud is investigated at different temperatures i.e. room temperature, 150^0C, 200^0C, 250^0C and 500^0C to know the suitable operating temperature for Red Mud. Again the Red Mud–Aluminium mixture and Sand sample treated with industrial gaseous effluents. Industrial effluent gas of Aluminum industry is used as the secondary gas in the fluidized bed reactor to study the abatement of fluorides.

4.3.1 Analysis for Red Mud at different Temperatures

Red Mud composition indicates that numbers of metals are present in it. This necessitates the preliminary studies to be carried out on Red Mud. Red Mud being used as bed materials acts as one of the reactants in FBR. Therefore attempt has been made to study the information on suitable operating temperature can be made available for FBR. The following characterizations have been performed on Red Mud with the help of various instruments.

4.3.1.1 Temperature Profile

Fig. - 4.9 show temperature profile of Red Mud inside the FBR. It takes almost 26 minutes to attain a temperature of 150^0C, 42 minutes to reach 200^0C, 58 minutes to reach 250^0C and 147 minutes to reach 500^0C.

4.3.1.2 XRD Analysis

The phase characterization and elemental analysis of Red Mud is necessary for catalytic reaction. Various researchers have already studied. But the compositions of Red Mud are found to be non-uniform because of its variation in elemental composition at

different places. Therefore it is necessary to know the composition of Red Mud at different temperatures and it is analyzed with the help of XRD patterns. The XRD patterns of Red Mud as observed at different temperatures are shown in **Fig. - 4.10**.

From the XRD peaks of Red Mud, it can be seen that the main components present at room temperature are Hematite (α-Fe_2O_3), Calcite ($CaCO_3$), Gibbsite (γ-$Al(OH)_3$), Rulite (TiO_2), Sodium aluminium silicate ($Na(AlSiO_4)$), Dicalcium silicate (Ca_2SiO_4) and Quartz (SiO_2). A peak of Tri-calcium aluminate ($Ca_3Al_2O_6$) starts appearing above 150^0C temperature. Gibbsite peak is found to be absent in Red Mud sample when treated at 500^0C in FBR. This may be due to the fact that at 500^0C Gibbsite decomposes to Al_2O_3 and H_2O according to the following reaction.

$$Al(OH)_3 \rightarrow Al_2O_3 + H_2O \qquad (4.1)$$

It is also found that Calcite ($CaCO_3$) starts decomposing to CaO and CO_2 [Sglavo et al. (2000)] at 500^0C according to the following reaction.

$$CaCO_3 \rightarrow CaO + CO_2 \qquad (4.2)$$

Di - calcium silicate (Ca_2SiO_4) and hematite (α-Fe_2O_3) are not affected by the temperature through the process of heating [Dimas et al. (2009)]. Thus the presence of these compounds in sample at 500^0C is confirmed by the peaks of XRD analysis. Literature shows that above transformation takes place at temperatures above 600^0C [Dimas et al. (2009)]. But in the present work the above transformation is found to occur at 500^0C which might have occurred due to proper heating of Red Mud sample in the FBR.

4.3.1.3 FT-IR analysis

The different characterization groups present in Red Mud at different temperatures are analysed and shown in **Table - 4.1** and **Fig. - 4.11**. It is observed that broad bands occur at certain wave numbers for different samples. This may be due to the stretching vibrations of O-H bonds and H-O-H bending vibrations of inter-layer adsorbed H_2O molecule [Xing and

Jiao (1993)]. Because of the large change in dipole moment of the water hydroxyl-stretching, the intensity of the infrared spectrum is more. But this bond is found to be missing in case of IR curve at 500^0C for the sample which may be due to the evaporation of moisture from the Red Mud particles. Stretching vibrations of C=O found in the samples for a particular wave number confirms the presence of carbonate groups [Yang et al. (2004)]. The main reason is the presence of chemisorbed CO_2 in Red Mud. Certain bands are observed for most of the Red Mud samples which corresponds to the characteristic bands of Si-O and O-Si-O group as shown in **Table – 4.1** thereby confirming the presence of silicate groups. This group is found to be absent in the Red Mud sample at 500^0C temperature due to the dissolution of minerals like $Na(AlSiO_4)$ [Xing and Jiao (1993)]. Presence of Al^{3+} - O^{2-} bonds are observed in most of the samples. Minor stretching vibrations of Fe-O is also observed in most of the cases at the region around 440 cm^{-1} wave number, but it is not very clear when the comparison among the graphs are carried out. Hence the FT-IR results support the evidence of phase change data of XRD analysis.

4.3.1.4 Thermo gravimetric analysis (TGA)

The TGA-DTA diagram (**Fig. - 4.12**) show the thermal decomposition of Red Mud in the temperature range of 28–500^0C. It is observed that as temperature rises, there are three weight loss steps in the profile. The first one occurs at 25-260^0C where the weight loss is about 4.3 % of total weight which is due to the evaporation of moisture. The second step occurs in the temperature range of 260-325^0C where weight loss is about 8.9% of total weight which is due to the removal of H_2O from $Al(OH)_3$. The third or the final step occurs in the temperature range of 325-500^0C where weight loss is about 10.9% of total weight which may be due to the release of CO_2 during the decomposition of $CaCO_3$. The DTA curve shows two broad peaks centered at around 60^0C and 290^0C corresponding to the adsorption of water physically and chemically respectively [Hajela et al. (1989)].

4.3.1.5 Particle Size analysis (PSA)

The particle size is one of the most influential parameters for the fluidization process as well as for the reaction purpose. The particle size is observed to undergo a significant change with the increased temperature. The particle size distribution of the Red Mud at room temperature is shown in **Fig. - 4.13**. It can be seen that the sieved Red Mud particles are mostly in the range of 0.137μm to 65 μm with a mean value of 11.8 μm. But the size of the Red Mud particles starts changing with the heat treatment inside the FBR, which is shown in **Fig. - 4.14**. When the temperature reaches 150^0C, the average particle size rises from 11.8 μm to 18.1 μm and then reaches 91.79 μm at 200^0C. The increase of the particle size may be influenced by the improvement in crystallization. From the XRD pattern (**Fig. - 4.10**), it is seen that except the Calcite ($CaCO_3$), Gibbsite (γ-$Al(OH)_3$) are vanishing phases whereas the crystallinities of the majority of phases of red mud i.e. Tri - calcium aluminate ($Ca_3Al_2O_6$) is improved by heat treatment [Dimas et al. (2009)]. This promotes the rise in the value of the mean particle size. But when the temperature reaches 250^0C, the particle size decreases to 22.9 μm and then further decreases to 19.1 μm at 500^0C. This is probably due to the inter-particle collisions / impact / wear taking place inside the FBR [Qiu and Qi (2011)]. This may also be due to the formation of CO_2 as it behaves as a weak acid and helps in dissolution of larger particles [Xing and Jiao (1993)]. The variation of particle size at different temperatures is also given in **Table – 4.2**.

4.3.1.6 FESEM and EDX analysis

A known amount of the Red Mud samples are dispersed in methanol and ultra - sonicated for 30 minutes. Then the samples are observed under Field Emission Scanning Electron Microscopy to analyze the morphological structures at different temperature. The FESEM images of Red Mud sample observed at different temperatures are shown in **Fig. - 4.15 (a-e)**. It is observed from **Fig. - 4.15 (a)** that the arrangement of the particles is relatively

loose or particles are poorly crystallized with high porosity and small particle size. On the contrary **Fig. - 4.15 (b)** and **Fig. - 4.15 (c)** it can be observed that the particle size of Red Mud increases at temperatures of 150^0 and 200^0C. Again from the **Fig. - 4.15 (d)** and **Fig. – 4.15 (e)**, it is found that at 250^0C and 500^0C, particle size further decreases which may be due to the attrition / collision effect of the particles inside the FBR. This increasing and decreasing trend is observed which is matching with the values measured by laser particle size analyzer (PSA). The EDX analysis of the Red Mud samples ensures the presence of particular elements in it which is shown in **Fig. - 4.16 (a-e)** and **Table - 4.3**. From this it is found that Aluminium and Oxygen content is more whereas Iron and Titanium content is less at 250^0C than at the other temperatures. This may be due to decomposition of Gibbsite to Alumina at 250^0C temperature.

4.3.1.7 BET analysis

The surface area of the Red Mud sample at different temperatures is analysed by BET apparatus. The samples are out-gassed at a temperature of 200^0C for 2 hrs. The surface area is observed to be 31.19, 31.24, 31.32, 31.39 and 31.66m^2/g of the samples at room temperature, 150, 200, 250 and 500^0C temperature respectively. The increase in the surface area is matching with the decomposition of $Al(OH)_3$ phases of gibbsite. This may be due to the formation of small pores as free H_2O is removed from the sample when the temperature increases. It may also be due to the attrition or particle-particle collision effects which occur inside the FBR thus resulting in the breakage of the particles thereby exposing more surfaces.

4.3.2 Analysis of Bed Materials with and without Industrial Effluent Gas

Industrial effluent gas is collected from Aluminium industry in a stainless steel sampling cylinder. The air is supplied as the primary medium by the blower and the effluent gas is supplied as a secondary medium to the fluidizer. The bed material is allowed to fluidize at a

temperature of 250°C and a residence time of 30 minutes is given for proper mixing of secondary medium with the bed materials.

4.3.2.1 For Red Mud and Red Mud-Aluminium as Bed Materials

The abatement of fluoride is carried out by using different bed materials i.e. Red Mud and Red Mud-Aluminium mixture. The bed materials are characterized by different techniques before and after the experiments to confirm the abatement of fluorides. The results thus obtained from the characterization of bed materials before and after the experiments are compared with each other.

4.3.2.1.1 Temperature Profile

Fig. - 4.17 compares temperature profiles of different bed materials upto the temperature of 250^{0}C in the FBR. The Aluminium, Red Mud and Red Mud-Aluminium mixture take almost 45, 58 and 50 minutes to reach 250^{0}C temperature within the FBR respectively.

4.3.2.1.2 XRD Analysis

XRD analysis results for different bed materials with and without addition of industrial gaseous effluent are compared in **Fig. - 4.18**. When only Aluminium particles fluidized at 250^{0}C in FBR is analyzed the XRD peaks shows Quartz (SiO_2), Aluminium (Al) and Alumina (Al_2O_3) present in it. XRD analysis of only Red Mud is already discussed in section 4.3.2. When the binary mixture of Red Mud-Aluminium fluidized at 250^{0}C temperature is analysed with XRD, Gibbsite (γ-$Al(OH)_3$), Dicalcium Silicate (Ca_2SiO_4), Sodium Aluminium Silicate ($Na(AlSiO_4)$), Hematite (α-Fe_2O_3), Calcite ($CaCO_3$), Rulite (TiO_2), Quartz (SiO_2), Tri Calcium Aluminate ($Ca_3Al_2O_6$) Aluminium (Al) and Alumina (Al_2O_3) are found to be present in it. These elements are confirmed from the peaks of XRD patterns.

Fig. - 4.18 also show the XRD patterns of these bed materials with the effluent gas. The XRD peaks for the Red Mud with the effluent gas at 250^0C are observed to contain Ferrous Fluoride (FeF_2), Ferric Fluoride (FeF_3) and minutes of Aluminium Fluoride (AlF_3) and Sodium Fluoride (NaF) in the bed materials after the reaction. This may be due to the reaction of the fluorides present in the effluent gas with Hematite (α-Fe_2O_3), Alumina (Al_2O_3) and Sodium Oxide (Na_2O) which are present in the Red Mud samples. The presence of these compounds in the Red Mud sample after the fluidization with industrial effluents confirms the occurrence of the catalytic reaction thereby indicating the abatement of gaseous fluorides by Red Mud in the FBR. The XRD results for the binary mixture of Red Mud-Aluminium particles with the industrial effluents gas after fluidization are also shown in **Fig. - 4.18**. It is observed that Ferrous Fluoride (FeF_2), Ferric Fluoride (FeF_3), Aluminium Fluoride (AlF_3) and Sodium Fluoride (NaF) are present in the sample. The Aluminium Fluoride (AlF_3) peak is observed to be more dominant. Reason may be the addition of Aluminium powder to the Red Mud. Much Aluminium Fluoride (AlF_3) might have formed by the reactions with all the bed materials in the presence of Rulite (TiO_2) which acts as catalyst. Aluminium (Al), Alumina (Al_2O_3), Hematite (α-Fe_2O_3), Calcite ($CaCO_3$), Gibbsite (γ-$Al(OH)_3$), Rulite (TiO_2), Sodium Aluminium Silicate ($Na(AlSiO_4)$), Di-Calcium Silicate (Ca_2SiO_4), Tri-Calcium Aluminate ($Ca_3Al_2O_6$) and Quartz (SiO_2) are found from XRD peaks which are actually the constituents of Red Mud and Aluminium particles. Thus it can be said that this analysis confirms the abatement of Fluorides.

4.3.2.1.3 FT-IR Analysis

FT-IR analysis results for different bed materials treated with industrial effluent gas are presented in **Table - 4.4** and shown in **Fig. - 4.19**. It is observed that broad bands for O-H and H-O-H groups occur at certain wave numbers for Red Mud samples treated with and without industrial effluent gas. Characterisation groups, Si-O and Fe-O are found with Red

Mud and Red Mud-Aluminium mixtures without treatment of industrial effluent gas at certain wave numbers. But O-Si-O, C=O, Al-O groups are observed to occur at certain wave numbers for all the samples treated with / without industrial gaseous effluents. Presence of Al^{3+} - O^{2-} bonds are observed in most of the samples. A minor stretching vibration of Fe-O is also observed in Red Mud and Red Mud-Aluminium mixtures. Hence it can be said that the FT-IR results support the evidence of phase change data of XRD analysis.

4.3.2.1.4 FESEM and EDX Analysis

The morphological structures of the two bed materials treated with / without industrial effluent gas at 250^0C are studied under the Field Emission Scanning Electron Microscopy (**Fig. - 4.20**). It is observed that particle size of Redmud i.e. 77µ increases to 90µ when treated with effluent gas. Similarly average particle size of Redmud-Aluminium mixture i.e. 123µ increases to 155µ after experiments. This may be due to the reaction of iron oxides, Gibbsite and Sodium Oxide with the gaseous fluorides present in effluent gas. This increased particle size is confirmed with the analysis by laser particle size analyzer. The EDX analysis of the respective samples ensures the presence of fluorides in the samples treated with industrial effluent gas and is shown in **Fig. - 4.21 (a-d)** and **Table – 4.5**.

4.3.2.1.5 ICP-MS Analysis

Three samples of Red Mud, Red Mud with Effluent gas and Red Mud-Aluminium with the Effluent gas are characterized using the ICP-MS analysis which gives the information about the amount of elements present in the samples (**Table – 4.6**).

The amount of Quartz (SiO_2) is observed to be more in case of the Red Mud-Aluminium mixture treated with the effluent gas. This might be due to the presence of Quartz (SiO_2) present in the commercial Aluminium particles. The Alumina (Al_2O_3) percentage is observed to increase from 13.72% in Red Mud to 16.19% in effluent treated Red Mud which may be due to the presence of minor amount of un-converted Gibbsite. As Gibbsite gets

oxidized during fluidization more Alumina might have formed resulting in increased percentage of Al_2O_3. In the case of Red Mud-Aluminium mixture treated with effluent gas, the amount of Alumina is found to be 37.41% which may be due to the oxidation of Aluminium (used as bed material with the Red Mud). Again the conversion of Gibbsite to Al_2O_3 might have further increased the Al_2O_3 percentage.

The Hematite content present in the Red Mud sample before experiment is found to be 50.29 % which decreases to 45.24% in the effluent gas treated Red Mud. The reason might be due to the reaction of iron present in the Red Mud samples with the gaseous fluorides present in the effluent gas. The maximum percentage of Hematite is found to be 47.51% in the effluent gas treated Red Mud–Aluminium mixture. This increase in Hematite percentage in case of the binary mixture than the case of only Red Mud confirms the increased rate of reaction between fluorides present in the gaseous stream with the bed material in the presence of Aluminium particles.

Another significant change in the composition of Red Mud is observed. Otherwise it can said that Sodium Oxide (Na_2O) is found to be present in all samples where the decrease in its amount confirms the probable reaction of Sodium Oxide with the fluorides resulting in the formation of Sodium Fluorides (NaF). Apart from these changes, it is also observed that many components show changes in their amounts, but these changes are considered to be insignificant because of their low values.

4.3.2.1.6 Particle Size Analysis (PSA)

The particle sizes of the bed materials treated with effluent gas are determined with the help of Particle Size Analyzer. The sizes are shown in **Table - 4.7** and **Fig. – 4.22**. It is observed that the Red mud and Red Mud-Aluminium mixture fluidized at 250^0C in a FBR have average particle sizes of 22.907 and 50.409 microns respectively. The average particle size of Red Mud treated with the effluent gas is found to increase from 22.907 μ to 38.390 μ

which might have occurred due to the formation of Ferrous/Ferric Fluorides, Aluminium Fluoride and Sodium Fluorides. On the other hand it is also observed that Red Mud-Aluminium mixture treated with effluent gas attained an average particle size of 72.017μ which increased from 50.409μ. This may be due to the formation of increased size products because of several reactions taking place within the FBR.

4.3.2.1.7 BET Analysis

The surface areas of the bed materials (i.e. Red Mud and Red Mud–Aluminium mixture) treated with / without industrial effluents gas have been analysed by BET apparatus. The surface areas measured at 250^0C are observed to be 31.39, 33.66, 43.99, 54.53, 46.47 m^2/g for Red Mud, Aluminium, Red Mud-Aluminium mixture, treated Red Mud and treated Red Mud-Aluminium mixture respectively. The surface area increases from 31.9 to 54.53 m^2/g when Red Mud is treated with the industrial effluent gas. This is because of the formation of Ferrous/Ferric Fluorides, Aluminium Fluoride and Sodium Fluoride. In case of other sample i.e. Red Mud-Aluminium mixture, surface area is observed to increase from 43.99 to 46.47 m^2/g when the sample is treated with the industrial effluent gas. The reason for small increase may be due to the decomposition of $Al(OH)_3$, oxidation of Al to Al_2O_3.

4.3.2.2 For Sand as Bed Materials

Sand is used as bed materials for studying the abatement of fluorides as a comparison against Red Mud. Sand is fluidized inside the FBR at a temperature of 250^0C and then bed materials are analysed by using different characterization techniques. Industrial effluent gas is also allowed to pass through the bed materials with the residence time of 30 minutes at a temperature of 250^0C. The bed materials treated with / without effluent gas are characterized by the following techniques.

4.3.2.2.1 Temperature Profile

Fig. - 4.23 show the temperature profile of the Sand within the FBR. It takes almost 65 minutes to attain a temperature of 250^0C.

4.3.2.2.2 XRD Analysis

XRD analysis is carried out for the Sand treated with / without industrial effluents being fluidized at a temperature of 250^0C. The comparison results are shown in **Fig. – 4.24**. It is found that the XRD peaks of Sand at room temperature contained Quartz (SiO_2) and Sodium Oxide (Na_2O). Again the minor peaks of Alumina (Al_2O_3) and Magnesium Oxide (MgO) are seen at room temperature for Sand. When the Sand particles are fluidized in a FBR at the temperature of 250^0C the dominant peaks of Quartz (SiO_2) and Sodium Oxide (Na_2O) with Sodium Peroxide (Na_2O_2) are found in XRD analysis. Sodium Peroxide is formed when Sodium reacts with excess Oxygen at the temperature of 250^0C. When the Sand particles is treated with industrial effluents gas in a FBR at a temperature of 250^0C minor peaks of Aluminium Fluoride (AlF_3), Silicon Tetra Fluoride (SiF_4) are found in XRD analysis. This may be due to the reaction of the fluorides present in the effluent gas with the Quartz (SiO_2), Sodium Oxide (Na_2O), Alumina (Al_2O_3) and Magnesium Oxide (MgO) which exist in the Sand particles.

4.3.2.2.3 FT-IR analysis

FT-IR analysis is carried out for Sand treated with or without effluent gas at 250^0C temperature. The results are shown in **Table - 4.8** and **Fig. - 4.25.** Different characterization groups are found to be present in Sand. It is observed that O-H, H-O-H groups are present in the range of 3500 - 2500 cm^{-1} wave numbers for different samples. This may be due to the stretching vibrations of O-H bonds and H-O-H bending vibrations of inter - layer adsorbed H_2O molecule [Xing and Jiao (1993)]. Certain characteristic bands of Si-O group are also observed and shown in **Table – 4.8** thereby confirming the presence of silicate groups. This

group is found to be absent in the Sand sample treated with effluent gas at 250^0C temperature due to the formation of Fluorides. The Carbonyl stretching of C=O is found in the samples for a particular wave number confirming the presence of carbonate groups. Minor stretching vibrations of Al-O, Fe-O groups are also observed in most of the cases at the region around 600 cm^{-1} wave numbers. But it is not very clear when the comparison is carried out in the graph. Hence the FT-IR results support the evidence of phase change data of XRD analysis.

4.3.2.2.4 Particle Size Analysis

The particle size of Sand treated with / without effluent gas are determined with the help of Particle Size Analyzer and are shown in **Fig.- 4.26 (a-c)**. It is observed that the average particle size of Sand is 70.013 and 58.71 μm at room temperature and 250^0C temperature respectively. The average particle size is found to decrease this may be due to removal of moisture from the sample. The particle size of Sand is observed to increase when it is treated with industrial effluent gas at 250^0C temperature i.e. upto 82.57 microns. This may be due to several reactions occurring within FBR by which several products like Aluminium Fluoride (AlF_3), Silicon Tetra Fluoride (SiF_4) and Sodium Fluoride (NaF) might have formed.

4.3.2.2.5 FESEM and EDX Analysis

The morphologies of Sands treated with and without industrial effluent gas at 250^0C are studied using Field Emission Scanning Electron Microscopy and EDX analysis is shown in **Fig. - 4.27**. It is seen from this figure that the particle size of Sand decreases from room temperature to 250^0C temperature. This may be due to the removal of moisture and volatile components from the material. Again it is seen that particle size increases when it is treated with the industrial effluent gas. This may be because of the reactions of Quartz (SiO_2), Sodium Oxide (Na_2O) and Alumina (Al_2O_3) with the effluent gas by which several products might have formed. Increase in particle size is further confirmed by the values measured by

laser particle size analyzer. The EDX analysis of the respective samples ensures the presence of particular elements in the sample and is shown in **Fig.- 4.27** and **Table – 4.9**. The analysis shows the presence of Si, O, Fe, Al, B, Na, Mg and F in the sample.

4.3.2.2.6 BET analysis

The surface areas of the Sand treated with / without industrial effluents gas have been analysed by BET apparatus. The surface areas are observed to be 0.73, 0.65 and 0.77 m^2/g for samples at room temperature, 250^0C and for treated sample respectively. Increase in surface area for treated sample might be due to the formation of Aluminium Fluoride (AlF_3), Silicon Tetra Fluoride (SiF_4) and Sodium Fluoride (NaF).

By comparing the results obtained from different characterisation techniques for Red Mud and Sand (**Table – 4.10**). It is observed that increase in surface area obtained through BET is more for Red Mud than Sand which indicates more products are formed with Red Mud being used as bed material. It is seen that Red Mud takes less time to reach temperature of 250^0C than Sand. Further it is seen that increase in average particle size (after the experiment) is more with Red Mud than Sand implying more conversion of gaseous pollutants with Red Mud being used as bed materials. From EDX analysis it is also seen that more metals / elements are present in Red Mud thereby further confirming more reaction of Red Mud with effluent gas. Again it is seen that more amount of solid metal fluorides (AlF_3, FeF_2 and FeF_3) are formed with Red Mud whereas only SiF_4 is formed with Sand. Thus it can be concluded that Red Mud is a suitable bed material to be used in FBR for abatement of fluorides from industrial gaseous effluents.

Table - 4.1: FT-IR bands observed for Red Mud treated at different temperatures

Group Characterization	**Wave number, cm^{-1}**				
	At 28 ^{0}C	At 150^{0}C	At 200^{0}C	At 250^{0}C	At 500^{0}C
O-H, H-O-H (Broad Bands)	2919.68	3003.92	3033.73	3002.68	-
C=O	1449.46	1452.68	1449.27	1451.9	-
Si-O	989.28	989.96	990.65	986.35	993.32
O-Si-O	534.60	536.55	547.0	544.87	-
Al-O	805.50	804.90	805.05	805.46	805.85
Fe-O	442.02	444.12	442.15	438.77	466.23

Table – 4.2: Variation of particle size for Red Mud treated at different temperatures

Temperature, ^{0}C	**Particle Size, Microns**		
	Minimum	Maximum	Average
28	0.137	65.335	11.767
150	0.177	82.5640	18.072
200	8.447	145.150	91.796
250	0.173	76.4825	22.907
500	0.179	71.159	19.084

Table - 4.3: EDX analysis report for elements of Red Mud at different temperatures

Major Elements	**Weight, %**				
	At 28 ^{0}C	At 150^{0}C	At 200^{0}C	At 250^{0}C	At 500^{0}C
Fe	40.71	43.17	52.01	41.11	44.97
O	35.35	40.91	43.03	56.18	37.74
Al	0.61	1.67	1.99	2.22	2.01
Ti	23.33	14.25	2.97	0.49	15.28

Table - 4.4: FT-IR bands observed for samples with / without effluent gas

Group Characterization	**Wave number of different samples, cm^{-1}**			
	Red Mud at 250^0C	Red Mud + E. Gas at 250^0C	Red Mud – Aluminium at 250^0C	(Red Mud – Aluminium) + E. Gas at 250^0C
O-H, H-O-H (Broad Bands)	3002.68	3245.79	--	--
C=O	1451.9	1403.5	1546.23	1598.7
Si-O	986.35	--	975.27	--
O-Si-O	544.87	803.9	871.29	743.4
Al-O	805.46	873.13	846.39	851.79
Fe-O	438.77	--	493.97	--

Table - 4.5: EDX analysis reports for bed samples with / without effluent gas

Major Elements	**Composition of Red mud, %**	**Composition of Red Mud treated with Effluent Gas, %**	**Composition of Red Mud-Aluminium mixture. %**	**Composition of Red Mud-Aluminum treated with the Effluent Gas, %**
Fe	41.11	33.77	68.40	40.09
O	56.18	43.09	5.92	22.46
Al	2.22	9.28	11.86	26.59
Ti	0.49	1.12	3.66	0.81
Na	--	4.13	5.31	2.65
C	--	4.85	2.76	2.90
Si	--	3.22	1.80	3.06
Ca	--	0.24	0.30	0.64
F	--	0.3	--	0.8

Table – 4.6: ICP-MS analysis report for samples treated without / with effluent gas

Elements	In Red Mud without Effluent Gas, %	In Red Mud with Effluent Gas, %	In Red Mud-Aluminium mixture with Effluent Gas, %
SiO_2	4.96	5.54	8.12
Al_2O_3	13.72	16.19	37.41
Fe_2O_3	50.29	45.24	47.51
TiO_2	5.08	5.83	5.31
CaO	0.32	0.71	0.59
MgO	0.094	0.112	0.133
Na_2O	4.62	3.94	2.73
K_2O	Not Found	0.04	0.544
S	0.064	0.062	0.109
P_2O_5	0.109	0.141	0.121
MnO	0.115	0.113	0.113
V	0.045	0.049	0.036
Cr	0.055	0.057	0.037
Co	Not Found	0.003	Not Found
Ni	0.005	0.005	0.0135
Cu	Not Found	Not Found	0.045
Zn	0.121	0.127	0.192
Pb	Not Found	0.007	0.023
As	Not Found	Not Found	Not Found
Y	0.001	0.001	0.0008

Table – 4.7: Particle size for different samples treated without / with effluent gas

Samples	Particle Size, Microns		
	Minimum	Maximum	Average
Red Mud	0.173	76.4825	22.907
Red Mud-Aluminium Mixture	2.536	350.489	50.409
Red Mud treated with Effluent Gas	4.348	170.395	38.390
Red Mud-Aluminium mixture with Effluent Gas	5.070	291.459	72.017

Table – 4.8: FT-IR bands observed for Sand sample

Characterization Group	Wave number, cm^{-1}		
	Sand without Effluent Gas		Sand with Effluent Gas at 250 ^{0}C Temperature
	At 28 ^{0}C	At 250 ^{0}C	
O-H, H-O-H	2924.89	2937.4	2941.57
Si-O	948.75	981.01	--
C=O	1789.4	1817.37	1837.9
Al-O	745.32	700.59	--
Fe-O	554.27	583.14	--
Al-O-Si	500.25	504.73	498.9

Table - 4.9: EDX analysis report for Sand with / without effluent gas

Elements	Sand without Effluent Gas, %		Sand with Effluent Gas at 250 ^{0}C Temperature, %
	At 28 ^{0}C	At 250 ^{0}C	
Si	44.74	57.35	34.53
O	43.91	39.50	26.38
Fe	--	--	13.11
K	0.16	1.51	11.24
Al	0.42	0.31	5.98
B	10.74	1.18	4.40
Na	0.02	0.14	1.35
Mg	0.01	--	0.12
F	--	--	2.74

Table – 4.10: Comparison of bed materials treated with effluent gas in FBR

Analysis	Red Mud treated with Effluents	Sand treated with Effluents
Time to reach 250^{0}C temp.	58 min	65 min
XRD Analysis	Major peaks of AlF_3	Minor peaks of AlF_3
	Formation of FeF_2 and FeF_3	--
	--	Formation of SiF_4
	Minor peaks of NaF	Minor peaks of NaF
PSA Analysis (Change in Size)	From 22.09 to 38.39 microns	From 70 to 82.57 microns
BET Analysis (Change in Surface area)	From 31.9 to 54.53 m^2/g	From 0.73 to 0.77 m^2/g
EDX Analysis	Si : 3.22%	Si : 34.53%
	Fe : 33.77 %	--
	O : 43.09 %	O : 26.38 %
	Al : 9.28 %	Al : 5.98 %
	Na : 4.13 %	Na : 1.35 %
	F : 0.8 %	F : 2.74 %

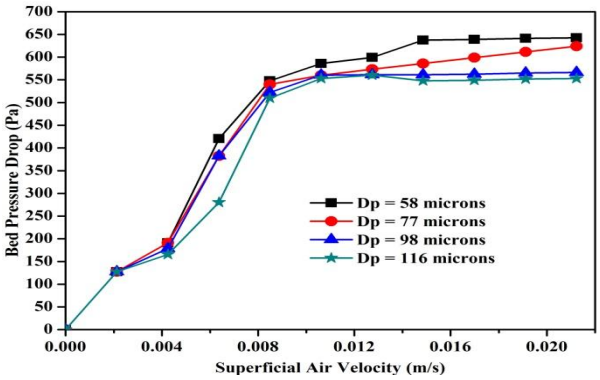

(a) For Different Particle Sizes

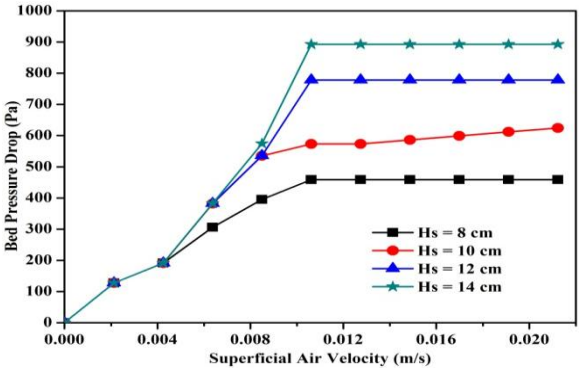

(b) For Different Static Bed Heights

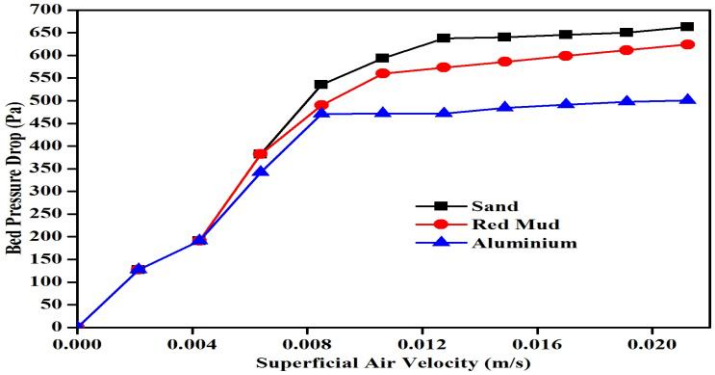

(c) For Different Particle Densities

Fig. – 4.1: Comparison of bed pressure drop against superficial air velocity

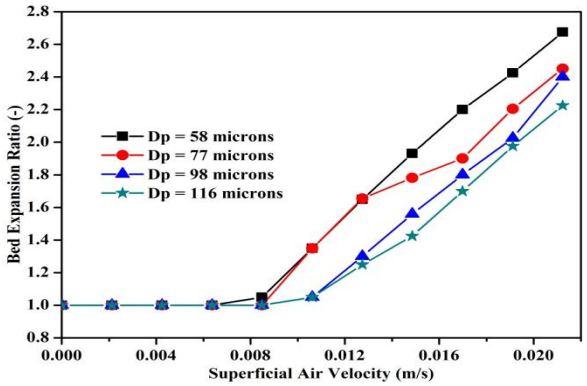

(a) For Different Particle Sizes

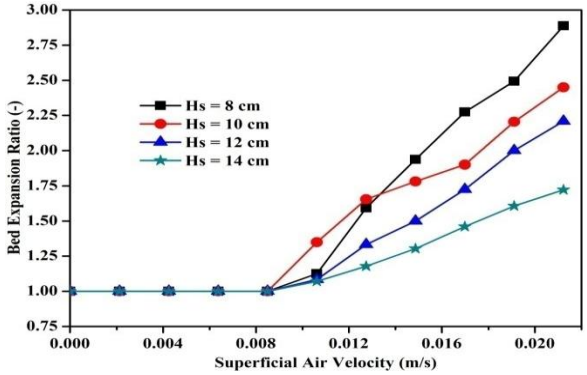

(b) For Different Static Bed Heights

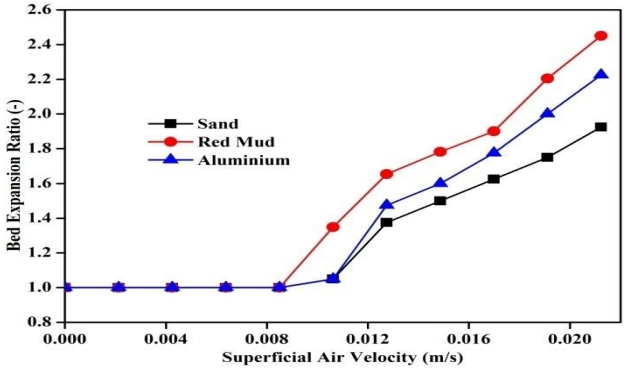

(c) For Different Particle Densities

Fig. – 4.2: Comparison of bed expansion ratio for single sized particles

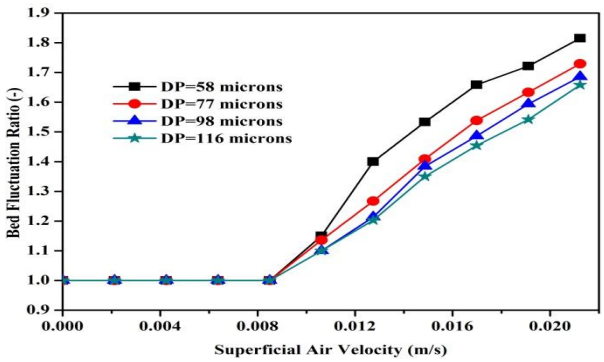

(a) For Different Particle Sizes

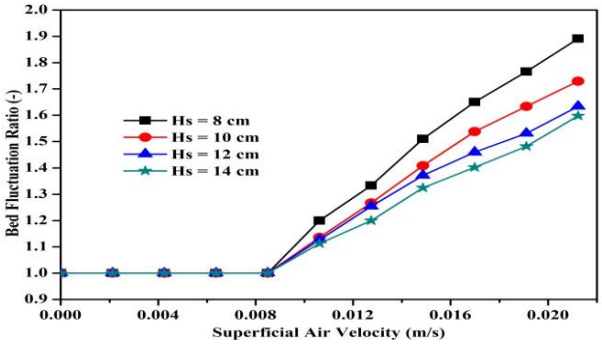

(b) For Different Static Bed Heights

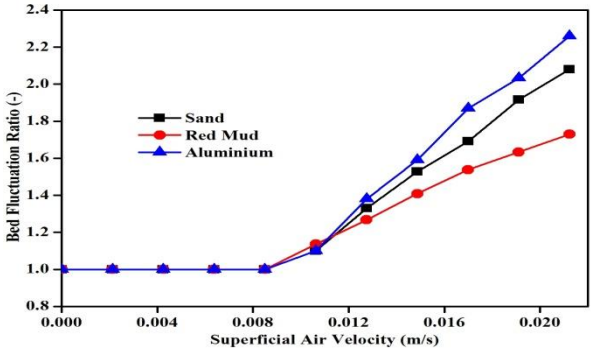

(c) For Different Particle Densities

Fig. – 4.3: Comparison of bed fluctuation ratio for single sized particles

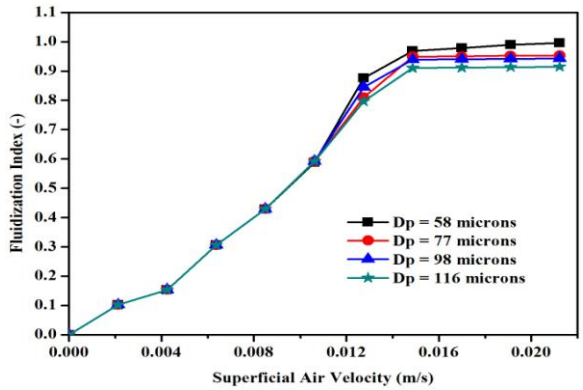

(a) For Different Particle Sizes

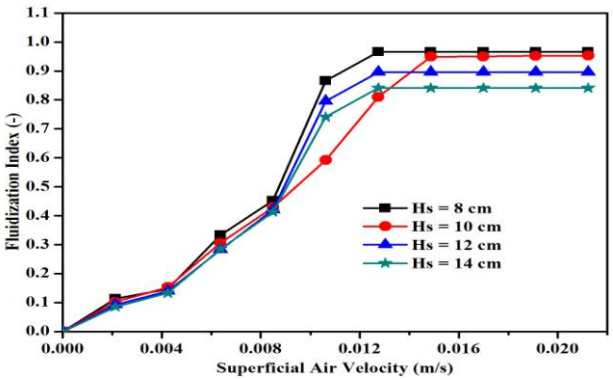

(b) For Different Static Bed Heights

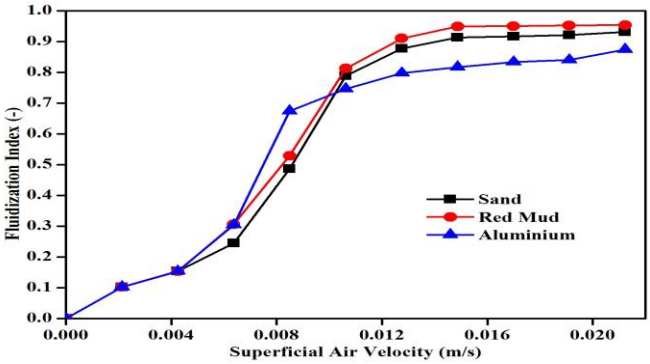

(c) For Different Particle Densities

Fig. – 4.4: Comparison of fluidization index for single sized particles

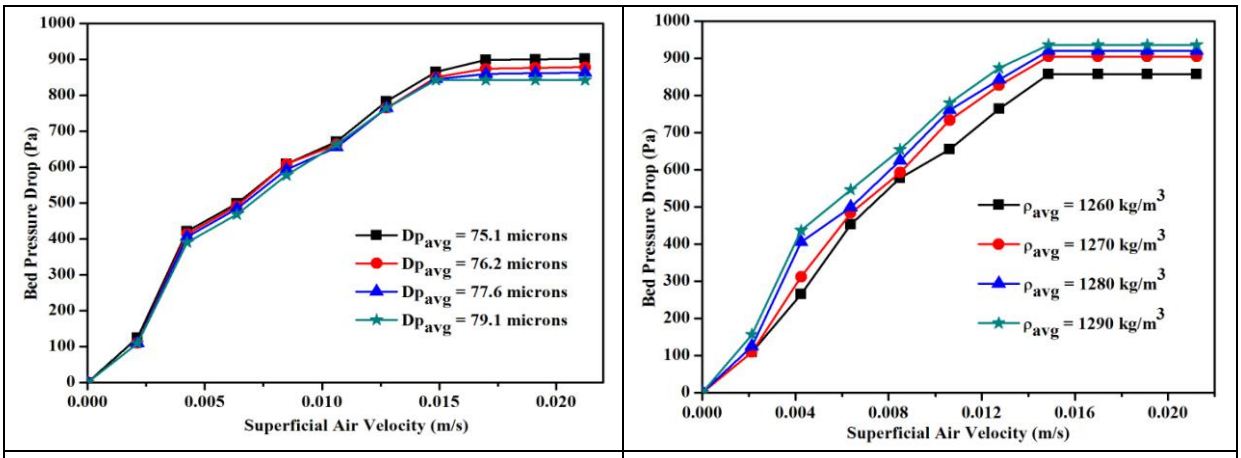

(a) Different Particle Sizes | **(b) Different Particle Densities**

Fig. – 4.5: Comparison for bed pressure drop for binary mixtures

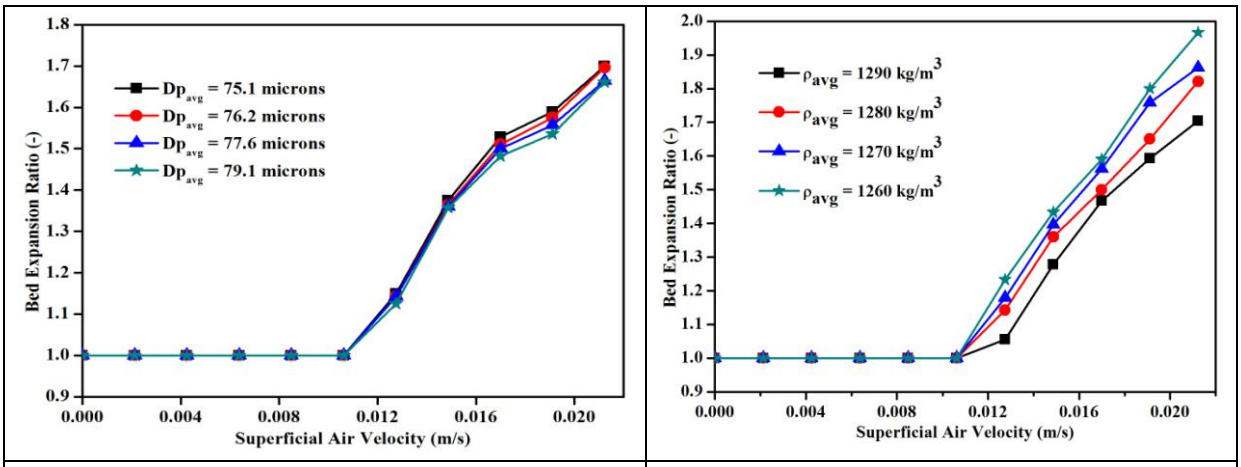

(a) Different Particle Sizes | **(b) Different Particle Densities**

Fig. – 4.6: Comparison of bed expansion ratio for binary mixtures

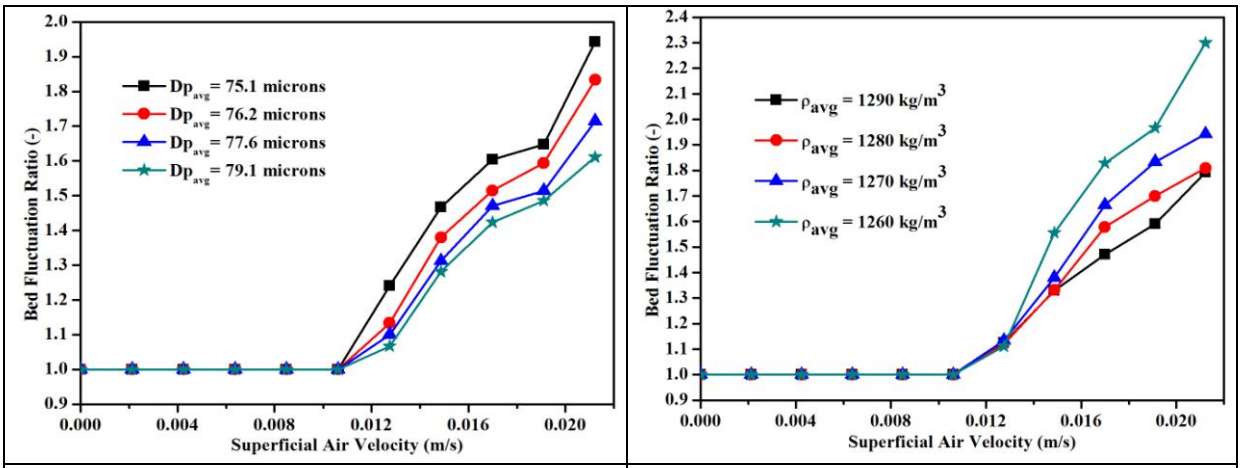

(a) Different Particle Sizes | **(b) Different Particle Densities**

Fig. – 4.7: Comparison of bed fluctuation ratio for binary mixtures

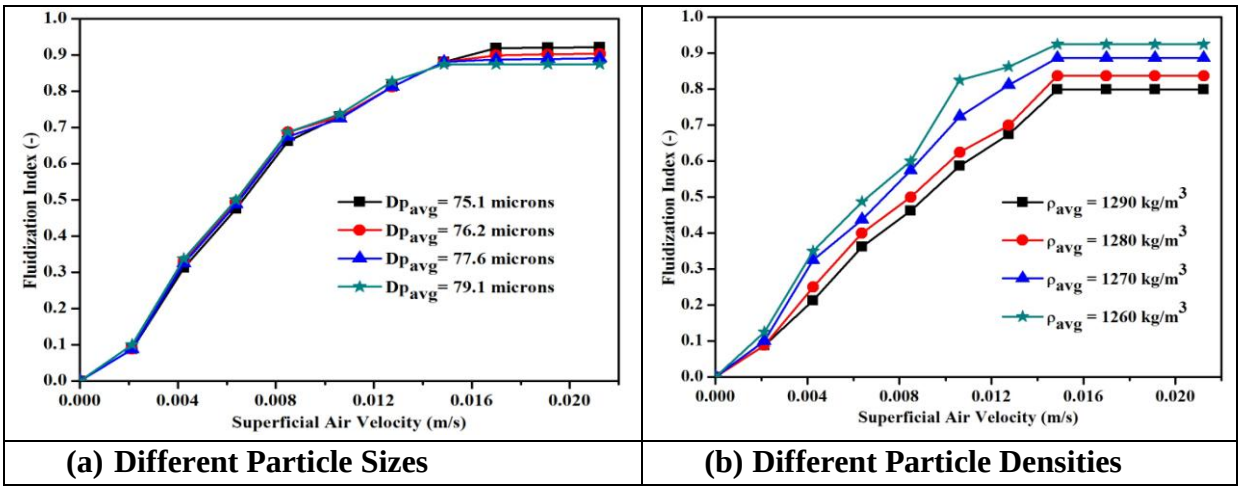

(a) Different Particle Sizes | **(b) Different Particle Densities**

Fig. – 4.8: Comparison of fluidization index for binary mixtures

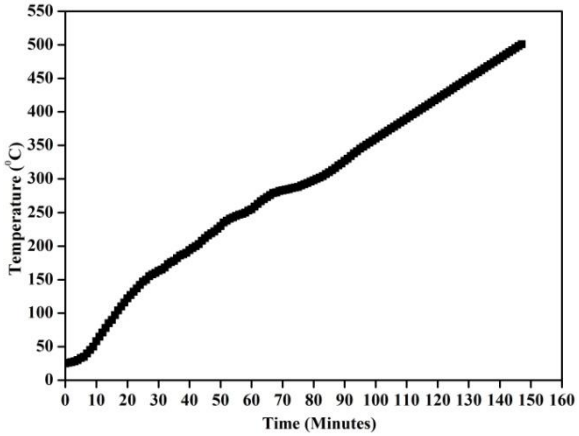

Fig. - 4.9: Temperature profile for Red Mud inside the FBR

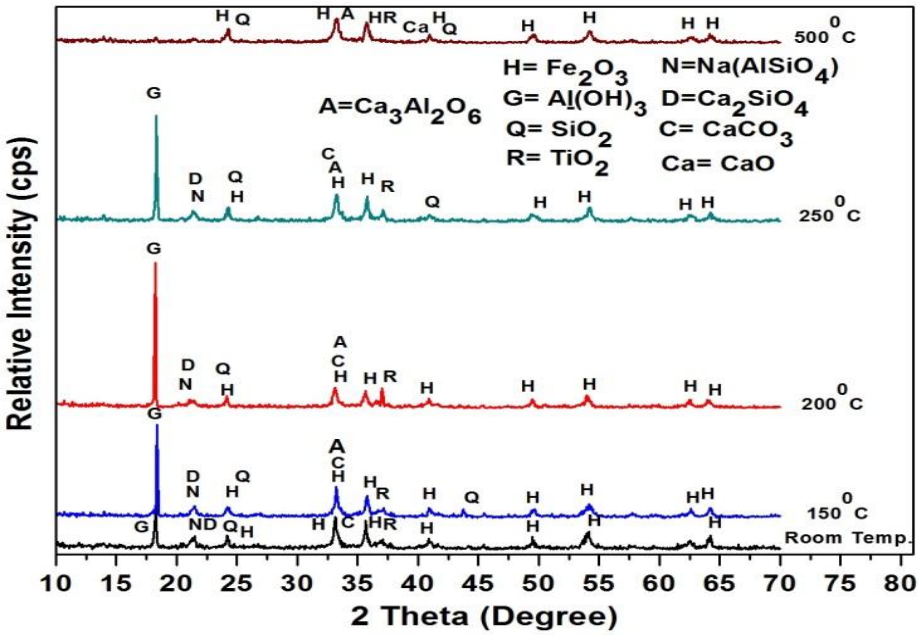

Fig. - 4.10: Comparison of XRD patterns for Red Mud at different temperatures

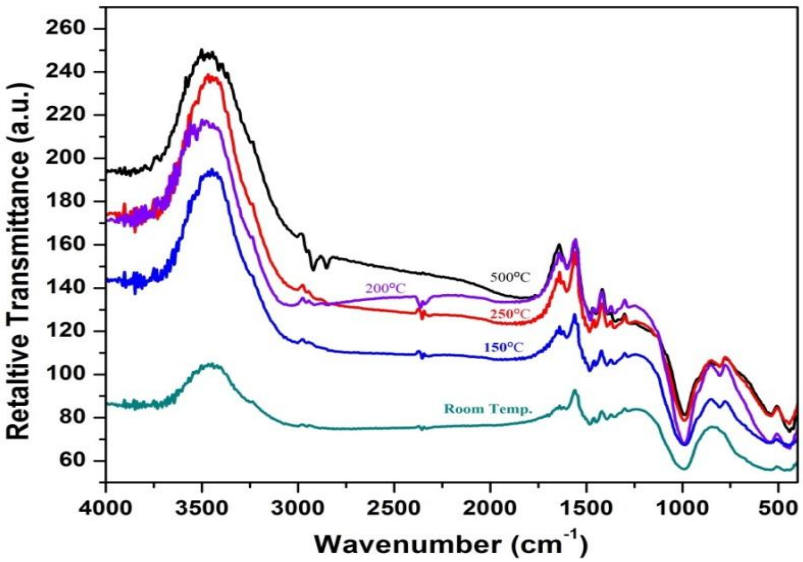

Fig. - 4.11: FT-IR spectra for Red Mud at different temperatures

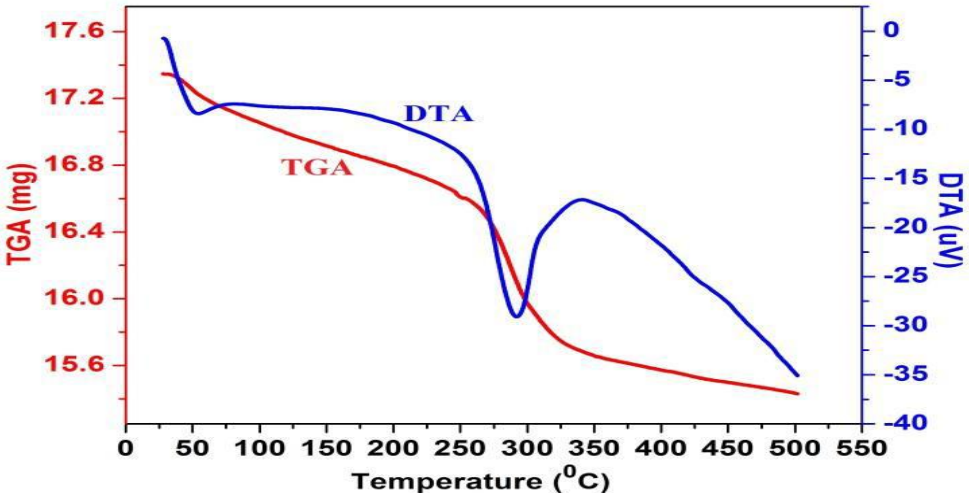

Fig. - 4.12: TGA-DTA diagram for Red Mud sample

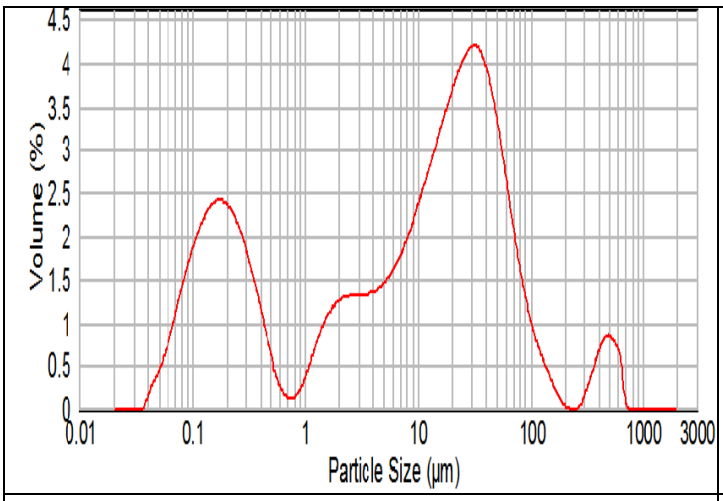

Fig. - 4.13: Particle size distribution for Red Mud at room temperature

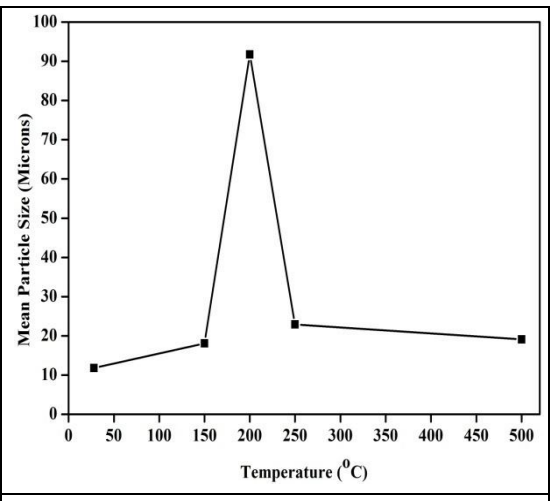

Fig. - 4.14: Particle size for Red Mud at different temperatures

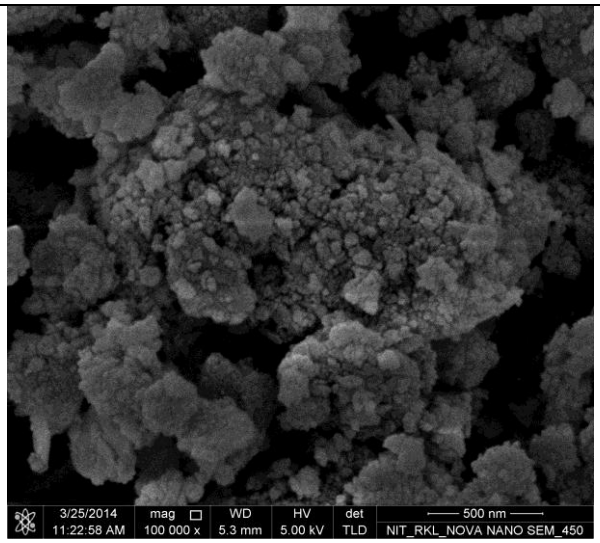

(a) At Room Temperature (28^{0}C)

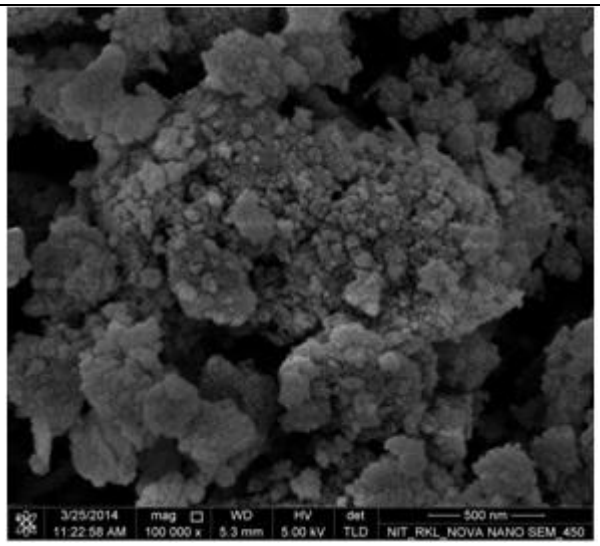

(b) At 150^{o}C Temperature

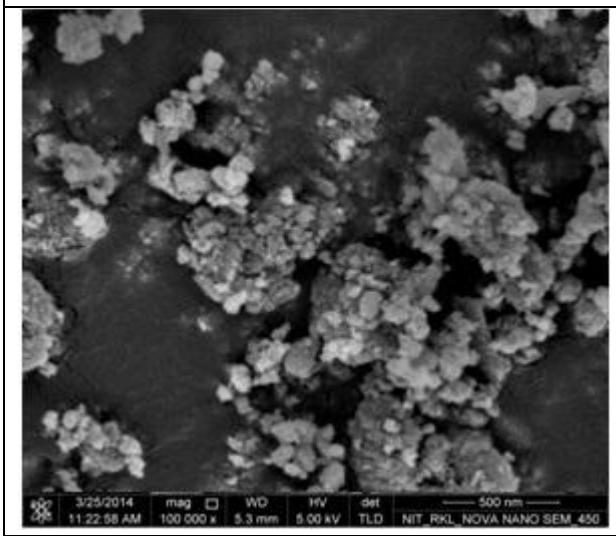

(c) At 200^{o}C Temperature

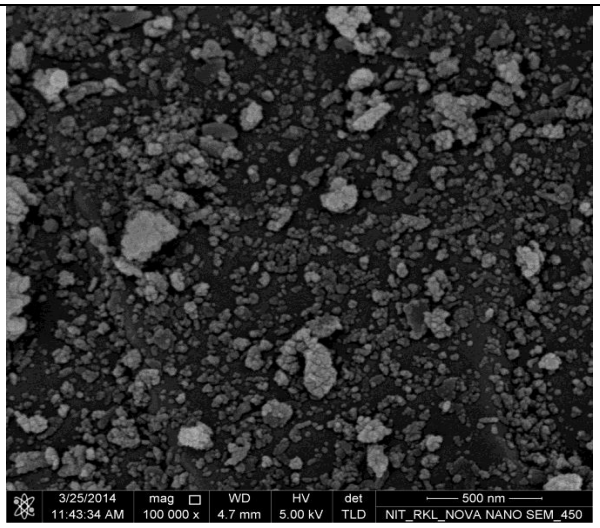

(d) At 250 ^{o}C Temperature

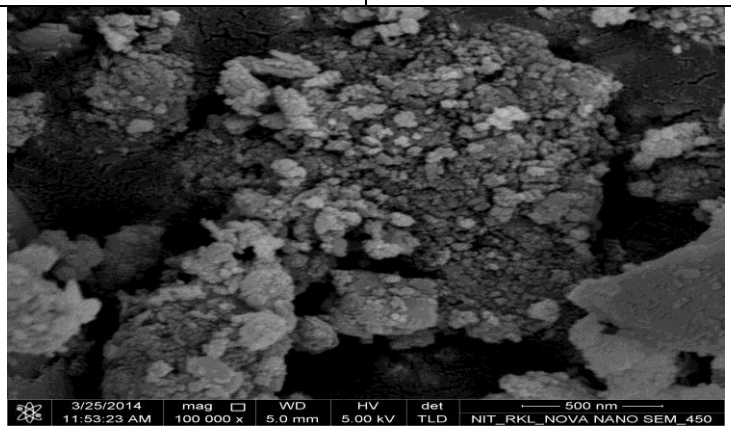

(e) At 500^{o}C Temperature

Fig. - 4.15: FESEM images for Red Mud at different temperatures

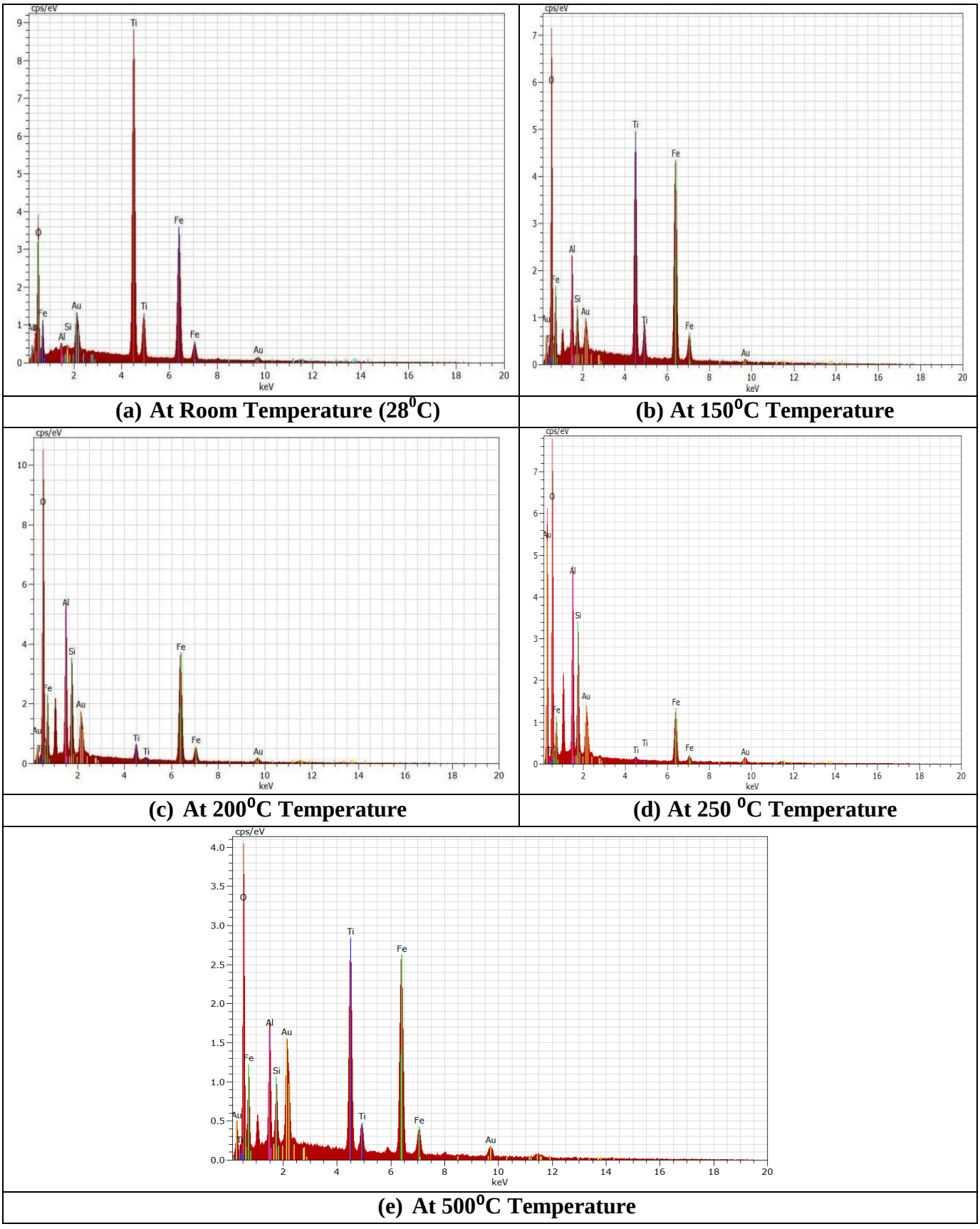

(a) At Room Temperature (28^{0}C)

(b) At 150^{o}C Temperature

(c) At 200^{o}C Temperature

(d) At 250 ^{o}C Temperature

(e) At 500^{o}C Temperature

Fig. - 4.16: EDX analysis chart for Red Mud at different temperatures

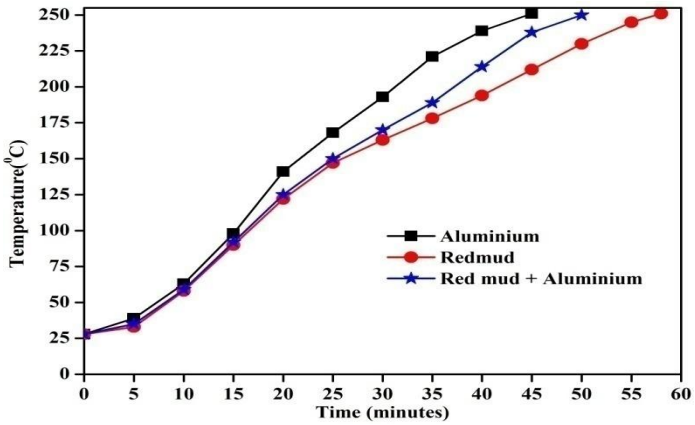

Fig. - 4.17: Temperature profiles for different bed materials

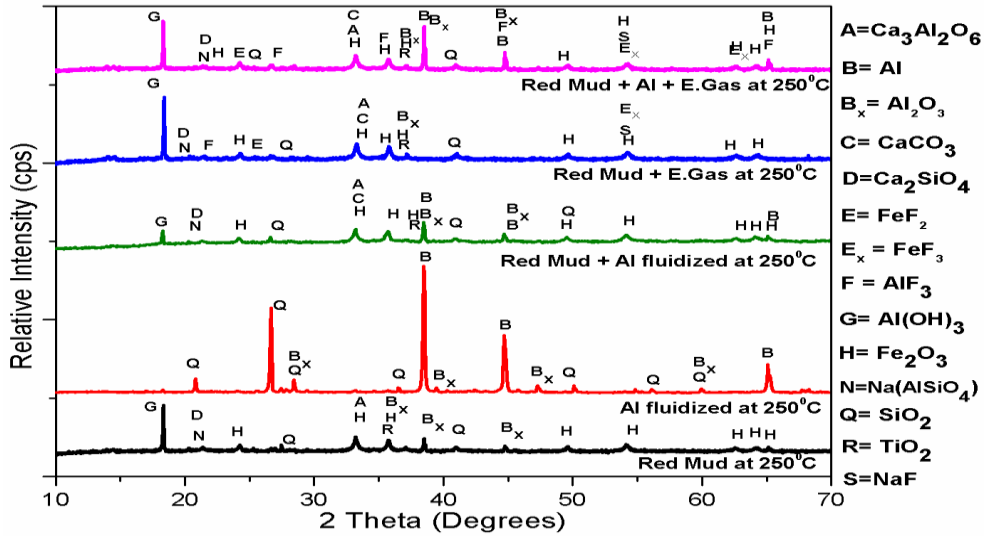

Fig. - 4.18: Comparison of XRD patterns for samples treated with / without effluent gas

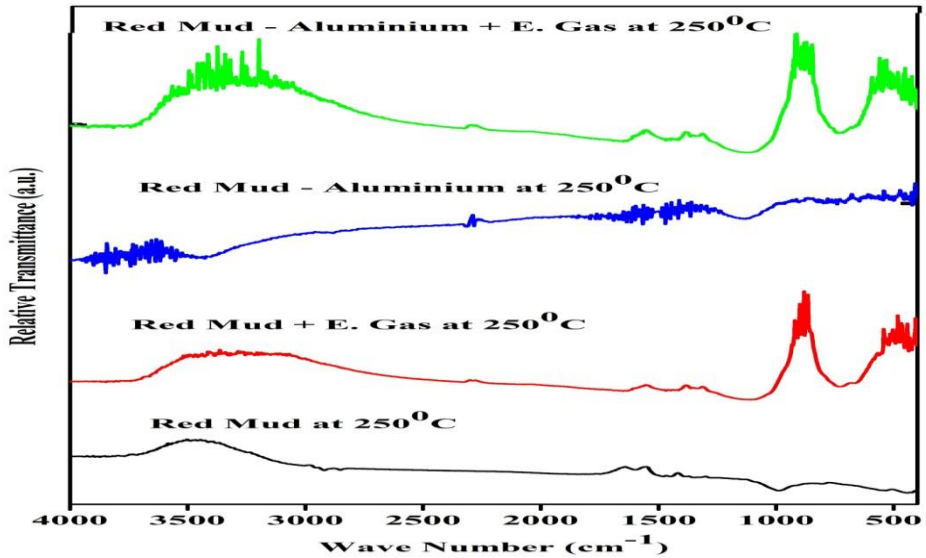

Fig. - 4.19: Comparison of FT-IR spectra for samples with / without effluent gas

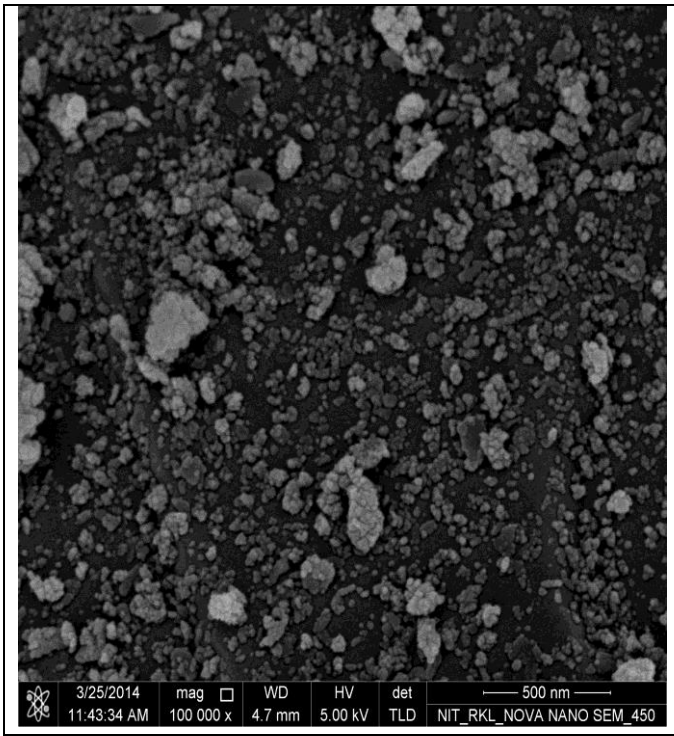

(a) Red Mud Sample

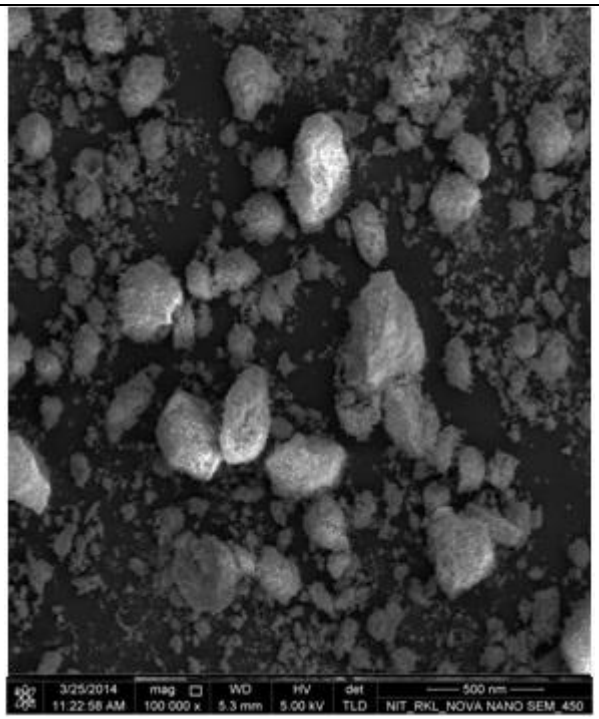

(b) Red Mud treated with Effluent gas

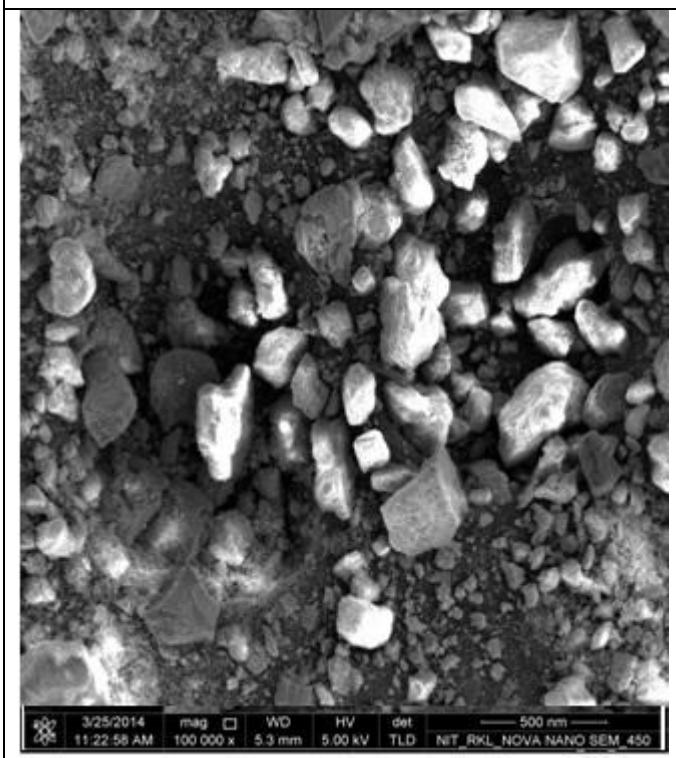

(c) Red Mud-Aluminium Sample

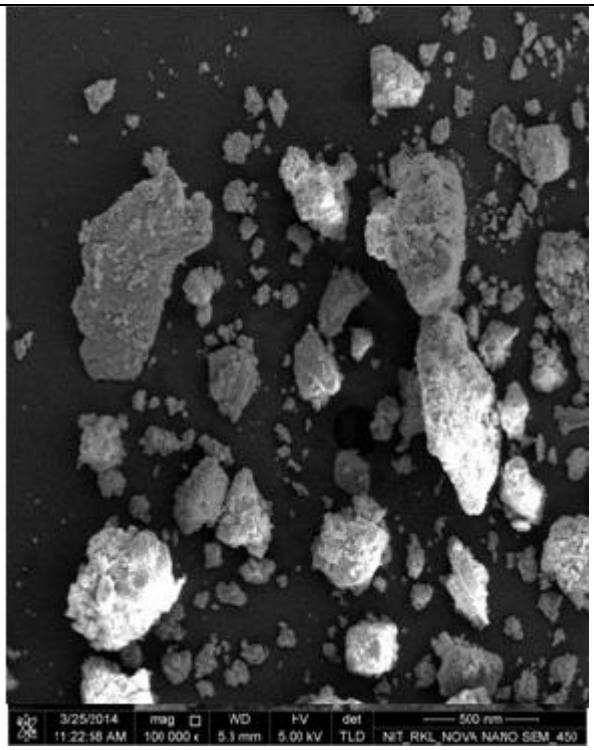

(d) Red Mud-Aluminium with Effluent gas

Fig. - 4.20: FESEM images for different samples at 250^{0}C with / without effluent gas

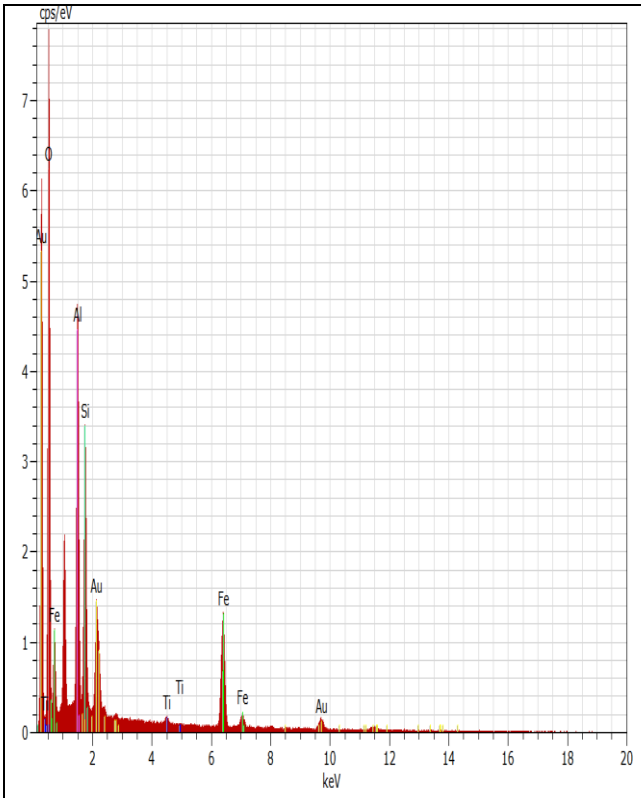

(a) Red Mud Sample

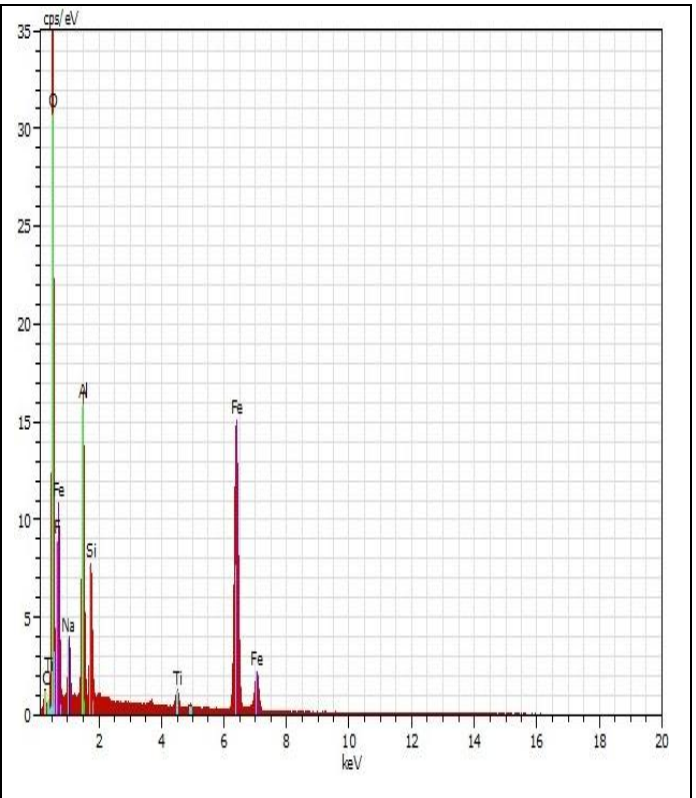

(b) Red Mud treated with Effluent gas

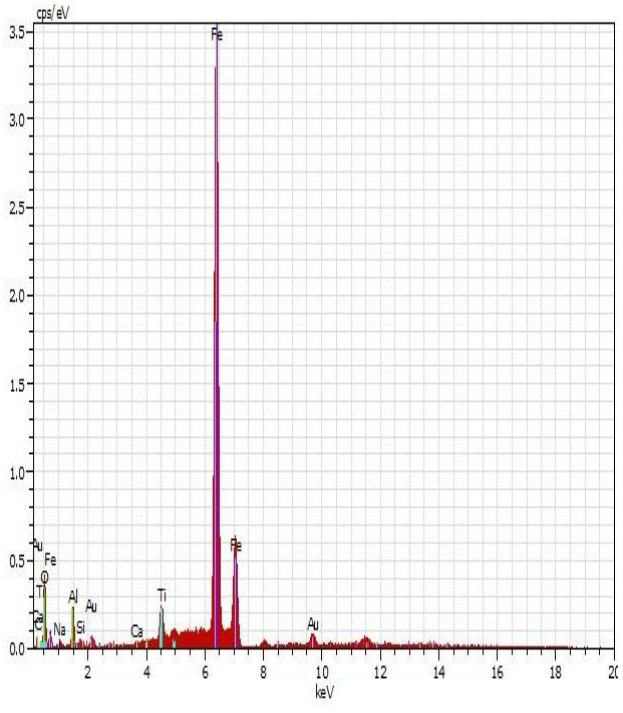

(c) Red Mud-Aluminium Sample

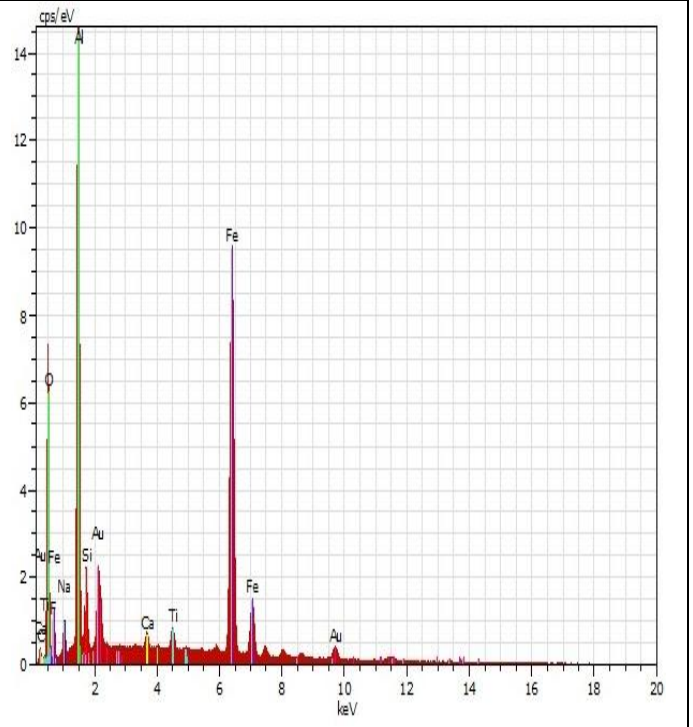

(d) Red Mud-Aluminum Sample with Effluent gas

Fig - 4.21: EDX analysis chart for different samples at 250^{0}C with / without effluent gas

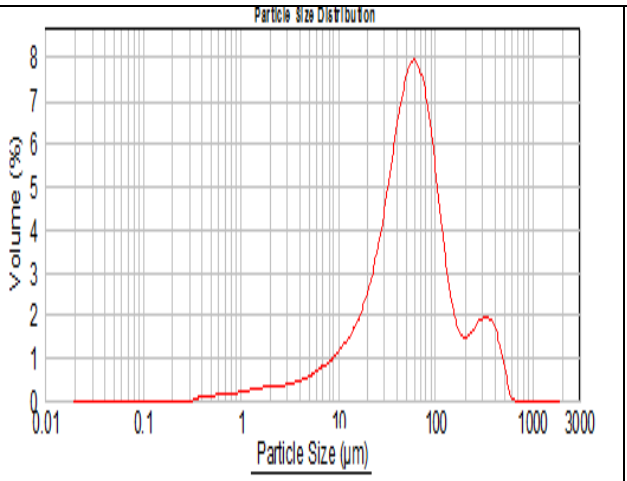

(a) Red Mud Sample

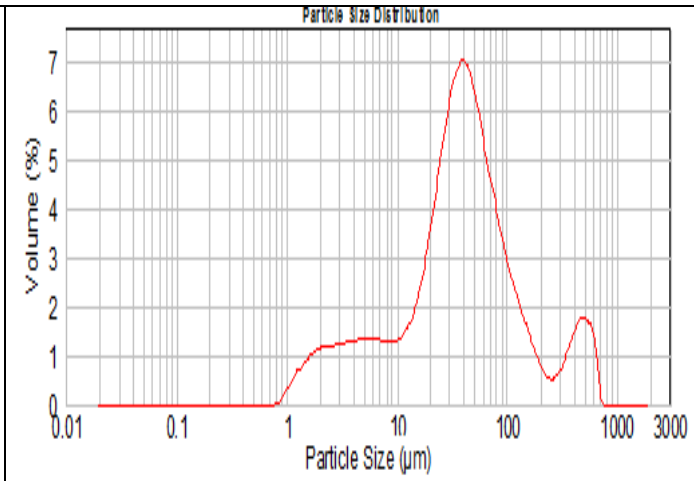

(b) Red Mud treated with Effluent Gas

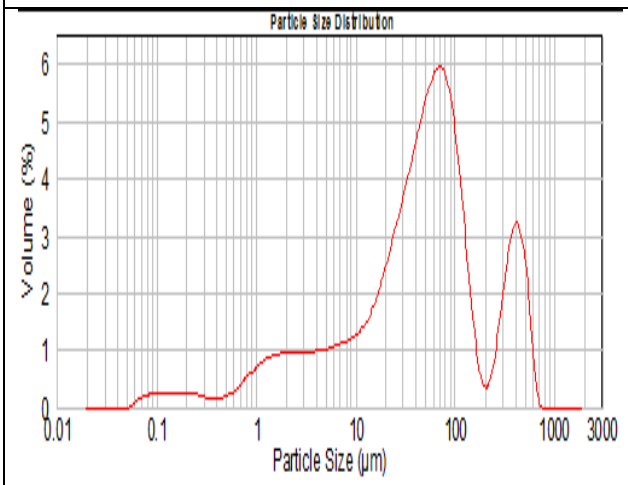

(c) Red Mud-Aluminium Mixture

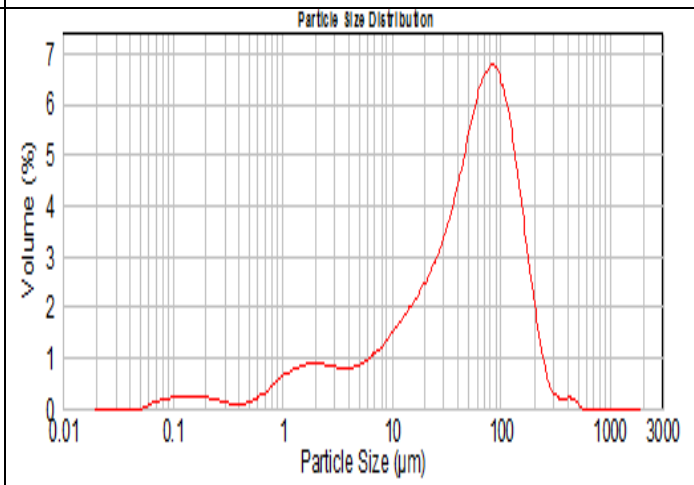

(d) Red Mud-Aluminium Mixture with Effluent Gas

Fig. – 4.22: Particle size distribution for samples at 250^{0}C with / without the effluent gas

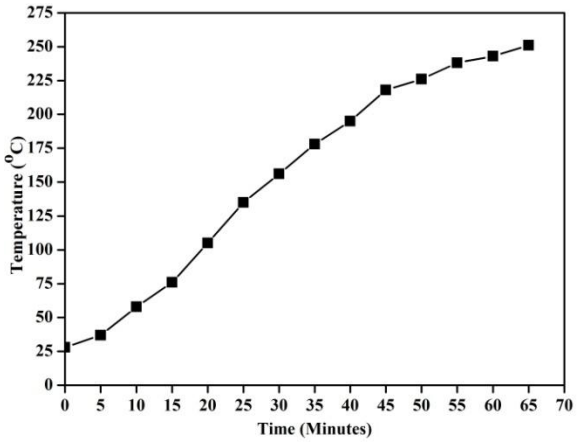

Fig. - 4.23: Temperature profile for Sand within the FBR

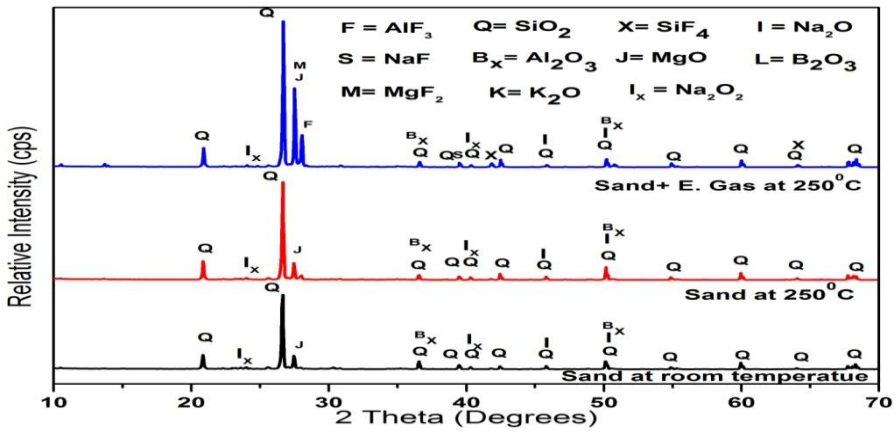

Fig. - 4.24: Comparison of XRD patterns for Sand treated with / without effluent gas

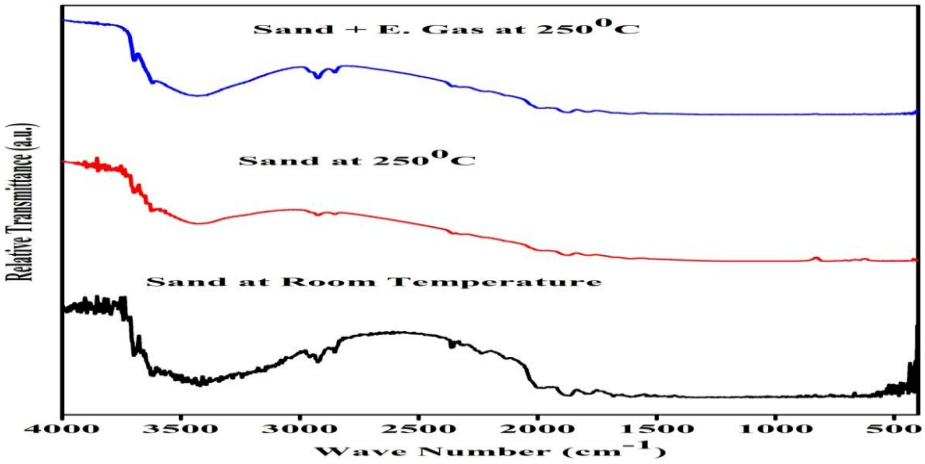

Fig. - 4.25: FT-IR spectra for Sand treated with / without effluent gas

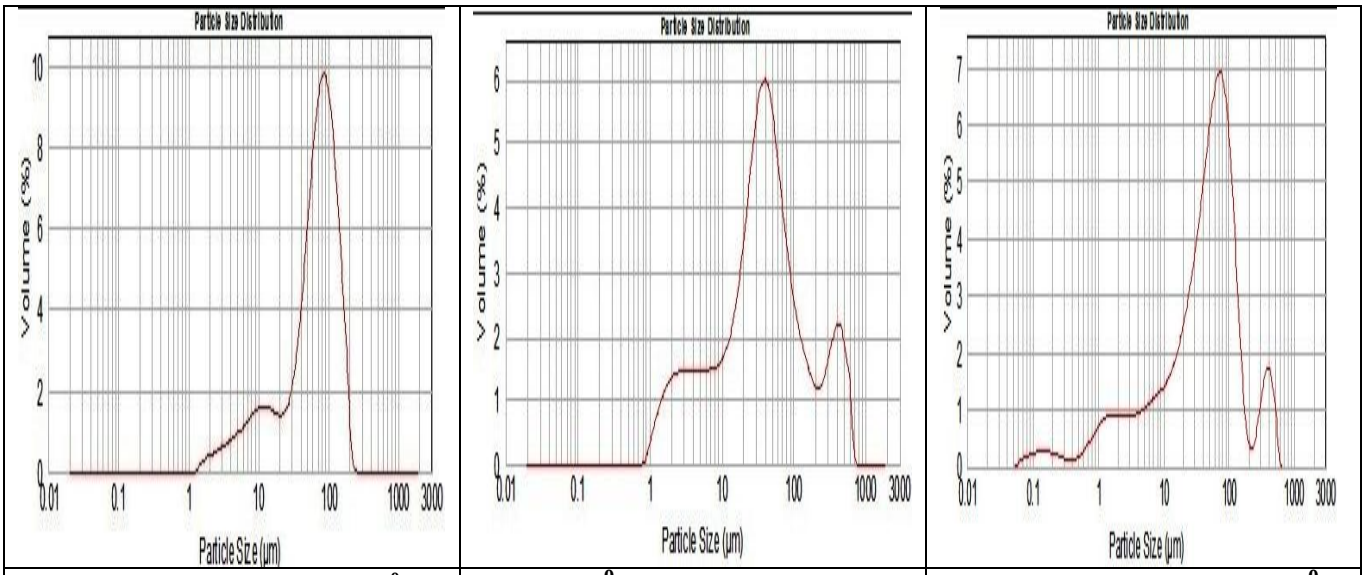

(a) at Room Temperature (28^{0}C)	(b) at 250^{0}C Temperature	(c) with Effluent gas at 250^{0}C

Fig – 4.26: Particle size distribution for Sand treated with / without effluent gas

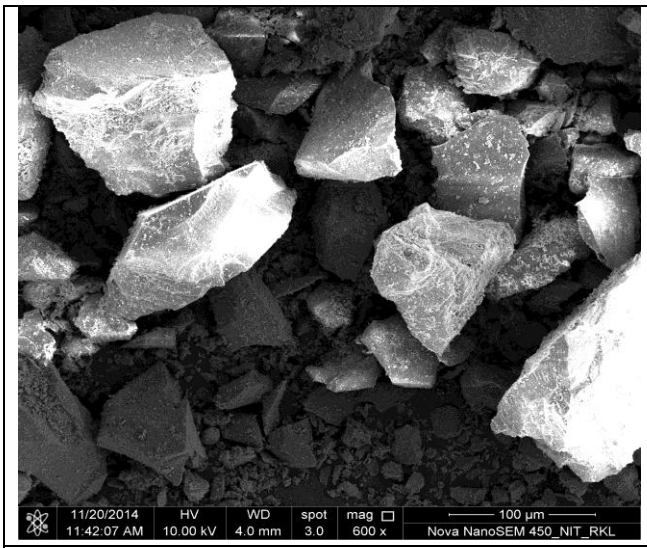

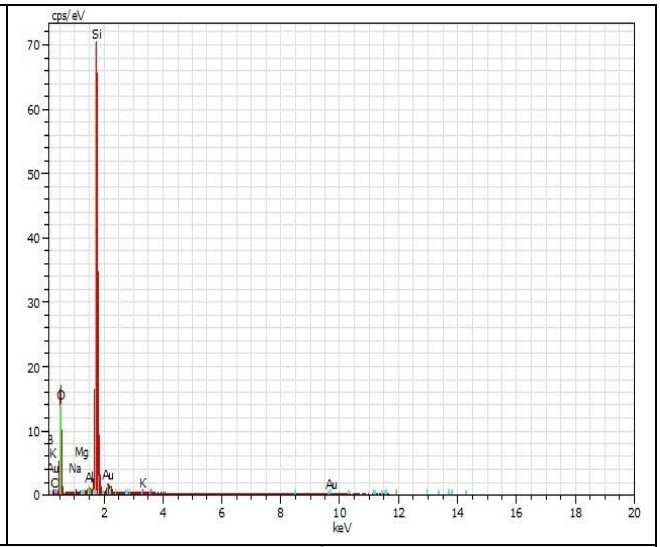

without Effluent Gas at Room Temperature (28^{0}C)

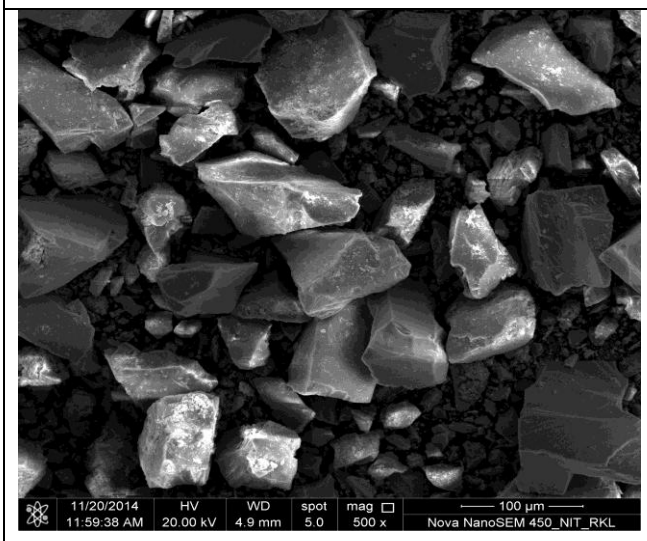

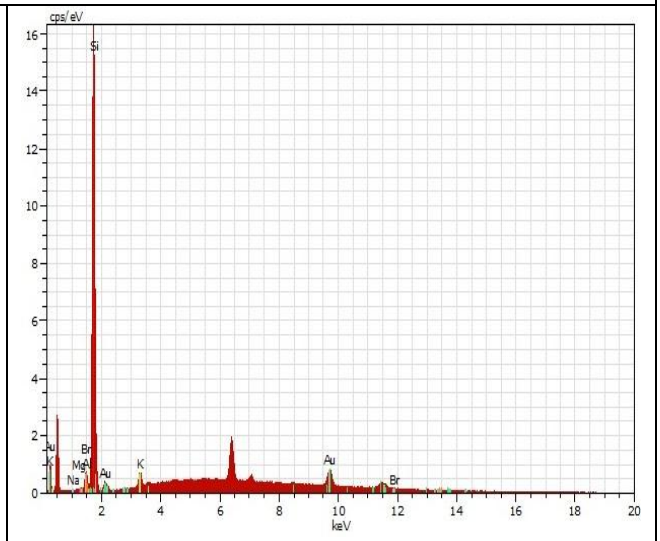

without Effluent Gas at 250^{0}C Temperature

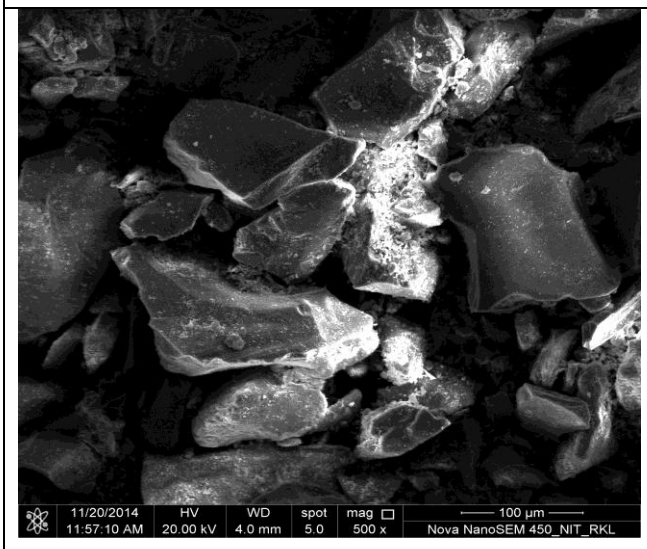

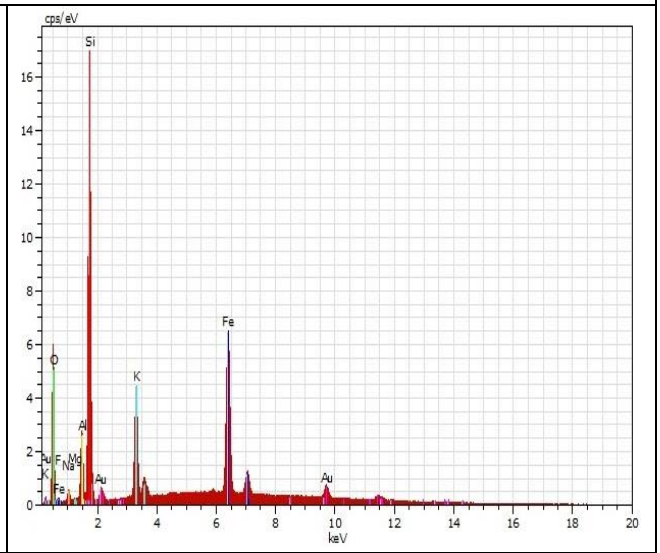

treated with Effluent Gas at 250 ^{0}C Temperature

Fig. – 4.27: FESEM and EDX analysis for Sand sample

CHAPTER - 5

CFD SIMULATIONS

5.1 INTRODUCTION

ANSYS FLUENT 13.0 is used for simulation where first order implicit unsteady solver is used for multiphase calculations. Standard k-ε dispersed Eulerian granular model with standard wall functions are used for modeling the transition nature of bubbling fluidized bed. The success of Eulerian–Eulerian approach depends on the proper description of all possible intra and interphase interactions, such as gas–solid interactions, collision and frictional interactions between particles, and interactions between wall and particles. Air is taken as continuous phase while solid particles are taken as dispersed phase which are treated as continua, interpenetrating and interacting with each other and everywhere in the computational domain.

5.1.1 Assumptions Made

For carrying out simulation on any process, certain assumptions are required for initializing the computational work. The basic assumptions considered for CFD simulations are isothermal, non-reactive, unsteady state gas-solid system, no lift force, no mass transfer between gas and solid phase for FBR unit. Constant pressure gradient and constant density of each phase are also assumed in the present work. Gas phase has been modelled with k-ε turbulent model and solid phases have been modelled with the kinetic theory of granular flow. In this work, bubbling fluidization is observed with bed material where viscosity is considered to be negligible. The motion of each phase is governed by their mass and momentum and energy conservation equations as described in chapter 2.

5.1.2 Geometry and Mesh

The reactor used for the bubbling fluidised bed is based on the experimental set up used in laboratory. **Fig. – 5.1(a)** and **(c)** shows 2D and 3D geometry of the reactor with its dimensions respectively. The bubbling bed zone has internal diameters of 12 cm and height of 70 cm.

The geometry is generated by using commercial software GAMBIT. After geometry creation, a uniform mesh has been generated. Quadrilateral element structure (height to width ratio of 1) is used for meshing the 2D geometry (**Fig. – 5.1(b)**). In this study, total of 21,154 numbers of cells with each cell size of 0.002m x 0.002m and 21,570 numbers of nodes are employed for simulating the fluidized bed. Similarly 54,742 total numbers of cells with each cell size of 0.007m x 0.007m and 58,038 numbers of nodes are employed for simulating the 3D bubbling fluidized bed (**Fig. – 5.1 (d)**).

5.1.3 Solution Techniques

The Phase Coupled SIMPLE method [Patankar (1980)] has been chosen for pressure – velocity coupling. The second-order upwind scheme has been used for discretization of momentum, turbulence kinetic energy and turbulence dissipation rate. The first-order upwind scheme has been used for discretization of volume fraction equations. Under relaxation factors for different flow quantities are mentioned in **Table – 1** of Appendix -2.

The time step is chosen as 0.001 of 1000 steps. The convergence criteria for all the numerical simulations are based on monitoring of the mass flow residual. The residual value is observed to be converging in the range of 1.0 e^{-03} as shown in **Fig.- 5.2**. The simulation is carried out using different flow quantities till the system reaches quasi-steady state. CFD simulation parameters are given in **Table – 5.1.** Used model equations are listed in Table – 5.1 (a). Mesh size, time step, convergence criteria and discretization method are listed in Table – 5.1 (b). Geometry and boundary conditions are listed in Table – 5.1 (c).

5.2 EFFECT OF DIFFERENT SYSTEM PARAMETERS ON BED HYDRODYNAMICS

Hydrodynamic studies give prior information about the flow behaviour of the bed materials within the bed. Bed dynamics such as bed pressure drop and expansion ratio are measured experimentally by varying different system parameters viz. superficial air velocity, particle size and static bed height. The experimental results are tried to be validated with the

simulated results. Therefore bed dynamics such as bed pressure drop, bed expansion ratio are also studied by CFD simulations. Comparisons of the model predictions and experimental measurements on the time-averaged bed pressure drop, bed expansion and qualitative gas-solid flow patterns are carried out at different operating conditions for the validations.

5.2.1 Effects of Gas Velocity on Bed Dynamics

Studying the effect of inlet velocity is very much essential as it plays an important role in fluidization process. In this work, fluidization velocities lying within the range of the minimum fluidization velocity and terminal velocity are used for experimentation which implies the occurrence of bubbling fluidization. In a gas–solid fluidization process the bubbling behaviour is observed for Geldart-A particles at the velocities lying in between the minimum fluidization and terminal velocities of the bed materials [Kunii and Levenspiel (1991)].

Experimental analysis is performed to achieve the steady bed pressure drop and expansion ratio at different superficial gas velocities varying from 0.008 m/s to 0.018 m/s. The hydrodynamic behaviours of fluidized bed are analyzed by monitoring the contour plots for volume fraction of bed materials, static pressure and fluid velocity etc. The bed pressure drop and expansion ratios are also measured experimentally for different superficial gas velocities. These outputs are then compared with the CFD simulated results.

5.2.1.1 Solid Volume Fraction Distribution

The comparison of contours for solid volume fraction distribution against gas velocity at different times of simulation is shown in **Fig. – A.1** of Appendix -1. It is observed that bubbles grow in size as time increases at any particular gas velocity. With increase on time, the volume fraction of solid material is observed to decrease indicating the bed expansion. It is also seen that the average bed heights increase with increasing time at any particular inlet gas velocity.

Using Gidaspow drag model, the contours of solid volume fraction distributions simulated for a time period more than 10 sec are obtained for six different gas velocities in the range of 0.008 m/s to 0.018 m/s (**Fig. – A.2** of Appendix -1). The results show an increase in bed expansion with increasing inlet gas velocity. Initially small bubbles are formed at the distributor which causes the movement of the particles. With the increase in gas velocity, bubble size increases as more gases are processed within the bubble. These bubbles gradually coalesce and convert to slug within the bed. At higher velocity, bubbles grow larger and consequently the bed expands significantly. It is observed that at the superficial gas velocity of 0.014 m/s, the bed surface is highly fluctuating. These fluctuations may be considered as the indication of transition from stable fluidization to turbulent fluidization, which agrees with the experimental observations. It is also observed that when the bed expands a large portion of bed materials is pushed towards the wall region as a result a high value of solid volume fraction is seen near the walls implying the formation of wall slug.

5.2.1.2 Phase Velocity

Fig. – A.3 of Appendix -1 shows the comparison among the vector plots of solid phase velocity and gas phase velocity against inlet gas velocities predicted at different simulation times. In all cases, the internal circulation of particles is observed to occur while gas is not found to be distributed evenly. The core - annulus structure shows that the solid and gas velocities in the core region are much higher than those in the annulus region while solid velocity and gas velocity near the wall are greatly decreased. This may be due to the back mixing and internal circulation which is also observed with the simulation of gas-solid flow.

5.2.1.3 Hydrodynamic Parameters in Radial Direction

Fig. – A.4 (a) of Appendix -1 shows variation in axial velocity against radial positions for solid phases. Axial velocity profiles of particles are found to be smoother in higher gas

velocities because of more transition in flow patterns. This transient flow pattern results a smoother velocity profile in the bed after reaching a quasi-steady state condition. With the increasing inlet gas velocity the maximum axial velocity of particles decreases to certain limit in the central region but it increases near the wall region. The reason for this may be as follows. Bed materials move upward with the movement of rising bubble. When bubble breaks particles are dispersed in the radial direction. As a result axial velocity decreases but in the wall region particle movement increases. Thus a decreased value of axial velocity causes the particles near the wall to show particle slip on the wall.

Fig. – A.4 (b) of Appendix -1 shows the computed gas velocity distribution versus radial distance for different inlet gas velocities. The simulated results show that in the central region of the bed, the velocity of gas is maximum which decreases from the core towards the wall of the bed. With the increase of inlet gas velocity, the energy of the high pressure gas is quickly converted to the kinetic energy of particles. With the increase of inlet gas velocity within the bed, the radial distribution of gas velocity becomes more uniform. Decreased velocities for solid particles in gas phase appear near the walls with increasing inlet gas velocities. This happens due to severe back mixing in the axial direction of the bed.

Fig. – A.4 (c) and **A.4 (d)** of Appendix -1 show the radial profiles for predicted turbulent kinetic energy of the gas phase and predicted granular temperature distribution of the solid phase respectively. Both the output parameters are observed to increase significantly with the increase in inlet gas velocity. The lower velocity is observed to give a low granular temperature where as a high fluctuating velocity per unit of mass is observed at higher inlet gas velocity. The particle fluctuating energy per unit of mass is found to increase from the central region of the bed towards the wall of the bed. At the wall, the granular temperature is found to decrease because of the wall effects.

Fig. – A.4 (e) of Appendix -1 shows the simulated time-averaged volume fraction of solid particles for static bed height of 10 cm at six different inlet gas velocities. It is observed that the volume fraction of solid particles increases toward the walls. It is also seen that at the higher velocity the volume fraction of particles increases more near the walls. At lower velocity of particles the volume fraction remains nearly same as before. As the inlet gas velocity increases, the particles tend to accumulate more at the walls than in the central portion of the fluidized column.

5.2.1.4 Bed Pressure Drop

Variation in bed pressure drop is mainly due to the gas–solid interactions during the fluidization process. **Fig. – A.5 (a)** of Appendix -1 shows the contours of pressure drop against the gas velocity and static pressure variations along the bed height with simulation time step of 10 sec. The bed pressure drop for a fluidized bed varies from maximum value at the bottom of the bed to minimum value at the top of the bed. It is evident from this figure that the pressure is maximum at the inlet which decreases gradually and becomes zero at the top. It is also found from **Fig. – A.5 (b)** of Appendix -1 that the higher velocity yields the higher static pressure as pressure drop is directly proportional to superficial air velocity. The pressure drop is found to be minimum in the bed height zone above 0.25 m which is the free board region for this system.

Fig. - 5.3 shows the variations of the bed pressure drop against time for different velocities. It is observed that as time increases, the bed pressure drop fluctuates and increases significantly. The higher superficial gas velocity gives the lower pressure drop than the lower superficial gas velocity for more drag force being exerted on particles (**Fig. – 5.3 (a)**). Initially the bed pressure drop is found to increase linearly with superficial velocity (**Fig. – 5.3 (b)**) indicating packed bed behaviour. The pressure drop becomes constant when all the materials start fluidizing. This is justified from orifice theory. It is also found that simulated

results are in good agreement with experimental results with a deviation of 4.09 % approximately.

5.2.1.5 Bed Expansion

The time-averaged voidage profiles for the gas–solid fluidized bed are shown in **Fig. – A.6 (a)** of Appendix -1 for six different velocities varying from 0.008 m/s to 0.018 m/s. It is found that initially, the bed height increases with bubble formation. As a result gas volume fraction increases. After some time expanded bed height remains constant at steady state of fluidization. In the beginning of the simulation, waves of voidage are created which travel through the bed. Subsequently bubbles coalesce to form large bubbles as the simulation progresses. It is also observed from this figure that for higher gas velocities the gas volume fraction is larger indicating more bed expansion. It is further observed that there are fluctuations in gas volume fractions. This may be due to frequent bubble formations and their breakage with increase in gas velocity within the bed.

In the bottom region of the column, concentration of solid particles is larger than that in the upper part. Therefore, the maximum gas volume fraction / voidage is found to occur in the top part of the column. The voidage then increases sharply to 1 at the top of the column which corresponds to the region with no solid particles present. Thus the expanded bed represents a clear interface between the fluidized regions and the free board regions. Gas volume fraction approaches the saturation condition when it is equal to 1. The maximum expanded bed heights for different velocity are given in **Table – 5.2**.

Solid volume fraction against bed heights for six different superficial gas velocities in the range of 0.008 m/s to 0.018 m/s are shown in **Fig. – A.6 (b)**. It is seen that at higher superficial gas velocity, the distribution of solid volume fraction decreases in the bed. At lower superficial gas velocity, the bed shows higher solid volume fraction because the solid particles are accumulated in the lower portion of the bed. When the superficial gas velocity

increases, the solid volume fraction distributions fluctuate more in the axial direction. Gradually solid volume fraction decreases and then reduces to zero at the bottom of the column. With increasing superficial gas velocity, the solid volume fraction generally increases with height in the bed. Finally solid volume fraction increases to 1 at the top of the bed beyond which there is no solid particles indicating it to be free board region.

Fig. – A.7 of Appendix -1 show the time-averaged solid volume fraction as a function of bed height for different inlet gas velocities for different times of simulation. Initially the solid volume fraction fluctuates and then it decreases as fluidization starts. It can also be seen at higher superficial gas velocity the distribution of solid volume fractions decreases more in bed than at the lower superficial gas velocity. Then solid volume fraction decreases sharply to zero at the bottom of the bed which is known as saturation condition. It is also observed from **Fig. – A.6** of Appendix -1 that with simulation time step of 10 sec the solid volume fraction is approaching saturation condition for all velocities (**Table – 5.2**).

Fig. - 5.4 (a) shows the bed expansion against time at six different inlet gas velocities varying from 0.008 to 0.018 m/s. The results show an increase in bed height with increasing inlet gas velocity (**Table – 5.2**). **Fig. – 5.4 (b)** shows the plot of variation in bed height against different superficial air velocities. The bed height is observed to increase linearly with inlet gas velocity indicating that the bed expands with increased velocity till steady state is attained. **Fig. – 5.4 (c)** shows the comparison of variation in bed expansion ratio against superficial / inlet air velocities for experimental and simulation results. The bed expansion ratio is found to increase linearly with inlet gas velocity. It is also found that simulated results are in good agreement with experimental results with a deviation of 9.76% approximately.

5.2.1.6 Comparison of Bed Hydrodynamics for 2D and 3D Simulation

Fig. – A.8 of Appendix -1 compares the 3D contours of solid volume fraction distribution against gas velocity. The results show an increase in bed expansion with increasing inlet gas

velocity. That means the volume fraction of solid material is observed to decrease indicating the bed expansion.

Fig. – A.9 (a) of Appendix -1 shows the comparison of 2D and 3D simulations of fluidized bed for granular temperature distribution of the solid phase. In fluidized bed granular temperature increases with the increase in the particle movements. The lower velocity is observed to give a low granular temperature where as a high fluctuating velocity per unit of mass is observed at higher superficial air velocity. It is evident that granular temperature is higher at the upper section of the fluidized bed because the volume fraction of the solid particles is less which oscillates the solid particle which led to increase in the granular temperature. **Fig. – A.9 (b)** of Appendix -1 shows the simulated time-averaged volume fraction of solid particles for 2D and 3D simulation of fluidized bed at different superficial air velocities. It is observed that the volume fraction of solid particles decreases as increase of superficial air velocities.

Fig. – A.9 (c) of Appendix -1 shows the plot of variation in expanded bed height for 2D and 3D simulation of fluidized bed against different superficial air velocities. The bed height is observed to increase linearly with inlet gas velocity indicating that the bed expands with increased velocity of air. **Fig. – A.9 (d)** of Appendix -1 shows the comparison for variation in bed expansion ratio for 2D and 3D simulation of fluidized bed against superficial air velocities. The bed expansion ratio is found to increase linearly with inlet gas velocity. **Fig. – A.9 (e)** of Appendix -1 shows the variations in the bed pressure drop for 2D and 3D simulations of fluidized bed against different superficial air velocities. It is observed that as superficial air velocity increases, the bed pressure drop increases significantly. The higher superficial air velocity gives the higher pressure drop than the lower superficial air velocity for more drag force being exerted on particles. From the following figures, it is observed that 3D simulations of fluidized bed show the highest and better results than the 2D simulations.

5.2.2 Effects of Particle Size on Bed Dynamics

Particle size is one of the many influential parameters in studying the overall performance of the fluidized bed. That is why CFD simulation is carried out for the effect of particle size. Simulation results thus obtained are compared with the experimental results for the bed dynamics.

5.2.2.1 Solid Volume Fraction Distribution

The contour plots of the solid fractions are shown in **Fig. – B.1** of Appendix -1 for four different particle sizes simulated for three different times of simulation. At time of 1 sec, the bed begins to expand with gas flowing into the bed from the bottom. The results show that the bubbles at the bottom of the bed i.e. at the distributor are relatively small. Same thing is also observed during experimentations. Small bubbles form near the bottom of the bed which grow further as they rise to the top and then coalescence of bubbles takes place with increased time. The elongation or enlargement of the bubbles is due to wall effects and interactions with other bubbles within the bed. It is further seen that at time of 5 sec, large bubbles form and start rising through the fluidized bed. At the same time other bubbles form, grow and rise causing agitation throughout the bed substantially. The solid phase is observed to disperse rapidly in the dense phase of the bed. After a period of 5 sec i.e. upto 10 sec, a dynamical equilibrium state / quasi steady state is achieved. The bed at this condition is said to be in fluidized state.

Comparing the contour plots for different particle sizes at any particular time of simulation, it is observed that the bed expansion and fluid bed voidage decrease with the increase in particle size (**Fig. - B.1** of Appendix -1). These are found to be more with particle size of 58 microns. This may be due to the fact that as soon as the gas velocity exceeds minimum fluidization velocity small sized particles (i.e. 58 microns) fluidize at a faster rate than others which result in more bed voidage thereby exhibiting bubbling behaviour.

5.2.2.2 Phase Velocity

The vector plots for solid phase and gas phase velocities are predicted by the CFD simulations with different sizes of particles (**Fig. – B.2** of Appendix -1). In all cases, the internal circulation of particles is observed to occur in solid phase. It is observed from the core-annulus structure that the solid velocities in the core region are much lower than those in the annulus region (**Fig. –B.2 (a)**). In the upper part of bed i.e. in fluidizing section the circulatory motion for solid particles (i.e. downward motion near the wall region and upward motion in the central zone) is observed. This leads to the back mixing and internal circulation as observed with the simulation of gas-solid flow in a fluidized bed.

From the velocity vector plot of gas phase (**Fig. –B.2 (b)**) it is observed that air / gas flow is always in the upward direction throughout the column. In the upper section of the column air velocity is high because it carries air bubbles along with it. In the lower section of the column solid particles obstruct the movement of bubbles for which effect of air velocity is less in this section. From this figure it is again observed that the gas / air velocity is more fluctuating in case of fluidization with larger sized particles. Thus non-uniform flow is observed with 116 μm sized Red Mud particles in comparison with other lower sized Red Mud particles.

5.2.2.3 Hydrodynamic Studies in Radial Direction

Particle size is also observed to have effect on the radial distributions of bed hydrodynamics such as voidage, solid / gas velocity, gas turbulent kinetic energy and granular temperature. Large sized particle systems are observed to show strong non-uniformity than the small sized particles. Therefore the effects of particle size on the radial distributions are analysed in this work and are shown in **Fig. – B.3** to **B.6** of Appendix -1.

(i) Gas volume fractions / Voidages

Fig. – B.3 of Appendix -1 shows the variations of time-averaged voidage against radial direction in the fluidized bed for different particle sizes (i.e. 58 to 116 microns). From **Fig. – B.3 (a)** and **(b)** of Appendix -1, it is seen that the highest peak of voidage is predicted for 58 micron sized particles. Voidage is observed to decrease with increase in particle size. From the **Fig. – B.3 (a)** of Appendix -1, it is observed that there is similarity in the void fraction profiles for four different particle sizes. Void fraction profile for larger size particles is seen more flat in the central region of the bed. It is also observed that voidage in the central region is less than that at the walls. It is seen from **Fig. – B.3 (b)** of Appendix -1 that the volume fraction of small sized particles is high in the wall region of the bed. Voidage is observed to increase with distance from the centre towards the wall region. The volume fraction for large sized particles is found to be more or less same radially in the column. This may be due to the frequent bubble breakage with large sized particles due to particle-particle collisions. This difference in the void fraction profiles results in the development of a certain flow pattern in the bed with respect to different particle sizes.

(ii) Particle velocity distribution

The computed particle velocity distribution carried out at a superficial gas velocity of 0.014 m/s is shown in **Fig. – B.4 (a)** of Appendix -1. From this figure it is observed that in the central part of the bed, the particle velocity is high. In the wall region, the velocities of the particles are less. This may be due to the fact that particles in the central region move upward with the rising bubbles, particles from wall region slide to the central region. Thus the velocity of all sizes of particles decreases from the central region towards the wall. The velocity of small sized particles is observed to be more than that of the large sized particles which may be due to frequent bubble breakages for particle-particle collisions. As a result large sized particles fall back and do not raise much.

(iii)Gas velocity distribution

Fig. – B.4 (b) of Appendix -1 shows the radial profile for the predicted gas velocity using different particle sizes at the superficial gas velocity of 0.014 m/s. Gas velocity is observed to be high at the centre and it is seen to decrease from the centre towards the wall. During the fluidization process the velocity of gas with the small sized particles is observed to be more than that with the large sized particles. This may be due to the high resistance offered by large particle because of more weight and / or frequent bubble breakage with large sized particles than the small sized particles.

(iv)Particle granular temperature distribution

The particle granular temperature is predicted for different particle sizes at a superficial gas velocity of 0.014 m/s (**Fig. –B.5** of Appendix -1). It is seen that the particle granular temperature increases from the centre of the bed towards the wall. At the wall, the granular temperature is more because of the wall effects on the solid particles. The reason may be due to fact that more particles rise with the bubbles in the central region. The wall region particles rush towards the central region to fill the voids created by rise of bubbles. Again when bubbles break the particles carried upwards with the bubbles scatter towards the wall. Thus there are always more collisions in the wall region for which granular temperature increases. It is also observed that the small sized particles have a low granular temperature. The reason may be that with breakage of bubbles larger particles having high momentum collide with the wall. On the other hand small particles having less momentum might not reach the wall when the bubble breaks. Sometimes fine particles remain in central region only. Therefore the granular temperatures for small sized particles are observed to be less than that of large sized particles.

(v) Gas turbulent kinetic energy

The gas turbulent kinetic energy distribution has been plotted for different particle sizes in **Fig. – B.6** of Appendix -1. It is found that the kinetic energy in the central region of the bed is lower than the wall region. This may be due to low solid volume fraction in the central region. The solid particles in the central region tend to move up along with the bubbles and scatter radially on breakage of bubbles. On the other hand, the particle turbulent kinetic energy increases near the wall due to the sliding of particles along the wall and movement of the particles towards centre from the wall. The above two reasons might have lead to more frequent interactions of solid particles and wall of the column thereby producing more turbulent kinetic energy.

Under free slip boundary condition, the solid volume fraction is maximum at the wall [Zhang et al. (1999)] which greatly reduces gas-particles collision effect and gas–solids interaction in the central region. The corresponding kinetic energy distribution in central region is therefore much lower but it increases in wall region as found in **Fig. – B.6** of Appendix -1. All sized particles show approximately same value of turbulent kinetic energy profile in the middle part of the radius (i.e. r/R = 0.3 to 0.85). Smaller sized particles show more kinetic energy in both wall and central region. This may be due to the fact that smaller particles tend to rise up with the bubbles.

5.2.2.4 Effect of Time on Hydrodynamics

The effects of particle size on hydrodynamics of fluidized bed with Geldart–A (i.e. Red Mud) particles are studied at superficial gas velocity of 0.014 m/s (**Fig. – B.7** to **B.9** of Appendix -1). The hydrodynamics with respect to different aspects such as volume fraction / voidage, axial velocity and radial velocity for both the phases are studied against different simulation times. In each case high disturbances are observed with the simulation time which may be due to the formation of bubbles. Such disturbances are observed to decrease with the increase

in particle size because of higher weight / more void space with large sized particles than smaller sized particles.

5.2.2.5 Bed Pressure drop

Pressure drop across the bed is one of the most important aspects of the fluidization process. Variations in bed pressure drop against particle size and simulation times are shown in **Fig. - 5.5.** As indicated in **Fig. - 5.5**, it is observed that the overall pressure drop in the bed decreases significantly at the beginning of fluidization which may be due to loosening of the bed materials at the onset of fluidization. Then bed pressure drop is found to fluctuate upto about 7 sec of simulation time. Steady state is observed after the simulation time of 7 sec. Pressure drop fluctuations are observed because of formation, coalescence and splitting of bubbles continuously in a transient manner in the fluidized bed. It is observed that bed pressure drop decreases with increase in particle size (**Fig. - 5.5**). The effect of particle size on total pressure drop is also important for proper design and optimisation of fluidized bed. That is why the effects of particle size on bed pressure drop are compared for experimental and computational studies (**Fig. - 5.6**). It is found that the pressure drop decreases with increase in particle size for both experimental and computational observations thereby implying a very good agreement. Observations with deviations are shown in **Table – 5.3**.

The contours of pressure drop and static pressure along the bed height are shown in **Fig. – B.10** of Appendix -1 for different particle sizes with a constant superficial velocity of 0.014 m/s. The axial bed pressure drop in a fluidized bed is observed to vary from higher value at the bottom of the bed to approximately zero value at the top of the column (**Fig. – B.10 (a)**). It is evident from this figure that the pressure is highest at the distributor which gradually decreases and becomes zero at the outlet. It is also seen from **Fig. – B.10 (b)** that the higher particle size has the lower static pressure because of more void space. In the fluidization zone (within which the particles fluctuate) the maximum pressure variation takes

place. Above this height i.e. the main free board region the pressure drop can be ignored. In this case this zone is observed to be within 0.23 m height. Similarly different height limits are observed for different particle sizes (**Table – 5.3**).

Bed pressure drop is also measured against different superficial air velocities experimentally for four different particle sizes. The results are compared with those predicted by CFD simulation in **Fig. – 5.7**. From this figure it is observed that in both the cases (i.e. simulation and experiments), the pressure drop varies linearly with the gas velocity upto certain extent and then remains constant indicating proper fluidization. This may be due to the fact that with increase in the gas velocity, the intensity of bubble formation and breakage increases. As a result all the bed materials are free to move and start fluidizing at which bed pressure drop remains constant.

5.2.2.6 Bed Expansion

The predicted volume fraction profiles against bed height for different sizes of solid particles for both solid and gas phases are shown in **Fig. - 5.8**. It is observed that value of the solid volume fractions increase with increase in particle size. It is also seen that in the dense phase of the bed the solid volume fractions decrease with increase in bed height upto certain point and then decreases gradually which finally reduces to zero (**Fig. – 5.8 (a)**). This represents a proper fluidized bed with zero solid in the top portion of the column and the solid particles being distributed in the rest of the column. The bed remains in full expanded state. At this stage solid volume fraction is maximum at the bottom and minimum at the top. The expanded bed heights of the dense phase are noted and tabulated in **Table – 5.3** for different particles sizes.

At the beginning of the simulation, waves of voidages are created which travel through the bed and subsequently flow back to form large bubbles as the simulation progresses. Initially the voidage increase slowly with height and then increase sharply to

attain 100% i.e 1.0 at the top of the bed as shown in **Fig. – 5.8 (b)** which corresponds to the region with no particles. The expanded height of the bed represents a clear interface between the fluidized regions and the free board regions. Therefore the maximum gas volume fraction / voidage occurs at the top of the column. The expanded bed heights obtained from the simulations are plotted against superficial velocity and compared with the experimental observations for bed expansion (**Fig. – 5.9**).

Bed expansion is a measure of fluidization quality. Effect of particle size on expanded bed height is also simulated and shown in **Fig. – 5.8**. From the **Fig. – 5.9** it is seen that increase in particle size decreases the expanded height of the fluidized bed. From this figure it is also observed that the expansion ratio increases with increase in superficial velocity. It is also found that small sized particles show more bed expansion than larger sized particles. This is may be due to lighter weight of smaller sized particles than larger sized particles. Comparison of the model predictions and experimental measurements on bed expansion ratio shows good agreement for which deviations are shown in **Table – 5.3**.

5.2.2.7 Comparison between 2D and 3D Simulations for Bed Hydrodynamics

Comparing the contour plot of solid volume fractions against particle sizes, it is observed that solid volume fractions increase with increase in particle sizes (**Fig. – B.11** of Appendix -1**)**. In other words it can be said that more voidage / more bed expansion are observed with smaller sized particles i.e. 58 microns. This may be due to the fact that as soon as the gas velocity exceeds minimum fluidization conditions small sized particles (i.e. 58 microns) are fluidized faster which result in more bed voidage thereby exhibiting more bed expansion.

Fig. – B.12 (a) of Appendix – 1 shows the simulated time-averaged volume fractions of solid particles for 2D and 3D simulation of fluidized bed for different particle sizes. It is observed that the volume fraction of solid particles increases with increase in particle sizes. Similar trends are observed in 2D and 3D simulations. Only higher solid fractions or lower

bed voidage are observed in 3D simulations in comparison with 2D simulations. **Fig. – B.12 (b)** of Appendix -1 shows the comparison between 2D and 3D simulations for bed expansion ratio against particle size. The bed expansion ratio is found to decrease with increase in particle size of Red Mud. This may be due to low solid volume fraction with smaller sized particles than larger sized particles. Similar trend but higher magnitudes of bed expansions are observed with 3D simulations in comparison with 2D simulations. **Fig. – B.12 (c)** of Appendix -1 shows the variations of the bed pressure drop for 2D and 3D simulations of fluidized bed against different particle sizes. It is observed that as particle size increases the bed pressure drop decreases significantly. With the larger sized particles the bed pressure drop is observed to be lower because of more void space among large sized particles for same static bed heights. From the above figures, it is also observed that 3D simulation of fluidized bed shows the higher pressure drop than the 2D simulations. Similar trend is also observed in both the simulations for pressure drop studies.

5.2.3 Effect of Static Bed Height on Bed Dynamics

Static bed height is considered as an important parameter for the hydrodynamics of gas-solid fluidized bed. Thus the effect of static bed height is analyzed in this work by varying it from 8 cm to 14 cm. CFD simulation is also carried out for the effect of static bed height.

5.2.3.1 Phase Velocity

The velocity vectors of solid phase and gas phase are shown in **Fig. – C.1** of Appendix -1 for different static bed heights. This figure reveals that solid particles move downward in the wall region and upward in the core/central region. It is also found that smaller static bed height shows a more turbulent velocity profile in the dense phase as less mass of bed materials fluidize faster than materials of higher static bed height. It is also observed that the concentration of solid particles is higher in the wall region than in the core of the bed (**Fig. – C.1(a)**). This is due to upward movement particles from the core region with the rising

bubbles. The velocity vector of gas phase (**Fig. – C.1(b)**) indicates that air/gas always flows in upward direction throughout the column. From this figures it is also observed that the gas / air velocity is more fluctuating in case of higher static bed height. This may be due to presence of more solid–solid and solid–wall collisions because of presence of more solids with higher static bed heights.

The time-averaged particle velocity distributions studied at superficial velocity of 0.014 m/s for 77 micron sized particles for four different static bed heights are shown in **Fig. – C.2** of Appendix -1. It is observed that velocity path is almost parabolic showing maximum in the central region and minimum in the wall region. It is again observed that there is sudden decrease in the velocity near the wall region. This may be due to the downward movement of particles in addition to the sliding of particles along the wall. Again there is a small increase in velocity which may be due to the upward movement of particles by the wall slugs. It is also observed that a higher static bed height has lower particle velocity than the lower static bed height. The reason for this may be the higher bed weight with higher static bed height needs more air force to move than the particles with lower static bed height.

5.2.3.2 Hydrodynamic Parameters in Radial Direction

When rising bubbles break the wake particles and particles trapped within the clouds are scattered. In this process some particles move in the axial direction and some particles scatter in horizontal i.e. radial direction. Therefore studies on bed dynamics in radial direction cannot be ignored for the complete study on hydrodynamics of fluidized bed reactor. Thus bed dynamics with respect to particle granular temperature, velocity distribution and volume fraction are studied. The particle granular temperature distribution predicted at superficial gas velocity of 0.014 m/s for different static bed heights are shown in **Fig. – C.3 (a)** of Appendix -1. From this figure it is seen that the particle granular temperature is low in the central region than the wall region because of more collisions in the wall region which has already been

explained in section of 5.2.2.3 for particle granular temperature. It is also observed that the small height of static bed have a low granular temperature than the higher static bed height. The reason may be the availability of more solid particles at any level of the bed with higher static bed heights than that with lower static bed height. As a result more collisions among solid particles occurred with higher static bed height.

Fig. – C.3 (b) of Appendix -1 shows the simulated time-averaged volume fraction of solid particles for different static bed heights. It is observed that the volume fraction of solid particles is more in the centre and near the wall. It is also observed that particle volume fraction decreases from the centre towards the wall but suddenly it increases near the walls. Reason may be fall back of vertically moved particles in the central region and sliding of horizontally scattered particles along the walls because of bubble breakage. It is also seen that higher static bed heights have more volume fraction of particles than the lower static bed heights. Reason is more particles with higher static bed height. Similar trend is observed for all the static bed heights. Variations in axial velocities for solid phase against radial positions for different static bed height are shown in **Fig. – C.3 (c)** of Appendix -1. Axial velocity profiles of 77 micron sized solid particles fluidized at a velocity of 0.014 m/s for different static bed heights are compared with each other in this figure. It is found that smaller static bed height shows comparatively smoother profile than other bed heights. This may be due to the smooth bed expansion with particles of smaller static bed height. For particles of higher static bed height, smooth expansion is not achieved because of more materials. With increasing static bed height the maximum axial velocity of particles is observed to decrease. Again with increasing radial direction the velocity is observed to decrease from the central region of the column towards the wall region. The reason may be that during fluidization process bubbles form at the distributor and then rise to the top. More bubbles form in central part of the bed, so more particles flow upward with the rising bubbles in the central part.

Some particles move up when the bubble breaks and some particles are dispersed in the radial direction which slide along the wall. As a result central region particles show higher velocity and velocities of the particles are less in the wall region.

5.2.3.3 Pressure Drop

Contours of bed pressure drops for different static bed heights are shown in **Fig. – 5.10 (a)**. From this figure it is observed that higher static bed has higher pressure drop because of more weight of bed in the column. It is also seen from **Fig. – 5.10 (b)** that the higher static bed has the higher static pressure. Expanded bed height limit is observed to be 0.285 m within which higher pressure loss occurs. Above this height the pressure drop can be ignored. Similarly different static pressure bed heights as observed for different static bed heights are listed in **Table – 5.5**. It is observed from **Fig. – 5.10 (c)** that the overall pressure drop in the bed decreases initially at the onset of fluidization and then fluctuates upto about 7 sec of simulation time. Pressure drop fluctuations may be due to the continuous bubble formation and breakage within the fluidized bed. After time step of 7 sec the pressure drop is observed to remain constant indicating complete fluidization. It is also seen that the pressure drop increases as the static bed height increases which is due to the increase in bed weights.

Pressure drop is also measured experimentally with the help of a manometer for different static bed heights (i.e. 8 cm to 14 cm) at different superficial gas velocities. The experimental values of bed pressure drop are compared with those predicted by CFD simulations (**Fig. – 5.10 (d)**). From this figure it is observed that in both the cases (i.e. with CFD simulations and experiments), the variation of pressure drop with the inlet gas velocity is linear. The bed pressure drop increases with increase in static bed height. Bed pressure drop is also found to increase with superficial velocity upto certain point i.e. minimum fluidization point for all static bed heights indicating the packed bed behaviour. Bed pressure drop is then seen to remain constant even with the increase in superficial velocity thereby

indicating complete fluidization. Same trend is observed with all the static bed heights both experimentally and computationally. Comparison of the model predictions and experimental values on pressure drop shows good agreement for different gas velocities with small deviations (**Table – 5.4**).

5.2.3.4 Bed Expansion

The time-averaged solid volume fraction profiles for four different static bed heights are shown in **Fig. – 5.11**. Higher static bed heights are observed to have higher distribution of solid volume fractions in bed. This may be due to the fact that bed weight increases with increase in static bed heights. During the fluidization process the solid volume fraction is observed to decrease with increase bed height which then sharply reduces to zero indicating the region beyond the maximum expanded height of fluidized bed. Such limits of maximum expanded bed heights are tabulated in **Table – 5.4**.

From **Fig. – 5.12** it is observed that the bed expansion ratio increases with the increase in superficial velocity for different static bed heights due to flow of more amount of air into the column. Smaller static bed heights show more bed expansion ratios than higher static bed heights because of less material. Comparison of the model predictions and experimental values on bed expansion ratios shows good agreement whose deviations are listed in **Table – 5.4**.

5.2.3.5 Comparison of Hydrodynamics between 2D and 3D Simulations

The contour plots of solid volume fraction profiles for four different static bed heights with 2D and 3D simulations are shown in **Fig. – C.4** of Appendix -1. It is observed that the volume fraction increases with increase in static bed heights because of increase in bed weight.

Bed dynamics with respect to particle granular temperature, bed expansion ratio / expanded bed height, particle volume fraction and bed pressure drop are also studied

computationally using 2D and 3D simulations (**Fig. – C.5** of Appendix -1). The particle granular temperature distribution predicted with 2D and 3D simulations carried out for different static bed height of fluidized bed (**Fig. – C.5 (a)**). It is seen that the particle granular temperature is low for the low static bed height. This may be due to the more bed expansion resulting in the low particle volume fractions in comparison with higher static bed height. Therefore the granular temperature is observed to increase from low static bed height to high static bed height. **Fig. – C.5 (b)** shows the simulated time-averaged volume fraction of solid particles for different static bed heights. The reason is same as explained above. In both the cases, 3D simulated results are found to be of higher magnitudes.

Variations in expanded bed height for 2D and 3D simulations of fluidized bed against different static bed heights are shown in **Fig. – C.5 (c)**. The expanded bed height is observed to increase linearly with the static bed height indicating that the bed height expands proportionately because of increased static bed height. **Fig. – C.5 (d)** shows the comparison made for variations in bed expansion ratios of fluidized bed obtained by 2D and 3D simulation. The bed expansion ratio is found to decrease linearly with increase in static bed height. Reason is same i.e. increased bed materials expand less. The bed pressure drop for 2D and 3D simulations of fluidized bed are observed to increase with increase in static bed height (**Fig. – C.5 (e)**). More bed weight with the higher static bed height results in higher pressure drop than the lower static bed height. It is also observed that 3D simulation of fluidized bed predicts higher value results in all cases implying that 3D simulation is better than the 2D simulation. Higher values with 3D simulations may be because of consideration of particles movement in all directions.

5.2.4 Effect of Particle Density on Bed Dynamics

Solid density is also another important parameter which can influence the hydrodynamics of fluidized bed reactor. Therefore the effect of density is studied by varying ρ_s as 1500, 1300

and 1100 kg/m^3 for the present work. Simulations have been carried out with initial static bed height of 10 cm.

5.2.4.1 Solid Volume Fraction Distribution

Contours of solid volume fraction at different superficial velocities for different bed materials are shown in **Fig. – D.1 (a), (b)** and **(c)** of Appendix -1. The solids motion is governed by the flow of gas, gravitational force on solids (resulting in slip velocity of solid between the gases) and the turbulent dispersion mechanism. As time passes the solid tend to settle in the column due to the effect of gravity as long as terminal velocity is greater than minimum fluidization velocity. The system attains stable state or quasi-steady state after about 30 sec of simulation time. It is also observed that bed expands with the inlet air velocity in each case.

Distribution of solid volume fractions against bed heights for different bed materials at different inlet air velocities are shown in **Fig. – D.2** of Appendix -1. It is observed that when air velocity increases, the solid volume fraction distributions fluctuate more in the axial direction. Initially the solid volume fraction fluctuates and then decreases as fluidization starts. Gradually solid volume fraction decreases and finally reduces to zero at the bottom of the column. It is also seen that at higher inlet air velocity the distribution of solid volume fractions decreases more in bed than at the lower air velocity. This may be because of more flow of air to bed. With increasing inlet air velocity, the gas volume fraction generally increases with the height in the bed. The volume fraction reaches maximum at the top of the bed beyond which there is almost no solid particles indicating it to be free board region.

Simulated values of solid volume fraction of bed against different inlet air velocities for different bed materials are shown in **Fig. – 5.13**. It is seen that at higher inlet air velocity, the distribution of solid volume fraction is less. It gradually decreases with increase in air velocity. Comparing solid volume fractions for different materials it is observed that the denser bed materials have higher solid volume fraction. This may be due to the fact that

denser materials need more force to move than the lighter particles as a result at any particular height within the main bed denser particles are found.

5.2.4.2 Bed Pressure Drop

The contour plots of 2D and 3D simulated pressure drops against the gas velocity for different materials are shown in **Fig. – D.3** of Appendix -1. The bed pressure drop for a fluidized bed varies from maximum value at the bottom of the bed to minimum value at the top of the bed. It is also evident in both of these figures (**Fig. – D.3 (a), (b)** and **(c)**). It is also found that the higher velocity yields the higher static pressure as pressure drop is directly proportional to superficial air velocity.

The comparison of bed pressure drop data for 2D and 3D simulations of fluidized bed for different bed materials are shown in **Fig. – 5.14 (a), (b)** and **(c)**. Experimental data are also compared with each other. It is observed that as superficial air velocity increases the bed pressure drop increases significantly. Experimental result data and simulated results are in good agreement with each other. Comparison results with deviation are listed in **Table – 5.5**. From the above mentioned figures, it is observed that 2D simulation of fluidized bed shows better results than the 3D simulation. Reason may be the differences in grid size / number of grids.

5.2.4.3 Bed Expansion Ratio

Simulated variations in expanded bed heights against inlet air velocities are compared for different materials **Table – 5.6**. It is seen that the expanded bed height increases with increasing inlet air velocity for all materials because of flow of more air into the bed till complete fluidization after which the bed does not expand further. Again comparing the expanded heights for different materials it is seen that denser materials have higher solid volume fraction than lighter materials. This is obvious because of higher weight of denser particles. Comparison among simulated values of expanded bed height carried out by 2D and

3D simulations reveals that results with 3D simulations are higher than those of 2D simulation. Results of 2D and 3D simulations are tabulated in **Table – 5.6**. Difference in the results may be due to the fact that there were differences in grid size and number of grids with 2D/ 3D simulations.

The comparison of bed expansion ratios obtained from 2D and 3D simulations with experimental values for different materials are shown in **Fig. – 5.15 (a), (b)** and **(c)**. From these figures it is found that the bed expansion ratio increases linearly with increase in superficial air velocity for all materials. This is because of more air flow to the bed which causes the material to move with the bubbles. From **Fig. – 5.15 (a), (b)** and **(c)** it is observed that experimentally observed values of bed expansion for Sand, Red Mud and Aluminium are much higher than simulated results. The reason may be that the simulated data cannot be same as the real data. Simulation is carried out based on certain assumptions which might not be proper. But same trend is observed in all cases. Comparison data are listed in **Table – 2** of Appendix -2.

5.3. EFFECT OF DIFFERENT CFD PARAMETERS ON BED HYDRODYNAMICS

The CFD parameters such as drag models, specularity coefficient and restitution coefficient are seen to affect the hydrodynamics of the fluidized bed. Therefore the effects of CFD parameters on the simulations are studied by varying different system parameters viz. particle size, static bed height and superficial air velocity. The comparisons among the model predictions and experimental measurements with the time-averaged bed pressure drop, bed expansion and qualitative gas-solid flow pattern are carried out under different conditions.

5.3.1 Effect of Drag Models

The drag force plays an important role in the fluidization process and thus becomes the key factor for modelling a fluidized bed. The drag force influences the flow regimes and pressure drop across the fluidized bed. Therefore it is essential to select a proper drag model for which

the best of three drag models (i.e. Gidaspow, Syamlal-O'Brien and Wen & Yu) is be selected in the present work. Simulation results are finally compared with the experimental results.

5.3.1.1 Effect of Drag Models on Bed Expansion

Bed expansion is one of the important aspects in fluidization process. The effect of drag model on bed expansion is therefore analysed by varying different parameters such as particle size, superficial air velocity and static bed height.

(i) Effect of particle sizes

Particle size being one of several influential parameters for proper fluidization affects the drag models. In the present work, particle size of Red Mud is varied from 58 μm to 116 μm to study its effect on different drag models thereby on the fluidization process. Simulation results thus obtained with different particle sizes for different drag models are compared with each other and also with experimental results. The time-averaged profiles of gas volume fraction for gas–solid fluidized bed are shown in **Fig. – E.1 (a)** of Appendix -1 for three different drag models.

The bed starts to expand when it attains minimum fluidization. After that at a particular flow rate the bed attains steady state when all particles fluidize freely. At this condition, concentration of solid particles is found comparatively more in the lower section of the column than in the upper section of the column. Therefore, maximum gas volume fraction/voidage is observed in the top section of the column. With increase in air flow voidage value increases sharply to 1 in the top section of the bed which represents a clear interface between the fluidized or main bed region and free board region. It is also observed from the **Fig. – E.1 (a)** of Appendix -1 that bed of small sized particles shows more gas volume fraction indicating more bed expansion for all the drag models. Thus it can be said that the voidage increases with decrease in particle size and this is true with all the drag models. This may be due to the fact that small sized particles being lighter exhibit smooth

bubbling fluidization in comparison with larger sized particles. As a result bed starts expanding smoothly above minimum fluidization velocity with the rise of bubbles. Some particles may also rise in the wake of the bubbles.

The distributions of solid volume fractions fluctuate more in the axial direction. As bubbles start to move, the solid volume fraction fluctuates and decreases gradually forming lean phase and finally reduces to zero. This corresponds to the interface region above which particles are not seen in the column. Large size particles are seen to be present in the lower section of the bed in all cases of simulations. **Fig. – E.1 (b)** of Appendix -1 indicates that, with increasing particle sizes, void fraction decreases in the bed for which minimum of void fraction is seen at lower portion of the fluidized bed. The expanded bed height and percentage increase in bed height with respect to static bed height for different particle sizes are shown in **Table – 3** of Appendix -2. From this it is observed that the Gidaspow drag model shows the higher percentage of bed expansion than the other two (i.e. Syamlal - O'Brien and Wen & Yu) models.

Simulated results obtained from all the three models are compared and are also compared with the experimental results for bed expansion ratios (**Fig. – 5.16**). From this figure it is observed that the expansion ratio decreases with increase in particle size for different drag models. Small sized particles show more bed expansion ratio than large sized particles because of easy movement of smaller sized particles than larger sized particles at any particular air flow rate. Same trends are obtained in all cases. This comparison shows a very good agreement among experimental and simulated results obtained from different drag models. The deviation of simulated result from experimental results for different drag models are listed in **Table – 5.7**. From this comparison it is observed that Gidaspow drag model shows least deviation among these three models.

(ii) Effect of superficial air velocity

In the present work air velocity is varied from 0.008 m/s to 0.018 m/s to analyse its effect on different drag models in turn on the fluidization process. Simulation results thus obtained with different air velocities for different drag models are compared with each other and also with the experimental results.

Contours plots of solid volume fraction against gas velocity for different drag models at different simulation time are shown in **Fig. – E.2** of Appendix -1. It is observed that bubbles formed at the bottom of bed are relatively smaller in size which gradually grows with time as they move up. This indicates that the bed expansion increases with more gas flowing into the bed i.e. with increase in velocity and with increase in time. At around 15 sec, a dynamical equilibrium state / quasi steady state is found to be achieved and the bed is said to be in fully fluidized state which is due to the rapid movement of bubbles within the bed. Similar trends are observed in all the cases for all the drag models. It is also observed that bed voidage remains same for the Gidaspow drag model at any time of simulation implying uniform fluidization whereas fluctuations in bed voidage are seen with other models (Syamlal – O'Brien and Wen & Yu).

The time-averaged solid volume fraction profiles for the gas–solid fluidized bed are shown in **Fig. – E.3** of Appendix -1 for three different drag models at six different superficial air velocities. It is observed that there are fluctuations in solid volume fractions. This may be due to the frequent formation and breakage of bubbles with increase in gas velocity within the bed. After some time of simulation expanded bed height remains constant implying steady state of fluidization. Gidaspow drag model shows higher solid volume fraction at any velocity than other models.

The time-averaged gas volume fraction profiles for different drag models are shown in **Fig. – E.3 (a)** at different velocities. It is found that the bed height initially increases with

the increase in bubble formation with increased air flow. As a result gas volume fraction increases. This is so because excess of the gas beyond minimum fluidization passes through the bed as bubbles by which gas volume fraction increases. Therefore maximum gas volume fraction / voidage occur at the top of the column. This voidage increases sharply to 1 in the upper part of the column corresponding to the region where particles are absent. Gas volume fraction approaches the saturation condition at a value of 1. Expanded bed heights measured at different velocities for different drag models are listed in **Table – 5.8** with percentage increase in bed heights.

Comparisons of solid volume fraction profiles for different drag models at different superficial gas velocities are shown in **Fig. – E.3 (b)**. It is seen that the solid volume fraction in the bed decreases with increase in velocity of air which is obvious for more flow of air. Bed expansion increases with increased velocity or solid volume fraction gradually decreases with velocity and reduces to zero in the top of the column. From **Fig. – E.3** and **Table – 5.8** it is observed that more bed expansion is achieved with Gidaspow drag model than the other two (i.e. Syamlal - O'Brien and Wen & Yu) models. Bed expansion ratios obtained from CFD simulations for different drag models are compared with each other and against the experimentally observed values of bed expansion (**Fig. – 5.17)**. It is observed that the bed expansion ratio increases with inlet gas velocity for all the models. It is also found that simulated results are in good agreement with experimental results. The deviations of CFD simulated results from the experimental results are found to be 19.33, 14.91 and 9.77% for Wen & Yu, Syamlal–O'Brien and Gidaspow models respectively. Least deviation with Gidaspow drag model suggests it to be a better model among three selected models with respect to hydrodynamic studies.

(iii)Effect of static bed height

Effect of static bed height is analyzed both experimentally and by CFD simulations using different drag models. Finally simulated results are compared against the experimental results with respect to bed expansion ratios.

The time-averaged gas and solid volume fraction profiles for different drag models with different static bed heights are shown in **Fig. – E.4 (a)** and **(b)** of Appendix -1 respectively. It is found that, the maximum voidage occur at top of the bed which attains a maximum value of 1 (**Fig. – E.4 (a)**). Similarly the solid volume fraction initially fluctuates and then gradually reduces to a value nearly equal to zero after which no particles are left in the bed (**Fig. – E.4 (b)**). It is also observed from these figures that low static bed height indicates more bed expansion with all types of drag models. That implies that at any particular gas velocity the voidage decrease with increase in static bed height because of more particles for all the drag models. From **Table – 4** of Appendix -2 it is seen that the bed expansion decreases with increasing bed heights. It is also seen that at any particular bed height Gidaspow drag model gives more expansion than the other two models.

The simulated data are compared with the experimental data in **Fig. – 5.18**. From this figure it is observed that the bed expansion ratio decreases with the increase in bed height for different drag models. This is obvious because of more bed weight with higher static bed height which needs more air flow to cause the fluidization of particles. Comparison between the model predictions and experimental results on bed expansion ratio shows a good agreement with least deviations of 3.74 % for Gidaspow models.

5.3.1.2 Effect of drag models on Pressure drop

The effect of drag models on pressure drop is analysed in details by varying different parameters like static bed height, particle size and superficial air velocity.

(i) Effects of static bed height

Comparisons among contours of bed pressure drop and static pressure predicted for different static bed heights is made for different drag models in **Fig. – E.5** of Appendix -1. The static pressure in a fluidized bed is observed to vary from a maximum value at the bottom of bed to approximately zero at the top of bed. It is also observed that beyond a particular height static pressure becomes zero. This height is termed as static pressure bed height. It is again observed that higher static bed height shows higher pressure drop and higher static pressure for all the models which may be because of more weight of bed materials in the column. **Table – 5.9** shows the maximum static pressure for different drag models against static bed heights. It is observed from this table that the maximum static pressure increases with the increase in static bed height for all the drag Models. Among these three drag models, the Gidaspow drag model is seen to predict lower maximum static pressure and higher static pressure bed height indicating higher fluidization zone with respect to static pressure variation.

Pressure drop across the bed determined experimentally for four different static bed heights at constant superficial gas velocity of 0.014 m/s. The observed results are compared with those predicted by CFD simulation for three drag models. The variation of bed pressure drop against static bed height for all drag models is compared in **Fig. – 5.19.** From this figure it is observed that, the bed pressure drop increases linearly with the static bed heights in both the cases i.e. CFD simulation and experimentation. Comparison of simulation predictions and experimental results on bed pressure drop shows a very good agreement with negligible deviations for all the models (**Table – 5.10).** For higher bed heights Gidaspow drag model shows less deviation in comparison with other models. Again it is observed from **Table – 5.10** that Gidaspow drag model shows negative deviation leading to a minimum deviation on an average than the other models. From this it can be concluded that Gidaspow drag model

predicts more accurate results with respect to the effect of static bed height on bed pressure drop.

(ii) Effects of particle size

Effect of particle size on bed pressure drop is studied for different drag models in the present work. It is observed that bed pressure drop decreases as the particle size increases. The higher particle size is observed to show the lower static pressure bed height in all cases of simulations because of large void spaces among themselves in comparison with smaller sized particles which helps in assisting the bubble rise. As a result bed pressure drop and static pressure are observed to be less for large sized particles.

The simulated values of maximum bed pressure and static pressure bed height are listed in **Table – 5** of Appendix -2 against different particle sizes of bed materials for different drag models. It is observed that pressure drop decreases as the particle size increases for both Syamlal - O'Brien and Wen & Yu Drag Models. But in case of Gidaspow drag model, the maximum value of pressure drop is observed to fluctuate to some extent. This may be due to the fluctuations in bed voidage caused by frequent bubble formation and breakage. In Gidaspow drag model the static pressure bed heights are observed to be 0.228, 0.214, 0.171 and 0.157 m for 58, 77, 98 and 116 micron sized particles respectively. This shows a regular pattern of decreased pressure in comparison with other two models from which it can be said that the Gidaspow drag model predicts more accurate simulation results than other two models with respect to bed pressure drop / static pressure.

Experimentally observed results are compared with those predicted by CFD simulations for different drag models (**Fig. – 5.20**). From this figure it is observed that in both the cases the pressure drop decreases linearly with the increase in particle size. Comparison of the model predictions with experimental results on bed pressure drop shows a very good agreement for all the three drag models. It is further observed that least deviation and more

consistency in bed pressure drop are achieved with increased particle size (**Table – 5.11**) for Gidaspow drag model.

(iii)Effect of superficial air velocity

Similarly effect of superficial air velocity is analyzed for different drag models by monitoring the contour plots of static pressure and bed pressure drop against air velocity. It is found that higher velocity yields higher static pressure for all types of drag models. It is also seen that with Gidaspow drag model, lower bed pressure drop is achieved than other two drag models. The simulated time-averaged pressure drop is compared with the experimental results for all the drags models (**Fig. – 5.21**). It is observed that in both cases the pressure drop varies linearly with the inlet gas velocity initially in the packed bed region. With further increase in gas velocity the bed pressure drop remains constant indicating proper fluidization regime. From this figure, it is also observed that Gidaspow drag model shows good agreements with the experimental results both qualitatively and quantitatively. It is also found that all the simulated results are in good agreement with experimental results with an average deviation of – 4.34, -8.46 and -5.58% for three different drag models (i.e. Gidaspow, Syamlal – O'Brien and Wen & Yu) respectively. Thus it can be said that Gidaspow drag model predicts comparatively more accurate results with least deviation among three different drag models.

5.3.2 Effect of Different Specularity Coefficient on Bed Hydrodynamics

Specularity coefficient is used to specify the shear condition at the walls in two phase granular flow. The specularity coefficient measures the fraction of collisions which transfers the momentum to wall. Its value varies from zero (for smooth walls) to one (for rough walls). Different specularity coefficients specify different levels of roughness or shear to the wall. When specularity coefficient is approaching zero, a free - slip boundary condition is obtained at the walls for the tangential velocity of solids. When this coefficient approaches unity, a significant amount of momentum is transferred. Values between zero and unity refer to a

partial-slip which increases with decreasing its value. The effect of specularity coefficients on the hydrodynamic behaviour of bubbling fluidized bed is studied in this section. Five different values of specularity coefficients i.e. 0, 0.25, 0.5, 0.75, 1.0 are considered for simulations. The effects of specularity coefficients are analysed in details for bed expansion and pressure drops with reference to particle size, superficial air velocity and static bed height parameters.

5.3.2.1 Effect of Specularity Coefficients on Bed Expansion

Although specularity coefficient is not analysed in experimental studies but CFD modelling will not be proper without proper selection of specularity coefficient. Other parameters such as particle size, static bed height and superficial air velocity affect the quality of fluidization. Therefore it is necessary to study specularity coefficient with respect to these parameters.

(i) *With respect to particle size*

The contours and time-averaged solid volume fraction is shown in **Fig. – F.1** of Appendix -1 for different values of specularity coefficients. The solid volume fraction distributions fluctuate more with the rising bubbles in the axial direction of the column and decreases gradually forming lean phase and finally reduces to zero. This corresponds to the region above which the particles are not seen in the column. Large size particles are seen to have more solid volume fraction in the bottom portion of the column for all values of specularity coefficients. This implies that with increasing particle sizes, void fraction decreases and minimum of void fraction is seen at lower portion of the fluidized bed. The expanded bed height and percentage increase in bed height against particle sizes for different specularity coefficients for are shown in **Table – 6** of Appendix -2. From this it is observed that better bed expansion is achieved with zero specularity coefficients than other values of specularity coefficients.

From **Fig. – F.1** and **Table – 6**, it is observed that increase in particle size decreases the simulated fluidized bed height for all the values of specularity coefficients. This may be due to the large size particle have more weight which move to a shorter distance than the small particles. The simulated results are compared with the experimental results for bed expansion ratios (**Fig. – 5.22**). From this figure it is observed that the expansion ratio decreases with increase in particle size for different specularity coefficients. It is further observed that specularity coefficients have no impact on bed expansion ratio for higher particle sizes i.e. beyond 95 microns approximately. For lower particle sizes bed expansion ratio is observed to decrease with increase in specularity coefficients. But the effect is not clear with the partial slip conditions. The reason may be attributed to the fact that with no slip condition, wall effect is negligible. That is why particles fluidize freely by the fluid. As a result particles move up with the rising bubbles thereby producing higher bed expansion ratio. Small sized particles show more bed expansion ratio than large sized particles. This comparison shows a very good agreement with experimental results for different values of specularity coefficient. The deviation of simulated result with specularity coefficient are calculated from experimental results and listed in **Table – 5.12**. From this it is observed that the no slip condition (Ø = 0) of specularity coefficient show the least deviation for different particle sizes.

(ii) *With respect to air velocity*

Comparisons of solid volume fraction profiles with different superficial gas velocities for different values of specularity coefficients are shown in **Fig. – F.2** of Appendix -1. It is found that the distribution of solid volume fraction decreases in the bed with increase in velocity of air which is obvious for more flow of air with increased velocity. From **Fig. – F.2** and **Table – 7** of Appendix -2 it is observed that the no slip condition i.e. specularity coefficients of 0.0

shows more bed expansion than the other two conditions (partial and free slip conditions with specularity coefficients of 0.25, 0.50, 0.75 and 1.0).

Bed expansion ratio obtained from CFD simulation for different values of specularity coefficients are compared against the experimentally observed values (**Fig. – 5.23)**. It is observed that the bed expansion ratio increases with inlet gas velocity for all cases. It is again observed that with no slip condition i.e. Ø = 0 bed expands with increased velocity. But for partial slip condition i.e. Ø = 0.25, 0.50 and 0.75 the bed expansion is not uniform. Although bed expansion increases it is observed that at higher velocity same amount of expansion is achieved. For free slip condition i.e. Ø = 1.0 it is found that initial bed expansion remains almost same. Above 0.016 m/s velocity, bed expansion is observed to increase with air velocity. Reason may be negligible wall effect at lower velocities. Thus it can be said that no-slip condition is proper for CFD simulation of fluidized bed with least deviation for bed expansion. It found that simulated results are in good agreement with experimental results. The deviations of CFD simulated results from the experimental results are calculated (**Table - 5.13**). Least deviation with no slip condition of specularity indicates it is a better condition of specularity than the others.

(iii) With respect to static bed height

The time-averaged solid volume fraction profiles against static bed height for different values of specularity coefficients are shown in **Fig. – F.3** of Appendix -1. Solid volume fractions are observed to increase with increase in static bed heights because of presence of more materials with higher static bed heights. In other words it can be said that at a particular velocity the voidage decrease with increase in static bed height. Increase in bed expansions with increasing static bed heights for different specularity coefficients are shown in **Table – 8** of Appendix -2. From this data table it is observed that with no slip i.e. Ø = 0 condition, more bed expansion is achieved than other conditions (i.e. Ø = 0.25, 0.50. 0.75 and 1.0).

The simulated data for bed expansion ratios are compared with the experimental data in **Fig. – 5.24**. From this figure it is observed that the bed expansion ratio decreases with the increase in bed height at any specularity coefficients. But clear decreasing trend is found with no slip condition only. Reason may be negligible wall effect. Again it is observed that bed expansion ratio decreases with increasing specularity coefficients while impact on specularity coefficients other than no slip condition (Ø =0) is not clear. Comparison between the models predicted values and experimental values on bed expansion ratio shows good agreement and the deviation are listed in **Table – 5.14**. It is observed that the no slip condition of specularity coefficients shows least deviation than the other values of specularity coefficients.

5.3.2.2 Effect of Specularity Coefficients on Pressure Drop

The effect of particle–wall collision on pressure drop is analysed in details in terms of specularity coefficients by varying different parameters.

(i) With respect to particle size

The effect of particle size on pressure drop is analysed for different values of specularity coefficients in **Fig.- F.4** of Appendix -1. From the contour plots, it is found that the bed static pressure varies from maximum value at the bottom of the bed to minimum value at the top of the bed. It is also observed that beyond static pressure bed height, static pressure becomes zero. The static pressure bed heights for different specularity coefficients (i.e. no slip, partial slip and free slip condition) are shown in **Table – 9** of Appendix -2. The static pressure height is observed to decrease with increase in particle size for all values of specularity coefficients. This may be due to the less expansion with large sized particles in comparison with the small sized particles. The maximum static pressure height is observed in no slip condition with a uniform reduction in pressure than the other conditions i.e. partial and free slip condition of specularity coefficients.

The bed pressure drops obtained from experiments are compared with those predicted by CFD simulations for different values of specularity coefficients (**Fig. – 5.25**). From this figure it is observed that, in the both cases (i.e. in CFD simulation and experiments), the pressure drop decreases linearly with the increase in particle size. Comparison of the model predictions and experimental measurements on pressure drop shows a very good agreement with different coefficients of specularity. It is also observed that no slip value of specularity coefficients gives least deviation as compared to other values (**Table – 5.15**). Reason for this may be the negligible wall effects.

(ii) With respect to air velocity

In a similar manner the effect of superficial air velocity is analyzed for different values of specularity coefficients by monitoring the contour plots of static pressure and bed pressure drop against air velocity (**Fig. – F.5** of Appendix -1). It is found out that higher velocity yields higher static pressure for all values of specularity coefficients. It is also found from **Table – 10** of Appendix -2 with increase in velocity the static pressure bed height increases. After certain limit static pressure reduces to zero for all the velocities. It is further observed that with no slip condition the higher static pressure bed height is achieved than the other values of specularity coefficients. For partial and free slip condition no clear trend is achieved which may be due to wall effects. But with no-slip condition higher static pressure bed height and clear difference in measurement of static pressure indicate that no wall effect is there for which static pressure is observed to be minimum.

The simulated time-averaged pressure drop is compared with the experimental results for different specularity coefficients as shown in **Fig. – 5.26**. It is observed that in both the cases (i.e. in CFD simulation and experimentation) the pressure drop varies linearly with the inlet gas velocity initially. From this figure, it is also observed that no-slip condition shows good agreements with the experimental results. It is also calculated quantitatively in terms of

percentage of deviation of simulated pressure drop from the experimentally measured values (**Table – 5.16**). From this it can be concluded that the zero value of specularity coefficients gives better prediction with least deviation among all values of specularity coefficients.

(iii)With respect to static bed height

Comparisons among contours of bed pressure drop and static pressure predicted at different static bed heights have been made for different values of specularity coefficients in **Fig. – F.6** of Appendix -1**.** Similarly the static pressure in a fluidized bed is observed to vary from a maximum value at the bottom of the bed to approximately zero value at the top of the bed. It is also observed that with increase in static bed heights the bed pressure drop and higher static pressure increase for all values of specularity coefficients. This may be due to more weight of bed materials with increased heights. From **Table – 11** of Appendix -2 it is seen that the static pressure bed height for different values of specularity coefficients increase with the static bed height. Among all conditions, the zero value of specularity coefficients (i.e. no-slip condition) shows the higher static pressure bed heights indicating higher zone for static pressure.

Pressure drop is determined experimentally for four different static bed heights at a constant superficial gas velocity of 0.014 m/s. The observed results are compared with those predicted by CFD simulation for different values of specularity coefficients (**Fig. – 5.27**)**.** From this figure it is observed that in both, CFD simulation and experimentation the pressure drop is observed to increase linearly with the static bed heights. Comparison of the simulation predictions and experimental measurements on pressure drop shows a very good agreement (**Table – 5.17).** From this it can be concluded that the no slip values of specularity coefficients predicts the better result with least deviation. Deviation from experimental values is observed to be increased with specularity coefficient indicating no slip condition is the better choice for simulation of bed pressure drop and static bed pressure.

5.3.3 Effect of Restitution Coefficient on Bed Hydrodynamics

The interactions among particles are also critical for the accurate prediction of the complex hydrodynamics in fluidized bed. The restitution coefficient (e) reflects the extent of elasticity / inelasticity during the collisions between particles and describes the amount of the dissipation of solid kinetic energy during collisions. Thus the effect of restitution coefficient is studied by carrying out CFD simulations with the restitution coefficients (e) for different values of 0.85 to 1.0 and results are compared.

5.3.3.1 Effect of Restitution Coefficients on the Bed Dynamics in Radial Direction

The effects of restitution coefficients on the radial distributions of gas and solid velocities are shown in **Fig. – 5.28.** The predicted gas velocity is observed to decrease from center towards the wall region of the column for all the restitution coefficients. But with different restitution coefficients very little differences are observed in the radial profiles of gas velocity during simulations. These differences may be due to particle–particle / particle–wall collisions. From **Fig. – 5.28 (a)** maximum air velocity is predicted as 0.35 m/s in the central region. The time-averaged radial particle velocity distributions are observed to increase from the wall region towards the central region (**Fig. – 5.28 (b)**). This reaches maximum in the centre and minimum at the wall side. Reason may be as follows. During fluidization more gas flow in the central region. Thus with gas the solid particles in the central region move with faster than those in the wall region. As a result voids are created in central region and particles move radially from wall region to fill up the void spaces. In the wall region, particles slide along the wall from top to bottom. Again when bubbles break, wake particles scatter horizontally adding to radial movement. It is also observed that the predicted radial solid velocity distribution profiles show some asymmetric pattern. That means the radial particle velocities are almost unaffected by the restitution coefficients which is evident with the literatures [Li et al. (2007, 2010)]. It is concluded that the restitution coefficient plays

only a minor role in numerical modeling of bubbling fluidized beds and spouted beds [Lan et al. (2012)].

Fig. – 5.29 describes the effect of different restitution coefficients on the radial distributions of solid volume fractions**.** The predicted solid volume fraction increases from centre of the bed to wall of the column. At the wall, solid volume fraction is more as compared to centre. This may be due to the stronger dissipation of kinetic energy of solid particles because of more bubble movement / solid movement in the central region. Consequently, more solids remain in the wall region and form a denser zone.

5.3.3.2 Effect of Restitution Coefficients on Bed Expansion

The effect of restitution coefficients on bed expansion is analysed in details by varying different system parameters viz. static bed height, superficial air velocity and particle size. Thus effects of restitution coefficients on bed dynamics are analysed with respect to these parameters.

(i) With respect to static bed height

The contour plots and time-averaged solid volume fraction profiles against bed height for different restitution coefficients with different static bed heights are shown in **Fig. – G.1** of Appendix -1. It is found that, the maximum voidage occur at the top of the bed. The solid volume fractions initially fluctuate and then decrease gradually which finally reduces to zero corresponding to the region beyond which the particles are absent. In this region gas volume fraction / voidage is maximum nearly equal to 1.0. From the contour plots it is seen that with lower static bed heights effect of restitution coefficient is negligible. Only with static bed height of 14 cm it is observed that restitution coefficient has some effect on bed voidage. Voidage slightly increases with restitution coefficient. But it is further seen that voidage with restitution coefficients of 0.9, 0.95, 0.97, 0.99 are almost same. Voidage with restitution coefficient of 0.85 is slightly less and voidage with restitution coefficient of 1.0 is slight

more. From this it can be said that effect of restitution coefficient is not significant on voidage. Slight increase in voidage with restitution coefficient of 0.85 and 1.0 may be due to other effects.

The expanded bed height and bed expansion ratios are calculated and plotted against of restitution coefficients in **Fig. – G.2** and **Fig. – G.3** of Appendix -1 respectively. It is observed from **Fig. - G.2** that the restitution coefficient does not show any significant change with increase in static bed height. It is seen that the expanded bed height is almost constant for any particular static bed height. Comparing among different static bed heights it is seen that expanded bed height increases with static bed heights at any value of restitution coefficient. From **Fig. – G.3** it is seen that the bed expansion ratio is decreasing with static bed heights. For higher static bed height bed expansion ratio is slightly less than the bed expansion ratio of the lower static bed heights. This may be due to higher bed weight with higher static bed height. Thus it can be said that restitution coefficient has no significant effect on expansion ratio with respect to static bed height. Again it is seen that expansion ratio does not change with increase in the restitution coefficient. By comparing the model predicted and experimental results on bed expansion ratios against restitution coefficients (**Fig. – 5.30)** it is observed that both are in good agreement.

(ii) With respect to air velocity

The effect of air velocity on the fluidization process with different restitution coefficients are studied through CFD simulations. Simulation results thus obtained with different air velocities for different restitution coefficients are compared with each other and also with experimental results.

The time-averaged solid volume fraction profiles against bed heights for different restitution coefficients are shown in **Fig. – G.4**. It is found that solid volume fraction in the bed fluctuates with an average value of 0.4 during fluidization for all restitution coefficients.

With increase in superficial velocity the solid volume fraction is found to decrease. But solid volume fraction is found to be almost independent of restitution coefficient at any superficial velocity. The reason might be due to the fact that effect of fine particle collisions specifically for Red Mud is negligible in comparison with the effect of air velocity on the movement of particles. It is further confirmed from plot of bed expansion against restitution coefficient (**Fig. – 5.31** and **Fig. – 5.32**) that the expansion ratio is almost same for all restitution coefficients at any particular velocity. With increasing superficial gas velocity solids start moving as a result the bed expands and bed expansion ratio increases. Thus it can be said that the restitution coefficient has no significant effect on the solid volume fraction as already explained by researchers [Rowe and Nienow (1976)]. The bed expansion ratios obtained from CFD simulations with different restitution coefficients are compared with experimentally observed values at different superficial air velocities (**Fig. – 5.32**). A good agreement is seen for different air velocities.

(iii)With respect to particle size

The effect of particle size on restitution coefficient has been studied during simulations. CFD simulation results obtained with different particle sizes for different restitution coefficients are compared with each other and also with experimental results.

The time-averaged solid volume fraction profiles for the gas–solid fluidized bed with different particle sizes for different restitution coefficients are shown in **Fig. – G.5** of Appendix -1. It is found that the solid volume fraction distributions fluctuate more in the axial direction of the column and decrease gradually forming lean phase and finally reduces to zero. This corresponds to the region above which the particles are not seen in the column i.e. free board region. Large size particles are seen to be in the lower section of the bed there by implying higher solid volume fraction for all values of restitution coefficients. But at a particular particle size the solid volume fraction is almost constant for all values of restitution

coefficient which implies that with any particle size solid volume fraction is almost independent of restitution coefficient. This is further confirmed from the comparison plot (**Fig. – 5.33** and **Fig. – 5.34**).

The bed expansion ratios obtained from simulations are plotted against restitution coefficients and are shown in **Fig. - 5.33**. It is observed from this figure that higher particle sizes have low expansion ratio. This may be because of higher void space in turn more bubble breakages. That means with increasing particle size gas volume fraction decreases, as a result the expanded bed height decreases. It is also seen that the restitution coefficient had almost negligible effect on the bed expansion for different particle sizes. The experimental results on bed expansion ratios are compared against those obtained from simulations for different restitution coefficients with different particle sizes (**Fig. - 5.34**). Both experimental and simulated results are found to agree well for all the particle sizes. It is observed that the restitution coefficients have almost negligible effect on bed expansion ratios for different particle sizes.

5.3.3.3 Effect of Restitution Coefficient on Bed Pressure Drop

The effect of restitution coefficient on pressure drop is analysed in details by varying different parameters such as static bed height, particle size and superficial air velocity.

(i) With respect to static bed height

The comparison of bed pressure drop against restitution coefficient for different static bed heights is shown in **Fig. – 5.35**. It is observed that the pressure drop decreases with increase in restitution coefficient for all the static bed heights. Decrease in bed pressure drop is observed to be more significant with higher static bed height i.e. 14 cm. This may be due to the more fluctuations in turn more kinetic energy generated by collisions among more particles. At a particular height bed pressure drop is observed to decrease with increase in restitution coefficient. Increased restitution coefficient means increased particle-particle

collisions. When all particles fluidize and bed volume increases and the process of fluidization is converted from bubbling to turbulent type by which bed pressure drop decreases.

Pressure drop is also determined experimentally for four different static bed heights with a U-tube manometer. The observed results are compared with those predicted by CFD simulation for different restitution coefficients (**Fig. – 5.36**)**.** A higher bed height is observed to show higher bed pressure drop with different values of restitution coefficients. This may be due to the more weight of bed materials with higher static bed height. Again experimentally observed bed pressure drop is compared with simulation results for different static bed heights (**Fig. – 5.36**). From this figure it is also observed that in both cases (i.e. in CFD simulation and experimentation) the bed pressure drop increases with the static bed heights and decreases with restitution coefficients. Comparison of the simulation predictions and experimental measurements on bed pressure drop shows a very good agreement in almost each case**.**

(ii) With respect to superficial air velocity

Comparisons of static pressures against bed height and bed pressure drop against restitution coefficient are carried out for different superficial velocities in **Fig. – 5.37** and **Fig. – 5.38** respectively. The static pressure in a fluidized bed is observed to vary from a maximum value at the bottom of the bed to approximately zero value at the top of the bed for all the velocities (**Fig. – 5.37**). It is also observed that static pressure increases with increase in superficial air velocity. Bed pressure drop is seen to increase with increase in restitution coefficient for the velocities upto minimum fluidization (**Fig. – 5.38**). For velocities above minimum fluidization it is seen that bed pressure drop is almost constant above particular restitution coefficient indicating two zones i.e. fixed bed and fluidized regions. Again

comparing among different velocities it is seen that at any particular restitution coefficient pressure drop increases with increase in velocity.

(iii)With respect to particle size

Effect of the particle size with restitution coefficient is also required for measuring bed correct pressure drop. Therefore different particle sizes are used to check its effect on pressure drop for different restitution coefficients in the present work. The effect of particle size on pressure drop is analysed for different restitution coefficients varying from 0.85 to 1.0.

From **Fig. – 5.39**, it is observed that the pressure drop decreases as the particle size increases for all the restitution coefficients. This may be due to the fact that large sized particles do have large void spaces among them in comparison with smaller sized particles. But pressure drop is found to increase with restitution coefficients for a particular particle size. This may be due to more solid-solid interaction among solid particles.

5.3.3.4 Effect of Restitution Coefficient on Bed Hydrodynamics

Fig. – G.6 of Appendix -1 shows the time-averaged granular temperature of solid phases for different restitution coefficients. It is observed that the averaged granular temperature of solid phase increases and becomes maximum in the fluidization region, but remains constant at minimum level. The reason may be due to the fact that maximum value of granular temperature occurs at the surface of the bed where particles fluidize freely. Initially as air is supplied particles do not collide in the fixed bed region. But once bed fluidizes after about 30 sec of time more particle collisions are seen. That is why granular temperature increases and reaches maximum value of $2* 10^{-7}$, $3.5 *10^{-7}$, $4*10^{-7}$, $4.5*10^{-7}$, $5*10^{-7}$ and $6*10^{-7}$ for restitution coefficient of 0.85, 0.9, 0.95, 0.97 and 1.0 respectively. Again comparing among different restitution coefficients it is seen that granular temperature increases with increase in restitution coefficient.

The variations of granular temperature and pressure for Red Mud at superficial velocity of 0.016 m/s are shown in **Fig. – G.7** of Appendix -1 for different restitution coefficients varying in the range of 0.85 to 1.0. It is observed that the granular temperature increases with increase of restitution coefficients. The particle pressure decreases with increase of restitution coefficients because more fluctuation within the bed.

5.4 MODEL VALIDATION FOR CFD SIMULATIONS

CFD modelling is carried out for studying the bed hydrodynamics of fluidized bed where Red Mud of particle size 77 microns is fluidized. Effects of different parameters are investigated for appropriate configuration of CFD model. The effects of various parameters i.e. grid independence / mesh resolution, time step, coefficient of restitution, convergence criterion, specularity coefficient, drag model, discretization scheme and laminar / turbulent model are studied and discussed in details.

5.4.1 Discussion on Effects of Different Parameters

(i) Time Step Size

Effects of time steps on the simulation results are studied. It is seen that time step of 0.001 sec is widely used for modeling gas flow in fluidized beds [Taghipour et al. (2005), Hulme et al. (2005) and Zimmermann et al. (2005)]. The effects of different time steps (i.e. 0.001, 0.005, 0.0005 and 0.01 sec) on the CFD simulation results are shown in **Fig. - 5.40**. It is observed that time steps of 0.001 and 0.005 sec yield to more stable results (**Fig. – 5.40 (a)** and **(b)**). Selection of a too small / too large time step size may increase the relative error by which the cell properties cannot be estimated accurately as the cell properties vary between two time steps (Cornelissen et al. 2007). The time step of 0.001 sec is selected as the base because time-step independent results are obtained.

(ii) Convergence Criteria

Two values i.e. 0.001 and 0.0001 are used to test the convergence for scaled residual components. Convergence criterion of 0.001 has been used widely and is thus considered as the standard value in many CFD softwares. Convergence criterion of 0.0001 increases computational cost / time with more iteration per each time step. A minor deviation is observed with this criterion in comparison with convergence criterion of 0.001 (**Fig. - 5.41 (a))**. Therefore the convergence criterion of 0.001 is applied in the model with the less relative errors. The overall bed voidage for the two different convergence criteria are also shown in **Fig. - 5.41 (b)** which do not differ significantly at steady state (i.e. after 15 sec of simulation time). This is further checked with contour plots where contours are compared for the two different convergence criteria (**Fig. – 5.42**). The simulation results obtained with both the criteria are found to be closer after 10 sec of simulation time. Different transient behaviours are observed upto 10 sec time. Therefore 0.001 is selected as the convergence criteria in the present simulation study.

(iii)Discretization Schemes

The contours of solid volume fraction for different discretization schemes are shown in **Fig. – 5.43**. The simulated results of solids volume fraction profiles for the first order discretization scheme are compared with those of second order discretization scheme at time step of 0.001 sec with 10^{-3} convergence criterion. It is observed that there is no significant difference either in overall hydrodynamic behaviour or in bubble shape. This indicates the implementation of numerical simulation to be adequate for measuring and capturing the correct hydrodynamic behaviours / characteristics of the bed. That is why first order discretization scheme is selected for the present study.

(iv) Flow Models

The comparison of simulation results for laminar and turbulent models is carried out by the contour plots of solid void fractions (**Fig. - 5.44**). From this figure it is observed that the bed expansion and variation of the fluid bed voidage increase in both the cases. At the beginning of the simulation, waves of voidage are created, which travel through the bed and subsequently form bubbles as the simulation progresses with the time. Initially the bed height increases with the formation of bubbles till it is levelled off at a steady height i.e. at the time of 10 sec in the present case. The value of solid volume fraction is found to be more in turbulent model than in laminar model. Bubbling fluidization is also found to be more prominent in turbulent model than the laminar model because these bubbles coalesce as they move upward thereby producing bigger bubbles.

Comparisons of laminar and turbulent model predictions are also carried out in **Fig. - 5.45** with respect to radial profiles of solid volume fractions, axial particle velocity, granular temperature and axial profiles of solid volume fractions. All the radial profiles of hydrodynamics are shown only for one half of the fluidized bed i.e. from centre to wall of the column for a bed height 0.05 m. From the time-averaged profiles of solid volume fractions, it is seen that solid volume fraction increases along the radial direction i.e. increases from the central region to wall region (**Fig. - 5.45 (a)**). From **Fig. - 5.45 (b)** it is seen that particle velocity decreases along the radial direction from centre to wall. The reason may be due to fact that mainly the solid particles move upward with the gas bubbles in the central region of the bed. When bubbles break particles scattered and reach the wall region. As the solid particles reach the wall they start moving downward along the wall. Particle movements in turn collisions are represented by granular temperature profiles. With the laminar model flow gives a low granular temperature value is observed than the turbulent model (**Fig. - 5.45 (c)**). Greater value of granular temperature means the solid particles collide more and fluidize

vigorously. It is seen that with laminar model granular temperature very less in the central region whereas with turbulent model granular temperature is very high in central region. Therefore a high fluctuating velocity per unit of mass is observed with the turbulent model. The axial profile of solid volume fraction is shown in **Fig. - 5.45 (d)**. It is observed that solid volume fraction is significantly higher with the turbulent model than with the laminar model.

It is observed that the turbulent model predicts higher solid volume fraction because of vigorous movement of particles (**Fig. - 5.45 (a)**). It is observed from **Fig. - 5.45** that higher values of bed dynamics are obtained with turbulent model in each case. Thus proper fluidization is achieved with turbulent model. Therefore taking into account the time averaged turbulent behaviour and the turbulent interaction between phases it can be concluded that turbulent model predictions are more realistic than laminar flow model.

Fig. – H.1 of Appendix-1 shows the contours of bed pressure drop for the laminar and turbulent models. From this figure it is observed that the bed pressure drop in a fluidized bed varies from higher value at the bottom of the bed to approximately zero value at the top of the bed in both the cases. This implies that the bed pressure drop is higher at the inlet which gradually decreases and becomes zero at the outlet. It is observed that the turbulent model has more bed pressure drop than the laminar model. This may be due to vigorous particle–particle interaction within the fluidized bed.

The vector plot of gas phase and solid phase velocities are predicted by the CFD simulations with different models (**Fig. – H.2** of Appendix -1). From the velocity vector plot of gas phase (**Fig. – H.2 (a)**) it is observed that air flow is always in the upward direction throughout the column. In the lower section of the column solid particles obstruct the movement of bubbles for which velocity of air is less within the main bed region compared to that in remaining part of the column. In the upper section of the column air velocity is high thus it carries air bubbles along with it. From these figures it is also observed that the gas / air

velocity is more fluctuating in case of turbulent model. The reason may be more / stronger resistance exerted by solid particles within the bed.

The core - annulus structure of the bed shows that the solid velocities in the core region are much higher than those in the annulus region for both the laminar and turbulent models (**Fig. – H.2 (b)**). In the upper part of bed circulatory motion (i.e. downward motion of the solid particles near the wall region and upward motion in central zone of the cylindrical column) is observed with turbulent model. With the turbulent model, higher velocity of solid is seen than the laminar model. This may be due to the higher back mixing and rapid internal circulation in gas-solid flows within the fluidized bed.

(v) Grid Independency

Grid independence tests have been performed with different grids to investigate the influence of grid refinement on the solution with 2D and 3D simulations (**Fig. – H.3** of Appendix -1).

Fig. – H.3 (a) shows a comparison of contour plot for solid volume fraction obtained with different mesh sizes. It is observed that all the mesh / grid sizes have similar distribution of solid volume fractions and no significant change in results is observed with different grid sizes. Similarly the time-averaged solid volume fraction profile shows the constant distribution of solids. It is observed from **Fig. – H.3 (b)** that solid volume fractions for all grids reduces to zero after 20 cm of bed height. Particle axial velocities obtained for different mesh sizes are compared in **Fig. – H.3 (c)**. The particle axial velocity decreases from central region towards the wall region. It is observed that there is no significant change in results for all the grids with both 2D and 3D simulations. The solid volume fraction increase from the central part of bed toward the wall of column. All grid sizes are observed to have similar distribution of solid volume fractions in radial direction of fluidized bed in both the cases i.e. 2D and 3D simulations (**Fig. – H.3 (d)**). Thus it can be said that reasonable mesh independence is achieved for both 2D and 3D simulations.

5.5. EFFECT OF DIFFERENT CFD PARAMETERS ON BED DYNAMICS WITH BINARY MIXTURE OF BED MATERIALS

The effect of CFD parameters i.e. drag models, restitution coefficient and specularity coefficient on bed dynamics such as bed pressure drop and expansion ratio are studied in this section. The bed dynamics are also measured experimentally by varying different system parameters viz. superficial air velocity, particle size and static bed height. Comparisons of the model predictions and experimental measurements on the time-averaged bed pressure drop, bed expansion and qualitative gas-solid flow pattern are carried out using binary mixtures of particles.

5.5.1 Effects of Inlet Air Velocity

Studying the effect of superficial air velocity on different drag models, restitution coefficient and specularity coefficient is essential to know the effects of these CFD parameters on bed dynamics. In the present work air velocity is varied from 0.014 m/s to 0.020 m/s. Binary mixtures of Red Mud and Aluminium particles are considered as bed materials. Simulation is carried out with different air velocity for different drag models, restitution coefficient and specularity coefficients. Predicted results are compared with each other and also with experimental results.

(i) Effect of Drag Models

(a) For bed expansion

Fig. – I.1 of Appendix -1 shows the comparisons for contours of solid volume fraction against gas velocity at different simulation times for different drag models. The bed begins to expand with gas flowing into the bed because of rising bubbles. After a time period of 30 sec, a dynamical equilibrium state / quasi steady state is achieved and the bed is said to be in fully fluidized state which may be due to rapid movement and interactions of bubbles within the bed. All experimental observations show a similar trend where bubbles start to form and

grow as they rise up with increased time as well as increased air velocity. The results show an increase in bed expansion with increasing inlet gas velocity. At a higher gas velocity bubbles grow larger as a result the bed expands significantly. It is also observed that bubbles grow in size with time at any particular velocity for a particular drag model. As a result the volume fraction of solid material at any section of the bed decreases with increase in time indicating the bed expansion. From this it is observed that the Gidaspow drag model predicts stable fluidization at any time of simulation.

The time-averaged solid volume fraction profiles for gas–solid fluidized bed for different drag models are shown in **Fig. – I.2** of Appendix -1 at different velocities. It is found that the bed height increases and the distribution of solid volume fraction decreases in the bed with increase in velocity of air. Reason may be same as already explained for single sized particle system. Thus maximum solid volume fraction is found at the bottom of the column. This solid volume fraction decreases sharply to a value nearly equal to zero. This corresponds to the region above which particles are not seen in the column. Expanded bed heights measured at different velocities along with percentage increase in bed heights for different drag models are listed in **Table – 12** of Appendix -2.

From **Fig. – I.1, I.2** and **Table – 12** it is observed that the Gidaspow drag model shows more bed expansion than the other two (i.e. Syamlal - O'Brien and Wen & Yu) models. Bed expansion ratio obtained from CFD simulation for different drag models are compared against the experimentally observed values (**Fig. – 5.46)**. It is observed that the bed expansion ratio increases with inlet gas velocity for all the models. It is also found that simulated results are in good agreement with experimental results. The deviations of CFD simulated results from the experimental results are shown in **Table – 5.18**. Least deviation with Gidaspow drag model finds it to be a better model among three selected models with respect to hydrodynamic studies of fluidized bed.

(b) For bed pressure drop

The static pressure in the fluidized bed is observed to vary from a maximum value at the bottom of bed to approximately zero value at the top of bed (**Fig. – I.3** of Appendix -1). It is also found that higher velocity yields higher static pressure for all types of drag models. **Table – 13** of Appendix -2 lists the maximum static pressure observed for different drag models against inlet air velocity. It is observed from this table that the static pressure increases with the increase in inlet air velocity for all the drag models. Among the three drag models, the Gidaspow drag model is seen to predict lower static pressure and higher static pressure bed heights indicating higher region of fluidization for bed materials.

The simulated time-averaged pressure drop is compared with the experimentally observed pressure drop for different drags models (**Fig. – 5.47**). It is observed that in both cases (i.e. in CFD simulation and experimentation) the pressure drop varies linearly with the inlet gas velocity initially which indicates the fixed bed region. With further increase in gas velocity the bed pressure drop remains constant implying the fluidization to be proper. From this figure, it is also observed that Gidaspow drag model shows good agreement qualitatively with the experimental results. It is also compared quantitatively with percentage of deviation for pressure drop (**Table – 5.19**). It is found that the simulated results are in good agreement with experimental results for different drag models. Gidaspow drag model is observed to give least deviation on an average and shows more consistency during CFD simulation (**Table – 5.19**).

(ii) Effect of Restitution Coefficients

(a) For bed expansion

The expanded bed height is calculated from the time-averaged solid volume fraction profiles and plotted against restitution coefficient (**Fig. – I.4** of Appendix -1). The expanded bed height is found to increase with increasing superficial gas velocity at any particular restitution coefficient. But at any particular velocity the bed expansion is found to be almost constant

with increase in restitution coefficients. The bed expansion ratios obtained from CFD simulations and experimentations are compared with each other **Fig. – I.5** of Appendix -1 with different restitution coefficients. Comparisons show very good agreement for different air velocities. It is further seen from both the figures that the restitution coefficient does not strongly influence the bed dynamics of fluidization process with binary mixtures of particles.

(b) For bed pressure drop

The comparison of bed pressure drop against restitution coefficient for different superficial gas velocities are shown in **Fig. – 5.48.** It is seen that higher superficial velocities have higher bed pressure drops than the lower velocity at any restitution coefficient. It is also seen that bed pressure drop increases upto certain value and then decreases with increase in restitution coefficient for all the velocities. Thus restitution coefficient affects the quality of fluidization with respect to the pressure drop. It is seen that at restitution coefficient of 0.9, bed pressure is maximum than the other values of restitution coefficient for all the velocities. The simulations show more pressure fluctuations implying more vigorous bubbling with increase in restitution coefficients. Thus it can be said that more pressure fluctuation is observed when more energy is dissipated.

(iii) Effect of Specularity Coefficients

(a) For bed expansion

The expanded bed height for different values of specularity coefficients are calculated from solid volume fraction profiles with different superficial gas velocities. It is found that the distribution of solid volume fraction decreases in the bed with increase in velocity of air. This may be due to the movement of more solid particles with increased gas velocity. The expanded bed heights and increase in bed expansion for different specularity coefficients are tabulated in **Table – 5.20**. From this table it is observed that the no slip condition of

specularity coefficients shows more bed expansion than the other values of specularity coefficients.

Bed expansion ratio obtained from CFD simulation for different values of specularity coefficients are compared against the experimentally observed values (**Fig. – 5.49**). It is observed that the bed expansion ratio increases with inlet gas velocity for all cases. It is also found that simulated results are almost in good agreement with experimental results. The deviations of CFD simulated results from the experimental results are calculated and listed in **Table – 5.21**. Least deviation with no slip condition of specularity indicates it to be the better condition of specularity than the others.

(b) For bed pressure drop

The simulated time-averaged pressure drop is compared with the experimental results for different specularity coefficients as shown in **Fig. – 5.50**. It is observed that in both the cases (i.e. in CFD simulation and experimentation) the pressure drop varies linearly with the inlet gas velocity. Only for no-slip condition bed pressure drop seems to be constant after certain point whereas with other values of specularity coefficients i.e. partial slip and free slip conditions bed pressure drop is in increasing trend. No-slip condition is found to agree to some extent with the experimental results. It is also calculated quantitatively in terms of percentage of deviation for pressure drop (**Table – 5.22**). From this it is concluded that the zero value of specularity coefficients gives better prediction with respect to bed pressure drop for fluidized bed with least deviation among all cases of specularity coefficients.

5.5.1.1 Comparison of Hydrodynamics between 2D and 3D Simulations

Fig. – I.6 of Appendix -1 shows the comparisons among 2D and 3D simulations for bed dynamics of fluidized bed. Granular temperature distribution of the solid phase is shown in **Fig. – I.6 (a)** where granular temperature is seen to increase with the increase in the particle velocity in turn with air velocity. The low granular temperature is observed at lower

velocities and high granular temperature is observed at higher velocities. **Fig. – I.6 (b)** shows the volume fractions of solid particles at different superficial air velocities for 2D and 3D simulation. It is observed that the volume fraction of solid particles decreases with increase in superficial air velocities as more particles move up.

The comparisons for variations in bed expansion ratios with 2D and 3D simulations are plotted against superficial air velocities (**Fig. – I.6 (c)**). The bed expansion ratio is found to increase linearly with inlet gas velocity for both the cases. That means the bed expands with increased velocity of air. **Fig. – I.6 (d)** shows the variations of the bed pressure drop against superficial air velocities for 2D and 3D simulations. It is observed that as superficial air velocity increases, the bed pressure drop increases initially and then becomes almost constant in both the cases of simulations. Initial part of this profile represents fixed bed region and constant pressure drop implies the proper fluidization zone. From all these figures, it is observed that 3D simulations yield higher predictions than 2D simulated predictions. Reason may be that the fluidizer is three dimensional in reality. Assumption of 2D for simulation might have resulted in the difference.

5.5.2 Effects on Particle Size

The effects of particle size of binary mixtures on different drag models, restitution coefficients and specularity coefficients are investigated in this section. In the present work particle size of Aluminium is varied from 58 to 98 microns while Red Mud size is kept constant at 77 microns. Average particle size is considered for the simulations. The simulation results obtained with different particle sizes of binary mixture for different bed dynamics are compared with each other and also with the experimental results.

(i) Effect of Drag Models

(a) For bed expansion

The expanded bed heights and percentage increase in bed heights at different sizes of binary mixtures for different drag models are listed in **Table – 14** of Appendix -2. From this table, it is observed that the Gidaspow drag model yields more bed expansion than the other two models.

Bed expansion ratio obtained from CFD simulation for different drag models are compared against the experimentally observed values in **Fig. – 5.51**. It is observed that the bed expansion ratio decreases with increase in average particle size for both Gidaspow and Wen & Yu drag models. But Syamlal - O'Brien drag models show constant ratio of bed expansion. It is also found that Gidaspow simulated results are in good agreement with experimental results. The deviations of simulated results from the experimental results are listed in **Table – 5.23**. Least deviation with Gidaspow drag model finds it to be the better model among three selected models with respect to the effect of particle size on bed expansion. Comparisons among contours of bed pressure drop and static pressures predicted with different particle sizes of binary mixtures are carried out for different drag models in **Fig. – I.7** of Appendix -1. It is found that higher average particle size gives lower static pressure for all the drag models. Among the three drag models, the Gidaspow drag model is observed to show lower static pressure and higher static pressure bed heights.

(b) For bed pressure drop

The simulated time-averaged pressure drop is also compared with the experimental results for different drags models (**Fig. – 5.52**). It is observed from this figure that the pressure drop decreases with increase in average particle size of Red Mud and Aluminium mixtures. That means the pressure drop decreases with the increase in size of Aluminium particles for all the drag models. From this figure, it is also observed that Gidaspow drag model shows good

agreements with the experimental results. From **Table – 5.24** it is again observed that Gidaspow drag model gives least deviation thereby implying that Gidaspow drag models is the better option for modelling the fluidized bed reactor.

(ii) Effect of Restitution Coefficient

(a) For bed expansion

The expanded bed heights calculated from the time-averaged solid volume fraction profiles against different restitution coefficients for different particle sizes of binary mixtures are shown in **Fig. – 5.53**. It is observed that expanded bed height is more for smaller particle sizes. That means it can be said that the bed expands more with decreasing size of Aluminium particles. The height of expanded bed is found to be almost constant with different restitution coefficients. Thus it can be said that the restitution coefficient does not influence the bed expansion. The bed expansion ratios obtained from CFD simulations with different restitution coefficients are compared with the experimental results (**Fig. – 5.54**). It is observed that the bed expansion ratio decreases with increase in size of Aluminium particles. The comparison with experimental findings further validates the CFD modelling thereby implying that restitution coefficient does not affect the bed dynamics with respect to expansion of fluidized bed.

(b) For bed pressure drop

The comparisons of bed pressure drop against restitution coefficient for different particle sizes are shown in **Fig. – 5.55.** It is seen that binary mixture having larger average particle i.e. binary mixture with larger sized Aluminium particles shows lower bed pressure drops at any value of restitution coefficient. It is also seen that at the restitution coefficient of 0.9 maximum bed pressure drops is observed for all the particle sizes indicating occurrence of vigorous bubbling at this value of restitution coefficient.

(iii) Effect of Specularity Coefficients

(a) For bed expansion

Bed expansion ratios against the average particle sizes obtained from CFD simulations for different values of specularity coefficients are compared with the experimentally observed values (**Fig. – 5.56)**. It is observed that the bed expansion ratio decreases with increase in average particle size for all the binary mixtures. It is also found that with no slip condition (i.e. Ø=0), the simulated results are in good agreement with experimental results. The deviations of CFD simulated results from the experimental results are calculated (**Table – 5.25**). Least deviation with no slip condition (i.e. Ø=0) indicates it as the better condition of specularity than the others.

(b) For bed pressure drop

The simulated time-averaged pressure drop is compared with the experimental results for different specularity coefficients in **Fig. – 5.57** against different particle size of binary mixture. It is observed that in both the cases (i.e. in CFD simulation and experimentation) the pressure drop varies decreases with the particle size of binary mixture and also shows good agreements qualitatively as well as quantitatively with the experimental results. From this it is conclude that the zero value of specularity coefficients gives better prediction with respect to bed pressure drop with least deviation among all values of specularity coefficients (**Table – 5.26**). This may be due to no shear force between particles and wall of the column.

5.5.2.1 Comparison between 2D and 3D Simulations

The comparison of 2D and 3D simulations for bed dynamics with respect to granular temperature, solid volume fraction, bed expansion and bed pressure drops are carried out for different particle sizes of binary mixtures. Distribution of the solid phase granular temperature is shown in **Fig. – I.8 (a)** of Appendix -1. The granular temperature is observed to increase with the increase in the particle size of the mixture. It is evident that granular

temperature is higher in the upper section of the fluidized bed because the volume fraction of the solid particles is less where the collisions of the solid particles lead to increased granular temperature. The simulated time-averaged volume fraction of solid particles for 2D and 3D simulation of fluidized bed for different particle sizes are shown in **Fig. – I.8 (b)** of Appendix -1. It is observed that the volume fraction of solid particles increases with increase in average particle size. **Fig. – I.8 (c)** of Appendix -1 shows the comparison of 2D and 3D simulations for bed expansion ratios against the average particle sizes. The bed expansion ratio is found to decrease with increase in average particle size of Red Mud-Aluminium binary mixture. This is may be due to frequent breakage of bubbles with larger sized irregular Aluminium particles which act as lubricants for fluidization of Red Mud. **Fig. – I.8 (d)** of Appendix -1 shows the variations of the bed pressure drops for 2D and 3D simulations against average particle sizes. It is observed that as particle size increases, the bed pressure drop decreases significantly. The higher particle size gives the lower pressure drop because of frequent breakage of bubbles leading to proper fluidization. From the above figures (**Fig. – I.8**), it is observed that 3D simulation of bed dynamics exhibit better results than the 2D simulations.

5.5.3 Effects of Particle Density

Red Mud and Aluminium particles are mixed in different proportions to be fluidized as binary mixtures. The density of bed materials varies with the proportion in which individual components are added. Thus the effect of density on bed dynamics is investigated. Effect of CFD parameters such as drag models, restitution coefficient and specularity coefficient on bed dynamics are analysed for different densities of bed materials. In the present work Red Mud–Aluminium mixture is prepared by adding the individual materials in different weight ratios i.e. 95:05, 90:10, 85:15 and 80:20. CFD simulation results of bed dynamics obtained for different weight ratios are analysed with respect to different system parameters.

(i) Effect of Drag Models

(a) For bed expansion

The expanded bed heights and percentage increase in bed heights with the different weight ratios of binary mixtures are listed in **Table – 15** of Appendix -2 for different drag models. From this table it is observed that Gidaspow drag model exhibits more bed expansion than the other two (i.e. Syamlal - O'Brien and Wen & Yu) models. Again it is seen that with increase in weight percentage of Aluminium particles both the static bed height and bed expansion increase for all the models. This may be due to the increase in bed voidage with decreased percentage of Red Mud or increased percentage of Aluminium particles. From this it can be said that the Gidaspow drag model predicts stable and proper fluidization at any time of simulation.

Bed expansion ratios obtained from CFD simulations with different drag models are compared against the experimentally observed values (**Fig. – 5.58)**. It is observed that the bed expansion ratio increases with the increased weight proportion of Aluminium particles for all the drag models. Gidaspow drag model is observed to show uniform increase in bed expansion with minimum deviation from experimental values. Thus it can be said that results of Gidaspow model are in good agreement with experimental results. The deviations of CFD simulated results from the experimental results are listed in **Table – 5.27**. Least deviation with Gidaspow drag model finds it to be a better model among three selected models with respect to hydrodynamic studies of fluidized bed.

(b) For bed pressure drop

The simulated time-averaged pressure drops are compared with the experimental results for different drags models (**Fig. – 5.59**). It is observed that in both CFD simulation and experimentation cases, the pressure drop varies linearly with the increased proportions of Aluminium in bed materials. Total bed weight is constant. Therefore increased bed pressure

drop may be for surface irregularities or roughness of Aluminium particles for all the drag models. From this figure, it is also observed that Gidaspow drag model shows minimum deviation implying good agreements with the experimental results in comparison with other models (**Table – 5.28)**.

(ii) Effect of Restitution Coefficient

(a)For bed expansion

The expanded bed heights is calculated from the time-averaged solid volume fraction profiles for different restitution coefficients with different weight proportions of bed materials (RM:Al). The bed expands with increasing weight proportion of Aluminium or decreasing weight of Red Mud (**Fig. – 5.60**). This may be due to increased bed voidage with more amounts of lighter materials. For any particular weight proportion of binary mixture the bed expansion is found to be almost constant with different restitution coefficients. The bed expansion ratios obtained from CFD simulations and experiments are compared with each other for different restitution coefficients (**Fig. – 5.61**). The bed expansion ratio is found to increase with the weight proportion of Aluminium particles but no effect of restitution coefficient is observed.

(b) For bed pressure drop

The comparisons of bed pressure drop against restitution coefficient for different weight proportions of bed materials are shown in **Fig. – 5.62.** It is seen that higher weight proportions of Aluminium particles have highest bed pressure drops at any restitution coefficient. It is also seen that bed pressure drop increases with restitution coefficient for all the velocities. The 0.9 value of restitution coefficient shows more bed pressure than the other values of restitution coefficient for all the velocities. After that pressure drop is observed to decrease and then remains constant. This implies that restitution coefficient of 0.9 and 0.95

corresponds to minimum fluidization and complete fluidization zones respectively. This implies that more pressure fluctuation is observed when more energy is dissipated.

(iii) Effect of Specularity Coefficients

(a) For bed expansion

The comparisons of simulated expanded bed heights and percentage increase in bed heights with different weight proportion of binary mixtures of Red Mud and Aluminium particles are made in **Table – 16** of Appendix -2 for different specularity coefficients. It is found that the distribution of solid volume fraction in the bed increases with increase in weights of Aluminium particles for all the specularity coefficients. The solid particles move to higher heights with decreased amount of Red Mud particles. From **Table – 16** it is observed that no slip condition of specularity coefficients shows more bed expansion than the other values of specularity coefficients. Again it is seen that increased amount of Aluminium particles in the bed mixtures increases the percentage of bed expansion for any specularity coefficients. Thus it can be said that addition of irregular metal particles improves the quality of fluidization for fine Red Mud particles.

Bed expansion ratio obtained from CFD simulation for different values of specularity coefficients are compared against the experimentally observed bed expansion values (**Fig. – 5.63)**. It is observed that the bed expansion ratio is more in no slip condition than other conditions although decrease in bed expansion is observed for all the specularity coefficients. It is also found that simulated results under no slip condition are in good agreement with experimental results. The percentage deviations of CFD simulated results from the experimental results are listed in **Table – 5.29**. Least deviation with no slip condition of specularity indicates it to be the better condition than other conditions (viz. partial or free slip conditions).

(b) For bed pressure drop

The simulated time-averaged pressure drop is compared with the experimental results for different specularity coefficients in **Fig. – 5.64** against different weight proportions of binary mixtures. It is observed that in both the cases the pressure drop varies linearly with the weight proportion of binary mixture. Bed pressure drop is also observed to increase with the increase in specularity coefficients. Increase in bed pressure drop under a particular condition implies that increase in weight proportion of Aluminium particles might have increased shear force in wall region. Comparison with the experimental results shows good agreements in all cases. From this it is further seen that zero value of specularity coefficient gives better prediction with respect to bed pressure drop with minimum deviation among all values of specularity coefficients (**Table – 5.30**). This may be due to no shear force between particles and wall of the column.

5.5.3.1 Comparison of Hydrodynamic studies with 2D and 3D Simulations

The hydrodynamic studies of fluidized bed with binary mixture of bed materials are simulated by both 2D and 3D simulations. A comparison among 2D and 3D simulated outputs are carried out in this section. Particle granular temperature predicted with different weight proportions of bed materials by 2D and 3D simulations are shown in **Fig. – I.9 (a)** of Appendix -1. It is found that the bed materials having high proportions of Red Mud show higher granular temperature. Granular temperature is found to decrease with decrease in Red Mud proportions in the binary mixtures. This may be due to more particle interactions because of higher proportion of Red Mud. As Red Mud proportion decreases in bed materials the collision among particle decreases. Addition of Aluminium particles increases the fluidity; as a result particle collision decreases. Therefore the granular temperature decreases. Time-averaged volume fraction of solid particles with different weight proportions are compared for 2D and 3D simulations in **Fig. – I.9 (b)** of Appendix -1. It is observed that the

volume fraction of solid particles decreases with increase in weight proportion of Aluminium particles in the bed materials. Reason is same as before i.e. increased fluidity with increase in Aluminium proportions. That means more particles are present for lower proportion of Aluminium particles in binary mixture at any region of the reactor.

Fig. – I.9 (c) of Appendix -1 shows the comparison of expanded bed heights for 2D and 3D simulations against different weight proportion of binary mixture. The bed height is observed to increase linearly with the increase in weight proportion of Aluminium particles as the fluidity of bed material increases. The comparison of bed expansion ratios for 2D and 3D simulations against different weight proportions of the binary mixture bed materials is shown in **Fig. – I.9 (d)** of Appendix -1. The bed expansion ratio is also found to increase linearly with the increase in Aluminium proportions in the bed materials. This may be due to frequent formation / breakage of bubbles because of more fluidity of bed materials. **Fig. – I.9 (e)** of Appendix -1 compares the bed pressure drop for 2D and 3D simulations against different weight proportions. It is observed that with increase in weight of Aluminium particles, the bed pressure drop increases. Higher weight proportion of Aluminium particles in binary mixture gives the higher pressure drop than the lower weight proportion because of more rough Aluminium particles. When more rough particles / irregular particles are present, they remain in the wall region during the fluidization for which pressure drop might be more. It is further seen that 3D simulations of fluidized bed show the higher and better results than the 2D simulation in all cases.

5.6 THERMAL ANALYSIS FOR BINARY MIXTURE BED MATERIALS INSIDE FLUIDIZED BED REACTOR

The temperature effect is also important for the fluidized bed reactor. This section aims to study the effect of temperature on the bed dynamics with the variations in different system parameters such as inlet air velocity, particle size and density. Three inter-phase thermal processes are considered within the gas–solid fluidized bed. These are wall-bed, gas– particle

and particle–particle heat transfer [Mihálykó et al. (2004)]. The velocity, volume fraction and temperature distribution for gas phase and solid phase are predicted in this section.

5.6.1 Effect of Inlet Air Velocity

Input gas velocity has an effective role on the thermal analysis of fluidized bed. In the present case input gas velocity is changed from 0.014 to 0.020 m/s for binary mixture of fine particles with average particle size of 77.6 microns. The variations in solid phase temperatures against bed heights of different gas velocities are shown in **Fig. – 5.65**. It is found that an increase in gas velocity causes a higher heat transfer between gas and solid phases that in turn leads to an increase in solid particle temperature. In addition, it is seen that temperature profile has a peak of 523K at around bed height of 25 cm which implies that volume fraction of particles in this area is higher which results in higher surface contact between gas and solid phases. The temperature gradient between solid and gas phases is higher in the bottom region of the bed which leads to a larger heat transfer rate compared to the top region of the bed. The rate of change of the solid temperature near the bottom of the bed is faster, which may be due to a larger heat transfer rate compared to the top region of the bed. It also indicates that an increase in the gas velocity causes a higher heat transfer between gas and solid phases which results in an increase in the solid particle temperature.

The gas enters the bed at a temperature of 523K. The solid particles are initially at room temperature i.e. at 300K. Thermocouples are fitted along the column as shown in **Fig. – 3.3**. The thermocouple probe is also used for measuring the temperature across the reactor. The gas phase temperatures along the bed are noted and plotted against the bed height for different air velocities (**Fig. – 5.66**). Gas temperature is found to be maximum at the bottom of the bed which then decreases. It is seen that the gas temperature gradually deceases with bed height because of the heat transfer between the comparatively colder solid particles and hot gas. Near the bottom of column, solid volume fraction is relatively high. Therefore gas

temperature decreases rapidly and the rate of decrease is higher. At top of the column, there are almost no particles (i.e. gas volume fraction is approximately one), for which the gas temperature is roughly constant. The same thing is observed for all the velocities. But rate of heat transfer is found to increase with increasing velocity. As a result higher velocity causes the more reduction in gas temperature for higher velocity than the lower velocity of gas.

Gas and solid phase temperature distributions in the reactor have been computed for a initial bed height of 14 cm. **Fig. – 5.67** illustrate the comparison of temperature distribution and volume fraction of solid phase with the inlet gas velocity of 0.016 m/s. From this figure it is observed that the solid volume fraction distributions fluctuate more in the axial direction. Gradually solid volume fraction is maximum in the bottom region which decreases and then reduces to zero at the top of the column. In the bottom region of the column, concentration of solid particles is larger than that in the upper part. Thus the expanded bed i.e. 28 cm represents a clear interface between the solid phase and the gas phase within the reactor. The solid phase temperature increases from room temperature at the bottom to maximum of 523K at top of expanded bed height in the reactor. This may be due to good contact of gas–solid particles within the reactor. In the top region of the reactor, solid phase temperature decreases again due to absence of solid particles. From this figure it is seen that in the region where the solid volume fraction is lowest the gas temperature is highest. It is also seen clearly that in the region with negligible solids and free gas flow, there is little heat transfer in the top region. In the lower part of the reactor, the solid volume fraction is higher for which the rate of heat transfer with the cooler particles is higher and the temperature of solid phase increases faster.

From **Fig. – 5.68,** distribution of the gas temperature and the gas velocity are observed against bed height of the reactor. The results show that gas temperature decreases as it moves upward in the reactor due to the heat transfer being reduced to solid particles and implies maximum temperatures at bottom of the bed. In addition, the gas temperature attains

uniform (constant temperature) condition in the upper region. This is because of absence of solid particles in the top region of the reactor. Therefore the rate of increase of gas temperature is reduced. The simulated results show that the velocity of gas increases from inlet to top of the reactor. This happens due to severe back mixing within the bed and absence of solid particles in the top region of the reactor.

The contours of air temperature against the simulation time are shown in **Fig. – J. 1** of Appendix -1. It is observed that the particle temperature is almost constant at bottom of the reactor throughout the simulation for all the simulation time. After 15 sec of simulation time, the temperature of gas phase is observed to decrease. This may be due to the interaction between gas and solid particles during the fluidization process. As a result heat is transferred from gas to solid inside the fluidized bed reactor. Once all the particles fluidize vigorously and attain maximum temperature, gas temperature remains constant at the minimum level.

5.6.2 Effects of Particle Size

As particle size affects the quality of fluidization its effect is considered for thermal analysis of the fluidized bed reactor. The effect of particle size is studied for the distribution of solid phase temperature against the bed height of the reactor in **Fig. – J.2** of Appendix -1. From this figure it is seen that the solid phase temperature increases first attains maximum value at around 523K and then decreases gradually upto certain point and then remains constant at a temperature in the top region of the reactor. It is also seen that same trend is observed for all the particle sizes. Again comparing among different particle sizes it is seen that larger size particles show lower temperature than the smaller size particles. Temperature of bed materials decreases with increase in particle size. Reason for this may be the availability of more surface area with smaller sized particles than the larger ones. As contact area increases with smaller particles heat transfer in turn temperature increases [Cai and Cen (1985) and Collier (2004)]. This fact implies that decreasing in the particle sizes benefits the gas–particle

heat transfer. In addition the temperature gradient between the solid phase and the gas phase is greater in the top region of the bed which leads to a larger heat-transfer rate compared to that in the bottom region of the bed. The reason may be that during fluidization most of the solid particles attain maximum temperature in the top region of the bed.

The influence of the size of the solid particles on the gas phase temperature is shown in **Fig. – J.3** of Appendix -1. This figure indicates that with the decrease in particle size gas phase temperature decreases. Reason may be the higher heat-transfer between the gas phase and the solid phase for smaller size particles. Thus more heat transfer leads to a lower gas temperature. Again it is observed that temperature profile trend is same for all the particle sizes. Gas phase temperature is initially constant at maximum level then it decreases as fluidization initiates and finally remains constant at minimum level when all the particles fluidize vigorously.

Fig. – J.4 of Appendix -1 illustrates the comparison of temperature and volume fraction of solid phase against bed height of the fluidized bed reactor. The simulated results show that solid volume fraction fluctuates initially at about 0.35 and decreases suddenly to about zero in the top region of the FBR. In the bottom region concentration of solid particles is more than that in the upper part of the reactor due to movement of particles during the fluidization process.

The solid phase temperature is observed to increase from bottom of the reactor with the height as contact between gas and solid particles increase with the intensity of fluidization process. This may be due to higher contact surface between the gas phase and the solid phase in the reactor. At the top of the reactor solid phase temperature attains a constant value and then decreases as concentration of solid decreases with height. The comparisons of temperature and velocity of gas phase are carried out for binary mixture inside the reactor (**Fig. – J.5** of Appendix -1). The temperature of gas is more when it enters FBR. The

simulated prediction shows that gas temperature decreases as it moves upward in the reactor due to the transfer of heat from gas to solid phase. It attains a minimum temperature in the top region of FBR and remains constant when the reaction starts taking place. The simulated results show that the velocity of gas increases from inlet to top of the reactor. Lower value of gas velocity in the bottom region of FBR is because of obstruction imposed by more solid particles to the gas flow. This may also be due to severe back mixing in the bottom region of the bed.

The contours of solid temperature against the simulation time are shown in **Fig. – J.6** of Appendix -1. It is observed that the solid temperature increases with the increase in simulation times. This may be due to the increased collisions among the solid particles with time. Thus good mixing and thereby good surface contact of gas–solid phases are achieved inside the fluidized bed reactor.

5.6.3 Effect of Particle Density

Two different materials are added in different weight proportions to make the binary mixture to be used as bed materials. The simulated temperature of solid phase and gas phase for different binary mixtures against the bed height are shown in **Fig. – J.7** and **Fig. – J.8** of Appendix -1 respectively. The solid phase temperature increases and reaches maximum temperature at the expanded bed height of the reactor. Again the temperature decreases and attains a constant temperature at the top of the reactor. It is also observed that the solid phase temperature increases with increase in weight of Aluminium particles. The reason may be that thermal conductivity of bed materials increases with increased Aluminium ratio in the binary mixture. This may be due to the higher thermal conductivity of metal Aluminium particles than Red Mud. That is why binary mixtures having higher percentage of Aluminium particles show more temperature than other mixtures within the FBR.

Similarly the gas temperature is maximum at the bottom of the reactor which then decreases with increase in height of reactor. The reason may be that the gas-solid contact increases during fluidization of bed materials for which heat is transferred from gas to solid. Again it is observed that gas phase temperature is more for less denser bed materials. Density of bed materials decreases with the increase in Aluminium content in the binary mixture. Because during fluidization process more solid particles are there in the bottom region of FBR to which more heat is transferred. Less dense materials (with higher percentage of Aluminium particles) get heated up faster rate than the dense bed materials for which gas phase with the less dense materials show higher temperature. In other words with denser bed materials (high percentage of Red Mud) low gas temperature is observed. Solid fraction decreases with increase in bed height as a result more gas-solid contact is achieved with height.

Fig. – J.9 of Appendix -1 shows the comparison of temperature and volume fraction distribution of solid phase for a particular bed density of 1290 kg/m^3 of binary mixture. The simulated results shows that solid volume fraction distributions fluctuate in the lower portion of bed at around 0.35 and suddenly decreases to zero at a height in the top region of FBR. This limiting height is called as the expanded bed height of the FBR which represents a clear interface between the fluidized regions and the free board regions. In the main fluidization zone (within which the particles fluctuate) the solid phase temperature is observed to increase from bottom of the reactor. This may be due to transfer of heat from gas to solid particles and heat of reaction being added up in the reactor. In the top region of the reactor solid phase temperature decreases and reaches a constant temperature as no more heat transfer takes place and very few particles are found beyond the maximum expanded bed height in FBR. The comparisons of temperature and velocity distributions of gas phase for a particular bed mixture (bed density of 1290 kg/m^3) are shown in **Fig. – J.10** of Appendix -1. The results

shows that gas temperature decreases as it moves upward in the reactor due to the transfer of heat from gas to solid particles. The simulated results show that the velocity of gas increases from bottom to top of the reactor. The decrease in temperature continues in the dense phase region where heat transfer continues to take place. As hardly few solid particles are found in free board region no heat transfer takes place because of which gas temperature remains constant. As inlet gas velocity is constant, gas flow to bed remains constant in the main bed region. But in free board region, velocity of gas increases because of two reasons.

Reason -1: No solid particle is found to obstruct the gas flow for which velocity increases.

Reason -2: Further breakage of bubbles or slugs at the bed surface level adds the extra amount of gas which forces to upward moving gas.

Solid phase contour plot for temperature and pressure are shown in **Fig. – J.11 (a)** of Appendix -1**.** Simulation is carried out for four different proportions of binary mixtures. It is observed that the temperature increases with the increased ratio of Aluminium (decreased density) in binary mixtures. This may be due to the good contact between gas–solid particles and higher thermal conductivity of Aluminium than Red Mud. **Fig. – J.11 (b)** of Appendix -1 shows the contours of pressure for the reactor with different density of binary mixtures. The axial bed pressure in a fluidized bed reactor varies from higher value at the bottom of the bed to minimum value at the top of the column. The pressure is observed to decrease with height and becomes same as atmospheric pressure at the outlet. It is also seen from **Fig. – J.11 (b)** of Appendix -1that the binary mixture having higher average density shows more pressure because of less void space among the solid particles.

5.6.4 Comparison of Bed Hydrodynamics with 2D and 3D Simulations

The temperature of solid phase increases with increase of both density and inlet air velocity for 2D and 3D simulation case (**Fig. – J.12** of Appendix -1). This may be due to the better reaction happens with weight ratio and inlet air velocity. The solid phase temperature

decreases with increase of particle size (**Fig. – J.12** of Appendix -1). This may be due to poor contact of particle and gas because of high size of particles in 2D and 3D simulation of fluidized bed. The 3D simulation result shows the better and higher results than the 2D simulation case. It is observed that 2D and 3D simulations yield same trend in all the cases of bed dynamics, only some magnitude difference is observed. In other words it can be said that 3D simulations yield higher value than 2D simulations for all aspects of bed dynamics.

Table – 5.1: CFD simulation parameters with base case settings

Description	Base case setting	Change compared to base case settings
(a) Model equations		
Kinetic viscosity	Syamlal–O'Brien (1989)	Fixed value
Granular bulk viscosity	Lun et al. (1984)	Fixed value
Frictional viscosity	Schaeffer (1987)	Fixed value
Angle of internal friction	30◦	Fixed value
Granular conductivity	Syamlal–O'Brien (1989)	Fixed value
Drag law	Gidaspow et al. (1992), Wen & Yu (1996)	Fixed value
Coefficient of restitution for particle – particle collisions	0.90	Fixed value
(b) Mesh size, time step, convergence criteria and discretization method		
Mesh resolution	0.002 × 0.002 m (2D) 0.007 × 0.007 m (3D)	Fixed value
Convergence criteria	10^{-3}	Relative / Fixed value
Maximum iterations	30	Fixed value
Discretization method	First order upwind	Fixed value
Time step	0.001 s	Fixed value
(c) Geometry, boundary, initial and operating conditions		
Bed width	12 cm	Fixed value
Bed length	70 cm	Fixed value
Initial bed height	10 cm	Fixed minimum value
Initial solids packing	0.80	Fixed value
Outlet boundary condition	Pressure outlet	Fully developed flow
Wall boundary condition	No slip condition [Hosseini et al. (2010)]	-
Gravitational acceleration	9.81 m/s^2	Fixed value
Operating pressure	1.013×10^5 Pa	Fixed value
Inlet boundary condition	Uniform velocity inlet	Fixed value

Table – 5.2: Comparisons of static bed height and expanded bed height

Superficial Air Velocity, m/s	Uo/U_{mf}	Static Bed Height, m	Expanded Bed Height, m	Increase in Bed Expansion, %
0.008	0.8	0.1	0.171	71
0.010	1	0.1	0.185	85
0.012	1.2	0.1	0.2	100
0.014	1.4	0.1	0.214	114
0.016	1.6	0.1	0.228	128
0.018	1.8	0.1	0.242	142

Table – 5.3: Comparison of static pressure bed height and expanded bed height for different particle sizes

Particle Size, Microns	Static pressure bed height, m	Deviation in Pressure drops, %	Expanded Bed Height, m	Deviation in Bed Expansion ratio, %
58	0.228	4.89	0.228	10.73
77	0.214	4.09	0.214	3.52
98	0.171	1.81	0.171	4.35
116	0.157	1.56	0.157	2.99

Table – 5.4: Comparison of static pressure bed height and expanded bed height for different static bed heights

Static Bed Height, m	Static Pressure Bed Heights, m	Deviation in Pressure drops, %	Expanded Bed Height, m	Deviation in Expansion ratio, %
0.08	0.186	7.29	0.186	6.82
0.10	0.214	3.49	0.214	9.76
0.12	0.257	5.14	0.257	7.14
0.14	0.285	8.86	0.285	5.07

Table - 5.5: Comparison of bed pressure drop for different density of particles

Superficial Air Velocity, m/s	Deviation in Bed Pressure Drop, %					
	Sand		Red Mud		Aluminium	
	2D Simulation	3D Simulation	2D Simulation	3D Simulation	2D Simulation	3D Simulation
0.012	4.22	4.82	4.09	6.61	1.08	5.9
0.014	5.15	5.99	3.94	5.34	0.92	5.44
0.016	5.65	6.20	3.67	5.03	1.61	6.01
0.018	5.6	6.41	4.50	5.56	2.83	7.08

Table – 5.6: Comparison of 2D and 3D Simulated Expanded Bed Heights for different Bed Materials

Inlet Air Velocity, m/s	Expanded Bed Heights, cm								
	Sand			Red Mud			Aluminium		
	2D	3D	Deviation, %	2D	3D	Deviation, %	2D	3D	Deviation, %
0.012	15.7	17.1	8.18	17.1	18.5	6.54	20	21.4	7.56
0.014	17.1	18.6	8.06	18.6	20	6.55	21.4	22.9	7.0
0.016	18.6	20	7.0	20	21.4	5.76	22.9	24.3	6.54
0.018	20	21.4	6.54	21.4	22.9	5.44	24.3	25.7	6.55

Table – 5.7: Deviation of Simulated bed expansion ratios from experimental results

Particle Size, microns	Deviation in Expansion Ratio, %		
	Gidaspow Model	Syamlal - O'Brien Model	Wen & Yu Model
58	15.02591	18.65285	22.27979
77	11.89675	15.82492	20.03367
98	13.14103	17.62821	22.4359
116	9.824561	15.08772	15.08772

Table – 5.8: Comparisons among expanded bed heights and percentage increase in expansion with different superficial air velocities for different drag models

Air Velocity, m/s	Static Bed Height, m	Expanded Bed Height, m			Increase in Bed Expansion, %		
		Gidaspow	Syamlal - O'Brien	Wen & Yu	Gidaspow	Syamlal - O'Brien	Wen & Yu
0.008	0.10	0.171	0.157	0.142	71	57	42
0.010	0.10	0.185	0.171	0.157	85	71	57
0.012	0.10	0.2	0.185	0.171	100	85	71
0.014	0.10	0.214	0.185	0.171	114	85	71
0.016	0.10	0.228	0.2	0.185	128	100	85
0.018	0.10	0.242	0.214	0.2	142	114	100

Table – 5.9: Comparisons of maximum static pressure and static pressure bed height for different drag models against initial static bed heights

Initial Static Bed Height, m	Maximum Static Pressure, Pa			Static Pressure Bed Height, m		
	Gidaspow Model	Syamlal - O'Brien Model	Wen & Yu Model	Gidaspow Model	Syamlal - O'Brien Model	Wen & Yu Model
0.08	731.347	734.053	736.149	0.185	0.17	0.157
0.10	899.276	898.76	901.799	0.214	0.2	0.185
0.12	1072.24	1101.38	1100.03	0.257	0.228	0.214
0.14	1260.42	1279.57	1274.01	0.285	0.271	0.257

Table – 5.10: Comparison of simulated bed pressure drop against experimentally observed values with different Bed Heights for different drag models

Static Bed Height, m	Bed Pressure Drops Deviation, %		
	Gidaspow Model	Syamlal - O'Brien Model	Wen & Yu Model
0.08	3.927	-1.4	-2.307
0.10	-4.101	-7.847	-4.721
0.12	- 2.307	-3.379	-3.407
0.14	- 9.607	-12.338	-12.611

Table – 5.11: Comparison of simulated bed pressure drop against experimentally observed values with different particle sizes for different drag models

Particle Size, Microns	**Deviation in Pressure Drop, %**		
	Gidaspow Model	Syamlal - O'Brien Model	Wen & Yu Model
58	- 2.275	- 3.732	- 2.612
77	- 4.101	- 7.847	- 4.721
98	3.058	- 1.531	4.092
116	3. 876	4.735	5.191

Table – 5.12: Comparison of simulated bed expansion ratios against experimentally observed values with different particle sizes for different specularity coefficients

Particle Size, Microns	**Deviation for Expansion Ratio, %**				
	Ø=0	Ø=0.25	Ø=0.5	Ø=0.75	Ø=1.0
58	15.025	15.025	22.279	18.652	18.652
77	11.896	15.824	19.753	19.753	19.753
98	13.141	13.141	13.141	13.141	13.141
116	9.824	9.824	9.824	9.824	9.824

Table – 5.13: Comparison of simulated bed expansion ratios against experimental values with inlet air velocity for different specularity coefficients

Inlet Air Velocity, m/s	**Deviation of Expansion Ratio from, %**				
	Ø=0	Ø=0.25	Ø=0.5	Ø=0.75	Ø=1.0
0.012	9.365	18.126	18.126	13.595	13.595
0.014	11.896	15.824	19.753	19.753	19.753
0.016	10.675	18.3	18.3	18.3	22.113
0.018	13.897	20.946	20.946	20.946	24.471

Table – 5.14: Deviation of bed expansion ratio from experimental values with different static bed heights for different specularity coefficients

Static Bed Height, cm	Deviation for Expansion Ratio, %				
	Ø=0	Ø=0.25	Ø=0.5	Ø=0.75	Ø=1.0
8	14.34	23.63	23.63	19.5	19.5
10	11.89	15.82	19.75	19.75	19.75
12	-2.66	7.33	7.33	3.33	3.33
14	-5.59	8.39	8.39	1.39	1.39

Table – 5.15: Comparison of bed pressure drops with different particle sizes for different specularity coefficients

Particle Size, Microns	Deviation of Pressure Drops, %				
	Ø=0	Ø=0.25	Ø=0.5	Ø=0.75	Ø=1.0
58	2.225	8.685	4.636	6.115	8.202
77	3.94	5.495	5.799	6.362	6.701
98	2.26	3.066	4.883	5.049	5.044
116	1.59	3.402	3.059	2.953	2.887

Table – 5.16: Comparison of simulated pressure drop against experimentally observed values with different velocities for different specularity coefficients

Inlet Air Velocity, m/s	Deviation in Pressure Drop, %				
	Ø=0	Ø=0.25	Ø=0.5	Ø=0.75	Ø=1.0
0.012	4.096	5.618	5.942	6.159	7.202
0.014	3.94	5.495	5.799	6.362	6.701
0.016	3.67	5.034	5.336	5.486	6.376
0.018	4.506	4.679	5.124	4.976	5.418

Table – 5.17: Comparison of simulated pressure drop against experimental values with static bed heights for different specularity coefficient

Static Bed Height, cm	Deviation in Pressure Drops, %				
	Ø=0	Ø=0.25	Ø=0.5	Ø=0.75	Ø=1.0
8	3.969	7.983	6.849	6.705	7.001
10	3.94	5.495	5.799	6.362	6.701
12	2.246	7.083	6.642	10.45	11.96
14	8.719	9.936	10.448	10.53	10.40

Table – 5.18: Comparison of simulated expansion ratios against experimental values with different air velocities for different drag models

Inlet Air Velocity, m/s	**Deviation for Expansion Ratios, %**		
	Gidaspow	Syamlal - O'Brien	Wen & Yu
0.014	-1.05	7.15	10.84
0.016	5.23	12.66	16
0.018	5.28	11.81	15.67
0.020	5.11	11.64	14.75

Table – 5.19: Comparison of simulated pressure drop against experimentally observed values with different velocities for different drag models

Inlet Air Velocity, m/s	**Deviation of Bed Pressure Drops, %**		
	Gidaspow	Syamlal - O'Brien	Wen & Yu
0.014	3.53	6.11	9.76
0.016	0.58	- 0.69	8.49
0.018	-1.27	- 1.74	7.32
0.020	-1.97	-2.43	6.03

Table – 5.20: Comparisons of expanded bed heights and increase in bed expansion with binary mixture at different velocities for different specularity coefficients

Inlet Air Velocity, m/s	**Expanded Bed Height, cm**					**Increase in Bed Expansion, %**				
	Ø=0	Ø=0.25	Ø=0.5	Ø=0.75	Ø=1.0	Ø=0	Ø=0.25	Ø=0.5	Ø=0.75	Ø=1.0
0.014	24.4	20	21.4	21.4	21.4	74.3	42.9	52.8	52.8	52.8
0.016	25.8	21.4	21.4	22.9	22.9	84.2	52.8	52.8	63.5	63.5
0.018	27.2	22.9	22.9	24.4	24.4	94.3	63.5	63.5	74.3	74.3
0.020	28.7	22.9	24.4	25.8	25.8	105	63.5	74.3	84.2	84.2

Table – 5.21: Comparison of simulated expansion ratios against experimental values with binary mixture at different velocities for different specularity coefficients

Inlet Air Velocity, m/s	Deviation for Expansion Ratio, %				
	Ø=0	Ø=0.25	Ø=0.5	Ø=0.75	Ø=1.0
0.014	-1.05	10.84	8.42	6.84	6.84
0.016	5.23	15.74	15.71	12.14	12.14
0.018	5.28	15.23	15.17	11.72	11.72
0.020	5.11	18.05	14.67	11.55	11.55

Table – 5.22: Comparison of simulated bed pressure drop against experimental values with binary mixture at different velocities for different specularity coefficients

Inlet Air Velocity, m/s	Deviation for Pressure Drop, %				
	Ø=0	Ø=0.25	Ø=0.5	Ø=0.75	Ø=1.0
0.014	3.53	5.93	7.15	7.39	7.37
0.016	0.58	4.54	6.19	6.19	6.51
0.018	-1.27	3.13	3.84	5.0	5.46
0.020	-1.97	2.09	2.55	3.6	3.94

Table – 5.23: Comparison of simulated expansion ratios against experimental values with different particle sizes of binary mixture for drag models

Average Particle Size, microns	Deviation for Expansion Ratios, %		
	Gidaspow Model	Syamlal - O'Brien Model	Wen & Yu Model
75.1	0.32	13.29	16.82
76.2	2.55	12.73	16.28
77.6	5.28	12.14	19.04
79.1	7.33	10.96	17.95

Table – 5.24: Comparison of simulated pressure drop against experimental values with different particle sizes of binary mixtures for different drag models

Average Particle Size, microns	Deviation of bed pressure drops, %		
	Gidaspow	Syamlal - O'Brien	Wen & Yu
75.1	3.0	8.68	10.8
76.2	0.92	6.87	8.36
77.6	0.58	5.59	7.22
79.1	1.89	4.39	6.65

Table – 5.25: Comparison of simulated expansion ratios against experimental values with different particle sizes of binary mixtures for different specularity coefficients

Average Particle Size, microns	Deviations of Expansion Ratios, %				
	Ø=0	Ø=0.25	Ø=0.5	Ø=0.75	Ø=1.0
75.1	0.32	3.29	6.58	13.4	13.35
76.2	2.55	5.96	12.8	14.2	16.29
77.6	5.24	12.1	15.7	15.7	19
79.1	7.34	12.4	18	18	18

Table – 5.26: Comparison of simulated bed pressure drops against experimental values with different particle sizes of binary mixtures for different specularity coefficients

Average Particle Size, microns	Deviations for Bed Pressure Drops, %				
	Ø=0	Ø=0.25	Ø=0.5	Ø=0.75	Ø=1.0
75.1	3.0	4.0	8.12	8.68	9.02
76.2	0.92	3.08	6.52	6.75	7.2
77.6	0.59	4.54	5.93	6.16	6.52
79.1	1.89	3.91	4.62	4.75	4.87

Table – 5.27: Comparison of expansion ratios with different particle densities of binary mixture for different drag models

Average Particle Density, kg/m^3	Deviation for Expansion Ratio, %		
	Gidaspow Model	Syamlal - O'Brien Model	Wen & Yu Model
1260	4.50	11.56	15.64
1270	5.23	10.57	12.14
1280	7.82	13.58	15.81
1290	8.38	14.46	13.95

Table – 5.28: Comparison of pressure drops with different particle densities of binary mixture for different drag models

Average Particle Density, kg/m^3	Deviation for Bed Pressure Drops, %		
	Gidaspow Model	Syamlal - O'Brien Model	Wen & Yu Model
1260	3.83	4.55	4.55
1270	0.58	1.51	5.82
1280	1.80	2.25	7.10
1290	1.41	3.58	5.76

Table – 5.29: Comparison of expansion ratios with different particle densities of binary mixture for different specularity coefficients

Average Particle Density, kg/m^3	Deviation for Expansion Ratio, %				
	Ø=0	Ø=0.25	Ø=0.5	Ø=0.75	Ø=1.0
1260	4.50	8.28	6.77	11.56	10.88
1270	5.23	8.57	8.57	12.14	11.33
1280	7.82	11.53	10.25	14.01	14.01
1290	8.38	12.6	11.53	14.46	14.46

Table – 5.30: Comparison of bed pressure drop with different particle densities of binary mixture for different specularity coefficients

Average Particle Density, kg/m^3	Deviation in Pressure Drops, %				
	Ø=0	Ø=0.25	Ø=0.5	Ø=0.75	Ø=1.0
1260	2.63	4.79	7.42	3.83	4.43
1270	0.58	3.37	6.75	3.02	5.35
1280	1.80	2.59	7.89	2.70	2.93
1290	1.41	3.04	2.82	2.93	4.13

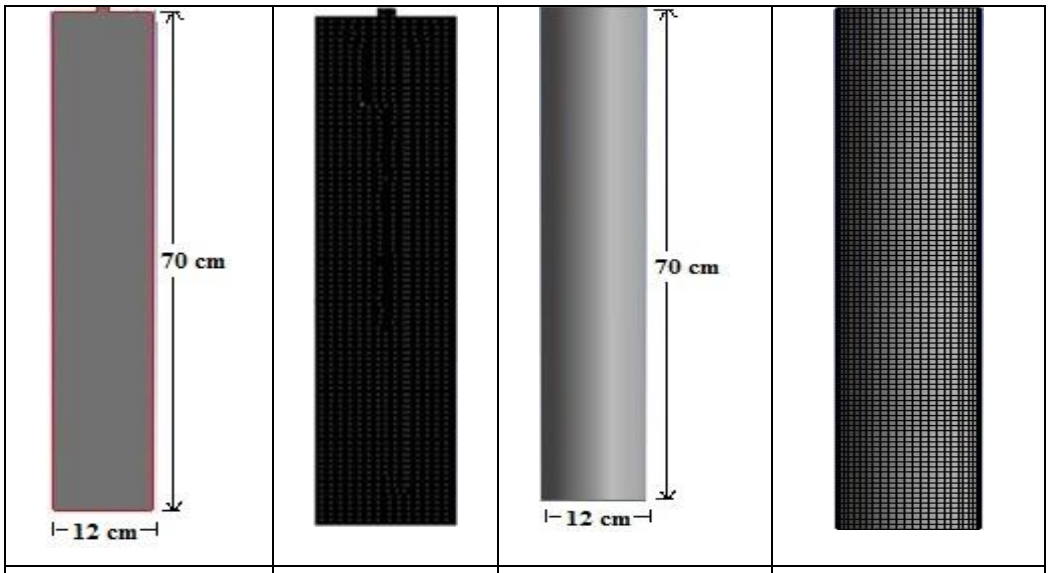

(a) 2 D Geometry	(b) 2 D Mesh	(c) 3 D Geometry	(d) 3 D Mesh

Fig.- 5.1: Fluidized bed details

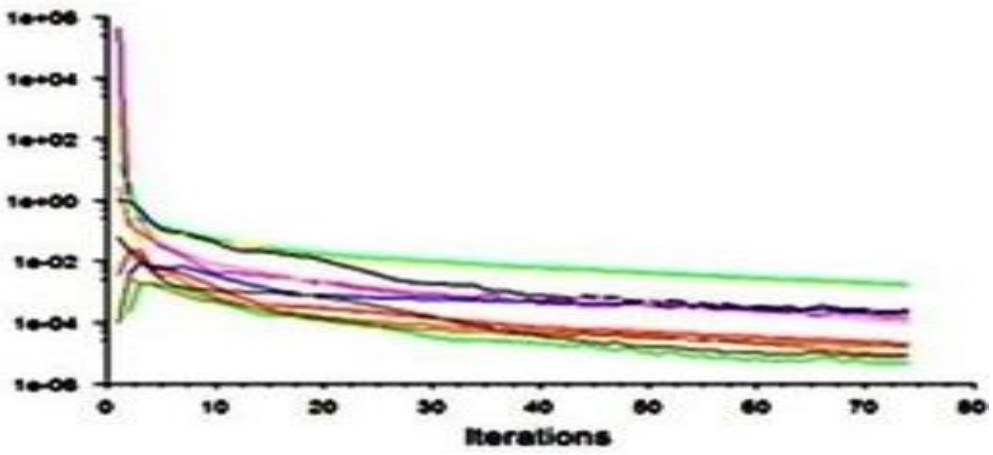

Fig. - 5.2: Residual plots

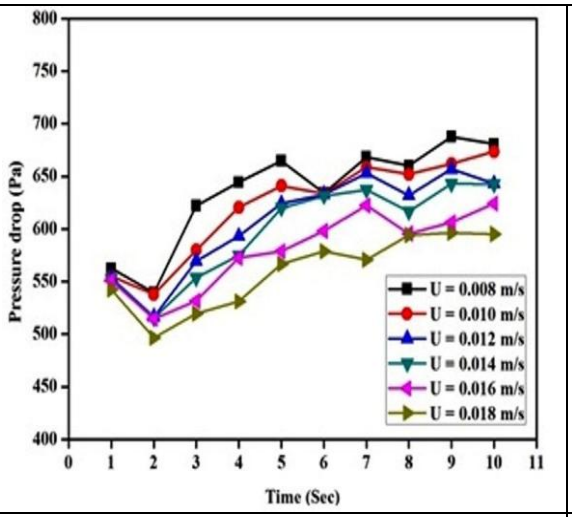

Fig. – 5.3 (a): Variation of bed pressure drop against time

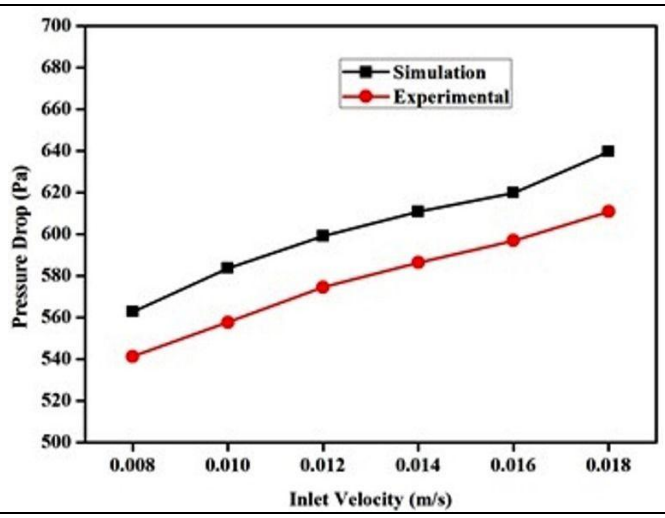

Fig. - 5.3 (b): Comparison plot of bed pressure drop

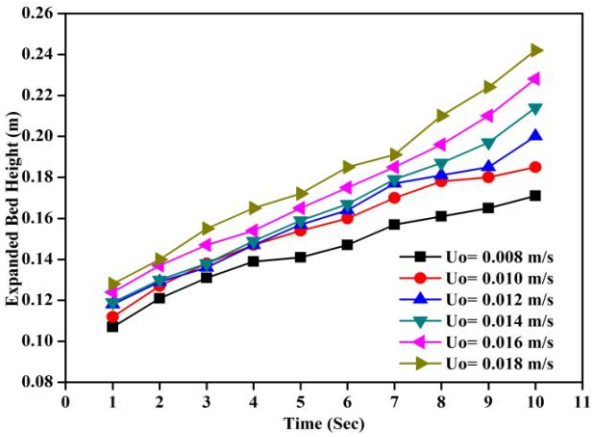

Fig. - 5.4 (a): Bed expansion against time

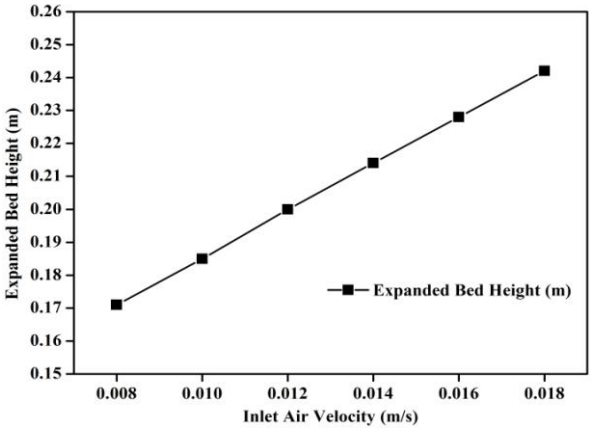

Fig. - 5.4 (b): Expanded bed height versus inlet air velocity

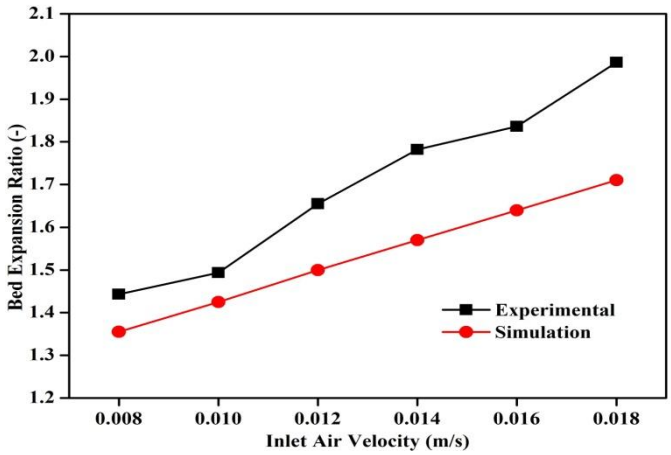

Fig.- 5.4 (c): Comparison plot of bed expansion ratio

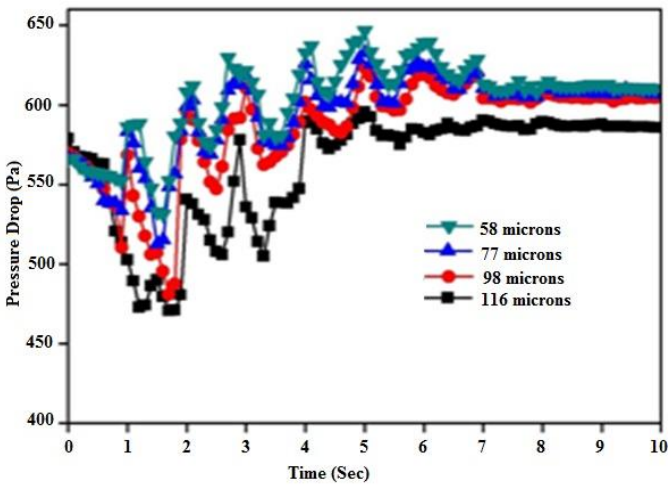

Fig. – 5.5: Comparison of simulated bed pressure drop for different particle sizes

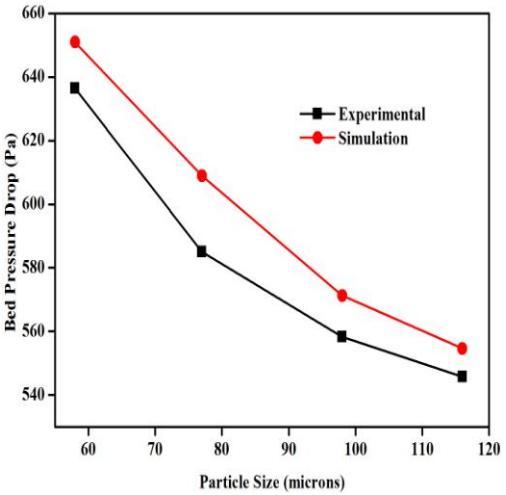

Fig. - 5.6: Effect of particle size on bed pressure drop

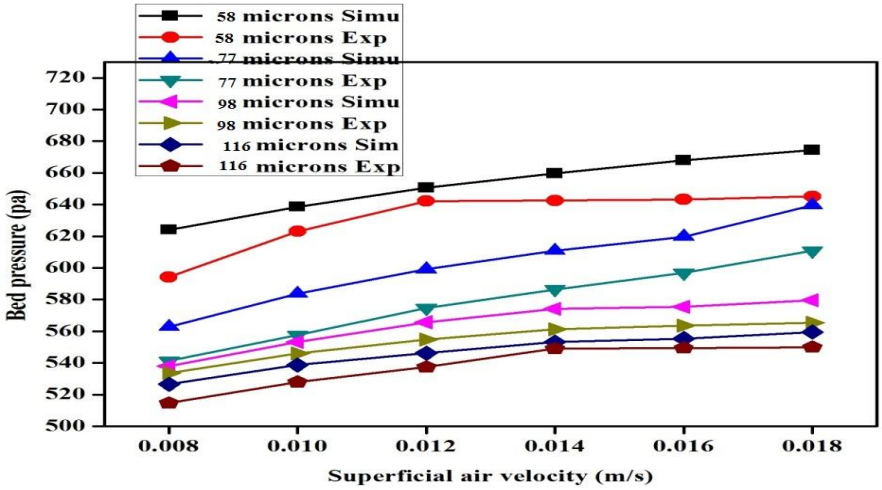

Fig. – 5.7: Comparison of experimental and simulated bed pressure drops for different particle sizes

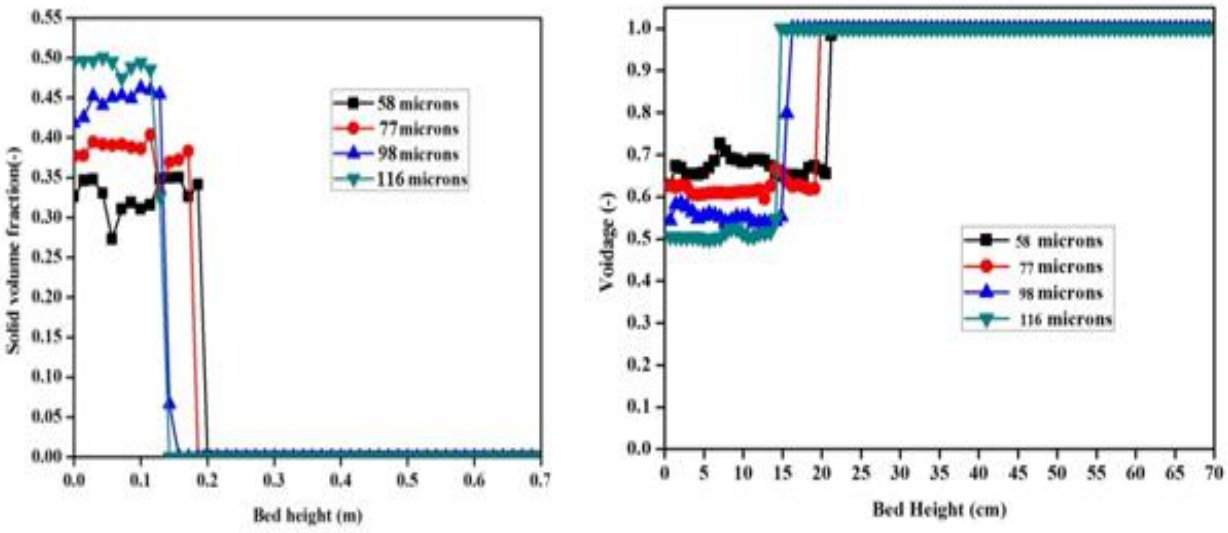

(a) For Solid Phase **(b) For Gas Phase**

Fig. - 5.8: Axial volume fraction profile for different particle sizes

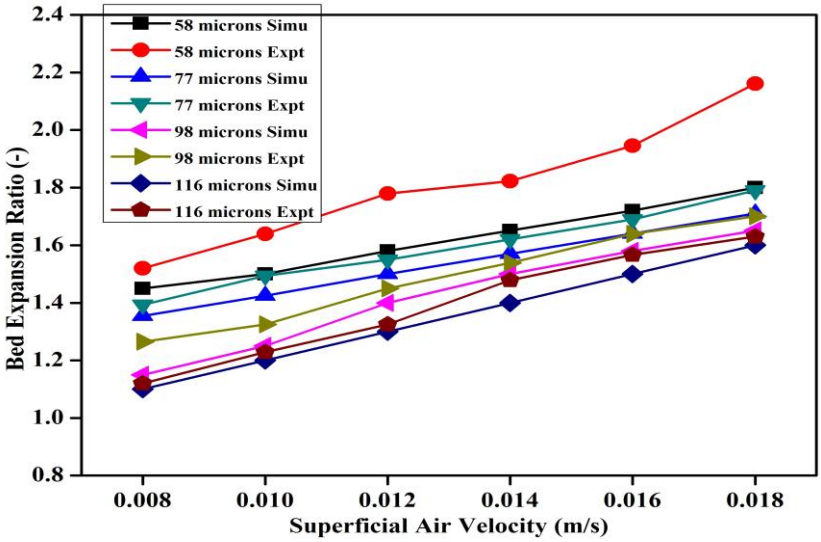

Fig. – 5.9: Comparison of simulated and experimental bed expansion ratios for different particle sizes

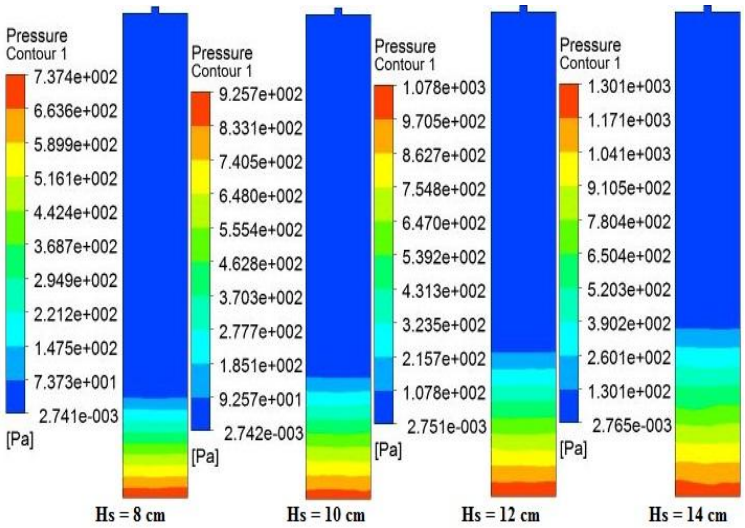

(a) Contour plot of pressure drop

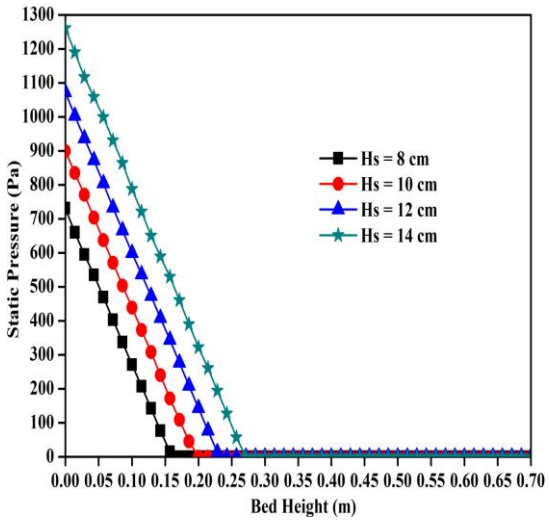

(b) Static pressure profile

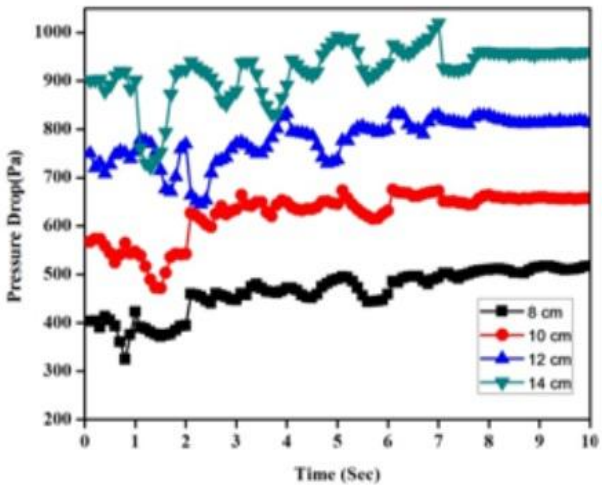

(c) Pressure drop versus simulation time

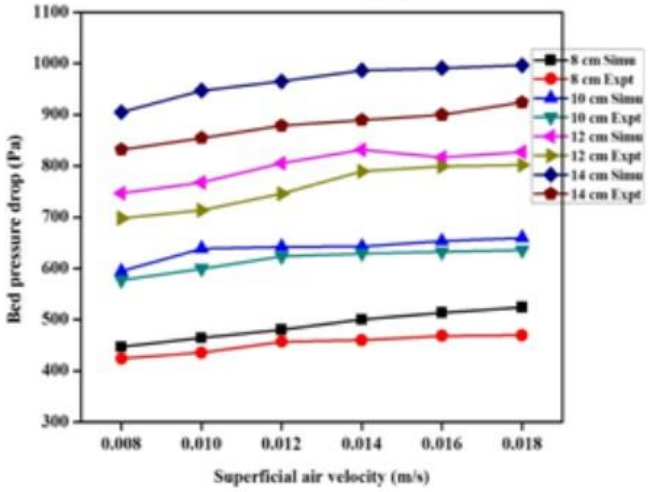

(d) Pressure drop versus superficial velocity

Fig. – 5.10: Pressure drop profiles for different static bed heights

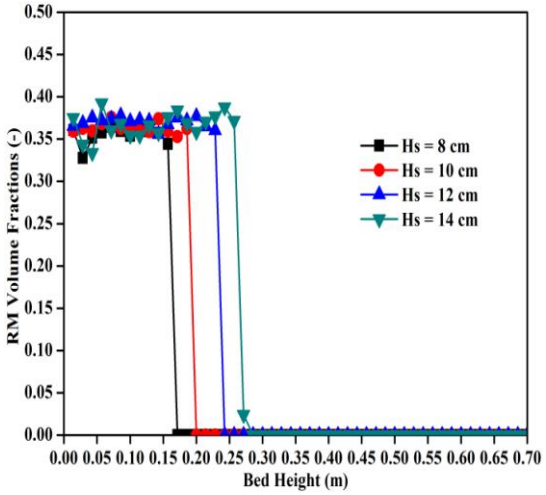

Fig. – 5.11: Distribution of axial solid volume fraction for static bed heights

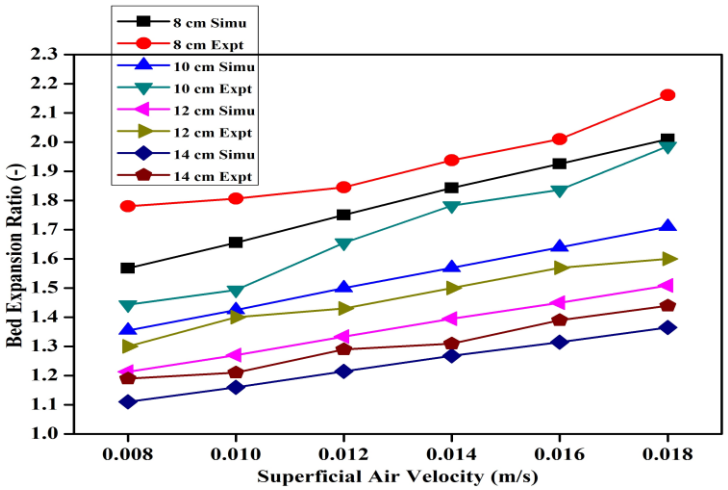

Fig.-5.12: Comparison of simulated and experimental bed expansion ratios for different static bed heights

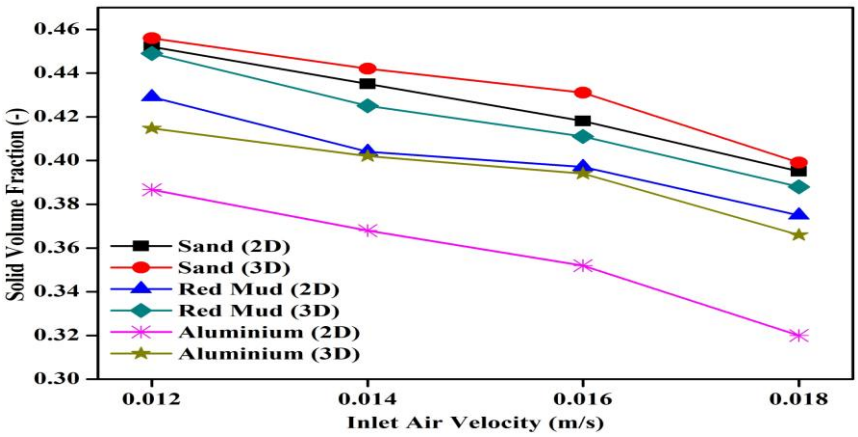

Fig. – 5.13: Comparison of solid volume fractions against air velocities for different materials

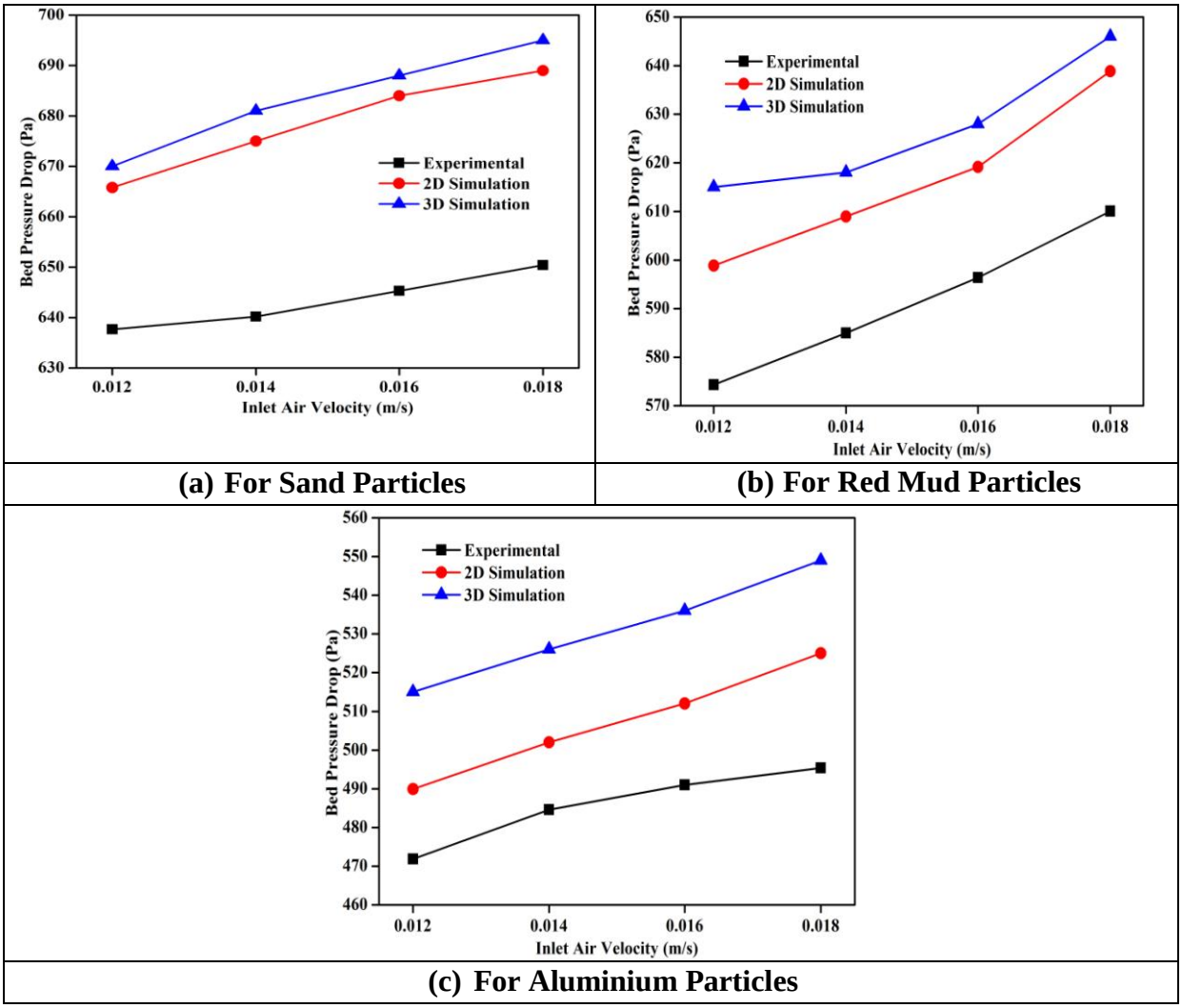

(a) For Sand Particles | **(b) For Red Mud Particles**

(c) For Aluminium Particles

Fig. – 5.14: Comparison between experimental and simulated results for bed pressure drop for different materials

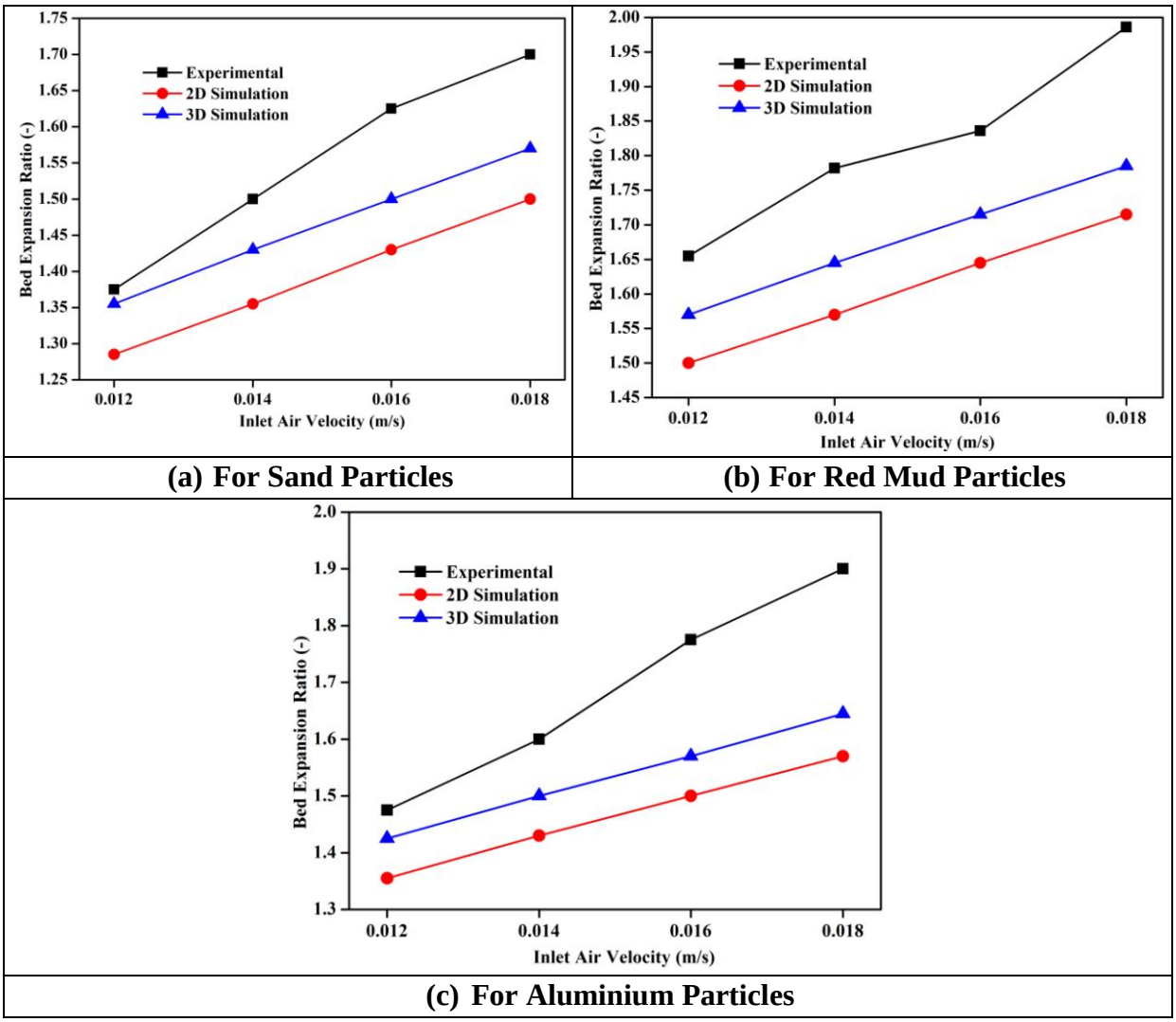

(a) For Sand Particles

(b) For Red Mud Particles

(c) For Aluminium Particles

Fig. – 5.15: Comparison between experimental and simulated results for bed expansion ratios for different materials

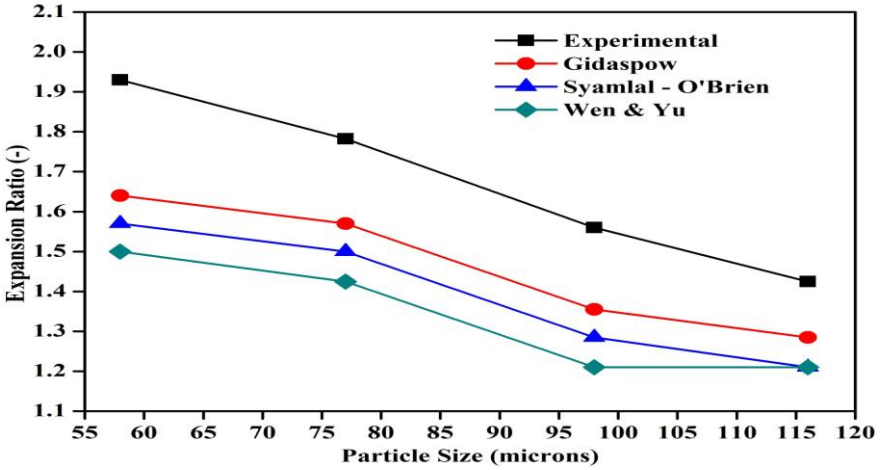

Fig. – 5.16: Comparison of simulated and experimental expansion ratios with particle sizes

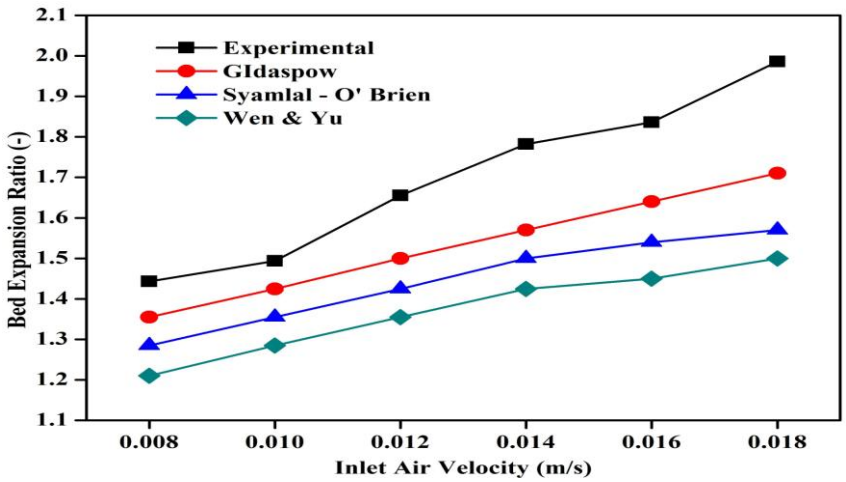

Fig. – 5.17: Comparisons of simulated and experimental values of expansion ratios with air velocities for different drag models

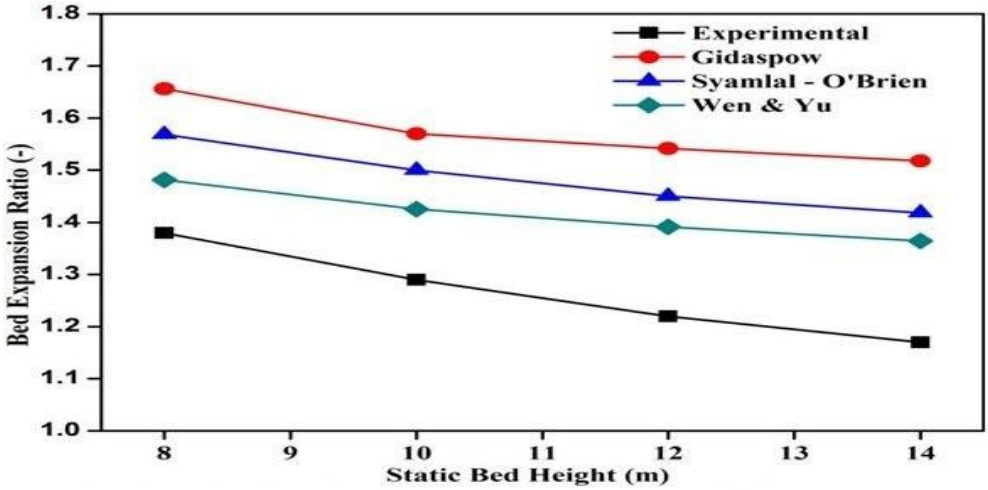

Fig. – 5.18: Comparison of bed expansion ratios with static bed height for different drag models

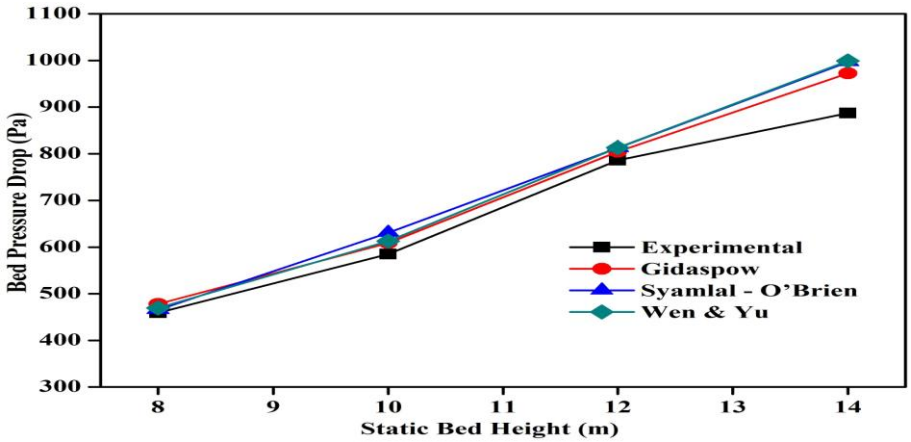

Fig. – 5.19: Comparison of simulated and experimental bed pressure drop with static bed heights for different drag models

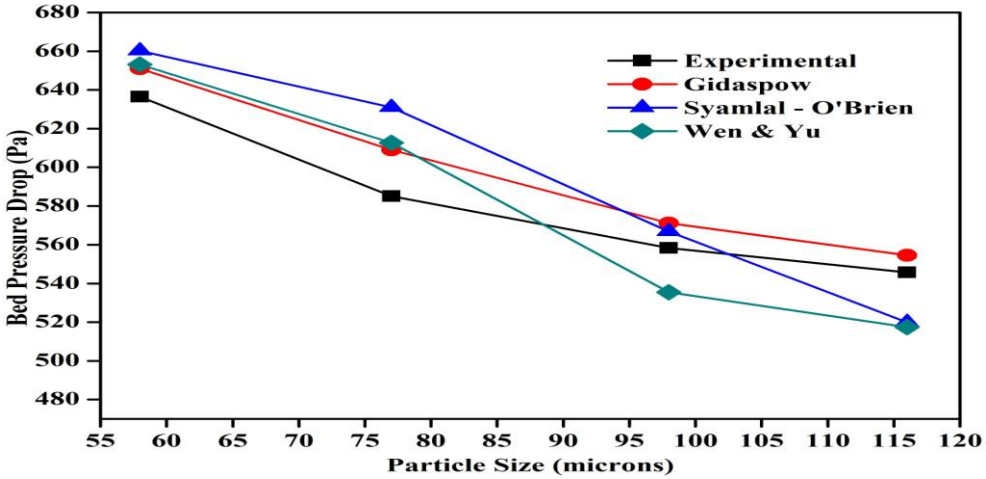

Fig. – 5.20: Comparison of simulated and experimental bed pressure drop with particle sizes for different drag models

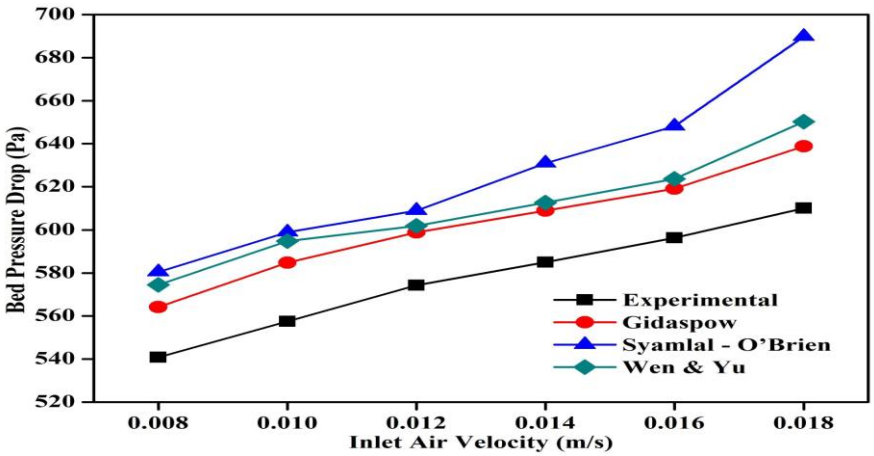

Fig. – 5.21: Comparison of simulated and experimental bed pressure drop with air velocities for different drag models

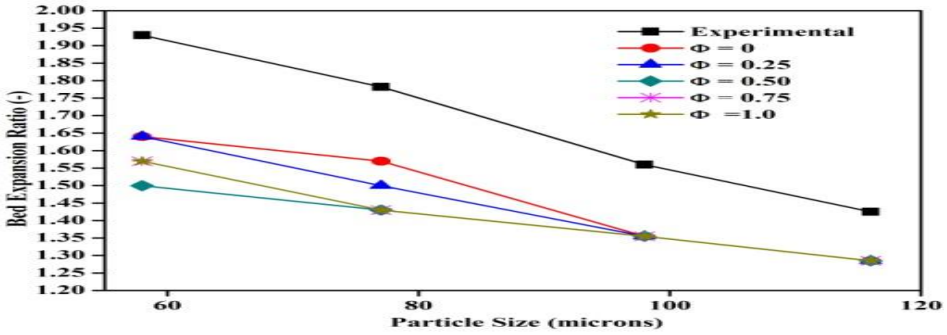

Fig. – 5.22: Comparison of simulated and experimental bed expansion ratios for different specularity coefficients

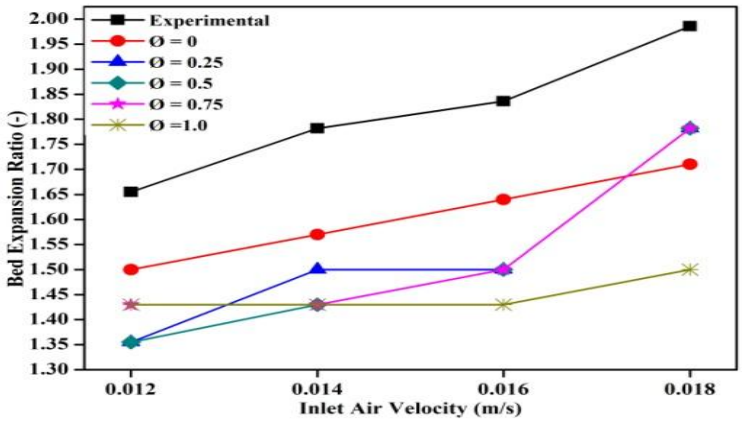

Fig. – 5.23: Comparison of bed expansion ratios simulated with air velocities for different specularity coefficients

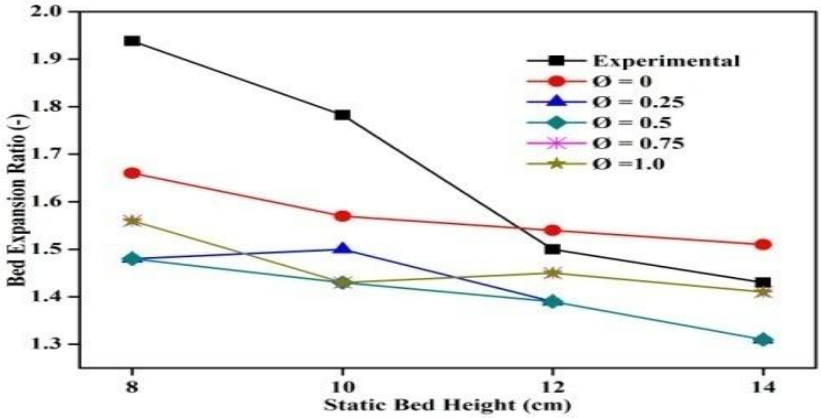

Fig. – 5.24: Comparison among simulated and experimental of bed expansion ratios with different static bed heights for different specularity coefficients

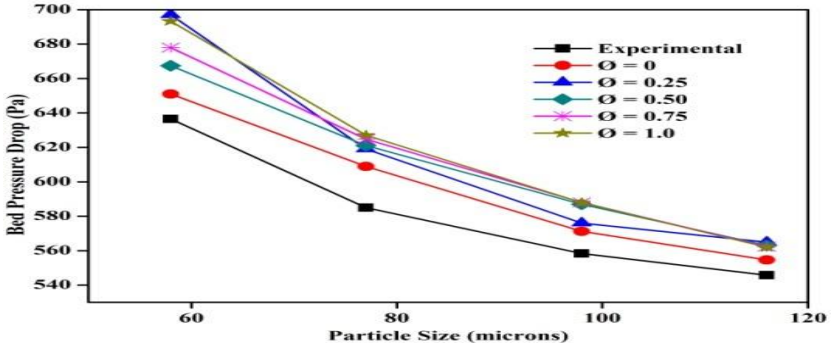

Fig. – 5.25: Comparison of experimental and simulated bed pressure drops with particle sizes for different specularity coefficients

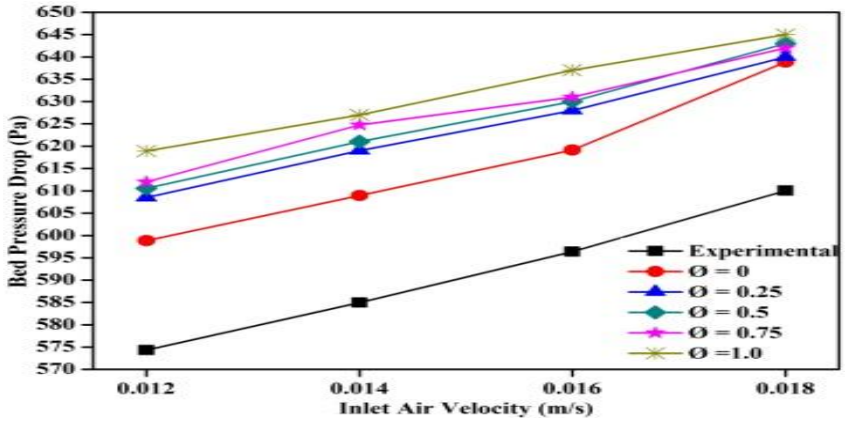

Fig. – 5.26: Comparison between simulated and experimental bed pressure drop with air velocities for different specularity coefficients

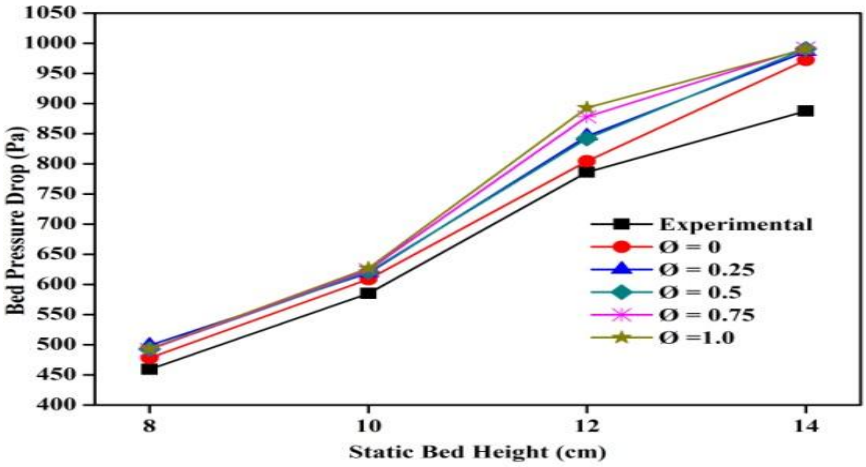

Fig. – 5.27: Comparison of bed pressure drop with static bed height for different specularity coefficients

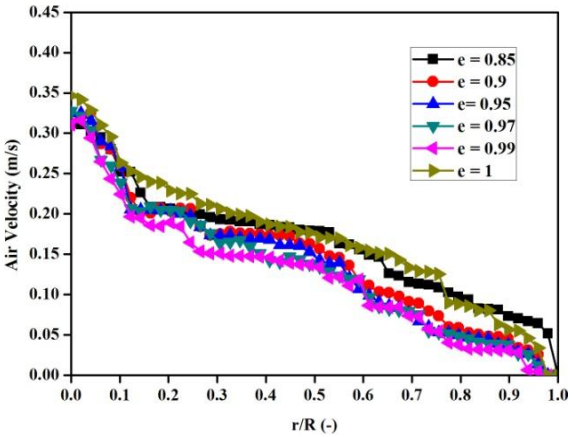

Fig. – 5.28 (a): Radial distributions of air velocity for different restitution coefficients

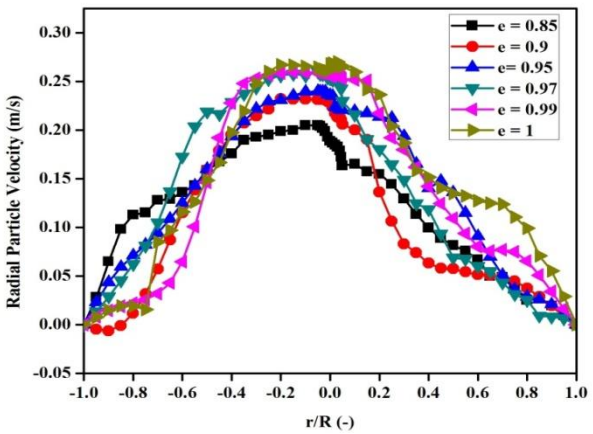

Fig. – 5.28 (b): Radial distribution of particle velocity for different restitution coefficients

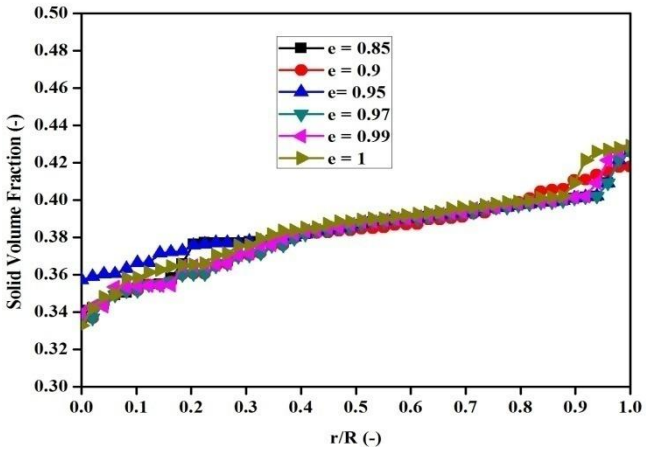

Fig. – 5.29: Radial distributions of solid volume fraction for different restitution coefficients

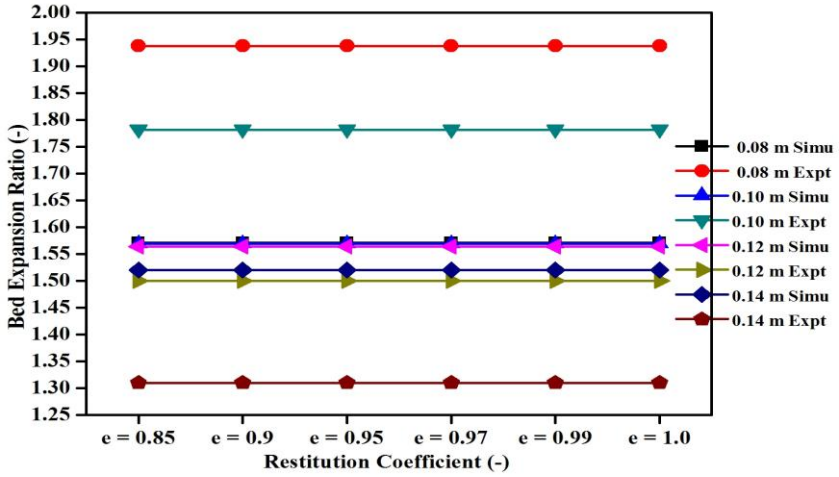

Fig. – 5.30: Comparison of simulated and experimental bed expansion ratio with restitution coefficient for different static bed heights

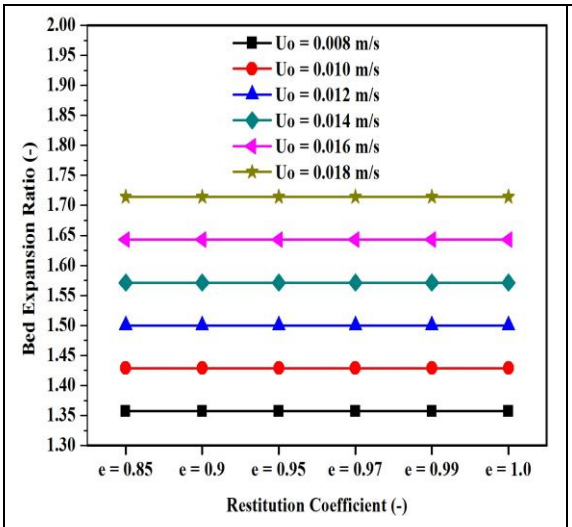

Fig. – 5.31: Comparison of bed expansion ratios against restitution coefficient for air velocities

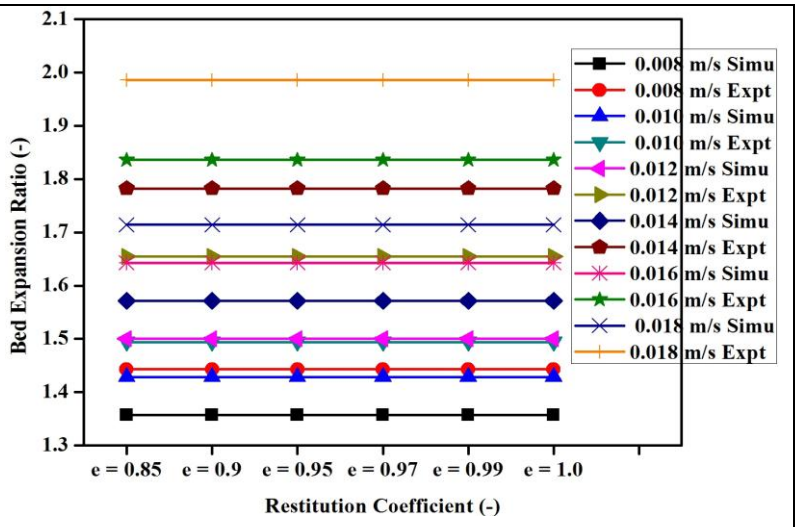

Fig. – 5.32: Comparison of simulated and experimental values of bed expansion ratios against restitution coefficients

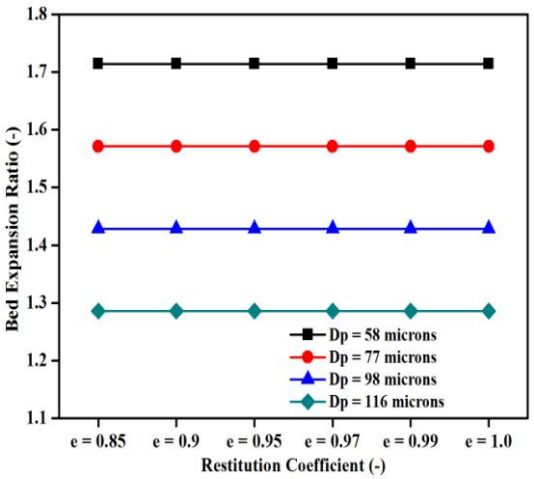

Fig. – 5.33: Comparison of bed expansion ratios against restitution coefficients for different particle sizes

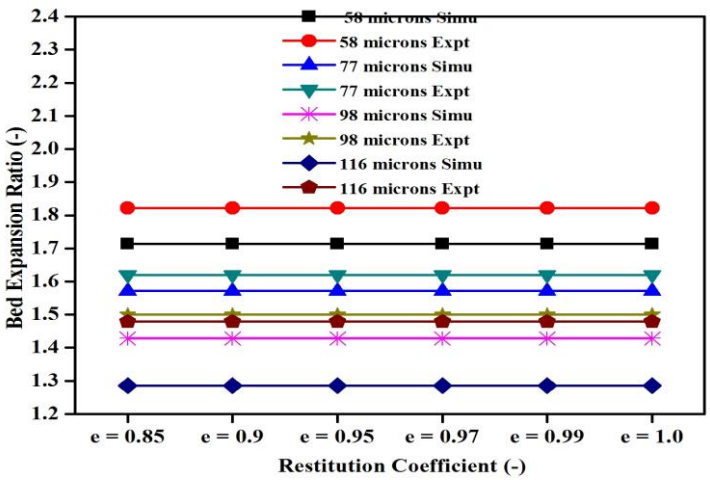

Fig. – 5.34: Comparison of simulated and experimental values of bed expansion ratios against restitution coefficients

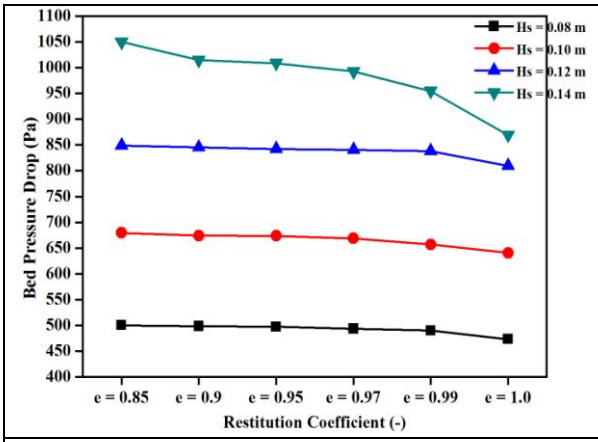

Fig. – 5.35: Variation of bed pressure drop against restitution coefficient with different static bed heights

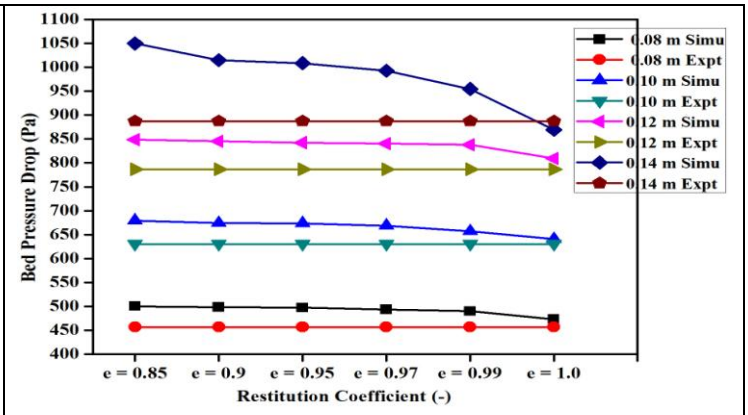

Fig. – 5.36: Comparison of simulated and experimental bed pressure drop with different static bed height for different restitution coefficients

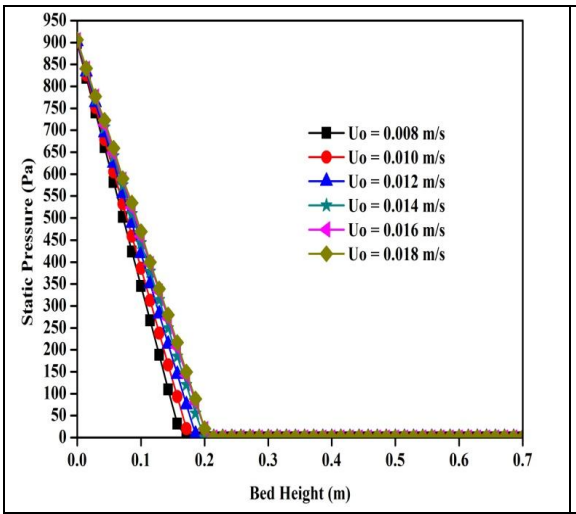

Fig. – 5.37: Variation of static pressure against bed height for air velocities

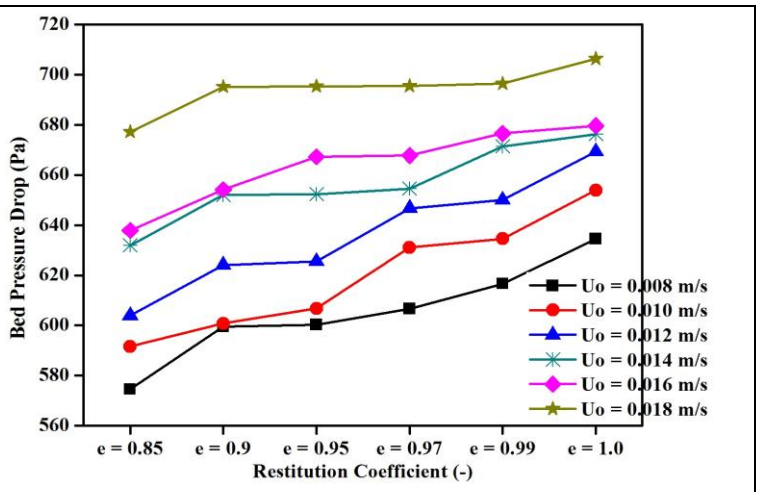

Fig. – 5.38: Variation of pressure drop against restitution coefficients for different air velocities

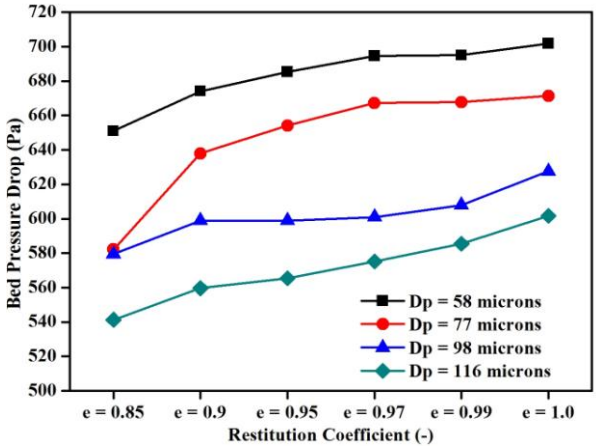

Fig. – 5.39: Variation of pressure drop against restitution coefficient for different particle sizes

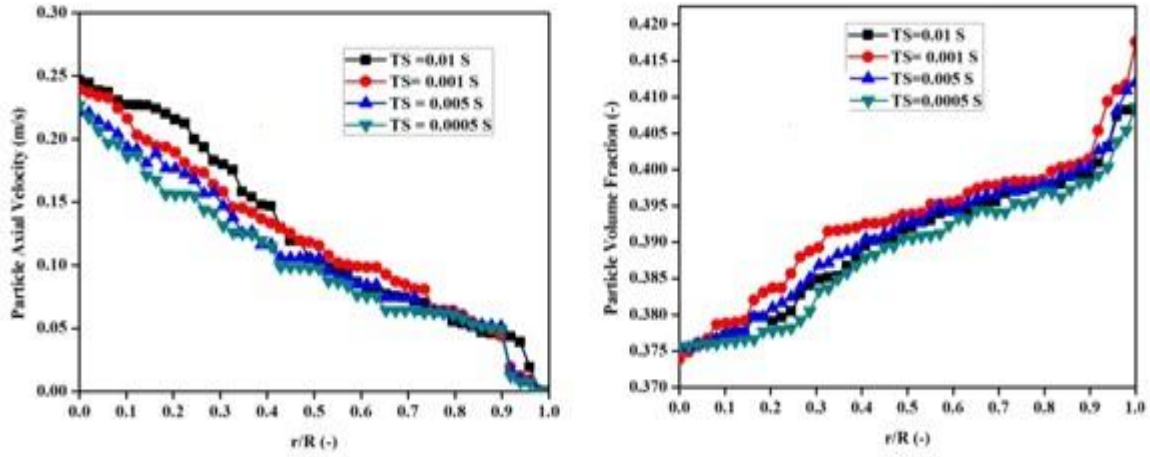

(a) Axial particle velocity **(b) Solid volume fractions**

Fig. – 5.40: Radial profiles of velocity for different time steps

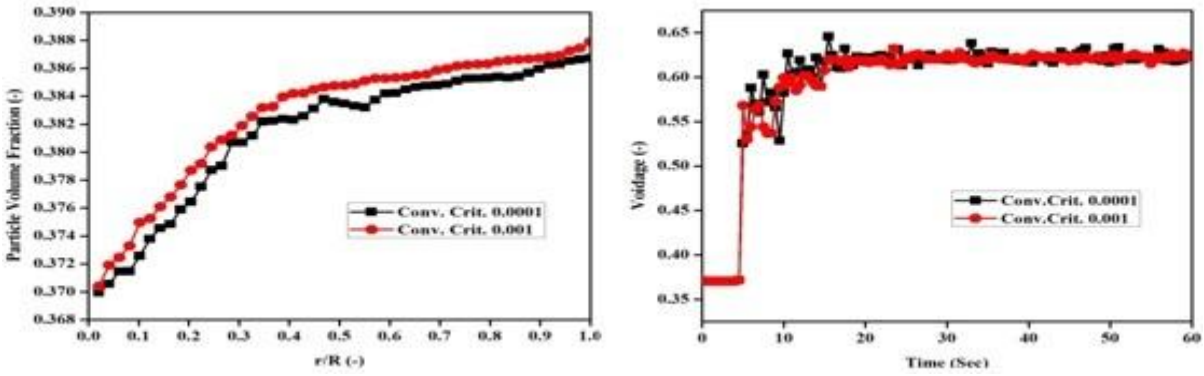

(a) Radial Solid volume fraction **(b) Voidage with Time**

Fig. – 5.41: Volume fraction of Solid and gas phase for different convergence criterion

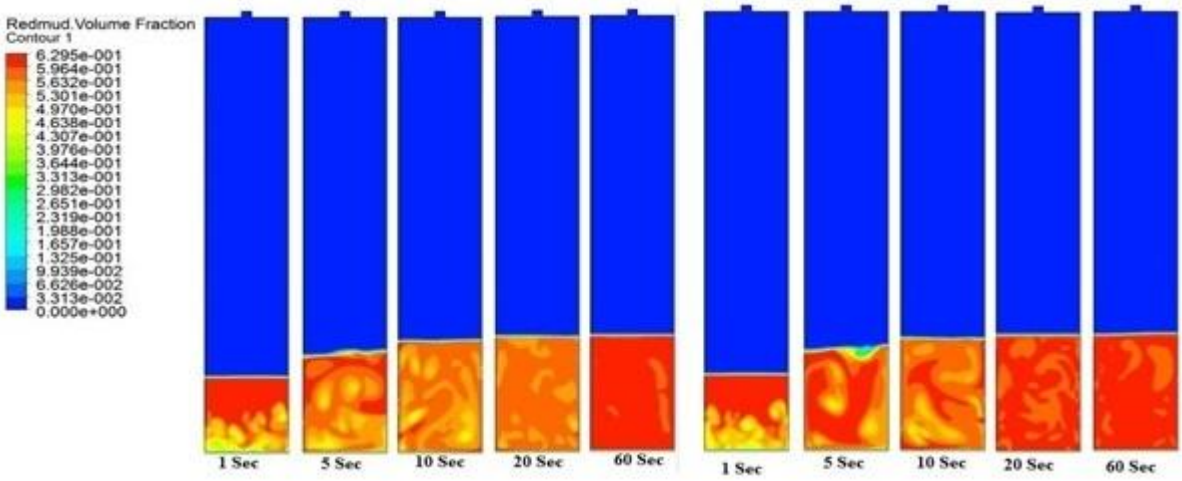

(a) Convergence Criterion 0.001 **(b) Convergence Criterion 0.001**

Fig. – 5.42: Contour plots with different convergence criteria

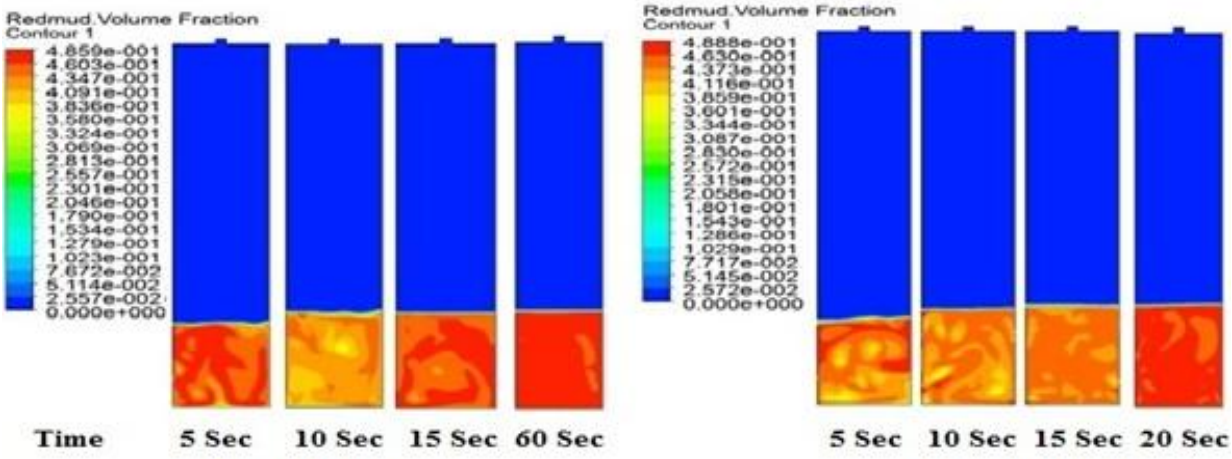

(a) First Order **(b) Second Order**

Fig. - 5.43: Contours of solids volume fractions for different discretization schemes

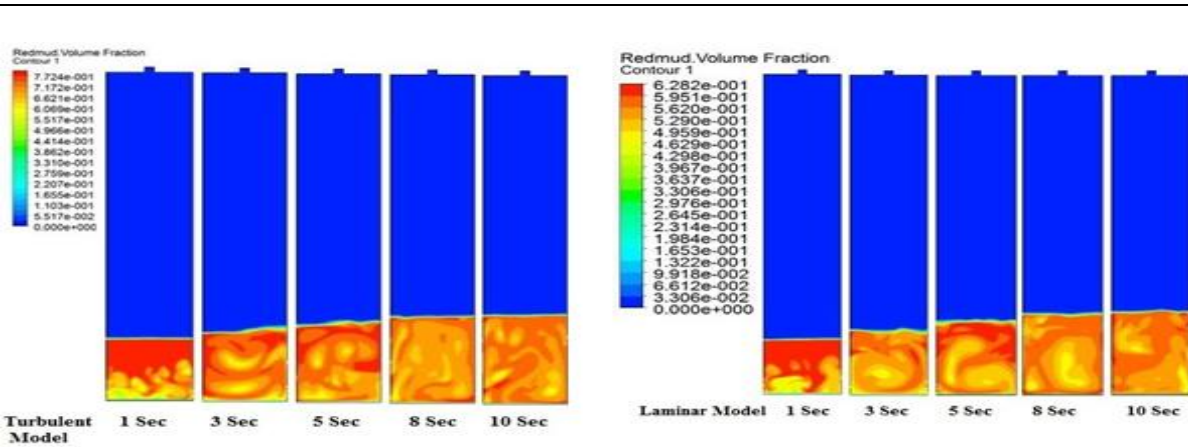

(a) Turbulent Model **(b) Laminar Model**

Fig. - 5.44: Comparisons of solid volume fractions for different flow models

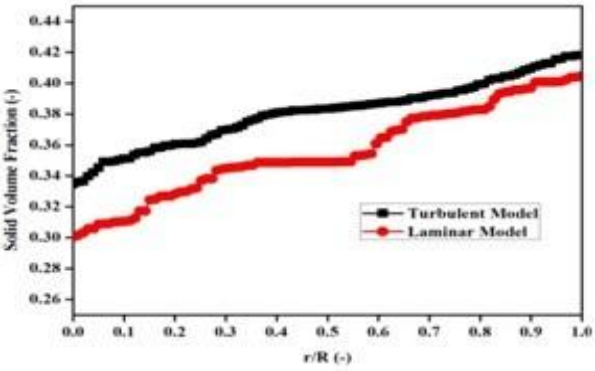

(a) Radial Solid Volume Fraction

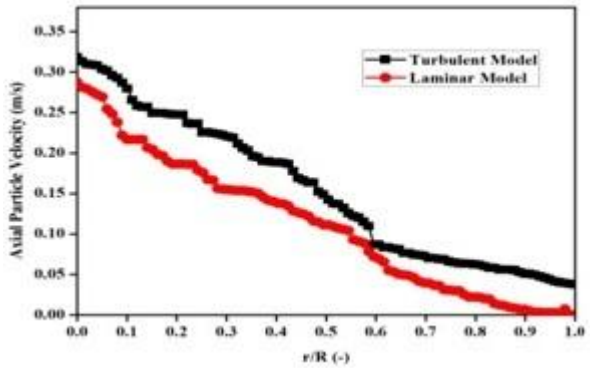

(b) Radial Axial Particle Velocity

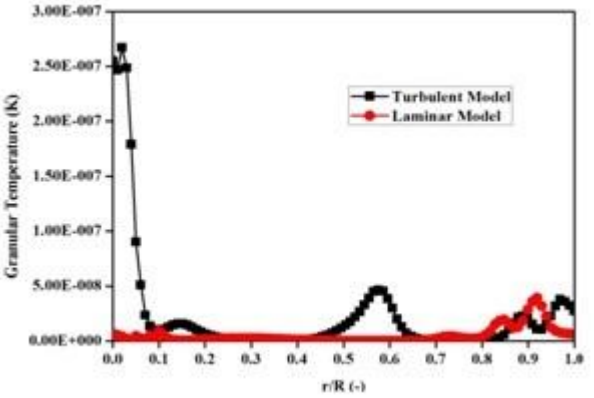

(c) Radial Granular Temperature

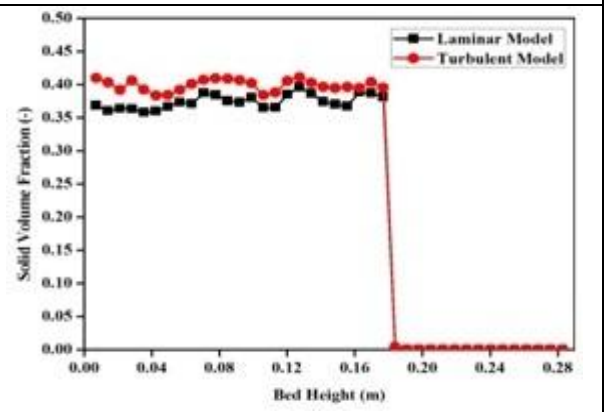

(d) Axial Solid Volume Fractions

Fig. – 5.45: Comparison of laminar and turbulent models for bed dynamics

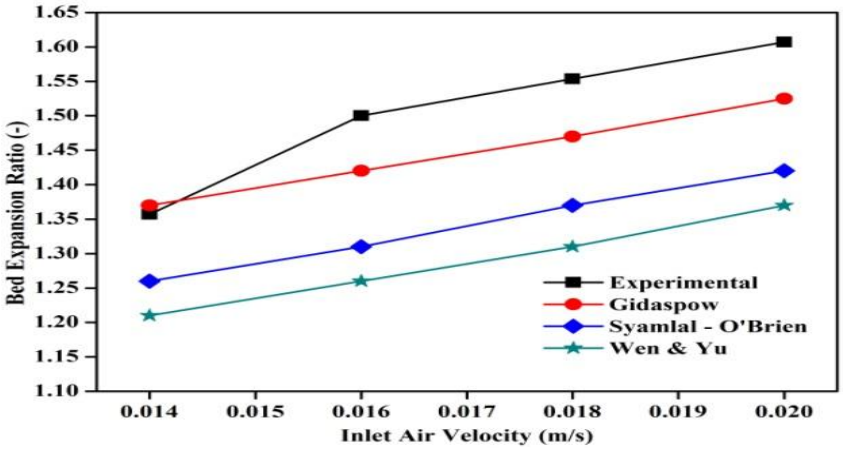

Fig. – 5.46: Comparison of bed expansion ratios with air velocities for different drag models

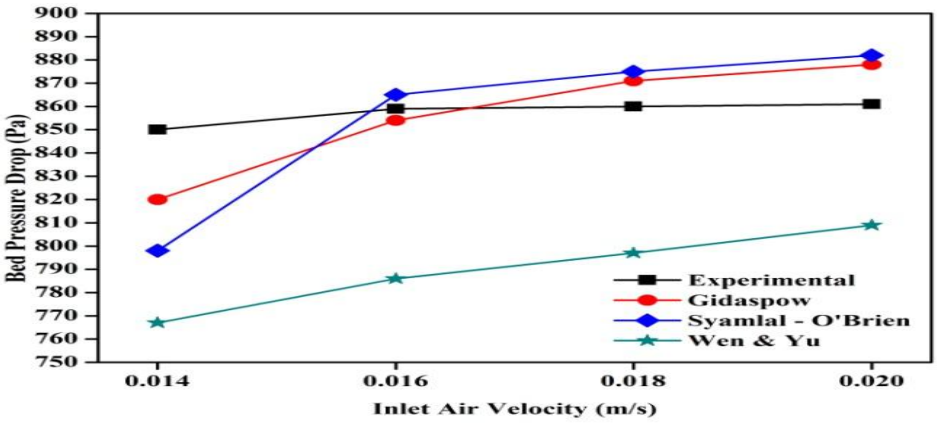

Fig. – 5.47: Comparison of bed pressure drop with air velocities for different drag models

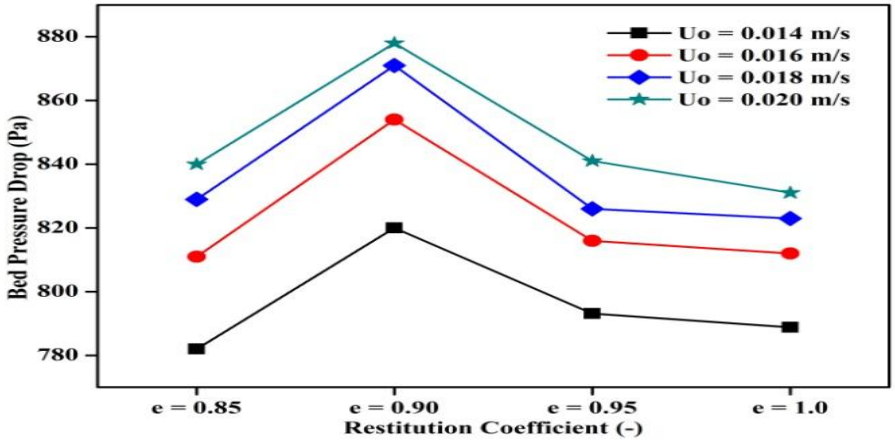

Fig. – 5.48: Comparison of bed pressure drop against restitution coefficients for different air velocities

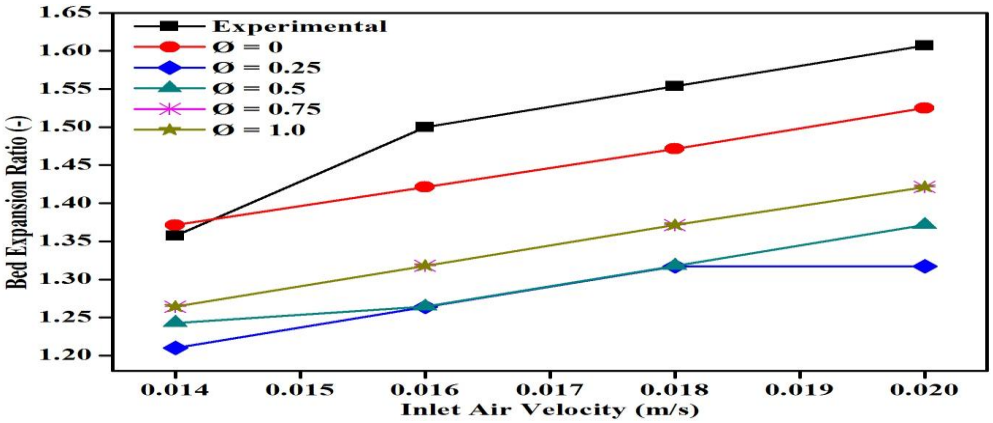

Fig. – 5.49: Comparison of bed expansion ratios against air velocities for different specularity coefficients

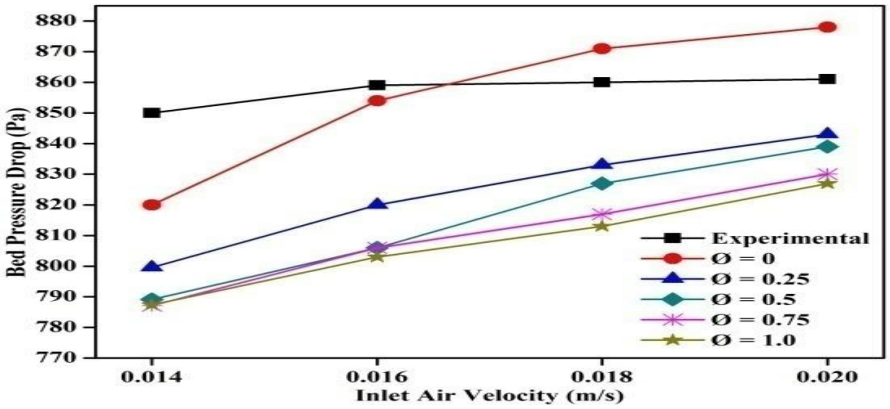

Fig. – 5.50: Comparison of bed pressure drop with different air velocities for different specularity coefficients

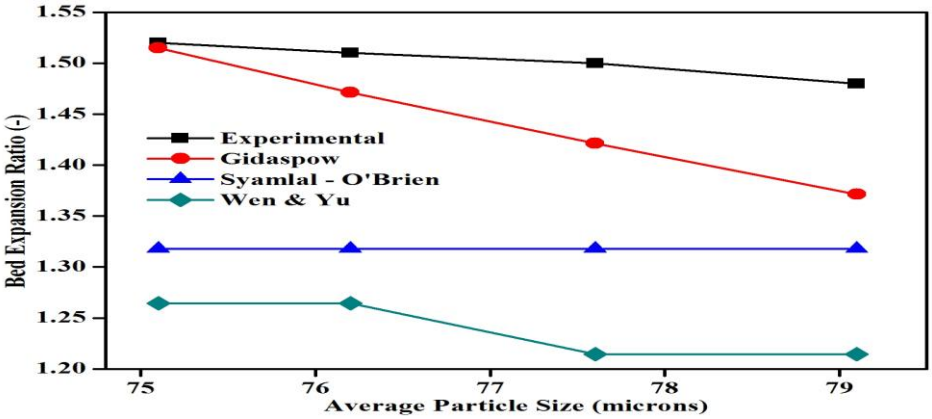

Fig. – 5.51: Comparison of experimental and simulated bed expansion ratios with different particle sizes of binary mixtures for different drag models

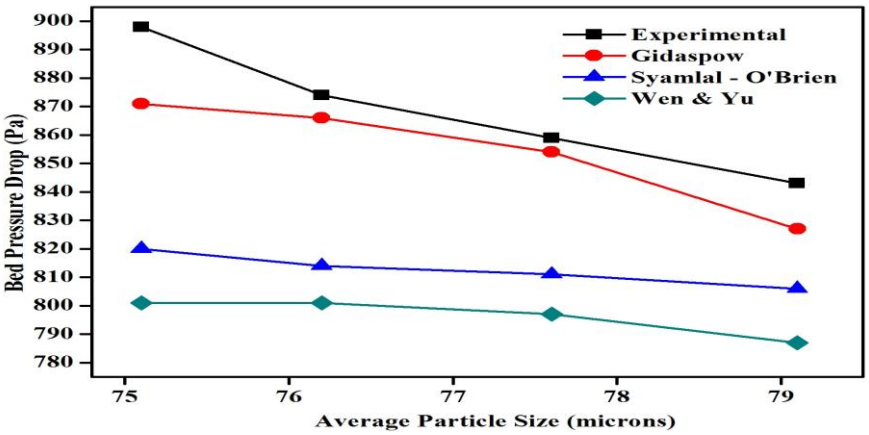

Fig. – 5.52: Comparison of bed pressure drop against particle sizes of binary mixture for different drag models

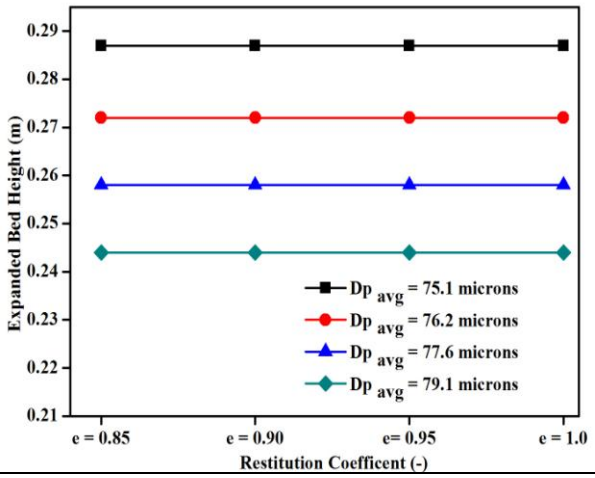

Fig. – 5.53: Expanded bed height against restitution coefficient for different particle sizes of binary mixture

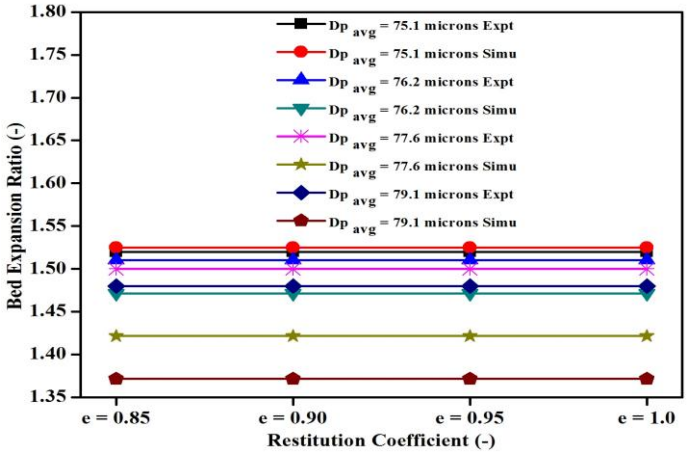

Fig. – 5.54: Comparison of simulated and experimental expansion ratio against restitution coefficient for different particle sizes of binary mixture

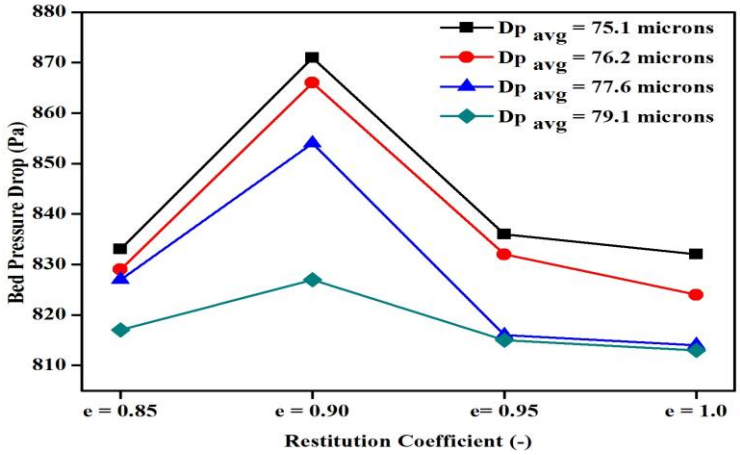

Fig. – 5.55: Comparison of bed pressure drop against restitution coefficients for different particle sizes of binary mixture

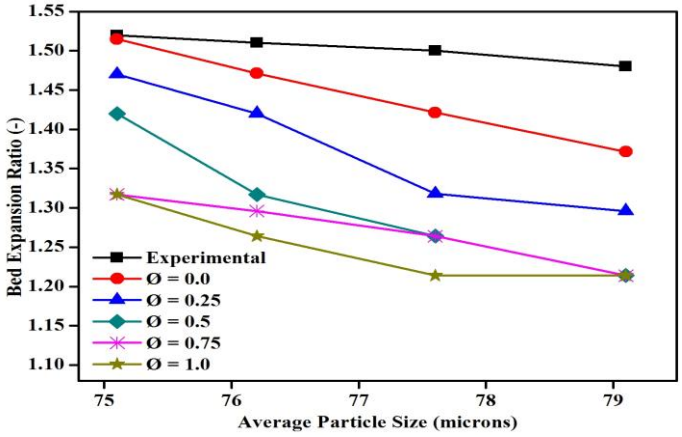

Fig. – 5.56: Comparison of simulated and experimental bed expansion ratios with different particle sizes of binary mixtures for different specularity coefficient

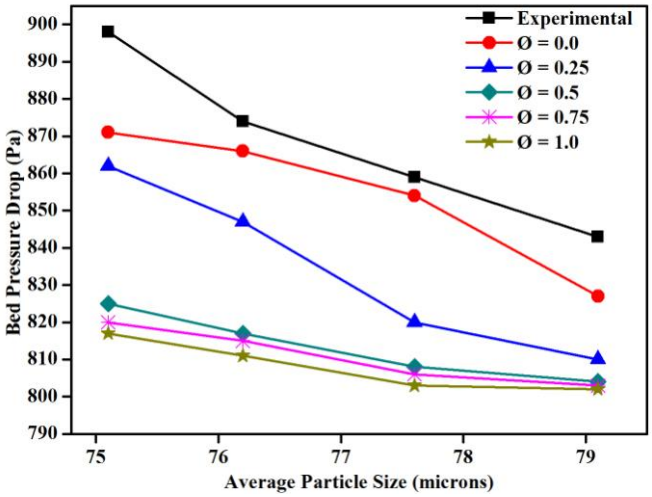

Fig. – 5.57: Comparison of simulated and experimental bed pressure drop with different particle sizes of binary mixtures for different specularity coefficients

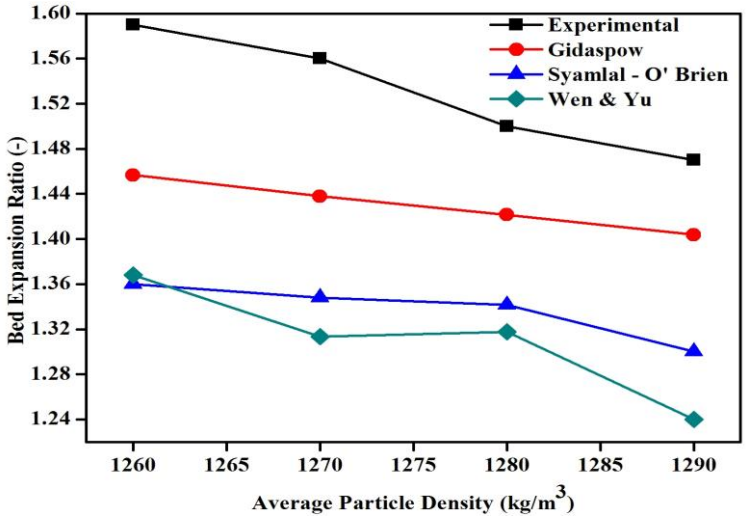

Fig. – 5.58: Comparison of simulated and experimental values of bed expansion ratios with different densities of binary mixtures for different drag models

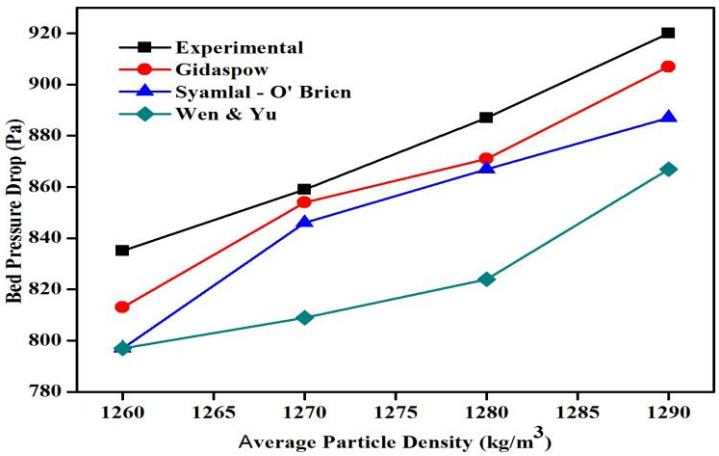

Fig. – 5.59: Comparison of simulated and experimental values of bed pressure drop with different densities of binary mixture for different drag models

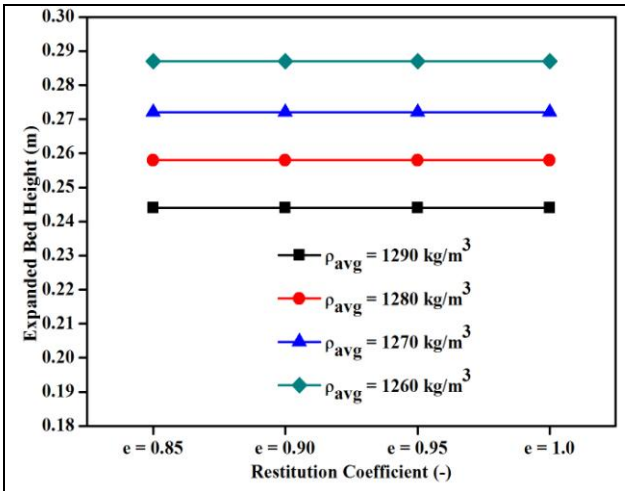

Fig. – 5.60: Expanded bed height against restitution coefficients for different densities of binary mixtures

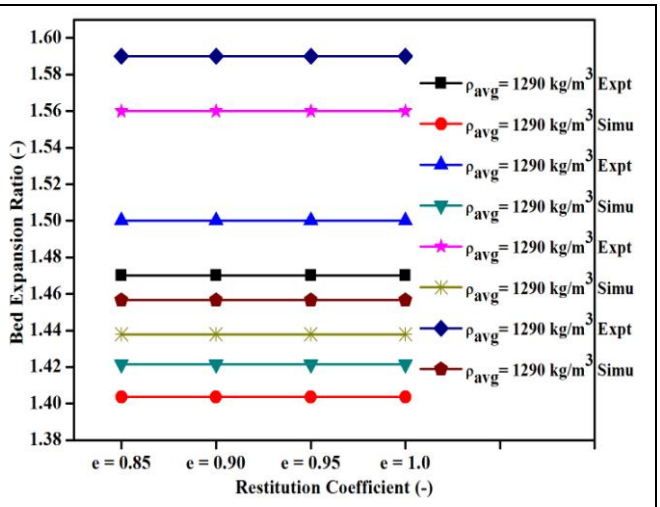

Fig. – 5.61: Comparison of simulated and experimental expansion ratio with densities of binary mixtures for restitution coefficients

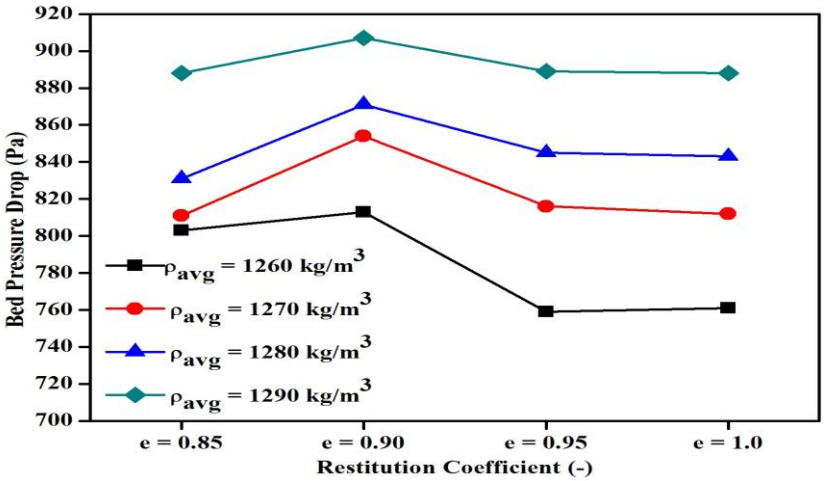

Fig. – 5.62: Comparison of bed pressure drop against restitution coefficients for different densities of binary mixture

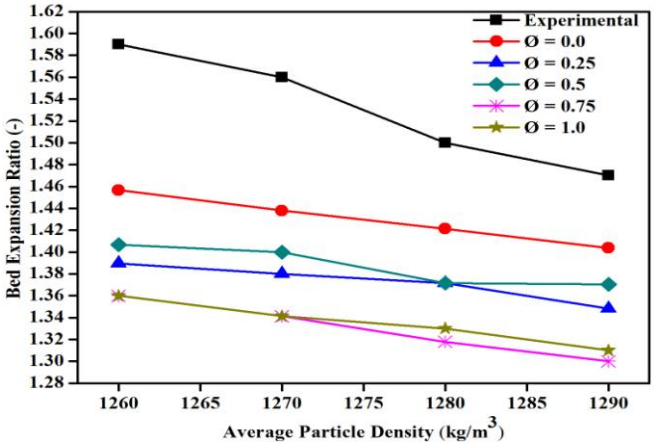

Fig. – 5.63: Comparison of simulated and experimental expansion ratios with different densities of binary mixtures for different specularity coefficients

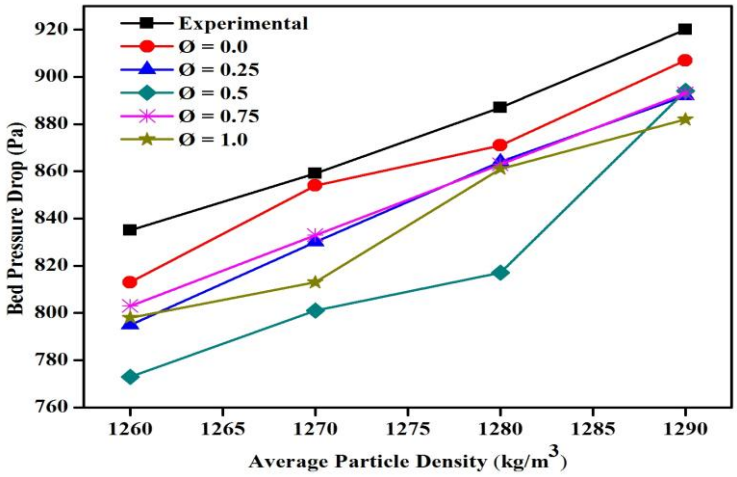

Fig. – 5.64: Comparison of simulated and experimental pressure drop with different densities of binary mixture for different specularity coefficients

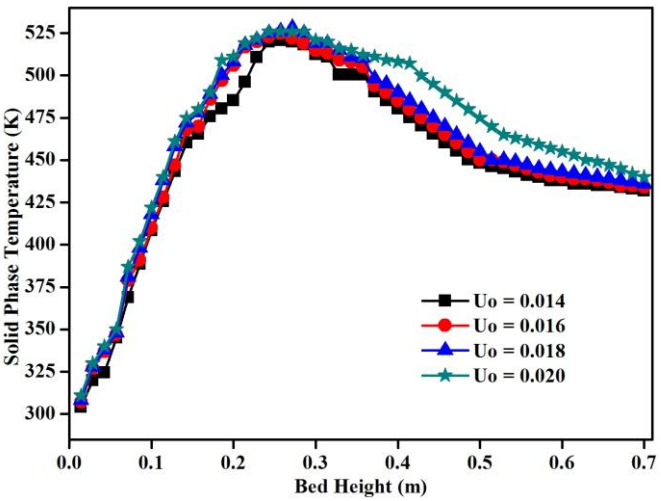

Fig. – 5.65: Effect of inlet gas velocity on solid phase temperature inside reactor

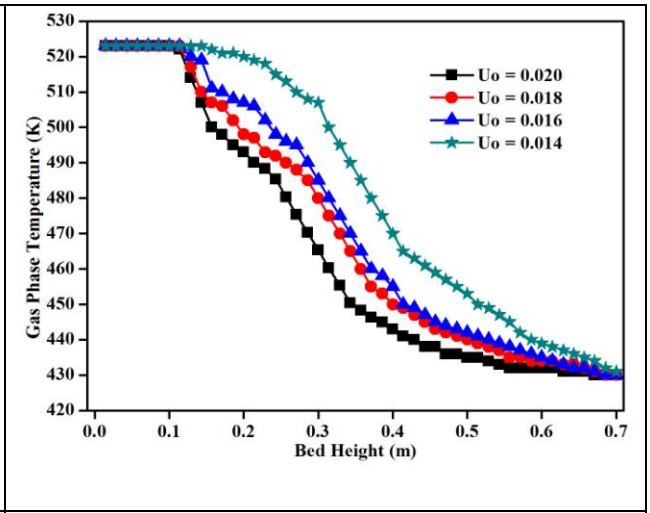

Fig. – 5.66: Effect of inlet gas velocity on gas phase temperature inside reactor

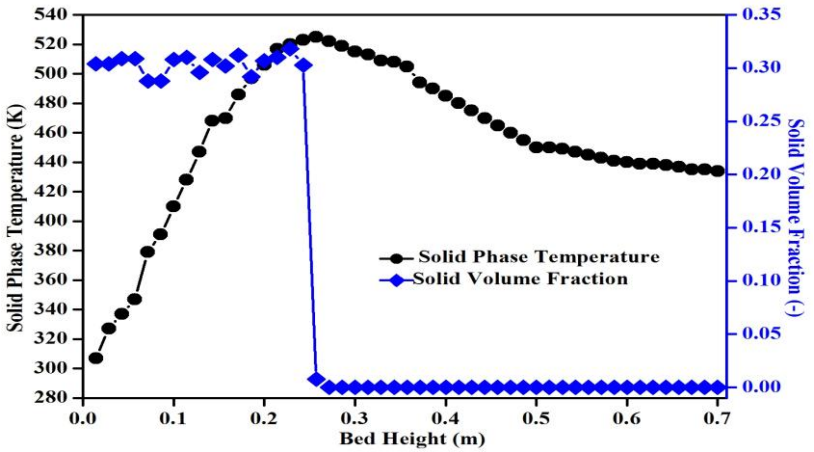

Fig. – 5.67: Comparison for distribution of temperature and volume fractions of solid phase against bed heights

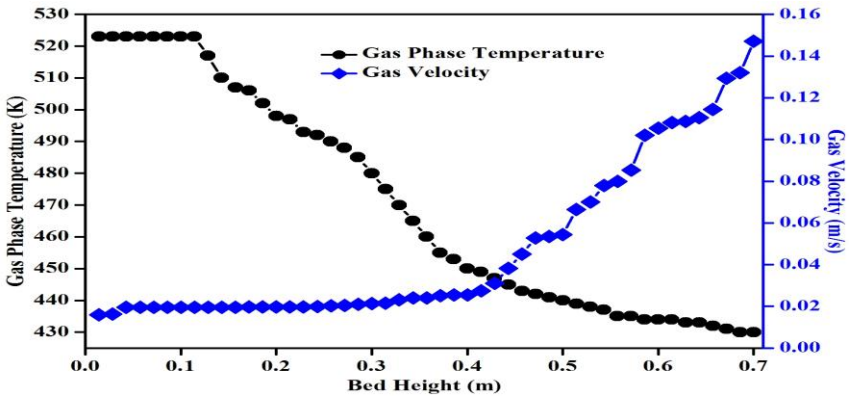

Fig. – 5.68: Comparison for distribution of temperature and velocity for gas phase against bed heights

CHAPTER - 6

CONCLUSIONS AND FUTUTRE WORK

Different bed materials such as Red Mud, Red Mud-Aluminium mixture and Sand are used in FBR for treatment of gaseous effluents containing fluorides during experimentation. These materials are characterized before and after the experiments with / without treatment with industrial effluent gas. In this work, the hydrodynamic studies of the FBR are carried out with respect to the bed pressure drop, expansion / fluctuation ratio and fluidization index under different operating conditions. CFD simulations are also carried out for FBR using the commercial CFD solver ANSYS/FLUENT 13. The results yield comprehensive information concerning the bed hydrodynamics and thermal-flow behaviours existing within the FBR. CFD simulations are carried out with different CFD parameters viz. drag models, restitution coefficient and specularity coefficients. Again effect of different system parameters viz. particle size, superficial air velocity and static bed heights are studied on these CFD simulations for single sized and binary mixture of bed materials. Temperature effect is also studied for gas phase and solid phase with respect to different system parameters. Finally a comparison is made for the results obtained in the simulations and experimental studies. The following conclusions are observed.

- Abatement of gaseous pollutant, fluorides is possible by fluidized bed technology.
- Red Mud a waste material is found to be suitable bed material for abatement of fluorides through different characterization techniques such as XRD, TGA-DTA, PSA, FESEM, FT-IR and BET. It is confirmed that reduction in concentration of fluorides is possible with FBR.
- Use of Red Mud-Aluminum mixture as bed material is found to abate more amounts of fluorides than Red Mud alone. This may be due to proper fluidization condition with binary mixture of bed materials or due to presence of more free flowing Aluminium particles in the bed.

- Through different characterizations it is found that Ferrous Fluoride (FeF_2), Ferric Fluoride (FeF_3), Aluminium Fluoride (AlF_3) and Sodium Fluoride (NaF) are present in the bed material sample of Red Mud, Red Mud-Aluminium after the experiments. Similarly Aluminium Fluorides (AlF_3), Silicon Tetra Fluorides (SiF_4) are found with Sand samples after the experiments. Thus it can be said that the abatement of fluorides has been made possible with FBR.

From the hydrodynamic studies the following conclusions are drawn.

- The minimum fluidization velocity is not a function of initial static bed height but dependent on particle size and density of bed materials.
- The bed pressure drop increases with increase in static bed height and density of particles because of more weight of particles. But the pressure drop decreases with increase of particles size because of more void spaces among larger sized particles.
- The bed expansion / fluctuation ratio decrease with increase in static bed height and density of particles because of more weight of particles.
- The bed expansion / fluctuation ratio is observed to decrease with increase in particle size because of more void spaces which causes frequent formation and breakage of bubbles with irregular shapes.
- The fluidization index decreases with increase in particle size, static bed height and particle density because of fluidization index directly proportional to pressure drop.

From the CFD simulations for hydrodynamic studies the following conclusions are made.

- Both the laminar and turbulent models are analyzed for CFD simulation. But, the turbulent model predictions are observed to agree well with the experimental data for the range of conditions investigated.
- Three drag models namely Gidaspow, Wen & Yu and Syamlal - O'Brien are used to predict the solid volume fraction and axial particle velocity profiles. However, the

predictions with the Gidaspow drag model are found to be in better agreement with the experimentally observed values.

- More solid fractions in turn more bed expansions and less bed pressure drops are predicted accurately with Gidaspow model than other two models. Gidaspow drag model is found to yield more stable fluidization with each system parameter than the other two drag models i.e. Syamlal – O'Brien and Wen & Yu.
- The effect of restitution coefficient on the hydrodynamic behaviour of gas–solid flow in a bubbling fluidized bed is also studied. The particle volume fraction, particle velocity, air velocity, granular temperature, bed expansion ratio and bed pressure drops are analyzed for different values of the restitution coefficient with respect to static bed height, superficial air velocity and particle size of bed materials.
- The restitution coefficient is found to have no effect on bed dynamics except on bed pressure drops. However, the restitution coefficient of 0.9 is observed to give more realistic results compared to other values.
- Different specularity coefficients corresponding to free-slip, partial-slip and no-slip conditions are used for checking its impact on the hydrodynamics of fluidized bed. It is found that the simulated predictions with no slip conditions agree reasonably well with the experimental results when tested with different system parameters.
- The CFD simulations are carried out for bed dynamics against different system parameters viz. particle size, static bed heights and air velocities. These simulated and the experimental results on different aspects of bed dynamics are found to be in very good agreement with each other implying proper validations.
- As increase in gas velocity causes a higher heat transfer between gas and solid phases which in turn leads to an increase in solid particle temperature because of more flow of hot gas. Similarly a decrease in average particle size causes a higher heat-transfer

between the gas and solid phase resulting in a higher contact surface which in turn leads to an increase in solid particle temperature. It is also observed that the solid phase temperature increases with increased proportion of Aluminium particle which is because of increased thermal conductivity of more metal particles than Red Mud. This leads to an increase in solid particle temperature.

- The predicted simulation models on the bed dynamics of the fluidized bed reactor with respect to distribution of pressure, temperature and bed expansion / fluctuation are found to be satisfactory.
- The CFD simulated and experimental results agree very well with each other implying that the developed FBR can be used in general for treatment of all types of gaseous pollutants being released to the atmosphere. Therefore it can be said that FBR has very good potential for controlling air pollution thereby providing it to be very much sustainable technology.

6.1 Future Work

- ❖ Other pollutants like NOx, Chloride and organics can be minimized by using FBR.
- ❖ The abatement of Fluoride gas from different industry like phosphatic fertilizer industries, semiconductor manufacturing industries etc can be compared.
- ❖ To study the various reaction kinetics occurring in the FBR leading to a better understanding and control of the reactions.
- ❖ Making the FBR more efficient by studying the various parameters such as residence time, PSD with FBR.
- ❖ To simulate the Reaction model in CFD for fluidized bed reactor.

REFERENCES

- Alary J., Bourbon P., Esclassan J., Lepert J. C., Vandaele J. and Klein F., Fluoride emissions from an electric arc furnace and their abatement using bag filters, Environmental Technology Letters, 3, 503-510, 1982.
- [a]Mansoori Z., Saffar-Avval M., Tabrizi H. B., Ahmadi G. and Lain S., Thermo-mechanical modeling of turbulent heat transfer in gas–solid flows including particle collisions, International Journal of Heat and Fluid Flow, 23, 792–806, 2002.
- Anderson T. B. and Jackson R., Fluid mechanical description of fluidized beds: Equations of motion, Industrial and Engineering Chemistry Fundamentals, 6:4, 527–539, 1967.
- ANSYS FLUENT 12.0. Theory Guide, ANSYS, Inc. 2009.
- Arno I. J., Apparatus and process for the abatement of semiconductor manufacturing effluents containing fluorine gas, Patent number EP1274499 A4, 2004.
- [a]Valverde J. M., Castellanos A., Mills P. and Quintanilla M. A. S., Effect of particle size and interparticle force on the fluidization behavior of gas-fluidized beds, Physical Review, 67, 051305, 2003.
- [a]Van Wachem B.G.M., Schouten J.C., Bleek C.M. V., Krishna R. and Sinclair J.L., Comparative analysis of CFD models of dense gas–solid systems, AIChE Journal, 47 :5, 1035–1051, 2001.
- Avidan A. A. and Yerushalmi J., Bed expansion in high velocity fluidization, Powder Technology, 32, 223-232, 1982.
- [a]Xu C. and Zhu J., Parametric study of fine particle fluidization under mechanical vibration, Powder Technology, 161, 135–144, 2006.
- Behjat Y., Shahhosseini S. and Hashemabadi S. H., CFD modelling of hydrodynamic and heat transfer in fluidized bed reactors, International Communications in Heat and Mass Transfer, 35, 357–368, 2008.

- Benyahia S., Syamlala M. and Brien T. J. O., Evaluation of boundary conditions used to model dilute, turbulent gas/solids flows in a pipe, Powder Technology, 156, 62–72, 2005.
- Benzarti S., Mhiri H. and Bournot H., Drag models for simulation gas-solid flow in the bubbling fluidized bed of FCC particles, World Academy of Science, Engineering and Technology, 6:1, 980-985, 2012.
- [b]Mansoori Z., Saffar-Avval M., Tabrizi H. B. and Ahmadi G., Modeling of heat transfer in turbulent gas-solid flow, International Journal of Heat and Mass Transfer, 45, 1173–1188, 2002.
- Bunner B. and Tryggvason G., Direct numerical simulations of dispersed flows. In: Proceedings of the Ninth Workshop on Two-Phase Flow Predictions, Germany, 13–19, 1999.
- [b]Valverde J. M., Quintanilla M. A. S., Castellanos A. and Mills P., Experimental study on the dynamics of gas-fluidized beds, Physical Review, 67, 016303, 2003.
- [b]Van Wachem B.G.M., Schouten J.C., Bleek C.M. V., Krishna R. and Sinclair J.L., CFD modeling of gas-fluidized beds with a bimodal particle mixture, AIChE Journal, 47:6, 1292–1302, 2001.
- [b]Xu C. and Zhu J. X., Effects of gas type and temperature on the particle fluidization, Particuology, 4:3-4, 114-121, 2006.
- Cady G. H. J., Reaction of fluorine with water and with hydroxides, Journal of the American Chemical Society, 57:1, 246-248, 1935.
- Cai A.M. and Cen K.F., Particle heat transfer in fluidized beds of coarse particles, Journal of Zhejiang University, 19, 82–91, 1985.
- Cardoso C. R., Ataide C. H. and Abreu J. M., Minimum fluidization velocity of fine particle, Material science forum, 591, 335-340, 2008.

- Chaddha M.J., Rai S.B. and Goyal R.N., Characteristics of red mud of Indian Alumina Plants and their possible utilization. National seminar on environmental concern and remedies in Alumina Industry at NALCO, Damanjodi, India, ENVICON 41-44. 2007.
- Cheng Y. and Zhu J., CFD modelling and simulation of hydrodynamics in liquid–solid circulating fluidized beds, Canadian Journal of Chemical Engineering, 83, 177–185, 2005.
- Chiba S., Chiba T., Nienow A.W. and Kobayashi H., The minimum fluidization velocity, bed expansion and pressure drop profile of binary particle mixtures, Powder Technology, 22, 255–269, 1979.
- Chiesa M., Mathiesen V., Melheim J. A. and Halvorsen B., Numerical simulation of particulate flow by the Eulerian–Lagrangian and the Eulerian– Eulerian approach with application to a fluidized bed, Computers & Chemical Engineering, 29, 291–304, 2005.
- Collier A. P., Hayhurst A. N. and Richardson J. L., The heat transfer coefficient between a particle and a bed (packed or fluidized) of much larger particles, Chemical Engineering Science, 59, 4613–4620, 2004.
- Cooper S. and Coronella C. J., CFD simulations of particle mixing in a binary fluidized bed, Powder Technology, 151, 27–36, 2005.
- Cornelissen J. T., Taghipour F., Escudie R., Ellis N. and Grace J. R., CFD modelling of a liquid–solid fluidized bed, Chemical Engineering Science, 62, 6334–6348, 2007.
- Coroneo M., Mazzei L., Lettieri P., Paglianti A. and Monante G., CFD prediction of segregating fluidized bidisperse mixtures of particles differing in size and density in gas–solid fluidized beds, Chemical Engineering Science, 66, 2317-2327, 2011.

- Cranfield R. R. and Geldart D., Large particle fluidisation, Chemical Engineering Science, 29:4, 935-947, 1974.
- Cui H. and Chaouki J., Effects of temperature on local two-phase flow structure in bubbling and turbulent fluidized beds of FCC particles, Chemical Engineering Science, 59, 3413-3422, 2004.
- Cui H., Sauriol P. and Chaouki J., High temperature fluidized bed reactor: measurements, hydrodynamics and simulation, Chemical Engineering Science, 58, 1071-1077, 2003.
- Delvosalle C. and Vanderschuren J., Gas–particle and particle–particle heat transfer in fluidized beds of large particles, Chemical Engineering Science, 40, 769–779, 1985.
- Dimas D. D., Ioanna P. and Panias D., Utilization of alumina red mud for synthesis of inorganic polymeric materials, Mineral processing and Extractive Metallurgy Review: An International Journal, 30:3, 211-239, 2009.
- Ding J. and Gidaspow D. A., A bubbling fluidization model using kinetic theory of granular flow, AIChE Journal, 36:4, 523–538, 1990.
- Du W., Bai X., Xu J. and Wei W., Computation fluid dynamics (CFD) modelling of spouted bed: influence of friction stress, maximum packing limit and coefficient of restitution of particles, Chemical Engineering Science, 61, 4558–4570, 2006.
- Enwald H., Peirano E. and Almstedt A. E., Eulerian two-phase flow theory applied to fluidization, International Journal of Multiphase Flow, 22, 21–66, Supplement, 1996.
- Fan L.S., Gas-Liquid-Solid Fluidization Engineering, Butterworth Series in Chemical Engineering, Butterworth Publishers, Boston, MA, 1989.
- Fan R., CFD Simulation of Polydisperse Fluidized-Bed Polymerization Reactors, Department of Chemical Engineering, Retrospective Theses and Dissertations, Iowa State University, 2006.

- Formisani B., Cristofaro G. D. and Girimonte R., A fundamental approach to the phenomenology of fluidization of size segregating binary mixtures of solids, Chemical Engineering Science, 56, 109–119, 2001.
- Formisani B., Girimonte R. and Mancuso L., Analysis of the fluidization process of particle beds at high temperature, Chemical Engineering Science, 53, 951-961, 1998.
- Formisani B., Girimonte R. and Pataro G., The influence of operating temperature on the dense phase properties of bubbling fluidized beds of solids, Powder Technology, 125, 28-38, 2002.
- Garcia-Ochoa F., Romero A., Villa J. C. and Bello A., A study of segregation in a gas–solid fluidized bed: particles of different density, Powder Technology, 58, 169–174, 1989.
- Geldart D. and Kapoor D. S., Bubble Sizes in a Fluidized Bed at Elevated Temperatures, Chemical Engineering Science, 31, 842-843, 1976.
- Gera D., Gautam M., Tsuji Y., Kawaguchi T. and Tanaka T., Computer simulation of bubbles in large-particle fluidized beds, Powder Technology, 98, 38-47, 1998.
- Gidaspow D. and Lu H., A comparison of gas–solid and liquid–solid fluidization using kinetic theory and statistical mechanics, In: L. S. Fan, T. M. Knowlton, (Eds.), Fluidization IX, Engineering Foundation, New York, 661–668, 1998.
- Gidaspow D., Bezburuah R. and Ding J., Hydrodynamics of circulating fluidized beds, kinetic theory approach, In: Proc. 7th Engineering Foundation Conference on Fluidization, Brisbane, Australia, COLL-75, 1992.
- Gobin A., Neau H., Simonin O., Llinas J., Reiling V. and Selo J. L., Fluid dynamic numerical simulation of a gas phase polymerization reactor, International Journal for Numerical Methods in Fluids, 43, 1199–1220, 2003.

- Goldschmidt M. J. V., Kuipersand J. A. M. and Swaaij W. P. M., Hydrodynamic modeling of dense gas-fluidized beds using the kinetic theory of granular flow: effect of coefficient of restitution on bed dynamics, Chemical Engineering Science, 56, 571-578, 2001.
- Goldschmidt M.J.V., Beetstra R. and Kuipers J.A.M., Hydrodynamic modeling of dense gas-fluidized beds: comparison and validation of 3D discrete particle and continuum models, Powder Technology, 142, 23–47, 2004.
- Grace J. R. and Taghipour F., Verification and validation of CFD models and dynamic similarity for fluidized beds, Powder Technology, 139, 99–110, 2004.
- Gunn D. J. and Hilal N., The expansion of gas-fluidised beds in bubbling fluidisation, Chemical Engineering Science, 52:16, 2811-2822, 1997.
- Guo O., Yue G., Suda T. and Sato J., Flow characteristics in a bubbling fluidized bed at elevated temperature, Chemical Engineering and Processing, 42, 439-447, 2003.
- Gupta C. and Sathiyamoorthy D., Fluid bed technology in materials processing, Boca Raton, FL, CRC Press, 1999.
- Hajela R. B., Gupta R. G. and Goel R. K., Disposal of solid wastes—red mud and fly-ash in the production of heavy clay products, International Journal of Environmental Studies. 33:1-2,125-132, 1989.
- Hamzehei M., Rahimzadeh H. and Ahmadi G., Studies of gas velocity and particles size effects on fluidized bed hydrodynamics with CFD modeling and experimental investigation, Journal of Mechanics, 26:3, 267-278, 2010.
- Hatate Y., Ohmagari K., Ikari A., Kondo K. and King D.F., Behavior of bubbles in cylindrical fluidized bed at an elevated temperature, Journal of Chemical Engineering of Japan, 21, 424-425, 1988.

- He J. and Simonin O., Non-equilibrium prediction of particle-phase stress tensor in vertical pneumatic conveying, gas–solid flows. ASME FED, 166, 253–263, 1993.
- Hilal N., Ghannam M. T. and Anabtawi M. Z., Effect of bed diameter, distributor and inserts on minimum fluidization velocity, Chemical Engineering and Technology, 24:2, 161-165, 2001.
- Hoffmann A.C., Janssen L.P.B.M. and Prins J., Particle segregation in fluidized binary mixtures, Chemical Engineering Science, 48, 1583–1592, 1993.
- Holmes J. T., Koppel L. B. and Jonke A. A., Fluidized Bed Disposal of Fluorine, I & EC Process Design and Development, 6: 4, 408-413, 1967.
- Hosseini S. H., Zhong W., Esfahany M. N., Pourjafar L. and Azizi S., CFD simulation of the bubbling and slugging gas-solid fluidized beds, Journal of Fluids Engineering, 132, 041301: 1-10, 2010.
- Hsiung T. H.-L. and Withers H.P., Destroying fluorine and / or chlorine trifluoride by reaction with iron, nickel, copper, calcium, magnesium, manganese, cobalt and/or tin metal particles; fluorination, salt formation, US. Patent No. 6352676, 1999.
- Huang X., CFD modeling of liquid–solid fluidization: Effect of drag correlation and added mass force, Particuology, 9, 441– 445, 2011.
- Huilin L., Wentie L., Feng L., Guangbo Z., Huilin H.L., Wentie L., Feng L., Guangbo Z. and Yurong H., Eulerian simulations of bubble behavior in a two-dimensional gas–solid bubbling fluidized bed, International Journal of Energy Research, 26, 1285–1293, 2002.
- Huilin L., Yunhua Z., Ding J., Gidaspow D. and L., Investigation of mixing / segregation of mixture particles in gas–solid fluidized beds, Chemical Engineering Science, 62, 301-317, 2007.

- Huilin L., Yurong H. and Gidaspow D., Hydrodynamic modeling of binary mixture in a gas bubbling fluidized bed using the kinetic theory of granular flow, Chemical Engineering Science, 58, 1197–1205, 2003.
- Hulme I., Clavelle E., Lee L. V. and Kantzas A., CFD modeling and validation of bubble properties for a bubbling fluidized bed, Industrial & Engineering Chemistry Research, 44, 4254-4266, 2005.
- Iwata K. and Hatakeyama T., Process for cleaning Harmful Gases, US. Patent No. 5417948, 1995.
- Jaraiz E., Kimura S. and Levenspiel O., Vibrating beds of fine particles: estimation of inter particle forces from expansion and pressure drop experiments, Powder Technology, 72, 23-30, 1992.
- Jia Z., Fang L., Hailing L., Wenjing W., Xiuqiong L. and Liyun M., Fluorinated wastewater abatement method and clean production in crystalline silicon photovoltaic manufacturing, 978-1-4799-3299-3/13/$31.00 ©2013 IEEE.
- John D. and Anderson J., Computational Fluid Dynamics, McGraw-Hill, Inc, 1995.
- Joseph G.G., Leboreiro J., Hrenya C.M. and Stevens A. R., Experimental segregation profiles in bubbling gas-fluidized beds, AIChE Journal, 53, 2804–2813, 2007.
- Kai T. and Furusaki S., Behavior of fluidized beds of small particles at elevated temperatures, Journal of Chemical Engineering of Japan, 18, 113-118, 1985.
- Kaneko Y., Shiojima T. and M. Horio, DEM simulation of fluidized beds for gas-phase olefin polymerization, Chemical Engineering Science, 54, 5809–5821, 1999.
- Kumar A. and Roy G. K., Bed dynamics of gas-solid fluidized bed with rod promoter, China Particulogy, 5, 261-266, 2007.

- Kumar A., Eskridge K., Jones D. D. and Hanna M. A., Steam–Air fluidized bed gasification of distillers grains: effects of steam to biomass ratio, equivalence ratio and gasification temperature, Bio resource Technology, 100, 2062–2068, 2009.
- Kunii D. and Levenspiel O., Fluidization Engineering, Second ed. Butterworth-Heinemann, Boston, 1991.
- Kusakabe K., Kuriyama T. and Morooka S., Fluidization of fine particles at reduced pressure, Powder Technology, 58, 125 – 130, 1989.
- Lan X., Xu C., Gao J. and Al-Dahhan M., Influence of solid-phase wall boundary condition on CFD simulation of spouted beds, Chemical Engineering Science, 69, 419–430, 2012.
- Laszuk A., Pabisand M. and Berengarten G., Fluidization of fine materials, Chemical and Petroleum Engineering, 44:9–10, 494-498, 2008.
- Lettieri P., Felice R. Di, Pacciani R. and Owoyemi O., CFD modelling of liquid fluidized beds in slugging mode, Powder Technology, 167, 94–103, 2006.
- Lettieri P., Newton D. and Yates J. G., High temperature effects on the dense phase properties of gas fluidized beds, Powder Technology, 120, 34-40, 2001.
- Lettieri P., Saccone G. and Cammarata L., Predicting the transition from bubbling to slugging fluidization using computational fluid dynamics, Chemical Engineering Research and Design, 82, 939–944, 2004.
- Lettieri P., Yates J. G. and Newton D., The influence of interparticle forces on fluidization behavior of some industrial materials at high temperature, Powder Technology, 110, 117-127, 2000.
- Li J. and Kuipers J.A.M., Effect of competition between particle–particle and gas–particle interactions on flow patterns in dense gas-fluidized beds, Chemical Engineering Science, 62, 3429–3442, 2007.

- Li T., Grace J. and Bi X., Study of wall boundary condition in numerical simulations of bubbling fluidized beds, Powder Technology, 203, 447–457, 2010.
- Lun C. K. K., Savage S. B., Jeffrey D. J. and Chepurniy N., Kinetic theories for granular flow: inelastic particle in Couette flow and slightly inelastic particles in a general flow field, Journal of Fluid Mechanics, 140, 223–256, 1984.
- Marzocchella A., Salatino P., Pastena V. D. and Lirer L., Transient fluidization and segregation of binary mixture of particles, AIChE Journal, 46, 2175–2182, 2000.
- Mawatari Y., Tsunekawa M., Tatemoto Y. and Noda K., Favorable vibrated fluidization conditions for cohesive fine particles, Powder Technology, 154, 54–60, 2005.
- Mckeen T. and Pugsley T., Simulation and experimental validation of a freely bubbling bed of FCC catalyst, Powder Technology, 129, 139–152, 2003.
- Mckenna T. F., Spitz R. and Cokljat D., Heat transfer from catalysts with computational fluid dynamics, AIChE Journal, 45, 2392–2410, 1999.
- Mihálykó C.S., Lakatos B.G., Matejdesz A. and Blickle T., Population balance model for particle–particle heat transfer in gas–solid systems, International Journal of Heat and Mass Transfer, 47, 1325–1334, 2004.
- Neri A. and Gidaspow D., Riser hydrodynamics: simulation using kinetic theory. AIChE Journal, 46, 52–67, 2000.
- Netzer W. D., Fluorine Disposal Processes for Nuclear Applications, Goodyear Atomic Corporation, 1977.
- Noda K., Uchida S., Makinno T. and Kamo H., Minimum fluidization velocity of binary mixture of particles with large size ratio, Powder Technology, 46, 149–154, 1986.

- Olivieri G., Marzocchella A. and Salatino P., Segregation of fluidized binary mixtures of granular solids, AIChE Journal, 50, 3095–3106, 2004.
- Page J.-F. L., Chatila S. G. and Davidson M., Resid and Heavy Oil Processing, IFP, Editions Technip, Paris, 1992.
- Pain C. C., Mansoorzadeh S. and Oliveira C. R. E., A study of bubbling and slugging fluidised beds using the two-fluid granular temperature model, International Journal for Multiphase Flow, 27, 527-551, 2001.
- Pan Y., Dudukovic M. P. and Chang M., Dynamic simulation of bubbly flow in bubble columns. Chemical Engineering Science, 54, 2481–2489, 1999.
- Pan Y., Dudukovic M. P. and Chang M., Numerical investigation of gas-driven flow in 2-D bubble columns. AIChE Journal, 46:3, 434 – 449, 2000.
- Patankar S.V., Numerical heat transfer and fluid flow, 1st edition, Hemisphere Washington, 1980.
- Qiu X. R. and Qi Y. Y., The reasonable utilization of red mud in cement production, Cement Technology, 6,103–105, 2011.
- Radmanesh R., Mabrouk R., Chaouki J. and Guy C., The effect of temperature on solids mixing in a bubbling fluidized bed reactor, International Journal of Chemical Reactor Engineering, 3, A16, 1-14, 2005.
- Rafique M., Chen P. and Dudukovic M. P., Computational modeling of gas-liquid flow in bubble columns. Reviews in Chemical Engineering, 20, 225–375, 2004.
- Ramos G., García Ruiz M., Prieto Marqués J. J. and Guardiola Soler J., Minimum fluidization velocities for gas-solid 2D beds, Chemical Engineering and Processing, 41:9, 761-764, 2002.
- Ranade V. V., Computational flow modeling for chemical reactor engineering, First Edition, Academic Press, New York, 2002.

- Rasul M. G., Rudolph V. and Carsky M., Segregation potential in binary gas fluidized beds, Powder Technology, 103, 175–181, 1999.
- Reddy N. G. and Chandra K. S., Characterization and comprehensive utilization of Red mud - an overview, International Journal for Scientific Research & Development, 2:1, 2014.
- Rhodes M. J., Wang X. S., Nguyen M., Stewart P. and Liffman K., Use of discrete element method simulation in studying fluidization characteristics: influence of interparticle force, Chemical Engineering Science, 56, 69-76, 2001.
- Rowe P. N. and Nienow A.W., Particle mixing and segregation in gas fluidized beds. A review, Powder Technology, 15, 141-147, 1976.
- Roy S. and Dudukovic M.P., Flow mapping and modelling of liquid–solid risers, Industrial & Engineering Chemistry Research, 40, 5440–5454, 2001.
- Russo P., Chirone R., Massimilla L. and Russo S., The influence of the frequency of acoustic waves on sound-assisted fluidization of beds of fine particles, Powder Technology, 82, 219-230,1995.
- Sahoo A., Bed expansion and fluctuation in cylindrical gas-solid fluidized beds with stirred promoters, Advanced Powder Technology Journal, 22,753-760, 2011.
- Sau D. C., Mohanty S. and Biswal K. C., Experimental studies and empirical models for the prediction of bed expansion in gas–solid tapered fluidized beds, Chemical Engineering and Processing: Process Intensification, 49, 418–424, 2010.
- Sau D. C., Mohanty S. and Biswal K. C., Minimum fluidization velocities and maximum bed pressure drops for gas-solid tapered fluidized beds. Chemical Engineering Journal, 132: 1-3, 151-157, 2007.

- Sau D.C. and Biswal K.C., Computational fluid dynamics and experimental study of the hydrodynamics of a gas–solid tapered fluidized bed, Applied Mathematical Modelling, 35, 2265-2278, 2011.
- Schaeffer D. G., Instability in the evolution equations describing incompressible granular flow, Journal of Differential Equations, 66, 19-50, 1987.
- Sglavo V. M., Campostrini R., Maurina S., Carturan G., Monagheddu M., Budroni G. and Cocco G., Bauxite 'red mud' in the ceramic industry Part 1: thermal behaviour, Journal of the European Ceramic Society, 20: 3, 235–244, 2000.
- Shah Y.T., Gas-liquid-solid reactor design. McGraw-Hill, New York, 1979.
- Shaul S., Rabinovich E. and Kalman H., Generalized flow regime diagram of fluidized beds on the height to bed diameter ratio, Powder Technology, 228, 264 – 271, 2012.
- Singh R. K. and Roy G. K., Prediction of fluctuation ratio for gas–solid fluidization in cylindrical and non-cylindrical beds, Indian journal of chemical technology, 13,139-143, 2006.
- Singh R. K. and Roy G. K., Prediction of minimum bubbling velocity, fluidization index and range of particulate fluidization for gas–solid fluidization in cylindrical and non-cylindrical beds, Powder Technology, 159, 168–172, 2005.
- Sokolichin A., Eigenberger G. and Lapin A., Simulation of buoyancy driven bubbly flow: established simplifications and open questions, AIChE Journal, 50, 24–45, 2004.
- Subramani H. J., Balaiyya M. B. M. and Miranda L. R., Minimum fluidization velocity at elevated temperature for Geldart's group-B powders, Experimental Thermal and Fluid Science, 32, 166-173, 2007.

- Syamlal M. and O'Brien T. J., Computer simulation of bubbles in a fluidized bed, AIChE Symposium Series, 85:270, 22 – 31, 1989.
- Syamlal M., The particle-particle drag term in a multi particle model of fluidization, National Technical Information Service, Springfield, VA, 1987.
- Taghipour F., Ellis N. and Wong C., Experimental and computational study of gas–solid fluidized bed hydrodynamics, Chemical Engineering Science, 60, 6857–6867, 2005.
- Tagliaferri C., Mazzei L., Lettieri P., Marzocchella A., Olivieri G. and Salatino P., CFD simulation of bubbling fluidized bidisperse mixtures: Effect of integration methods and restitution coefficient, Chemical Engineering Science, 102, 324–334, 2013.
- Tonnis E., Vartanian V., Beu L., Lii T., Jewett R., Daniels J. and Graves D., Evaluation of a Litmas "Blue" Plasma Abatement Device for Perflurocompound (PFC) Destruction, UC-Berkeley; SEMATECH Technology Transfer # 98123605A-ENG. Austin, TX: SEMATECH., 1998 .
- Tonnis E., Vartanian V., Graves D., Jewett R., Wofford B., Bevan J., Hartz C., Gunn M., Beu L. and Lii T., Plasma Abatement Reduces PFC Emission, Semiconductor International, 2000.
- Valverde J. M., Espin M. J., Quintanilla M.A.S. and Castellanos A., Magneto fluidization of fine magnetite powder, Physical Review, 79, 031306, 2009.
- Van Wachem B. G. M., Schouterf J. C., Krishnab R. and Bleek C. M. V., Eulerian simulations of bubbling behaviour in gas-solid fluidized beds, Computers Chemical Engineering, 22, 299–306, 1998.

- Visuri O., Wierink G. A., Alopaeus V., Investigation of drag models in CFD modeling and comparison to experiments of liquid–solid fluidized systems, International Journal of Mineral Processing, 104 -105, 58 – 70, 2012.
- Wang Z., Kwauk M. and Li H., Fluidization of fine particles, Chemical Engineering Science, 53:3, 377-395, 1998.
- Wen C. Y. and Chang T. M., Particle–particle heat transfer in air fluidized beds, Proceedings of International Symposium on Fluidization, 1967.
- Wen C.Y. and Yu Y. H., Mechanics of fluidization, Chemical Engineering Progress Symposium Series, 62, 100–111, 1966.
- Wild G. and Poncin S., Chapter 1: Hydrodynamics, In: Three-phase sparged reactors, Nigam K. D. P. and Schumpe A., Gordon and Breach Publishers, Amsterdam, The Netherlands, 1996.
- Wu S.Y. and Baeyens J., Segregation by size difference in gas fluidized beds, Powder Technology, 98, 139–150, 1998.
- Xing G. and Jiao Z. Z., The development of non-autoclaved brick made of red mud and fly ash, Rare Metals Cemented Carbides, 6,154–177, 1993.
- Yang J. K., Zhang D. D. and Xiao B., Study on glass-ceramics mostly made from red mud and fly ash, Glass & Enamel. 32, 9–11, 2004.
- Yang N., Wang W., Ge W. and Li J., CFD simulation of concurrent-up gas–solid flow in circulating fluidized beds with structure-dependent drag coefficient, Chemical Engineering Journal, 96, 71-80, 2003.
- Yang W., Handbook of fluidization and fluid particle systems, New York, Marcel Dekker Inc., 2003.

- Zhang H., Zhu J. X. and Bergougnou M. A., Hydrodynamics in down flow fluidized beds (1): solids concentration profiles and pressure gradient distributions, Chemical Engineering Science, 54, 5461-5470, 1999.
- Zhiping Z., Yongjie N. and Qinggang L., Effect of pressure on minimum fluidization velocity, Journal of thermal science, 16:3, 264—269, 2007.
- Zhou D., Dong S., Wang H. and Bi H. T., Minimum fluidization velocity of a three-phase conical fluidized bed in comparison to a cylindrical fluidized bed, Industrial & Engineering Chemistry Research, 48, 27-36, 2008.
- Zimmermann S. and Taghipour F., CFD modeling of hydrodynamics and reaction kinetics of FCC fluidized bed reactors, Industrial & Engineering Chemistry Research, 44, 9818 –9827, 2005.

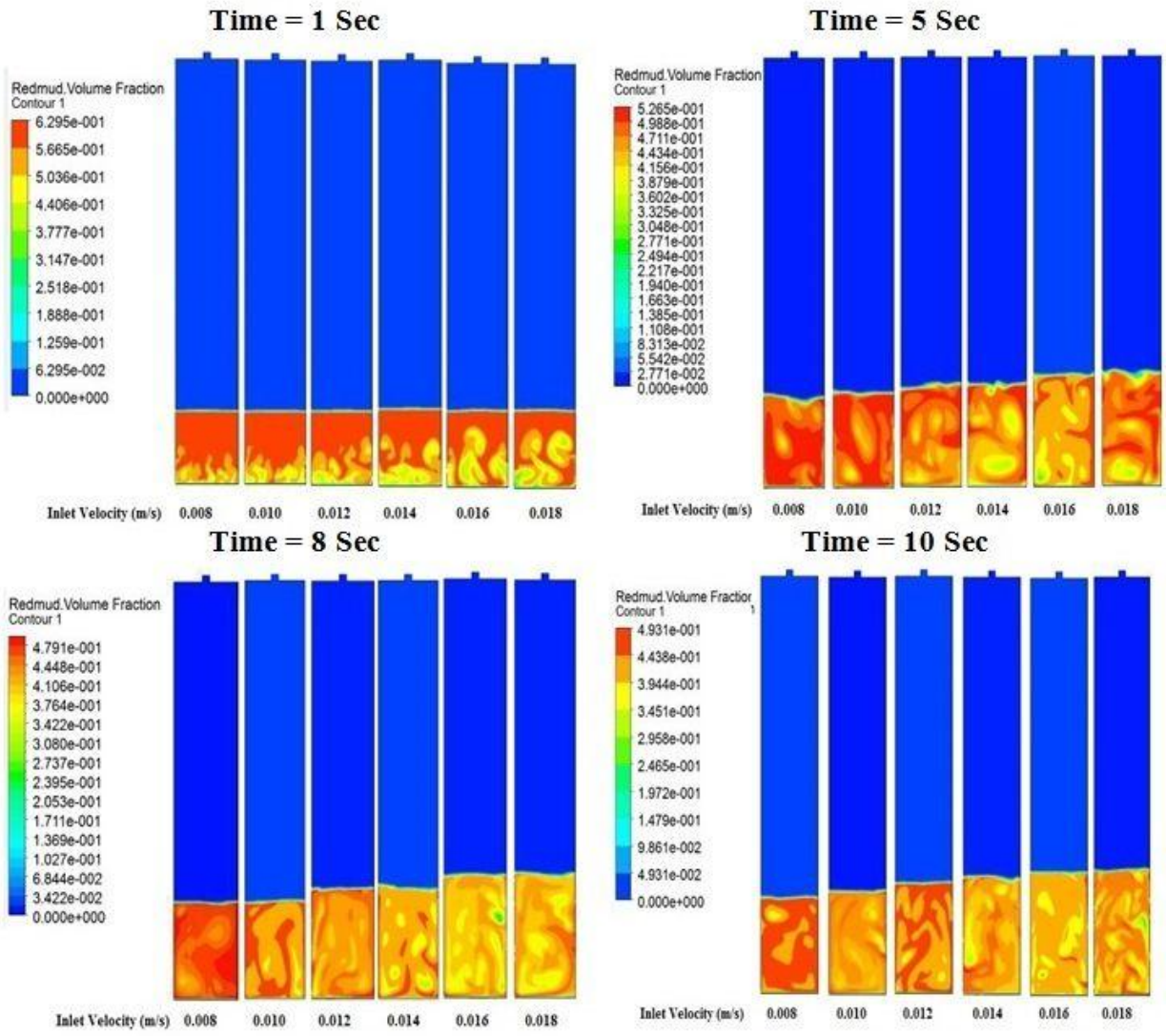

Fig.- A.1: Solid volume fractions against inlet gas velocities at different simulation times

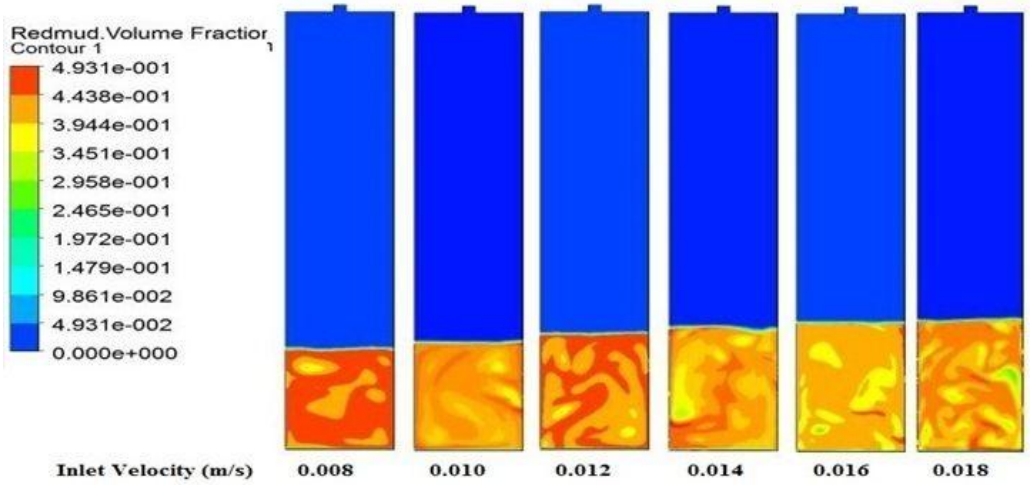

Fig. – A.2: Solid volume fraction for different gas inlet velocities

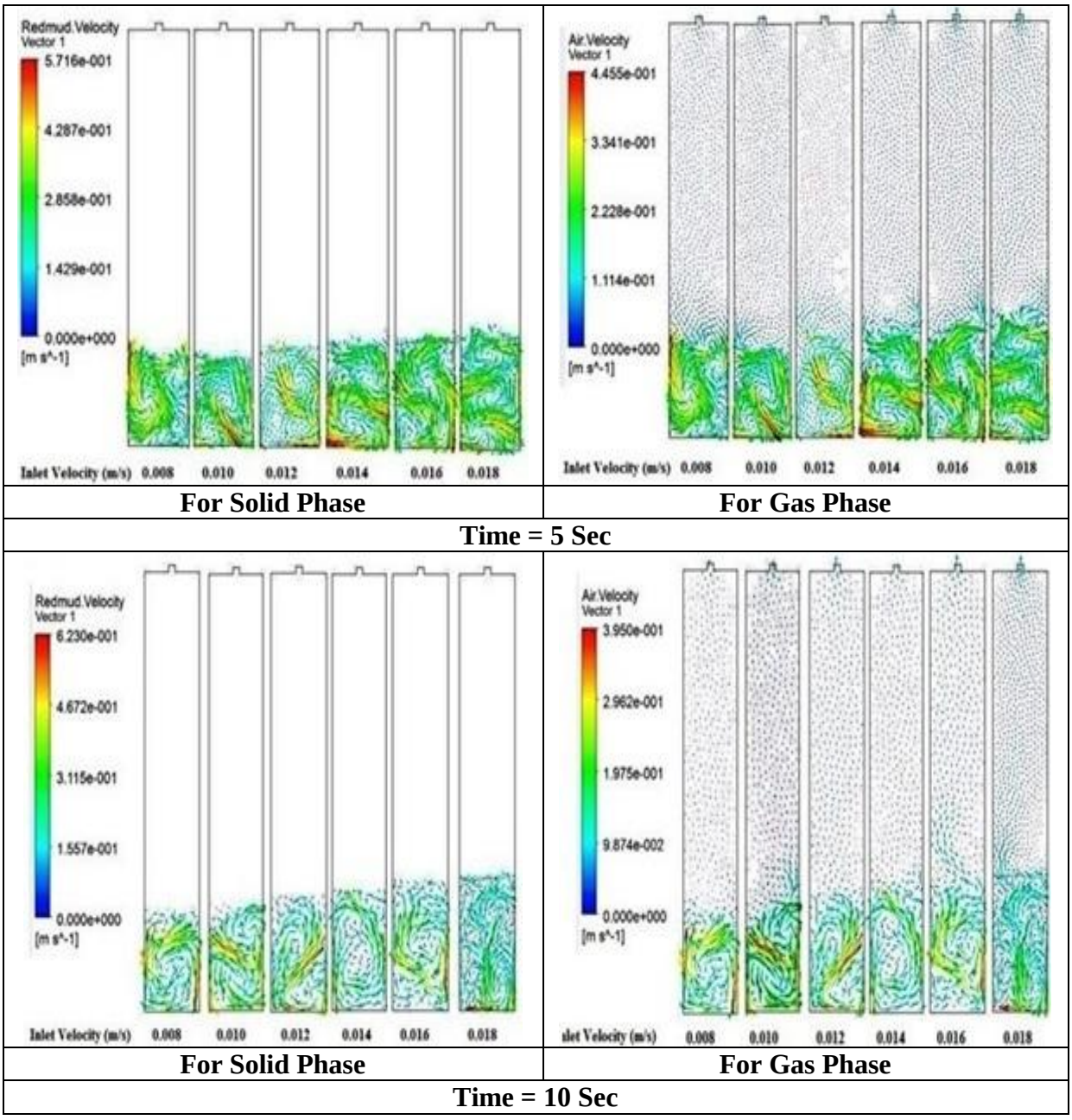

Fig. – A.3: Comparison of velocity vectors with different simulation times

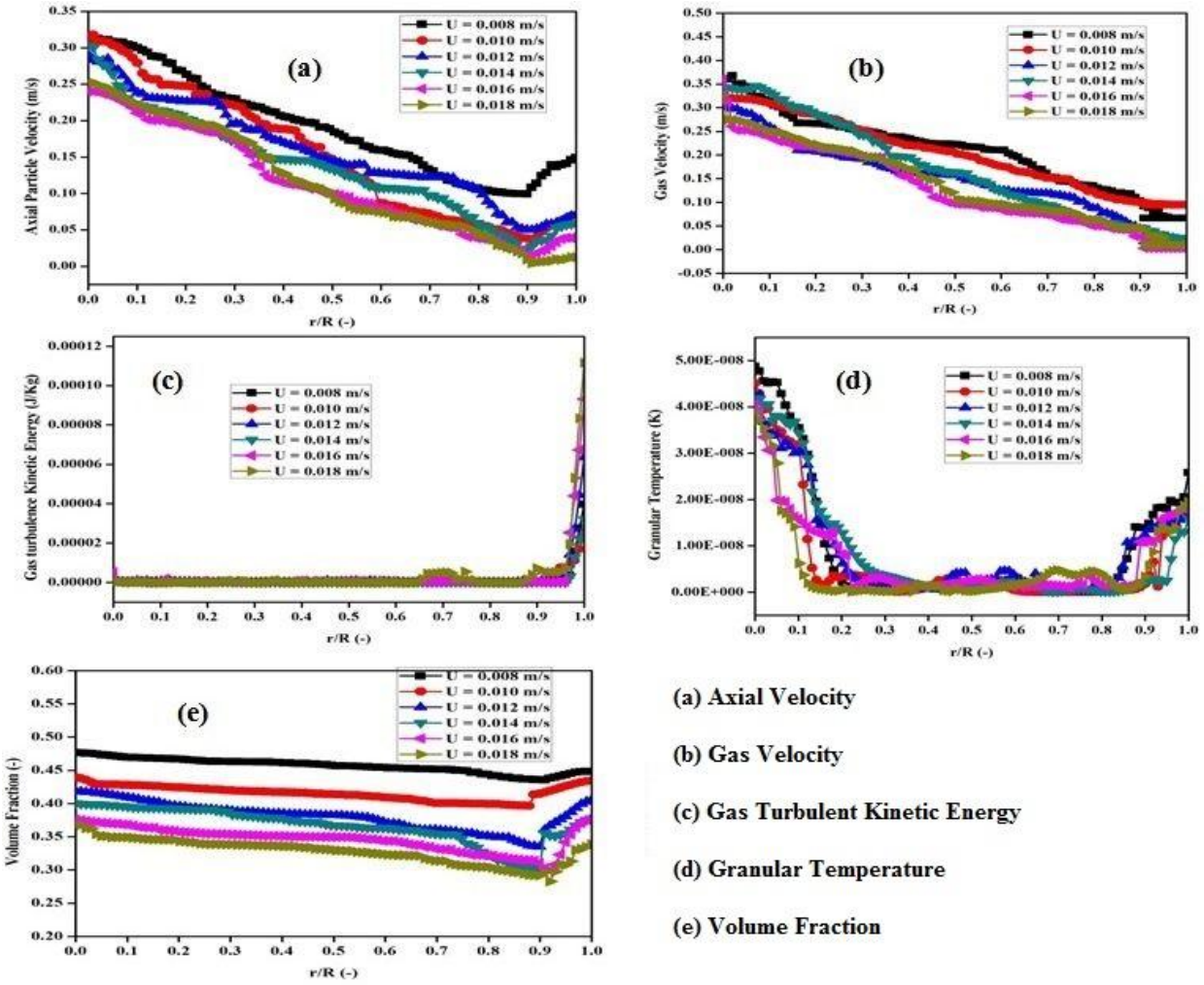

Fig. – A.4: Radial profiles for different gas inlet velocities

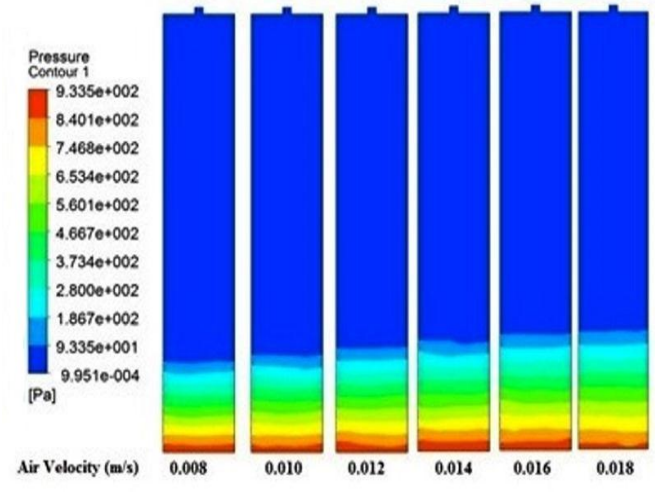

Fig.- A.5 (a): Contour of bed pressure drop against air velocity

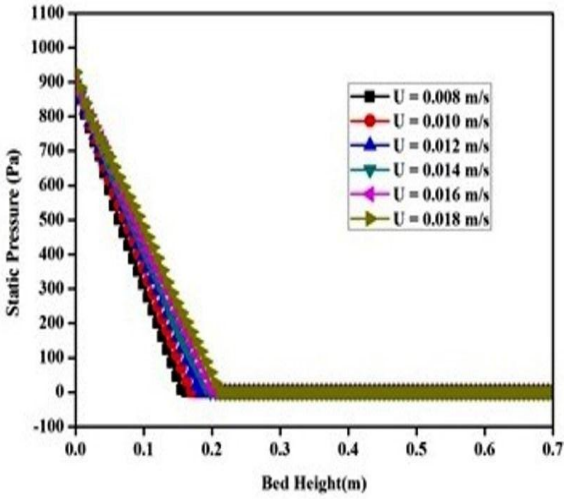

Fig. – A.5 (b): Variation in static pressure along the bed height

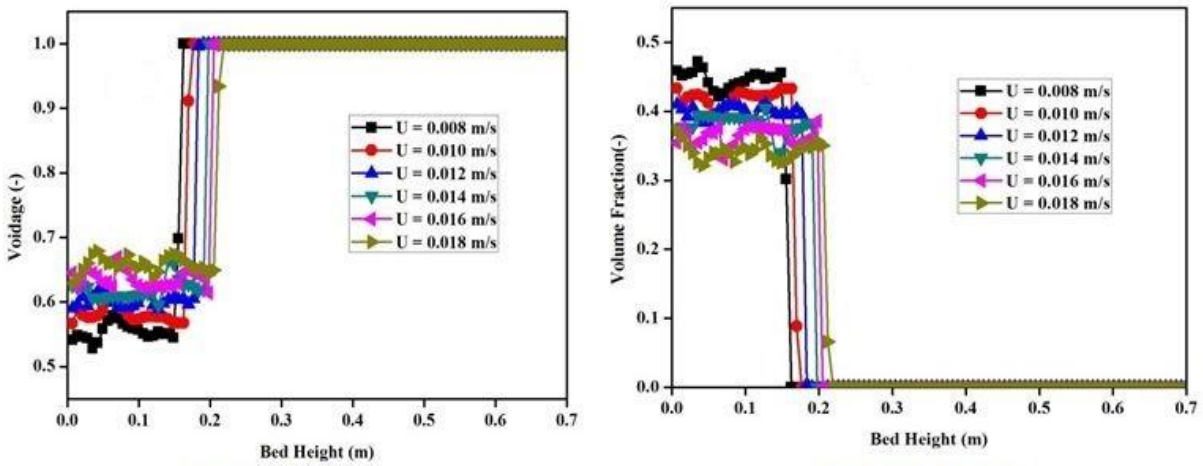

(a) Gas Phase (b) Solid Phase

Fig.- A.6: Comparison of volume fractions for different velocities

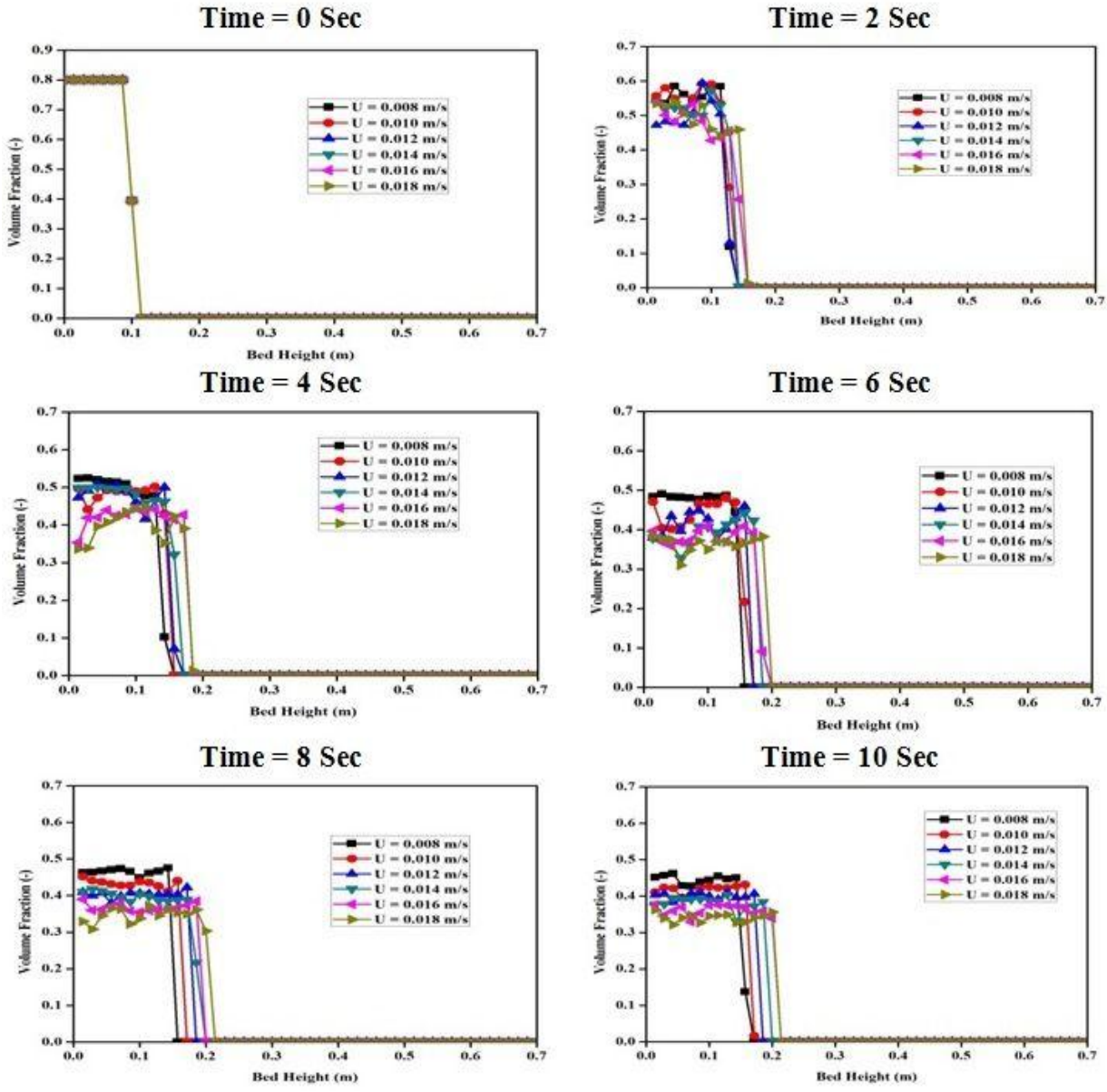

Fig. – A.7: Distributions of volume fraction with variation of time

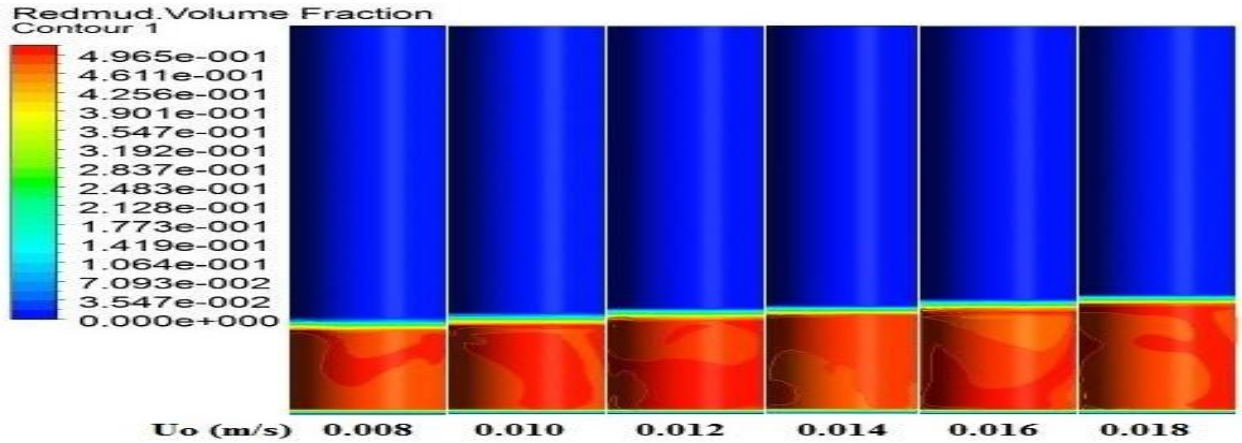

Fig. – A.8: 3D simulated solid volume fraction against gas inlet velocities

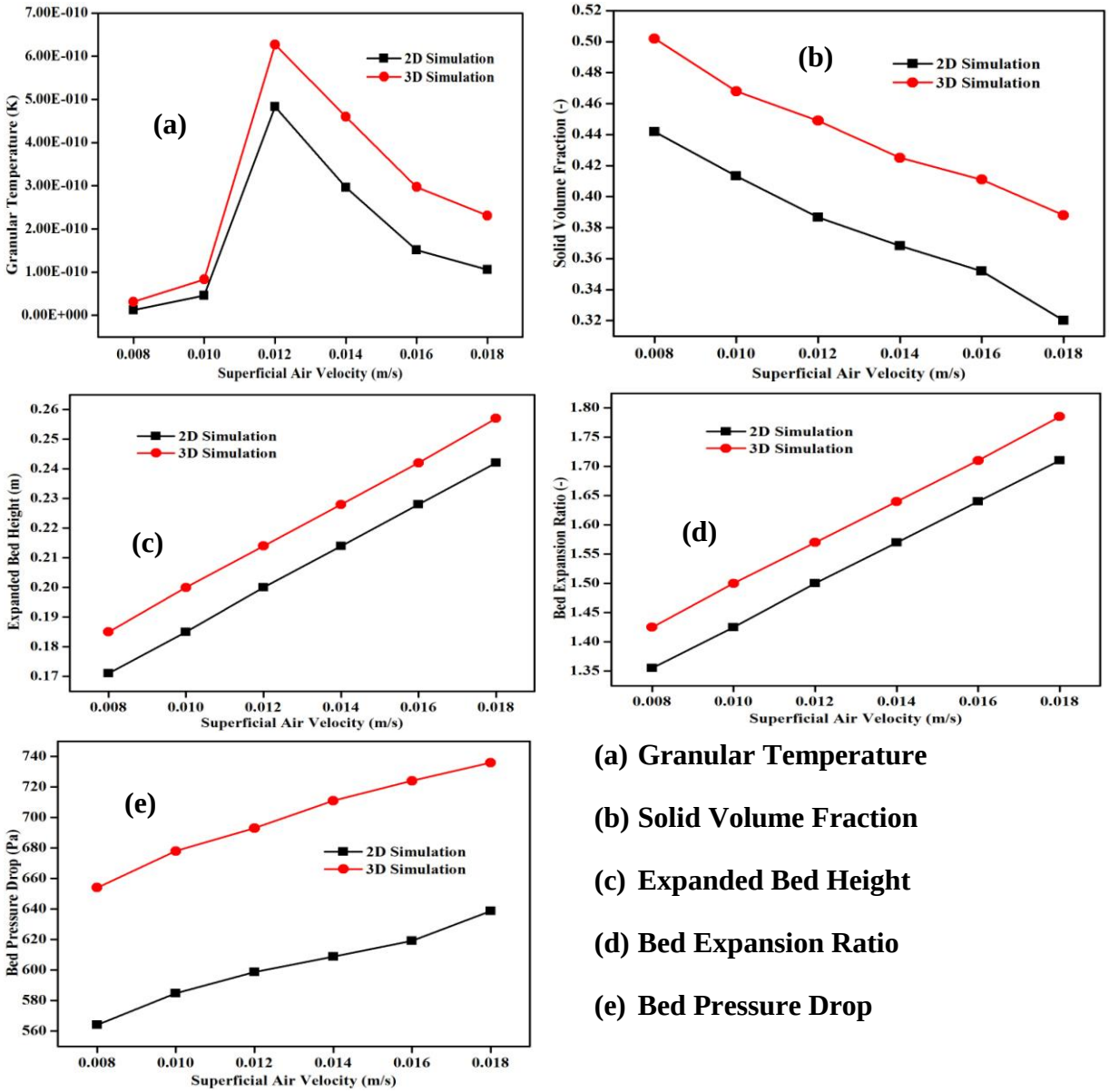

(a) Granular Temperature

(b) Solid Volume Fraction

(c) Expanded Bed Height

(d) Bed Expansion Ratio

(e) Bed Pressure Drop

Fig. – A.9: Comparisons of 2D and 3D simulated bed dynamics against velocities

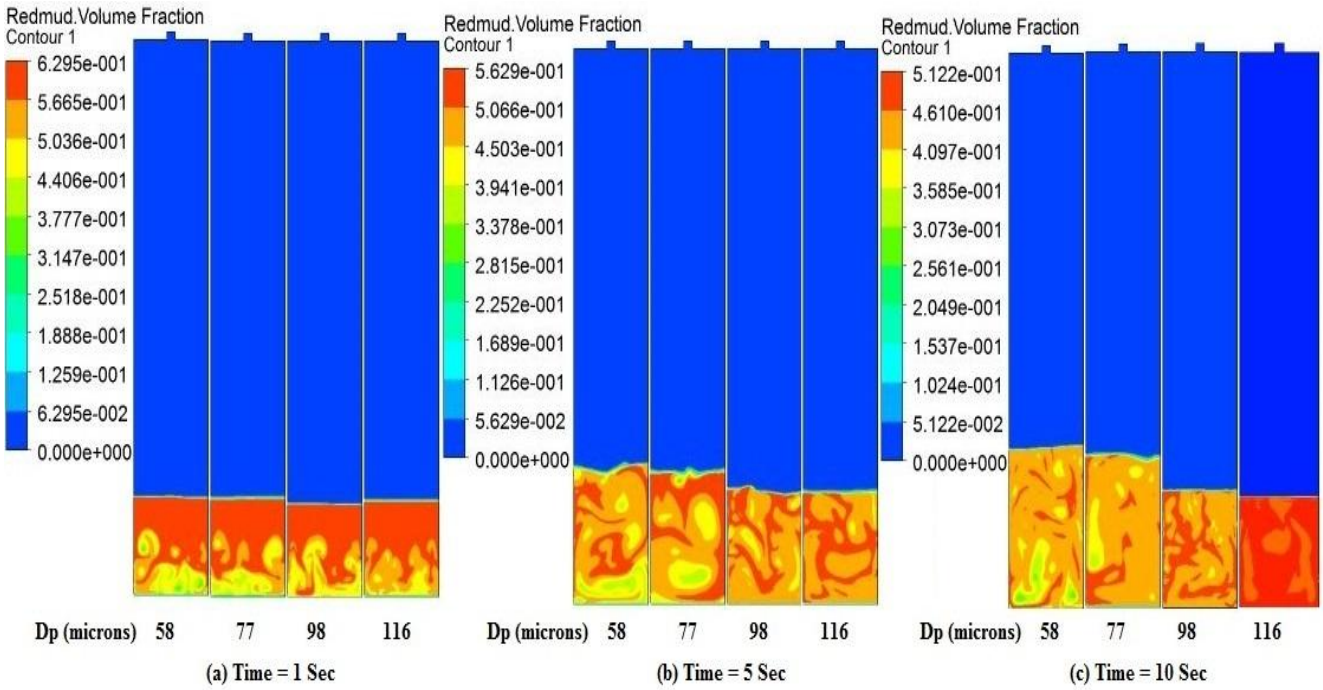

Fig. –B.1: Comparison of solid volume fraction for different particle sizes

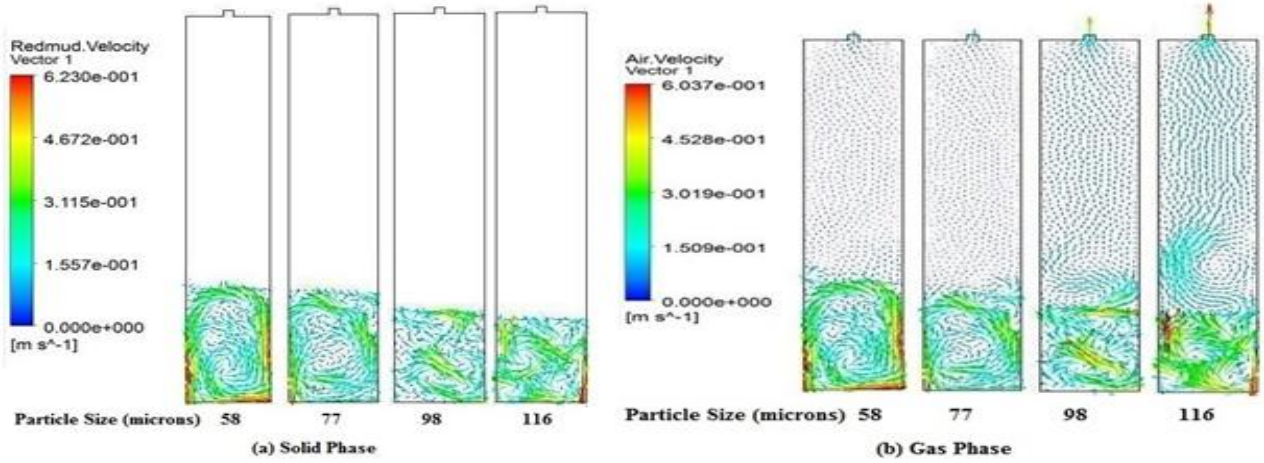

Fig. –B.2: Velocity vector plots for different phases of different particle sizes

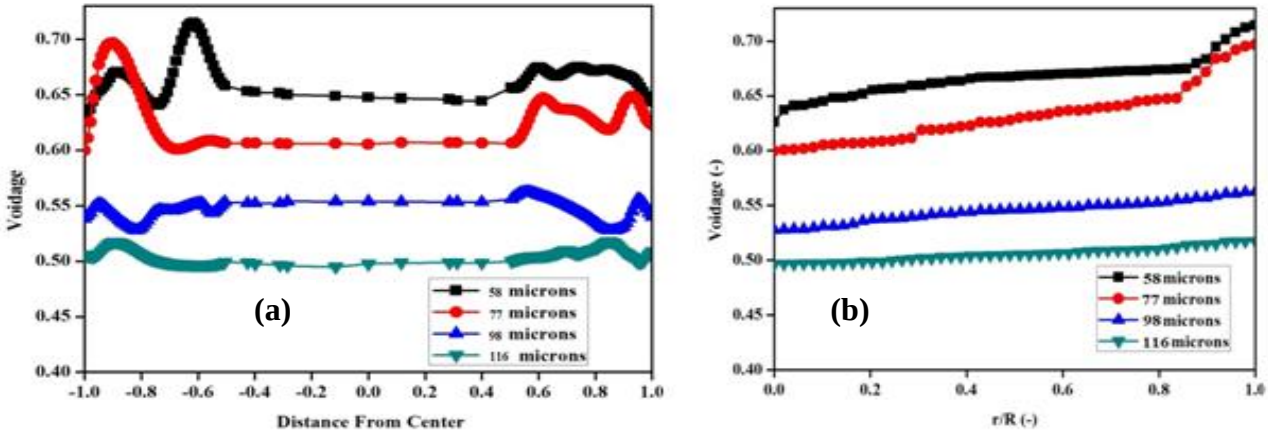

Fig. – B.3: Radial variation of void fractions for different particle sizes

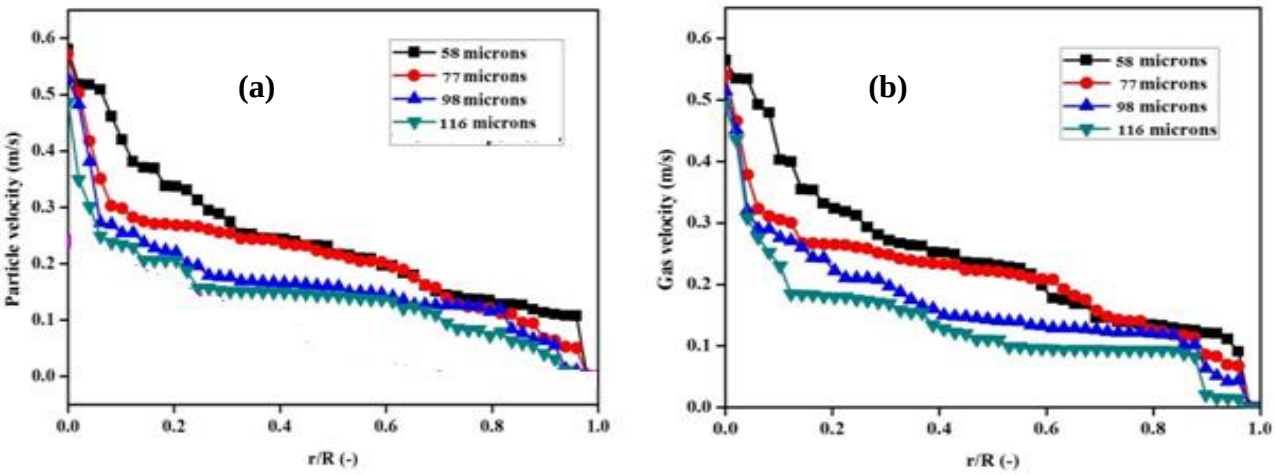

Fig. –B.4: Radially simulated particle and gas velocity distributions

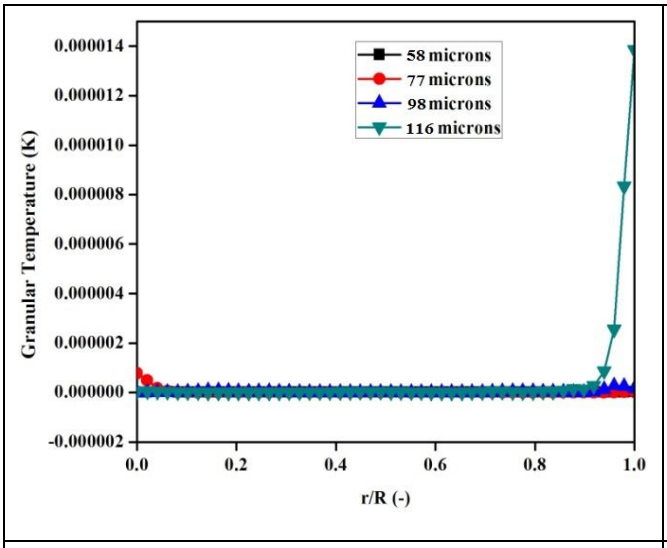

Fig. – B.5: Radial distribution of granular temperature

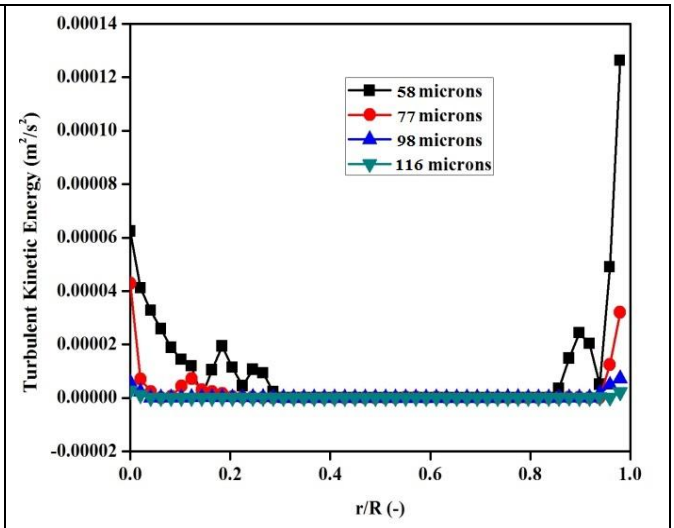

Fig. – B.6: Radial distribution of turbulent kinetic energy

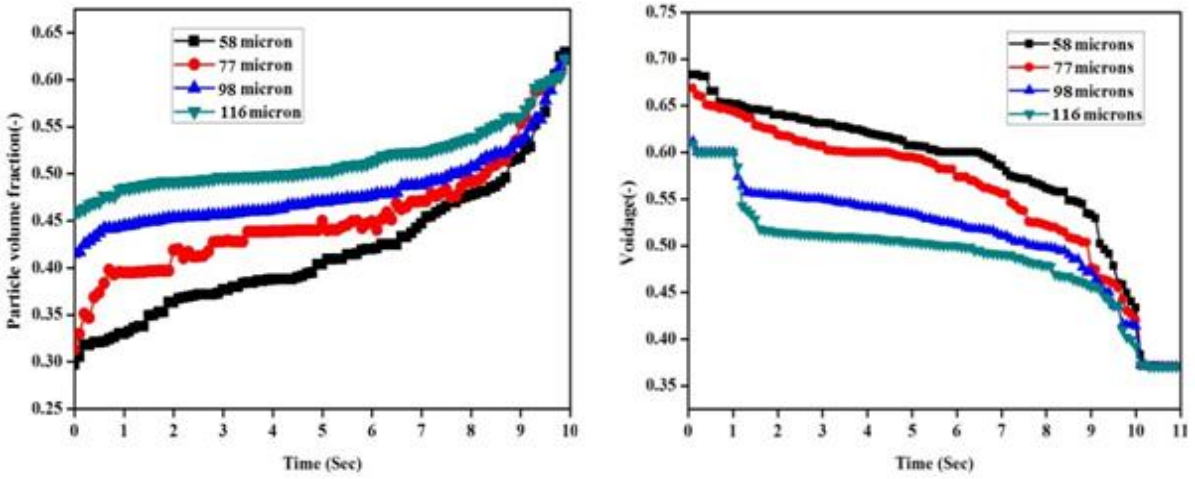

(a) For Solid Phase **(b) For Gas Phase**

Fig. – B.7: Effect of simulation time on volume fractions

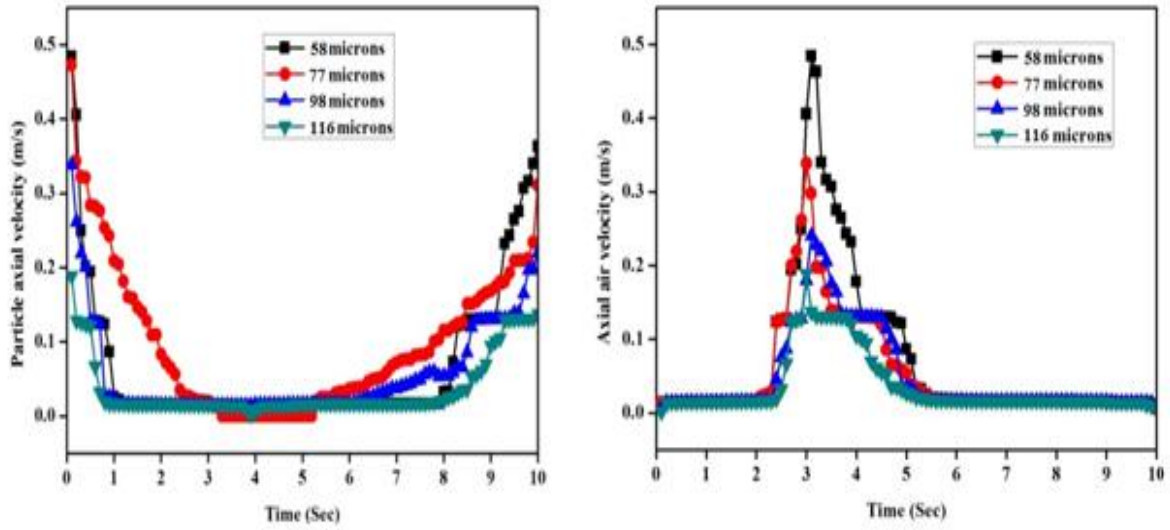

(a) For Solid Phase **(b) For Gas Phase**

Fig. – B.8: Effect of simulation time on axial velocity

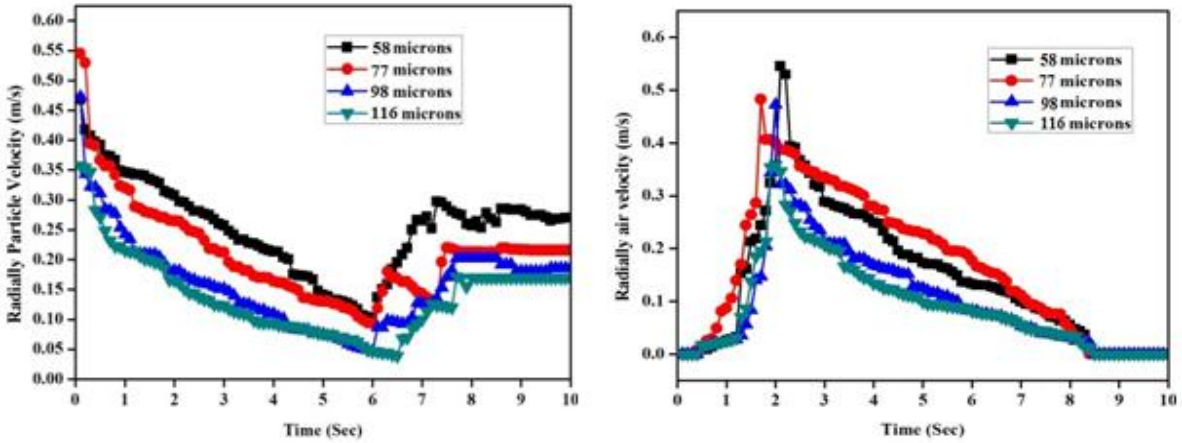

(a) For Solid Phase **(b) For Gas Phase**

Fig. – B.9: Effect of simulation time on radial velocity

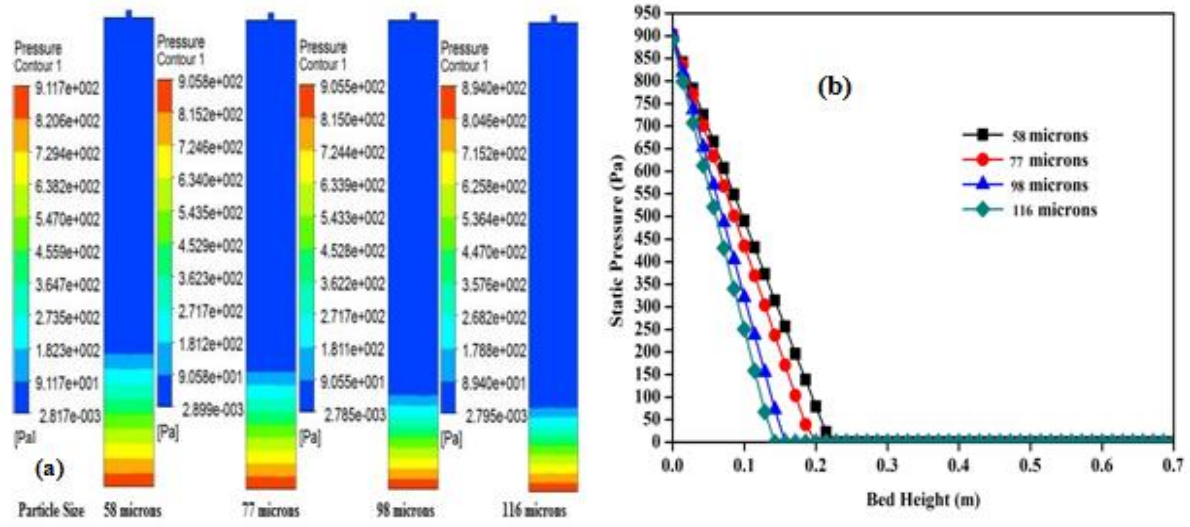

(a) Against of Particle Sizes **(b) Against of Bed Height**

Fig. – B.10: Contours plots of static pressures

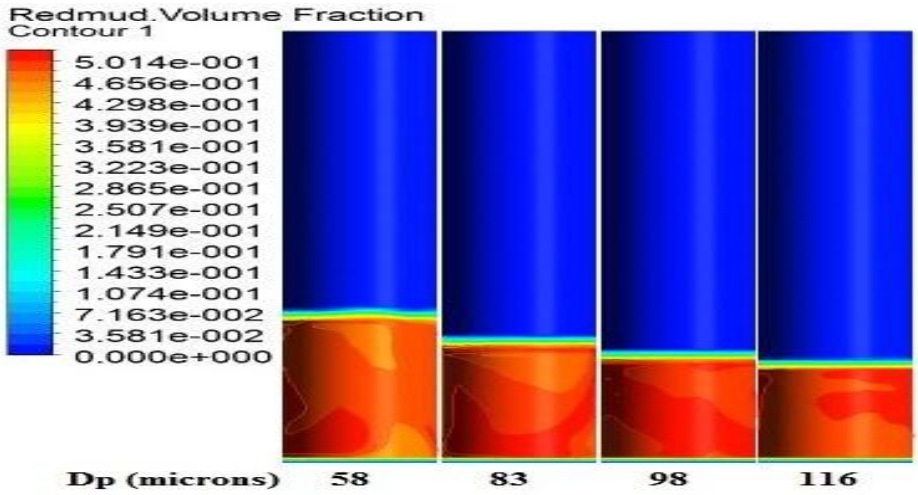

Fig. –B.11: 3D simulated contours of solid volume fractions for different particle sizes

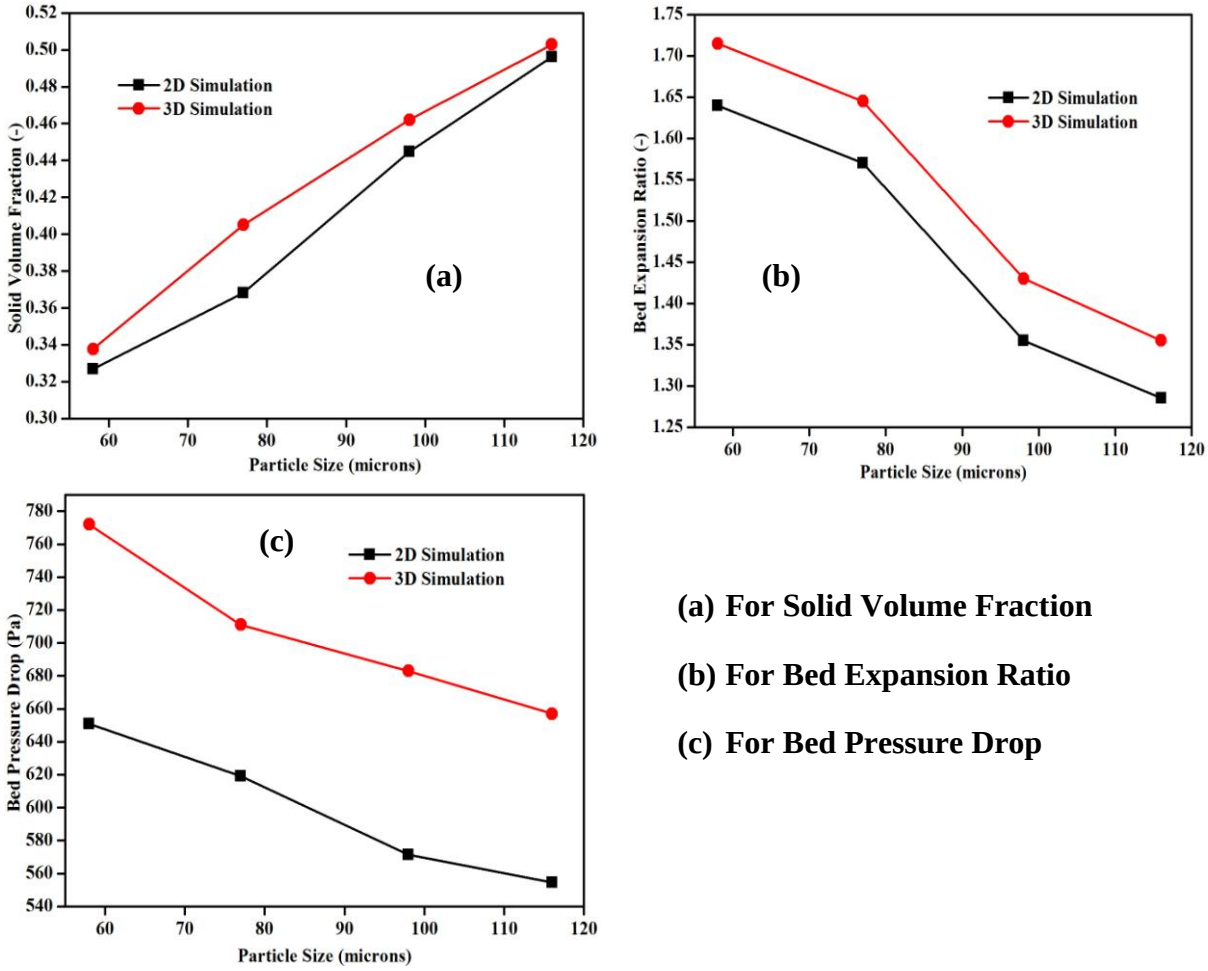

(a) For Solid Volume Fraction

(b) For Bed Expansion Ratio

(c) For Bed Pressure Drop

Fig. – B.12: Comparison between 2D and 3D simulated for bed dynamics against particle sizes

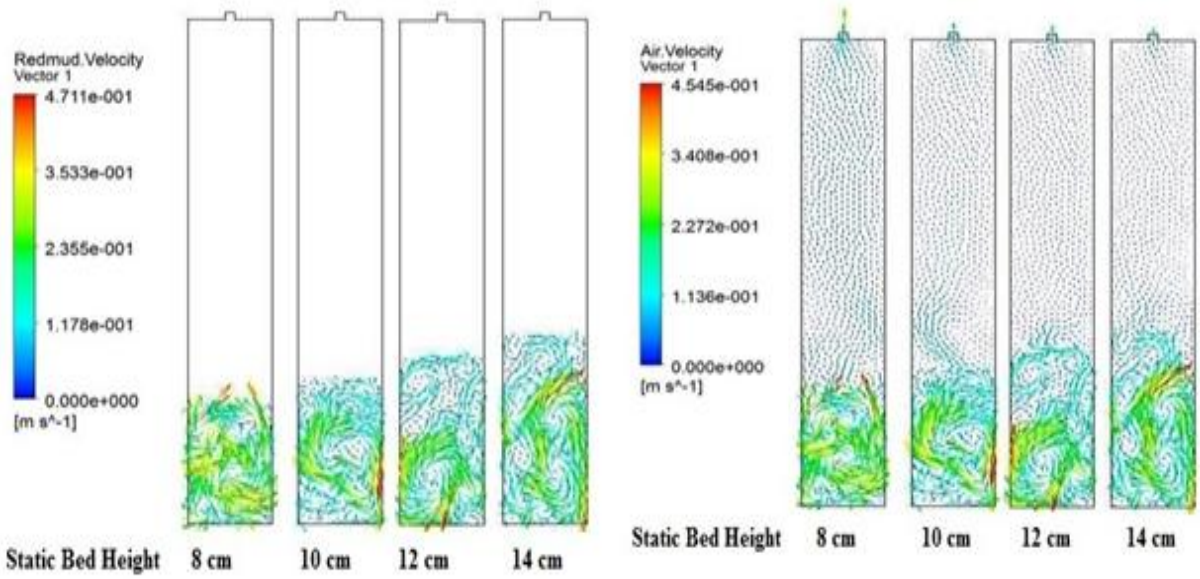

(a) Solid Phase **(b) Gas Phase**

Fig. – C.1: Velocity vector plots for different static bed heights

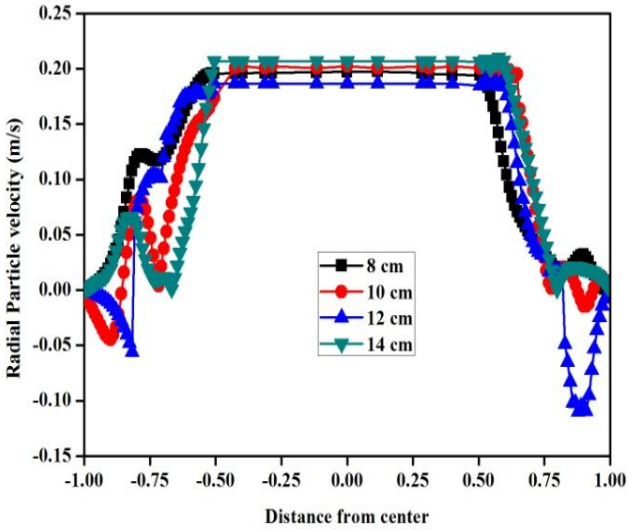

Fig. – C.2: Radial profile of particle velocity for different static bed heights

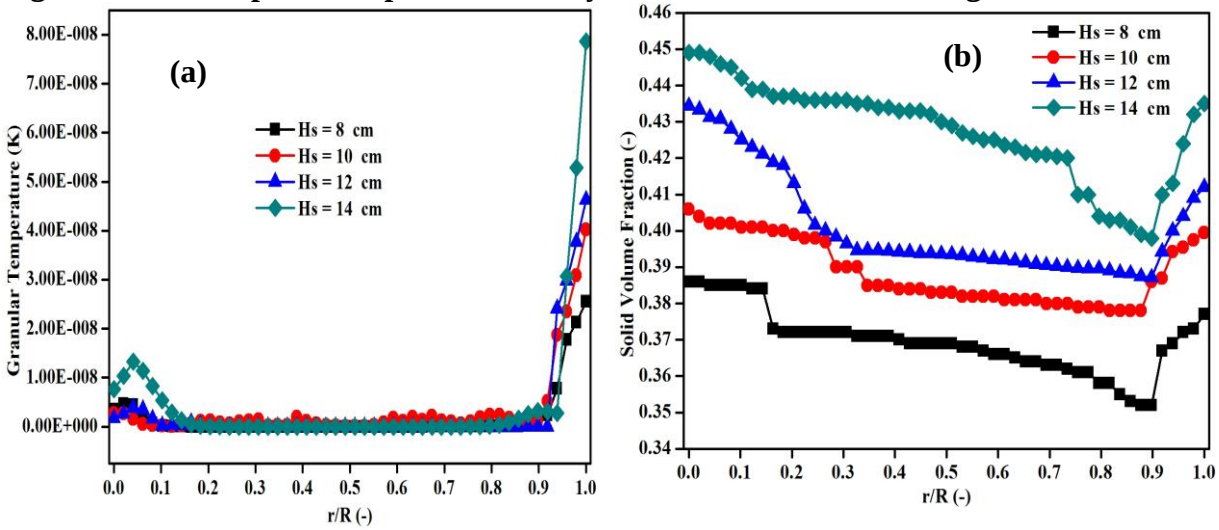

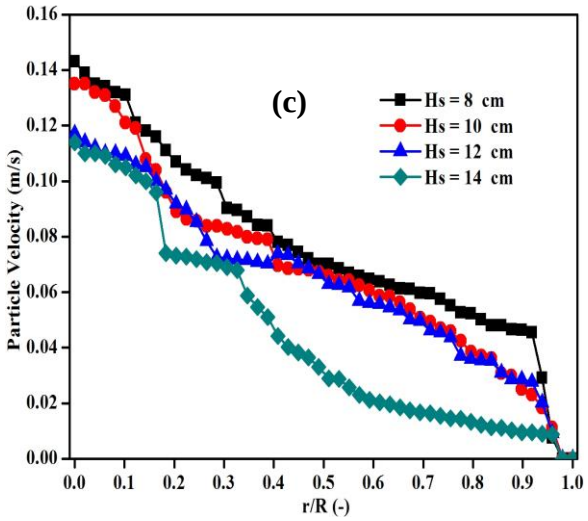

(a) For Granular Temperature Distributions

(b) For Particle Volume Fraction Distributions

(c) For Particle Velocity Distributions

Fig. – C.3: Radially simulated profiles for bed hydrodynamics

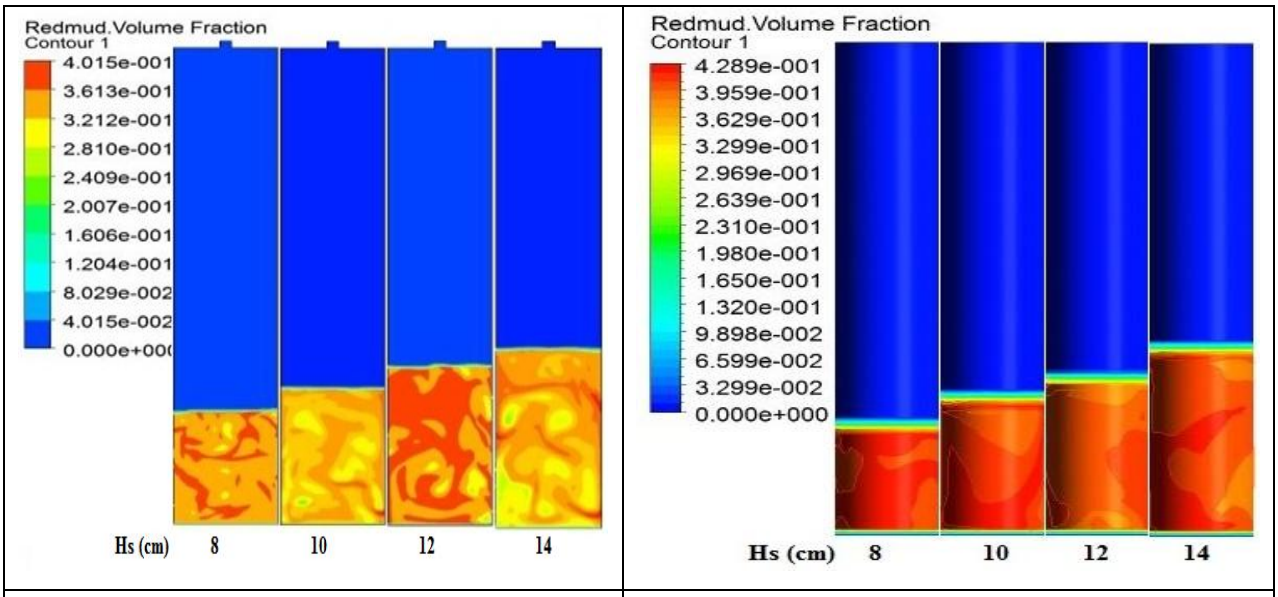

(a) 2D Simulation | **(b) 3D Simulation**

Fig. – C.4: Contours of solid volume fraction for different static bed heights

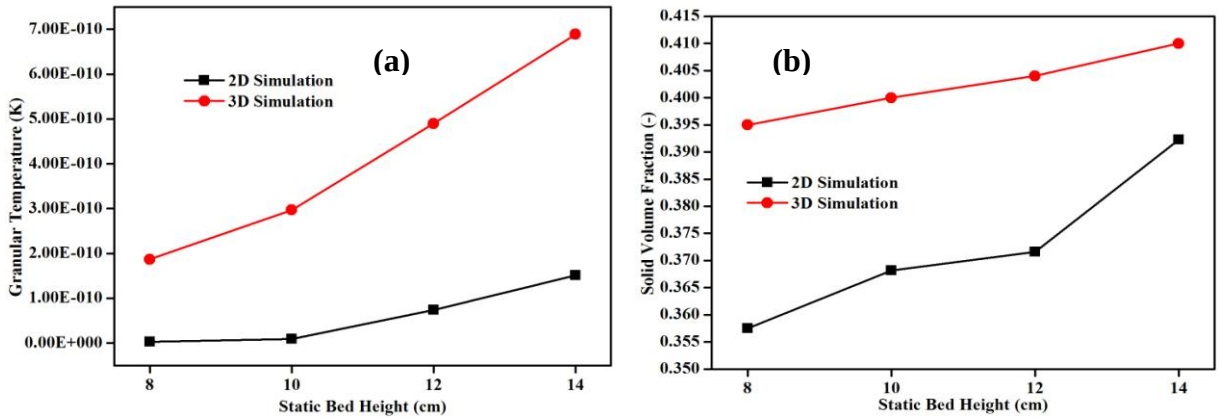

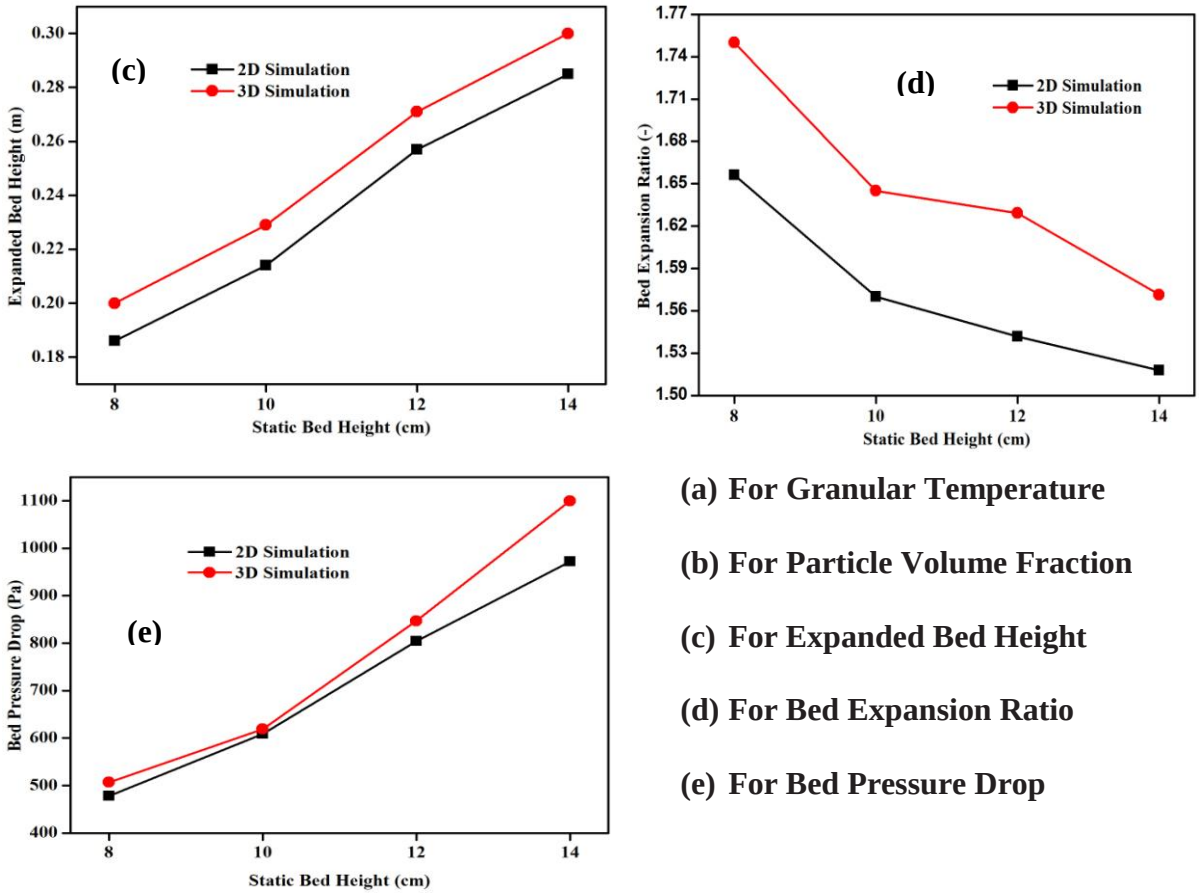

(a) For Granular Temperature

(b) For Particle Volume Fraction

(c) For Expanded Bed Height

(d) For Bed Expansion Ratio

(e) For Bed Pressure Drop

Fig. – C.5: Comparison between 2D and 3D simulated results for bed dynamics

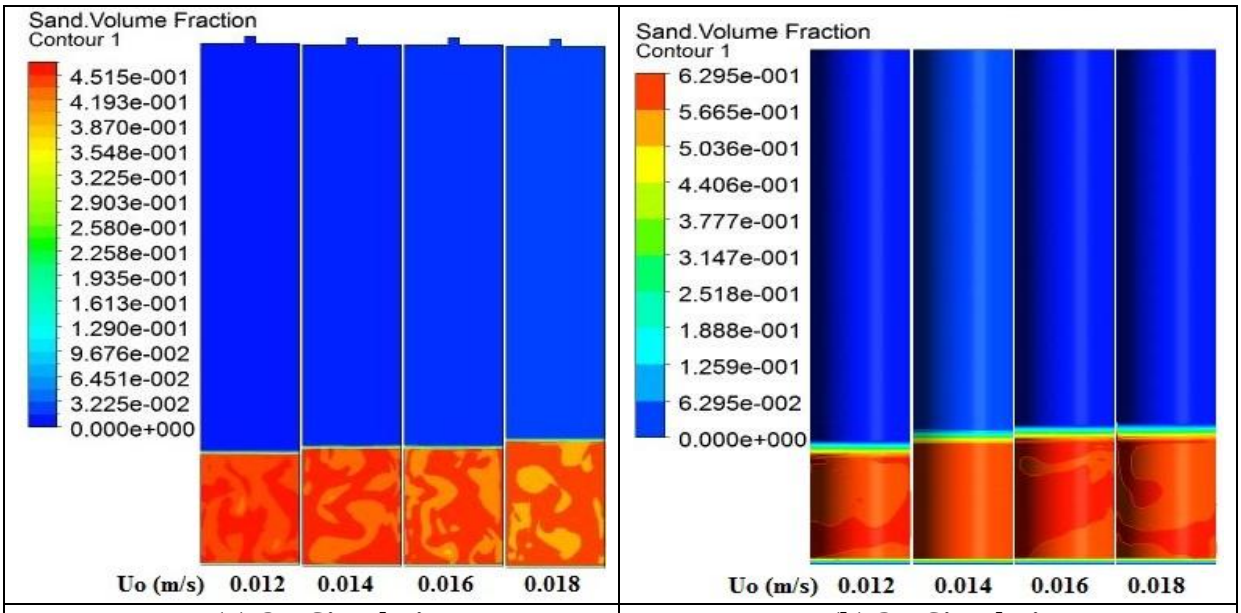

(a) 2D Simulation | **(b) 3D Simulation**

Fig. – D.1 (a): Contour plot of solid volume fraction for Sand particles

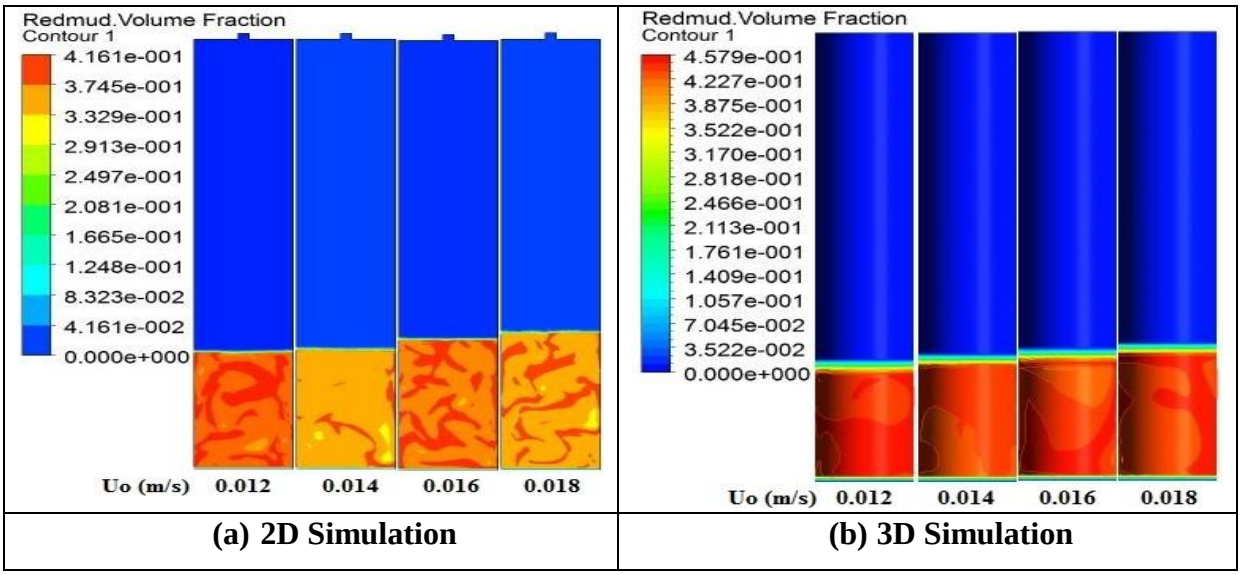

(a) 2D Simulation **(b) 3D Simulation**

Fig. – D.1 (b): Contour plot of solid volume fraction for Aluminium particles

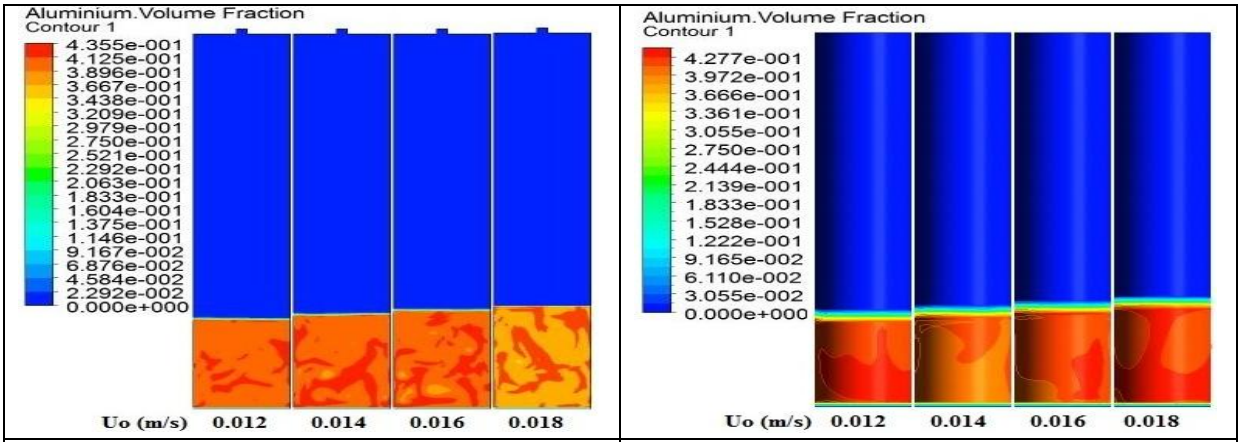

(a) 2D Simulation **(b) 3D Simulation**

Fig. – D.1 (c): Contour plot of solid volume fraction for Red Mud particles

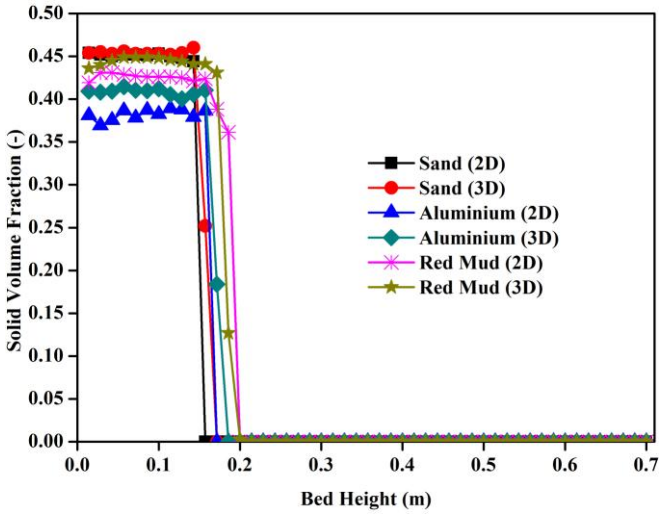

Uo = 0.012 m/s

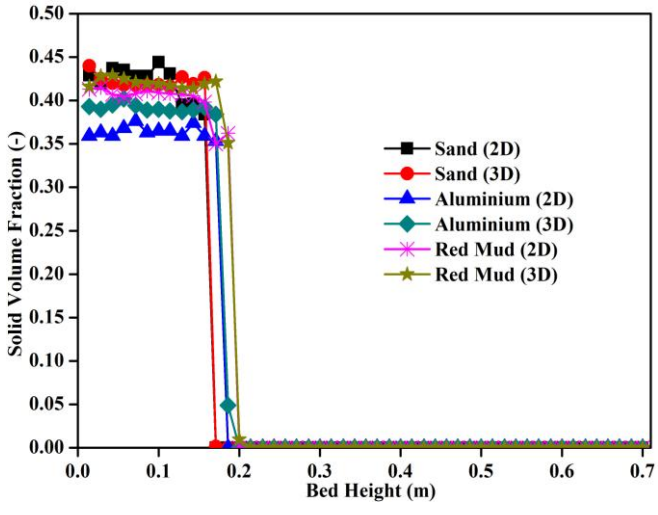

Uo = 0.014 m/s

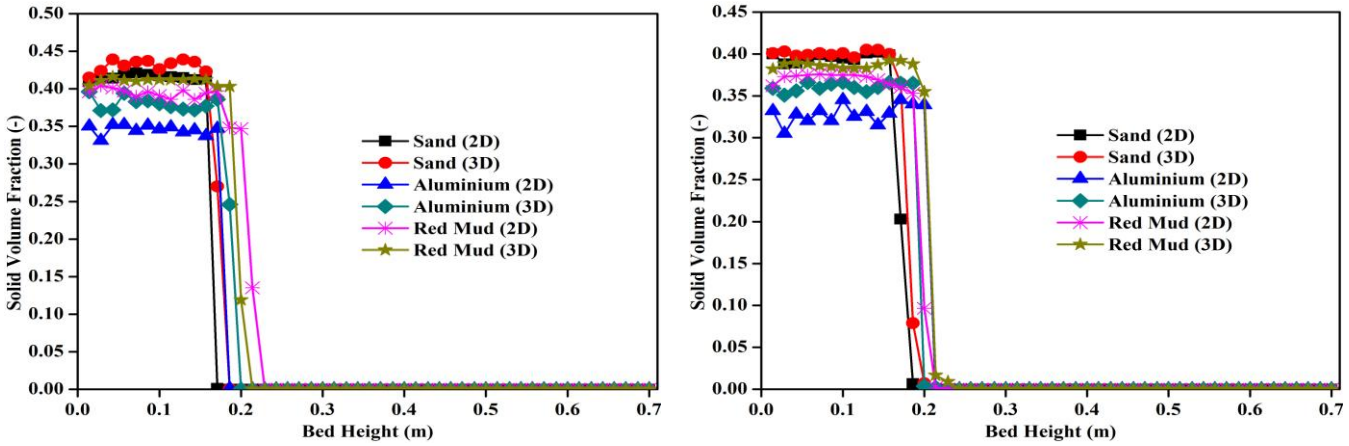

Uo = 0.016 m/s **Uo = 0.018 m/s**

Fig. – D.2: Distribution of solid volume fractions at different air velocities for different bed materials

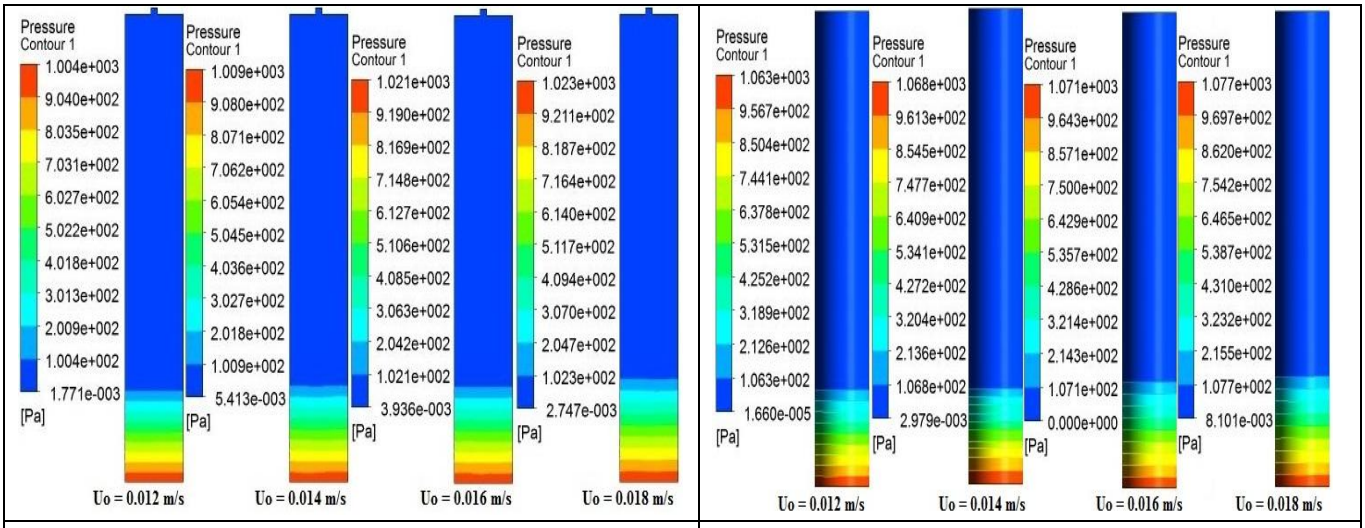

(a) 2D Simulation **(b) 3D Simulation**

Fig. – D.3 (a): Contour plot of pressure for Sand particles

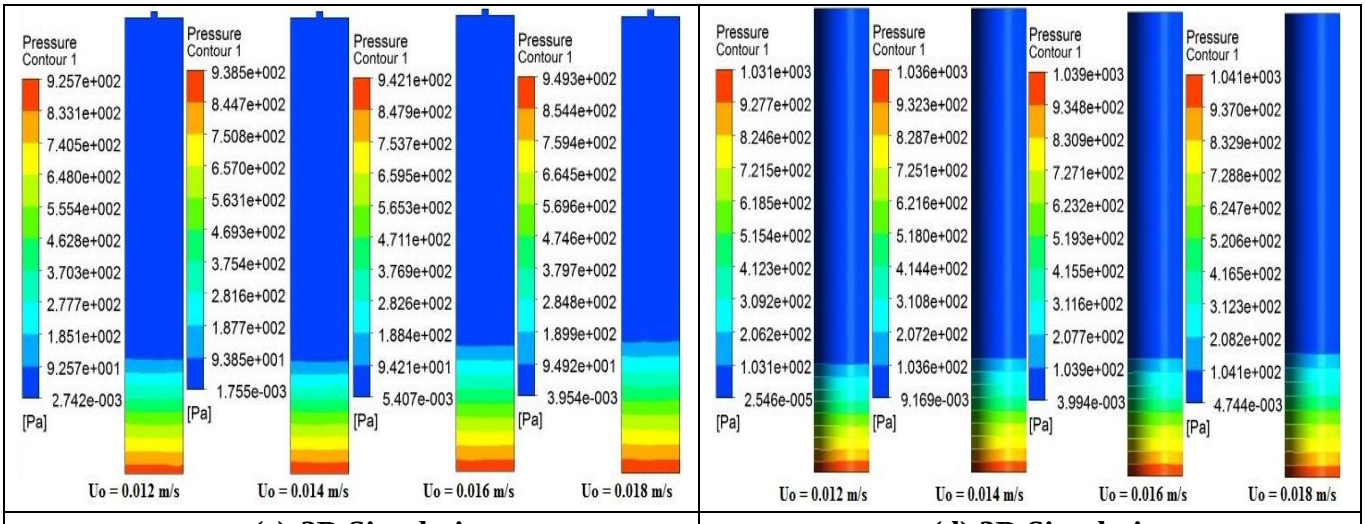

(c) 2D Simulation **(d) 3D Simulation**

Fig. – D.3 (b): Contour plot of pressure for Red Mud particles

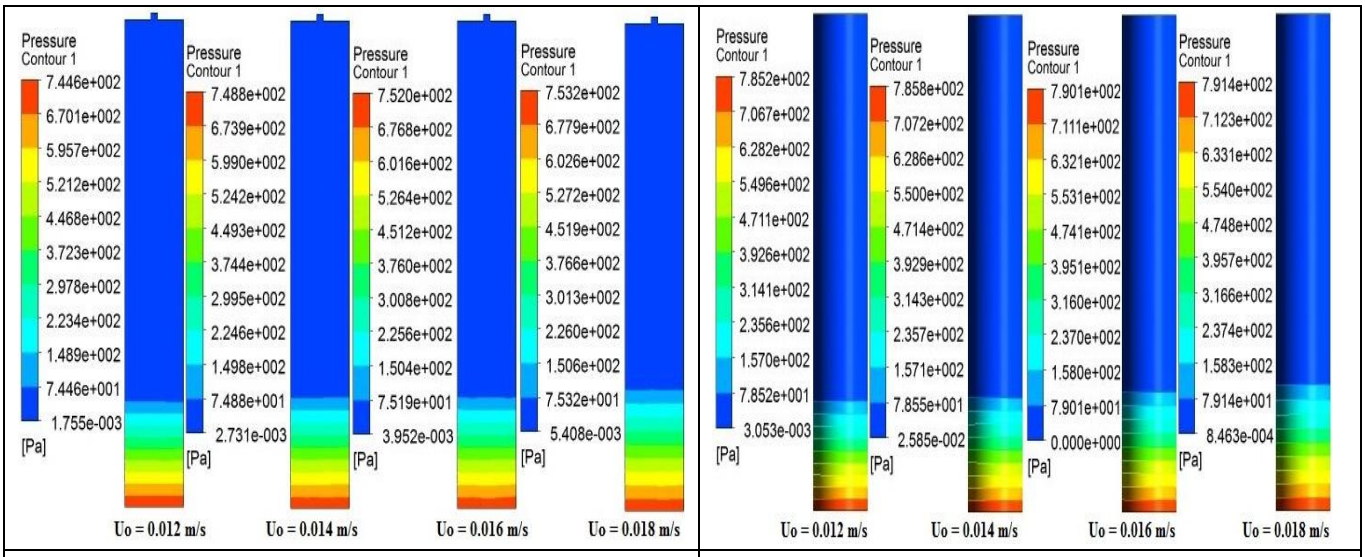

(e) 2D Simulation **(f) 3D Simulation**

Fig. – D.3 (c): Contour plot of pressure for Aluminium particles

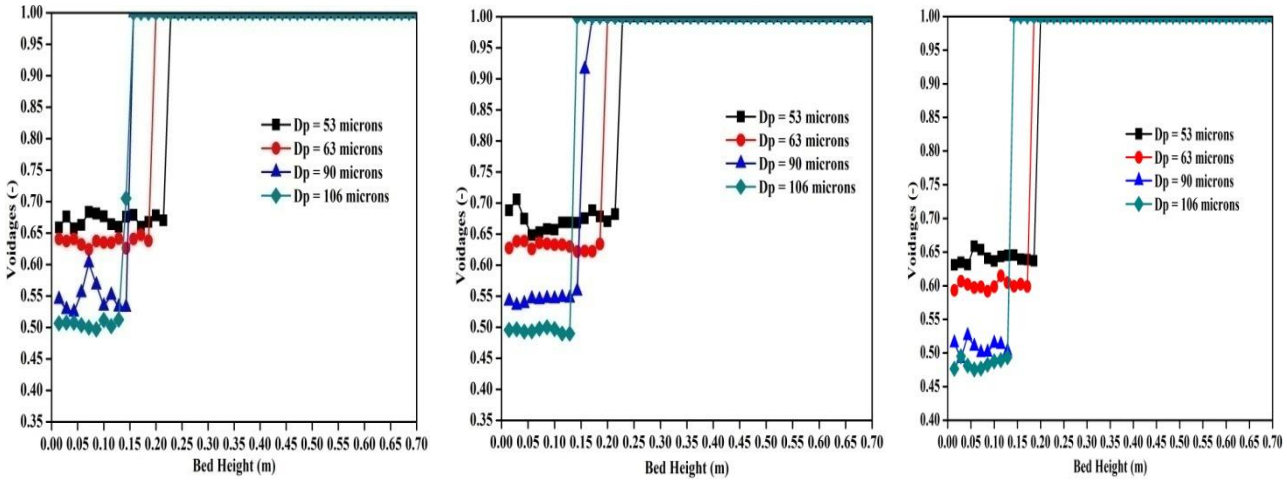

Gidaspow **Syamlal - O'Brien** **Wen & Yu**

Fig. – E.1 (a): Axial void fraction for the gas phase with different drag models

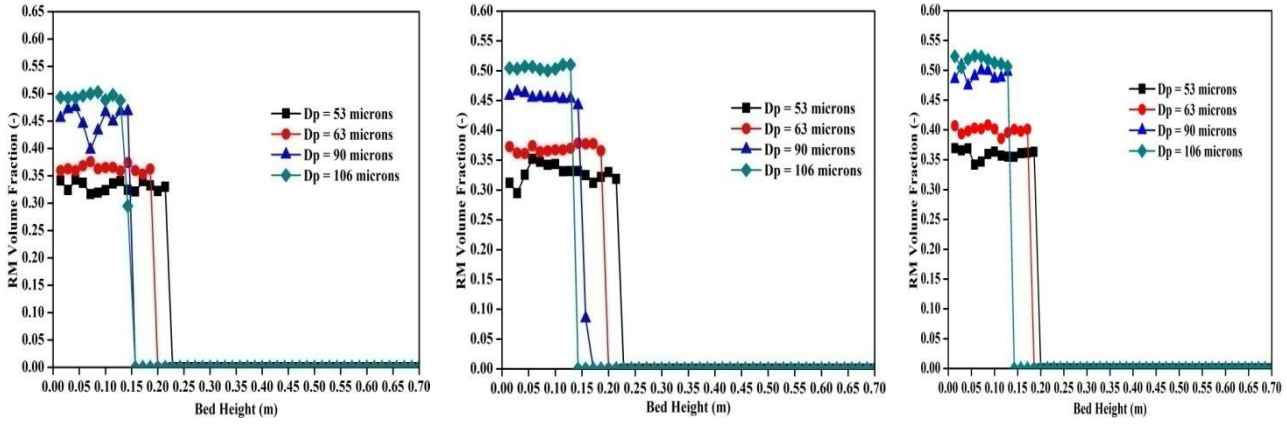

Gidaspow **Syamlal - O'Brien** **Wen & Yu**

Fig. – E.1 (b): Axial volume fraction for the solid phases with different drag models

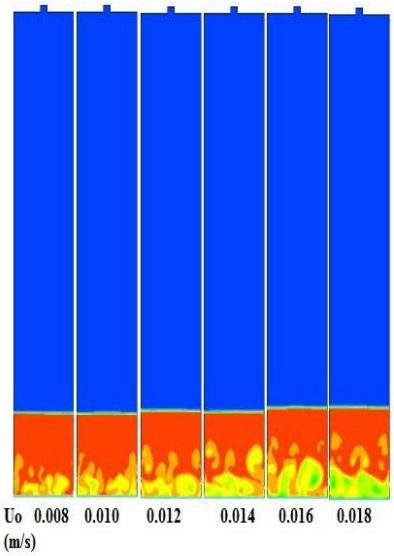

Gidaspow at T = 1 Sec

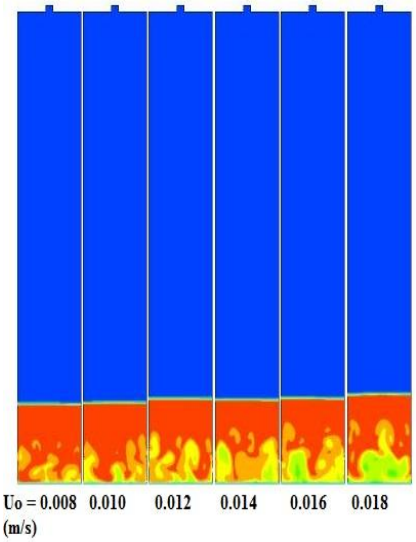

Syamlal - O'Brien at T= 1 Sec

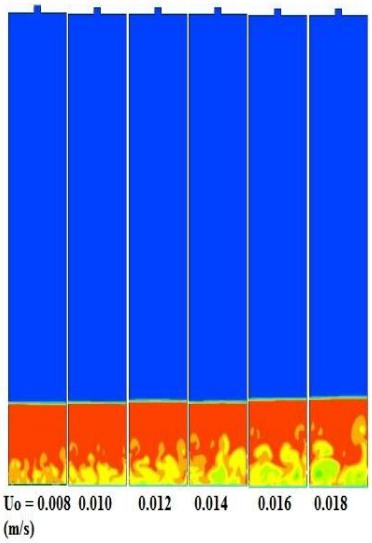

Wen & Yu at T = 1 Sec

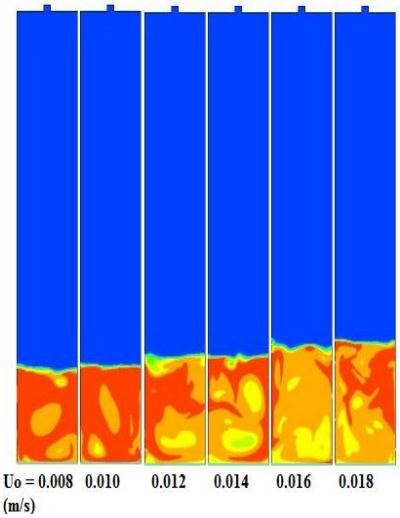

Gidaspow at T = 5 Sec

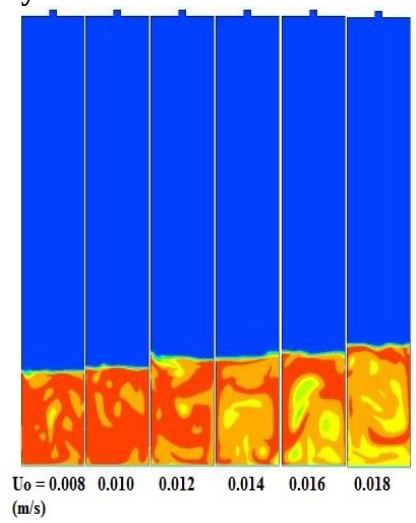

Syamlal-O'Brien at T=5 Sec

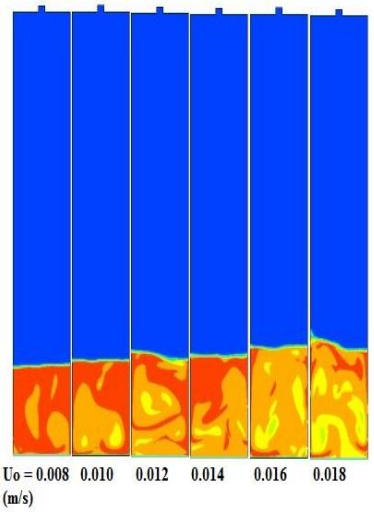

Wen & Yu at T = 5 Sec

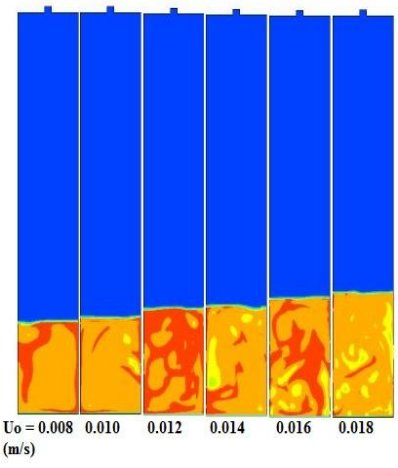

Gidaspow at T = 10 Sec

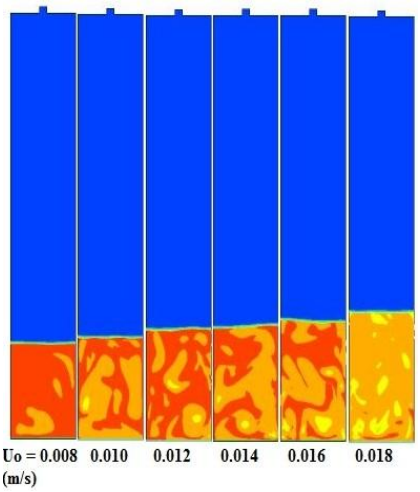

Syamlal-O'Brien at T=10 Sec

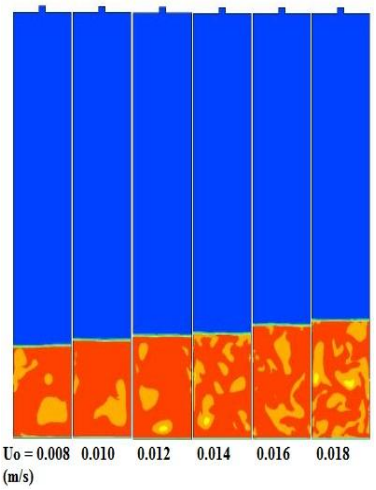

Wen & Yu at T = 10 Sec

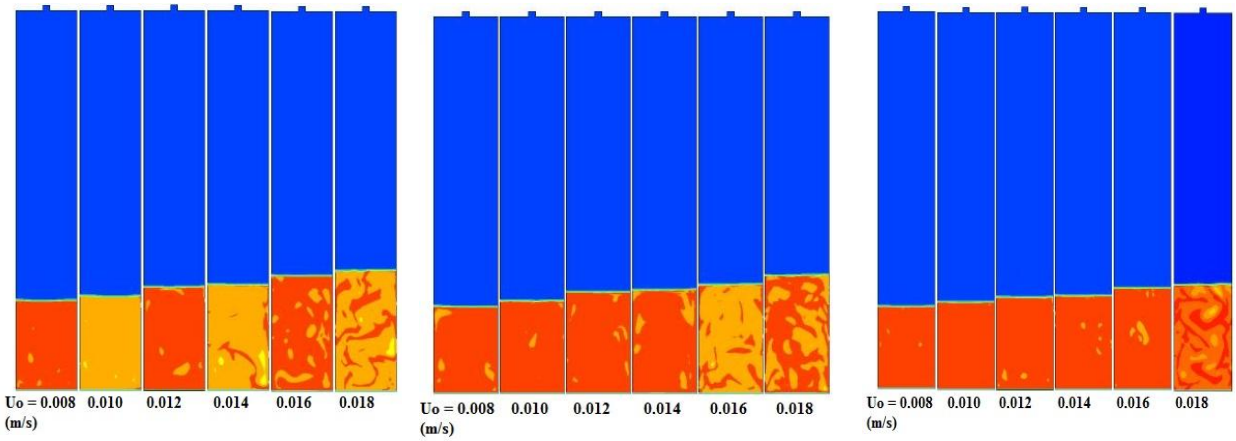

Gidaspow at T = 15 Sec **Syamlal-O'Brien at T=15 Sec** **Wen & Yu at T = 15 Sec**

Fig. – E.2: Solid volume fractions with inlet gas velocities for drag models

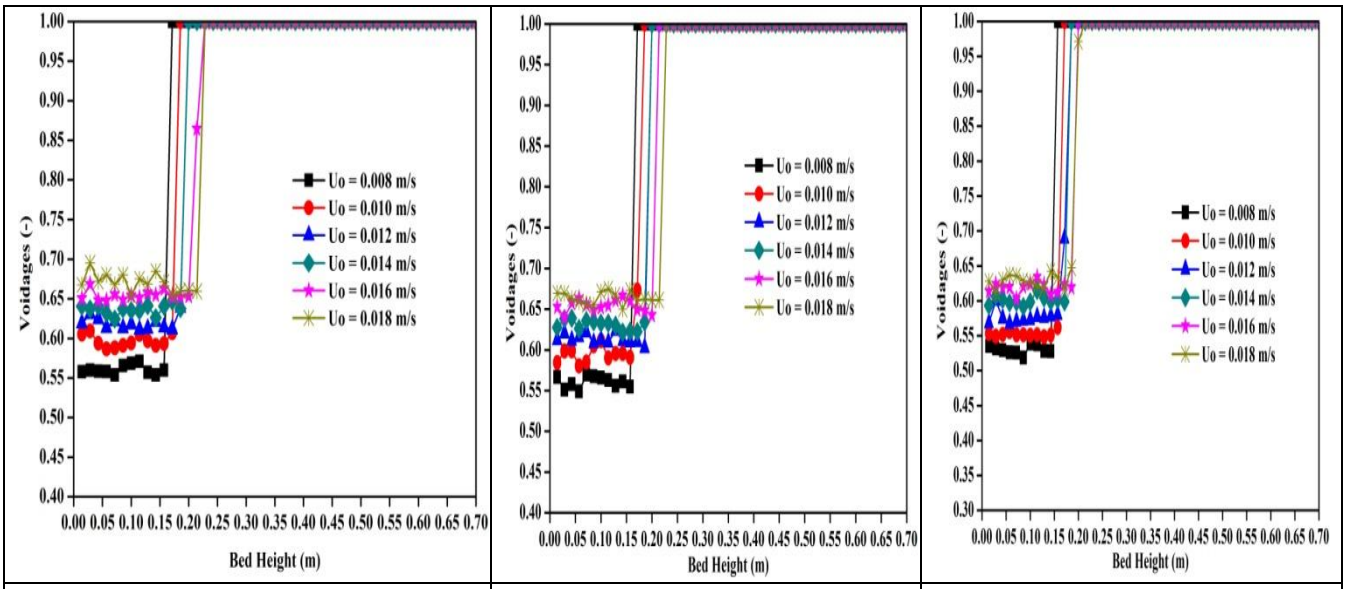

Gidaspow **Syamlal - O'Brien** **Wen & Yu**

Fig. – E.3 (a): Axial gas volume fraction for different drag models

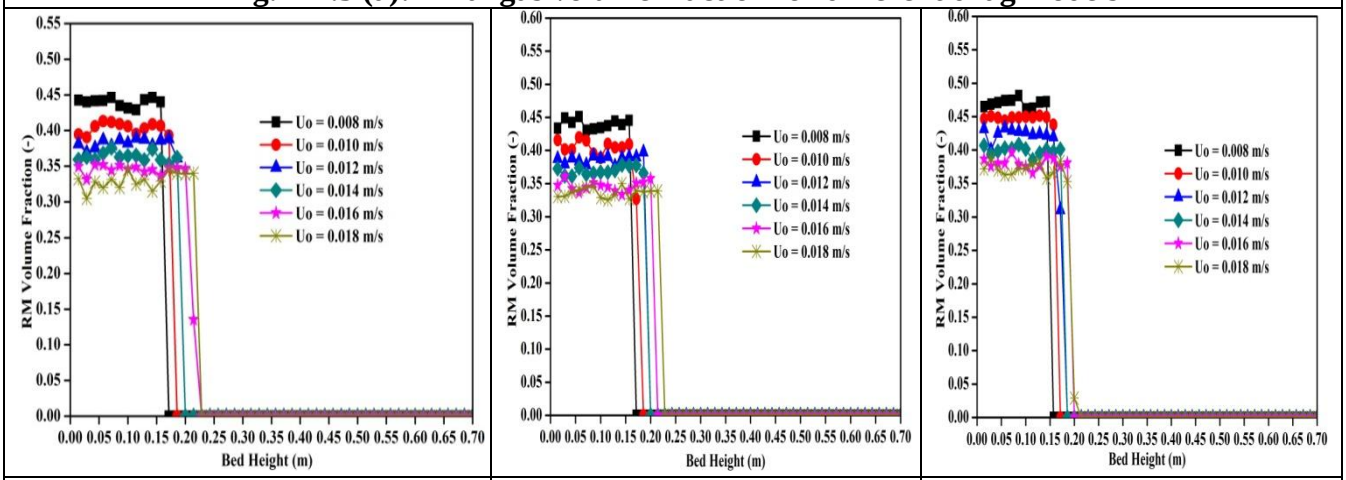

Gidaspow **Syamlal - O'Brien** **Wen & Yu**

Fig. – E.3 (b): Axial solid volume fraction for different drag models

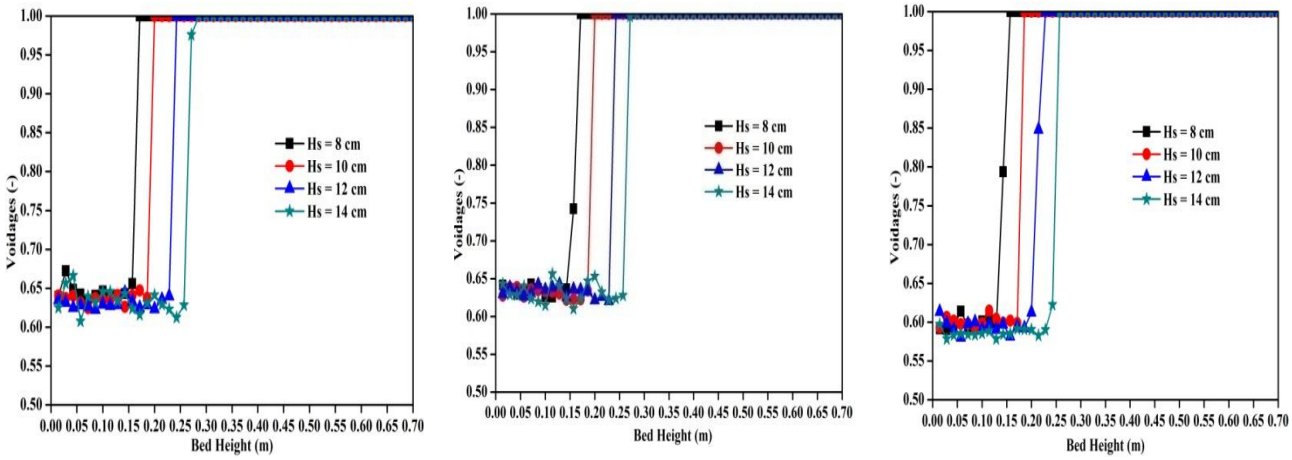

Gidaspow **Syamlal - O'Brien** **Wen & Yu**

Fig. – E.4 (a): Axial void fraction of gas phases for different drag models

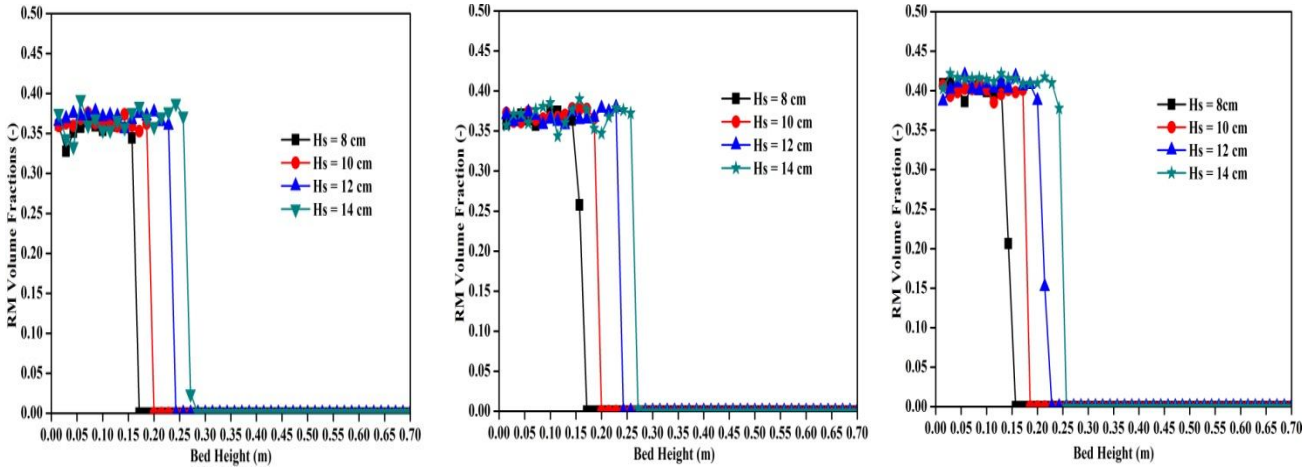

Gidaspow **Syamlal - O'Brien** **Wen & Yu**

Fig. – E.4 (b): Axial volume fraction of solid phases for different drag models

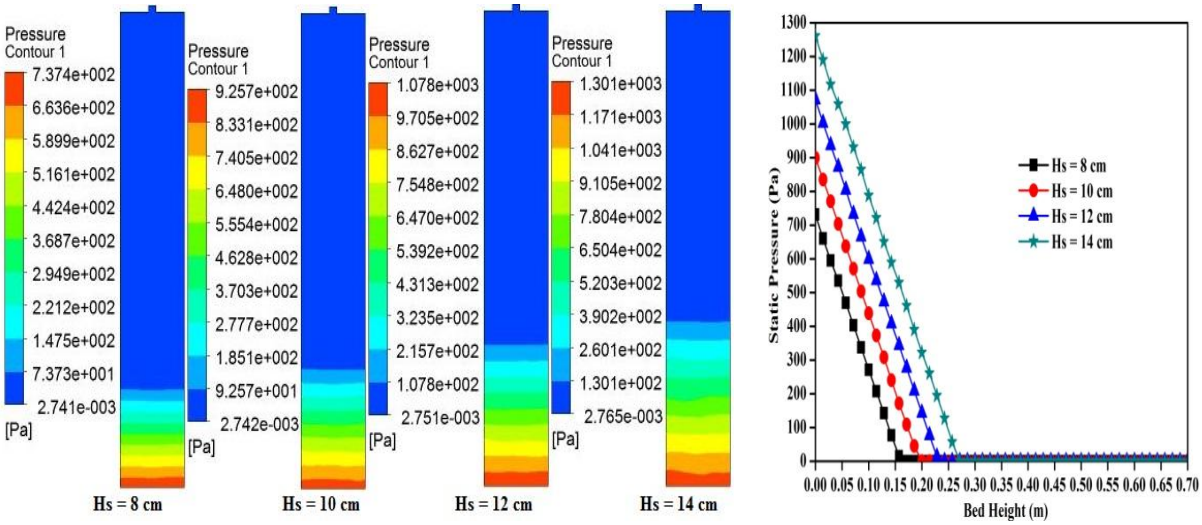

Gidaspow Drag Models

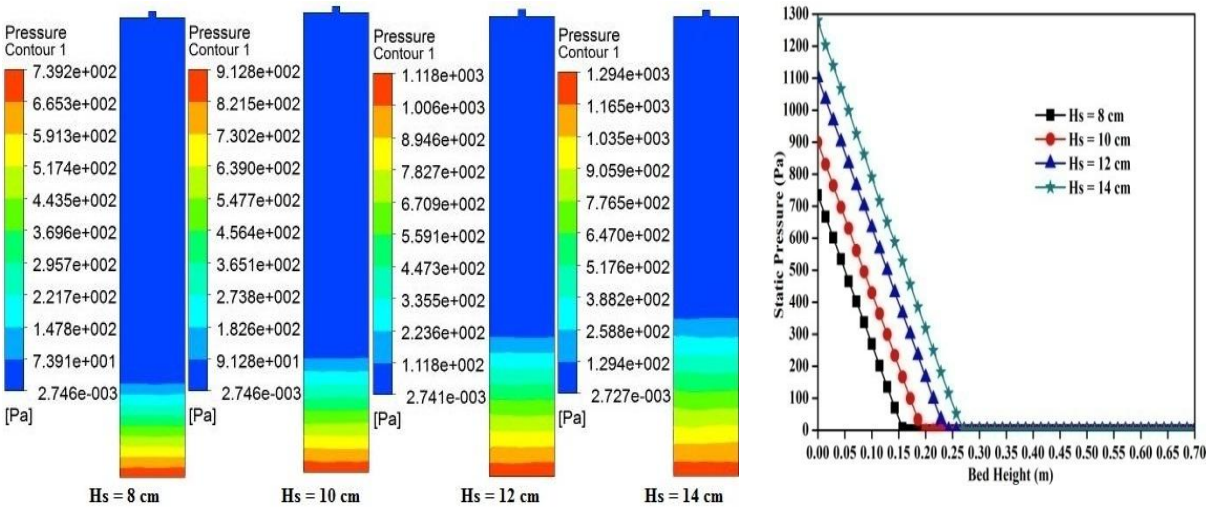

Syamlal - O'Brien Drag Models

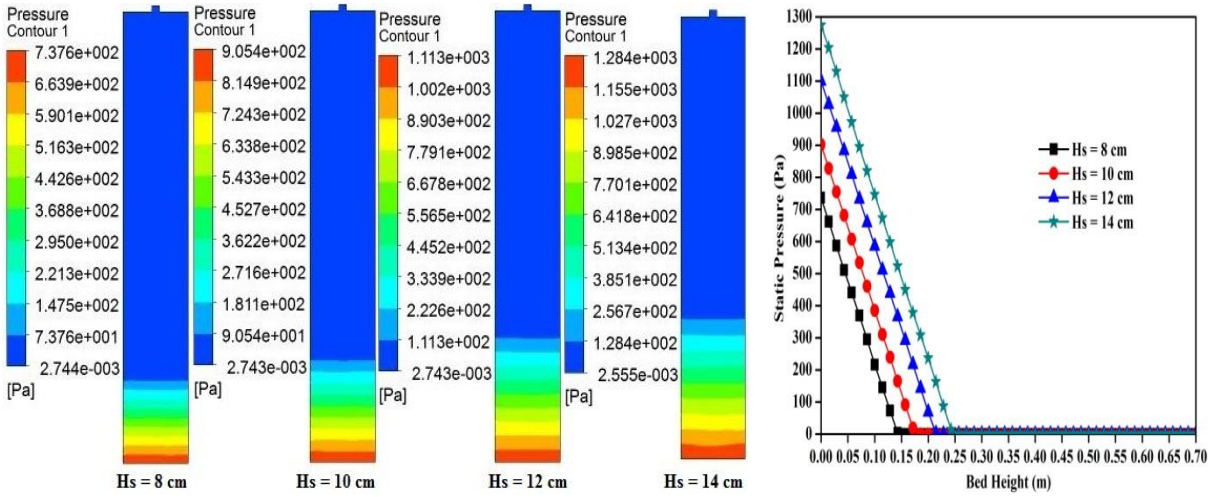

Wen & Yu Drag Models

Fig. – E.5: Comparisons of contours of bed pressure drop and static pressure for different drag models

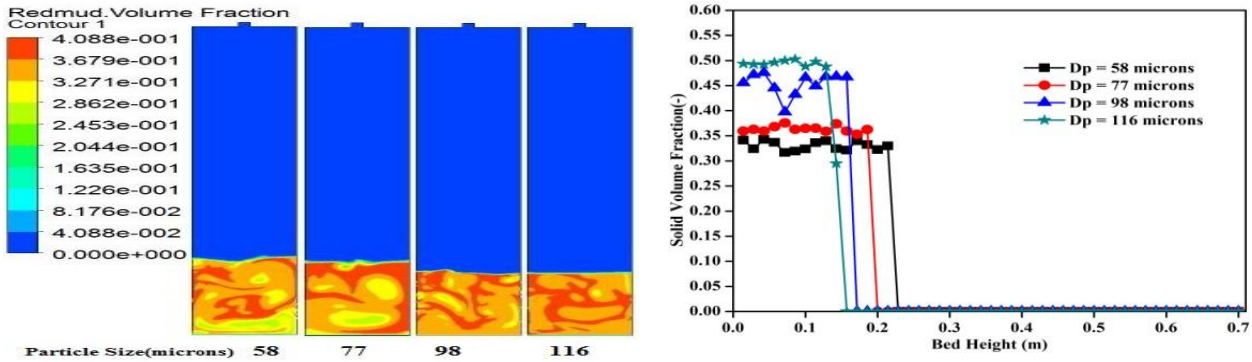

For Specularity Coefficient (Ø) of 0.0

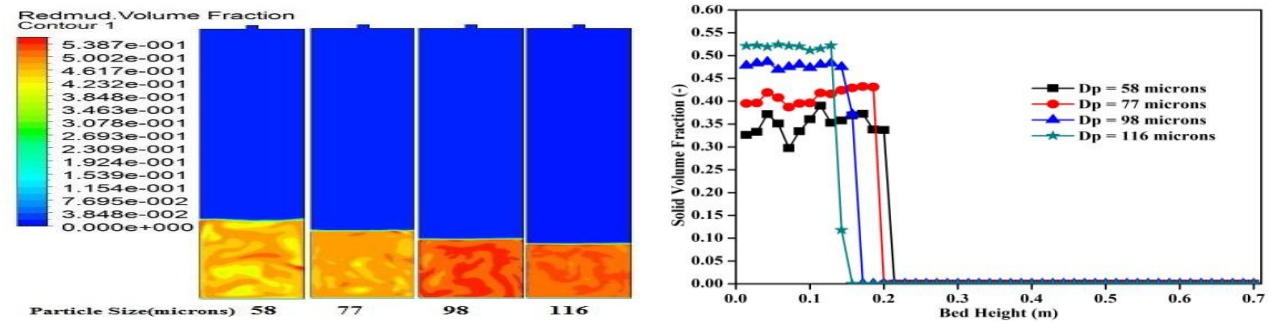

For Specularity Coefficient (Ø) of 0.25

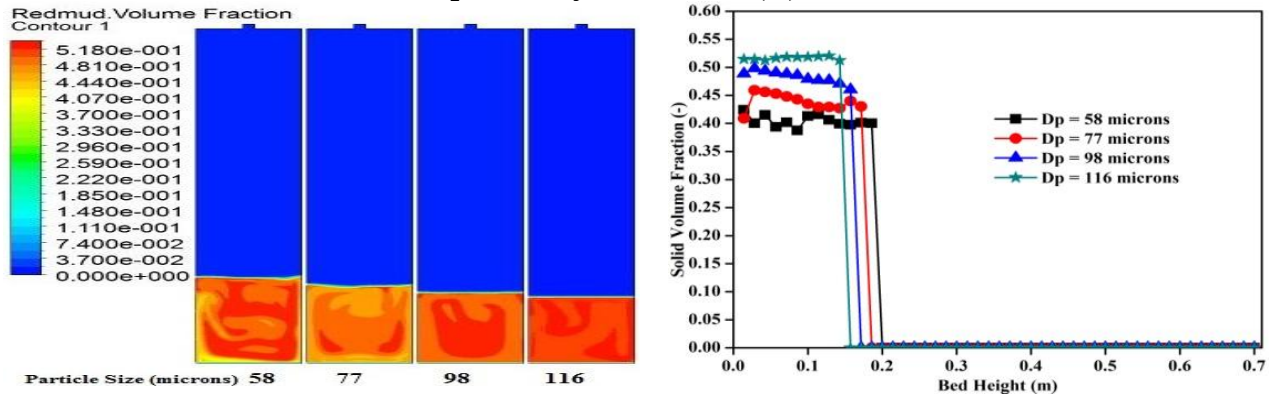

For Specularity Coefficient (Ø) of 0.50

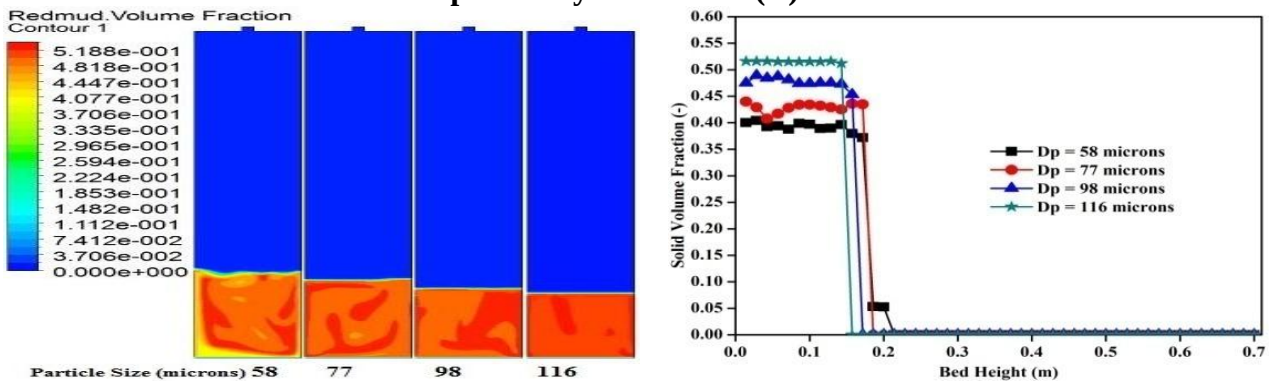

For Specularity Coefficient (Ø) of 0.75

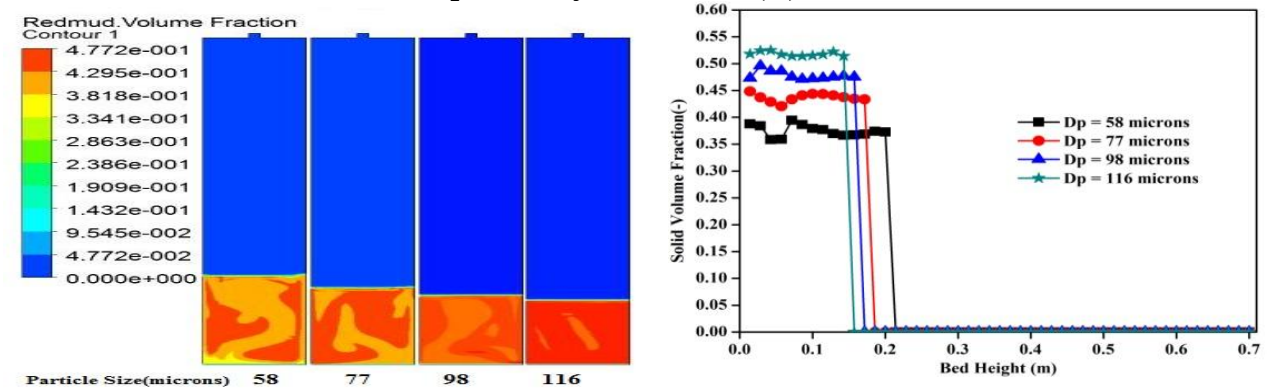

For Specularity Coefficient (Ø) of 1.0

Fig. – F.1: Time-averaged particle volume fraction profiles with particle sizes for different specularity coefficients

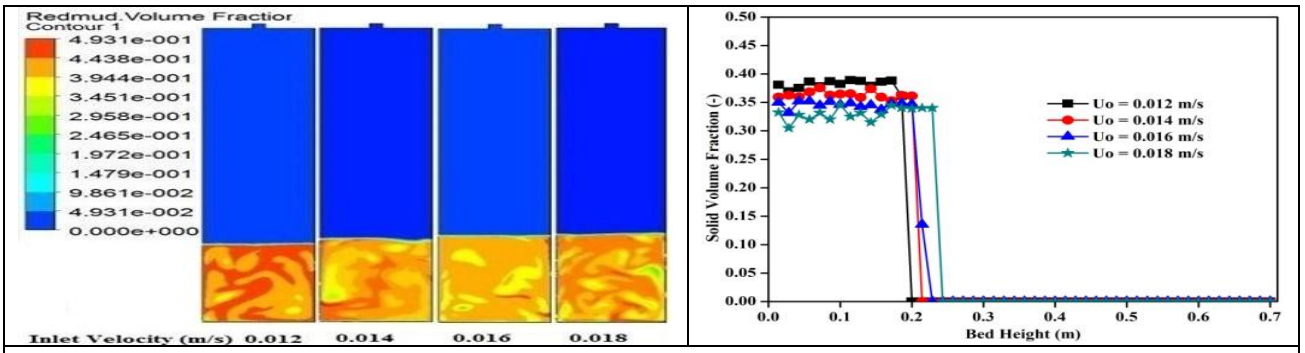

For Specularity Coefficient (Ø) of 0.0

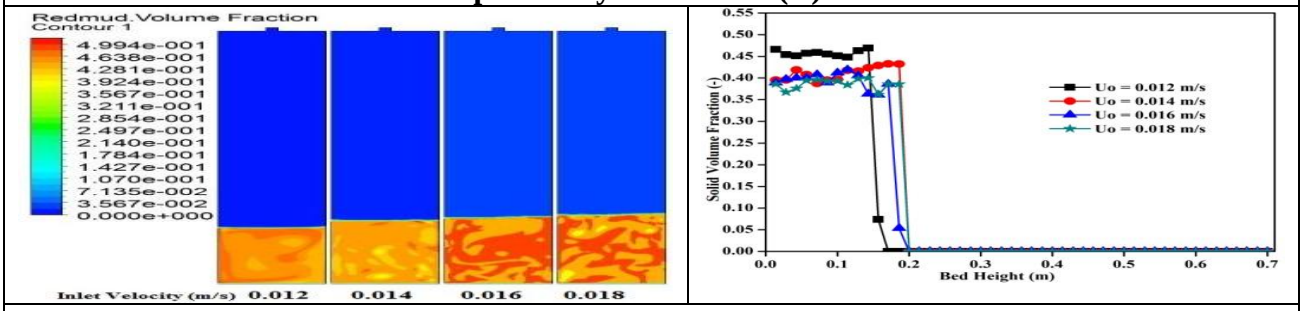

For Specularity Coefficient (Ø) of 0.25

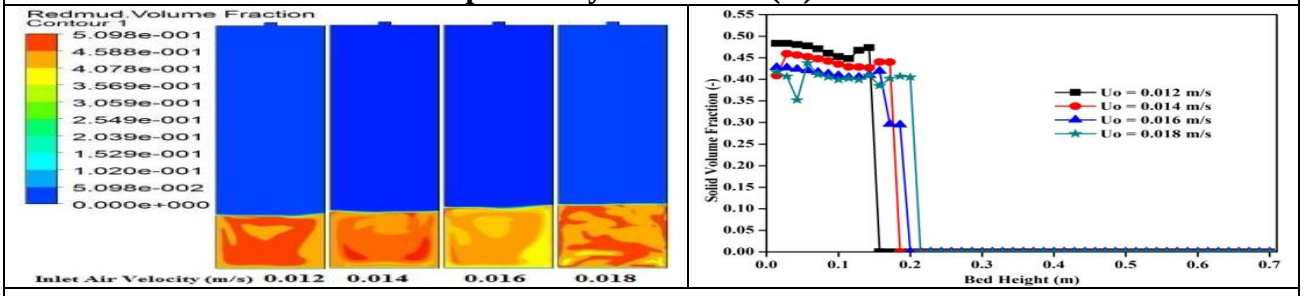

For Specularity Coefficient (Ø) of 0.50

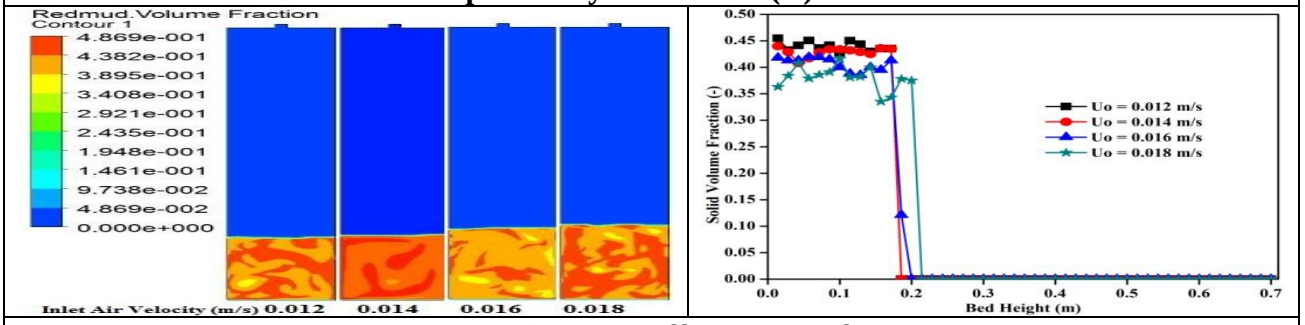

For Specularity Coefficient (Ø) of 0.75

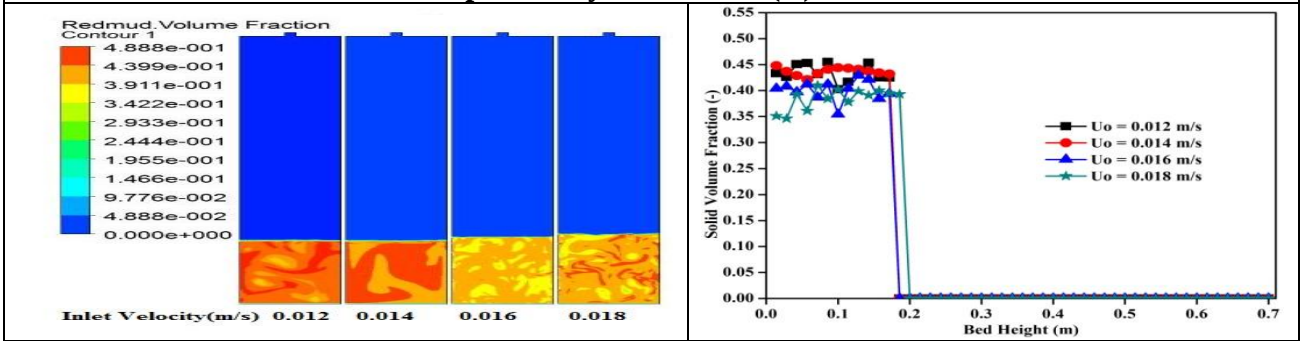

For Specularity Coefficient (Ø) of 1.0

Fig. – F.2: Solid volume fraction profiles with air velocities for different specularity coefficients

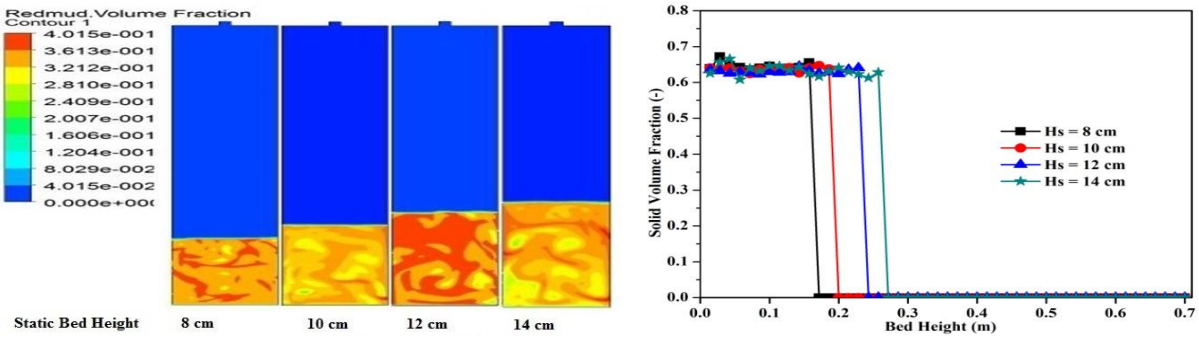

For Specularity Coefficient (Ø) of 0.0

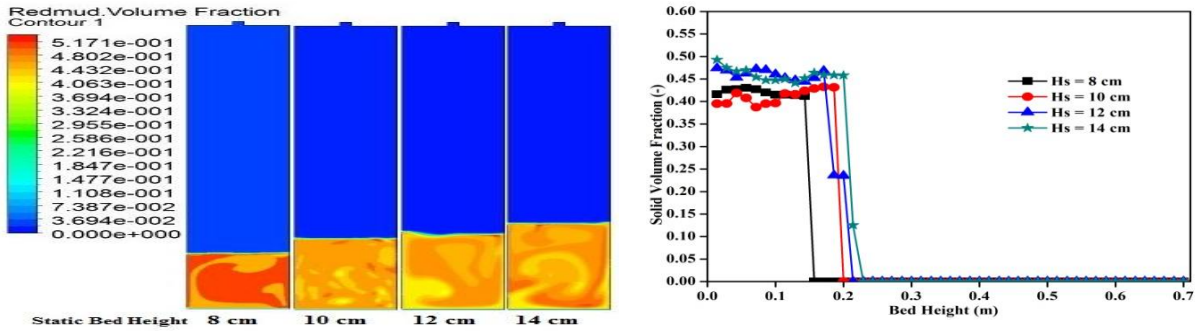

For Specularity Coefficient (Ø) of 0.25

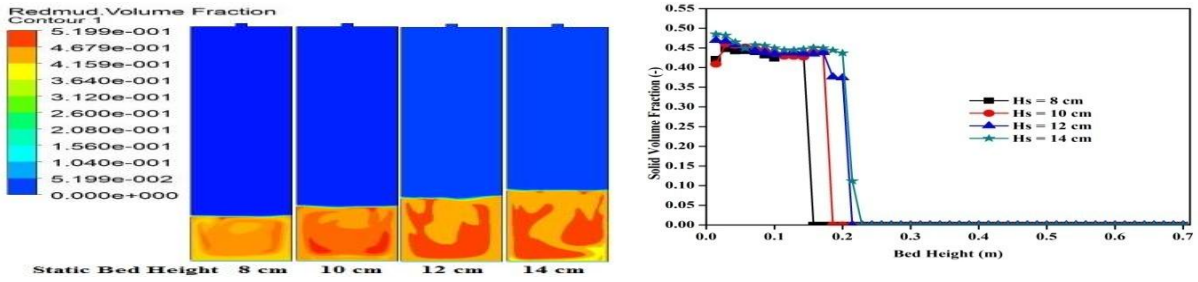

For Specularity Coefficient (Ø) of 0.50

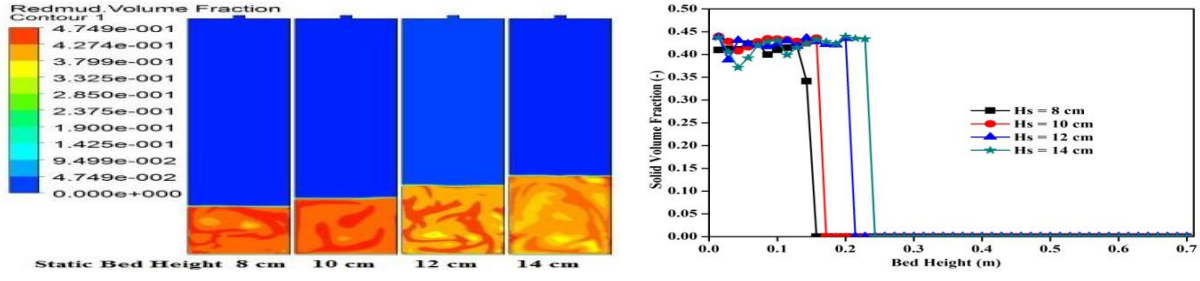

For Specularity Coefficient (Ø) of 0.75

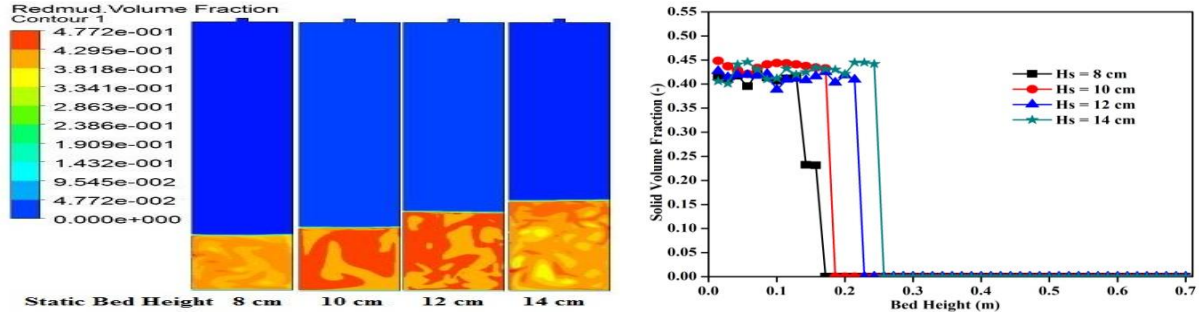

For Specularity Coefficient (Ø) of 1.0

Fig. – F.3: Solid volume fractions with static bed heights for different specularity coefficients with different static bed heights for different specularity coefficients

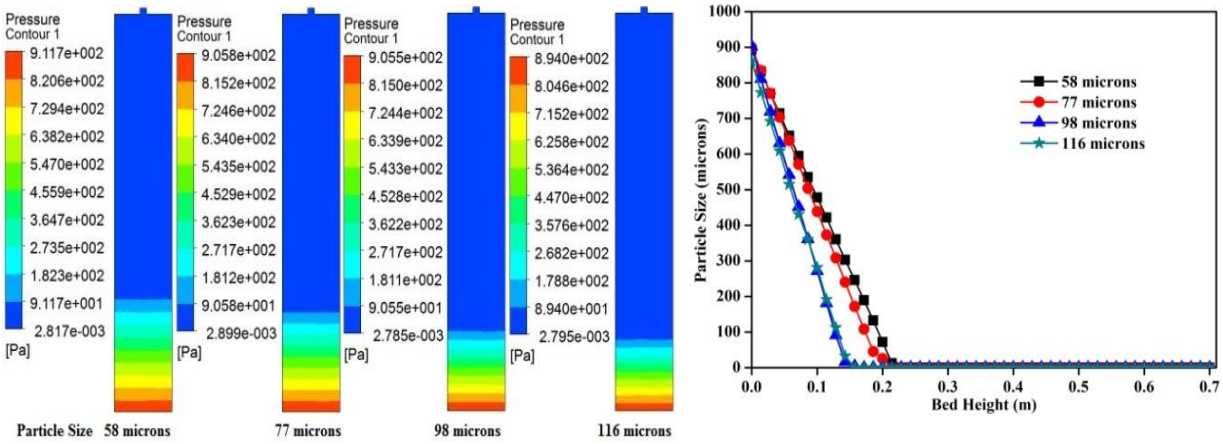

For Specularity Coefficient (Ø) of 0.0

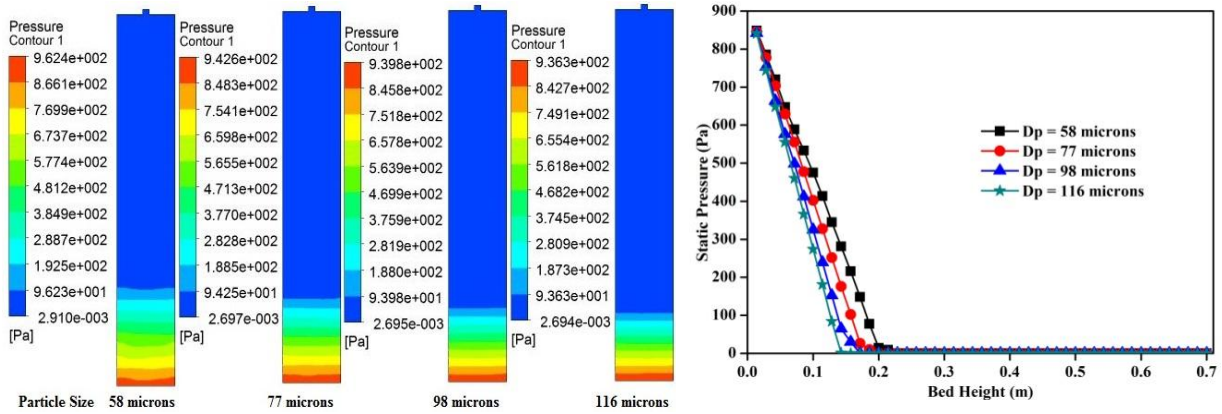

For Specularity Coefficient (Ø) of 0.25

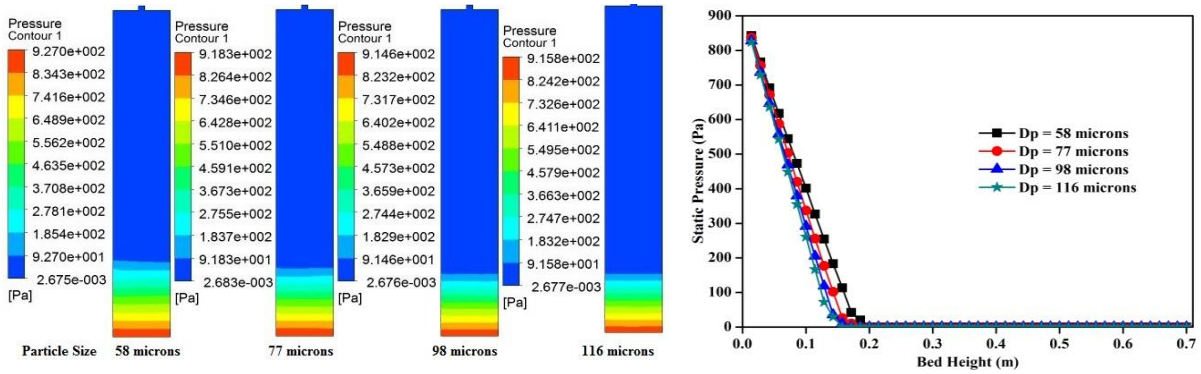

For Specularity Coefficient (Ø) of 0.50

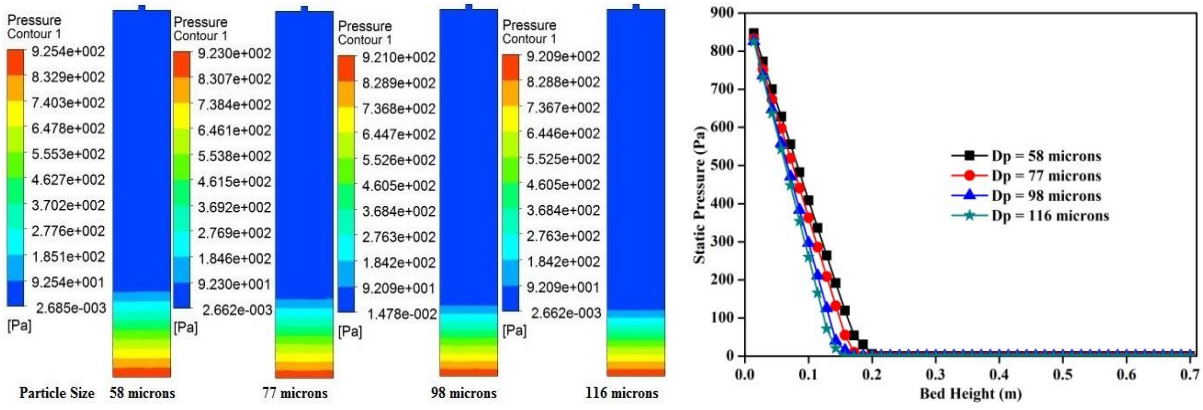

For Specularity Coefficient (Ø) of 0.75

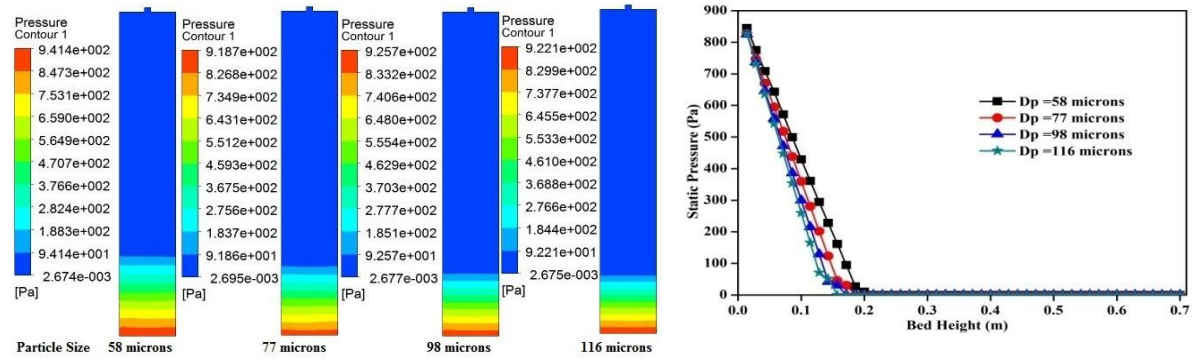

For Specularity Coefficient (Ø) of 1.0

Fig. – F.4: Comparison of contours of pressure drop and static pressure with particle sizes for different specularity coefficients

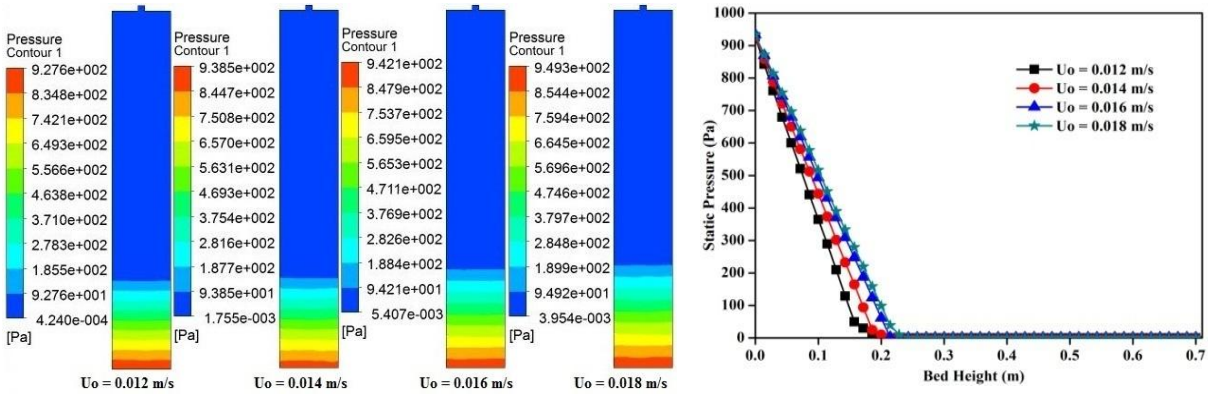

For Specularity Coefficient (Ø) of 0.0

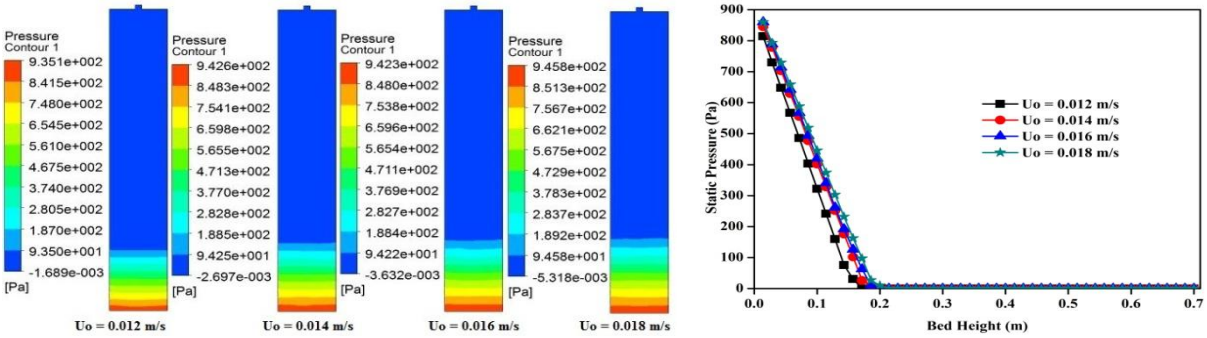

For Specularity Coefficient (Ø) of 0.25

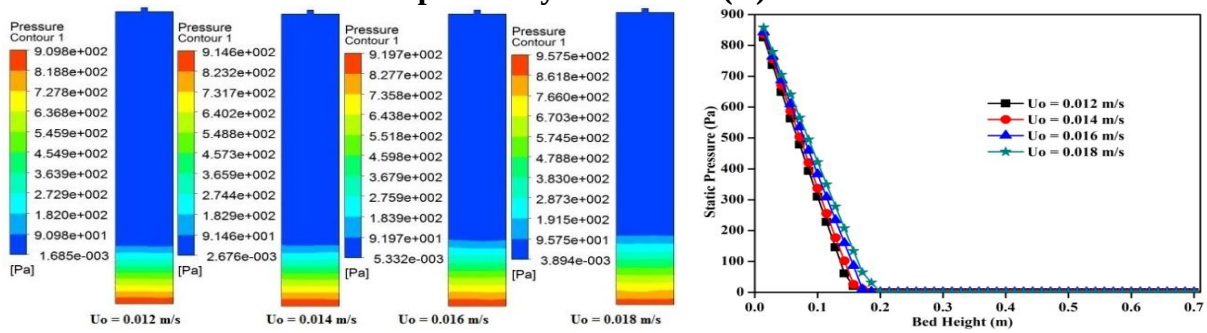

For Specularity Coefficient (Ø) of 0.50

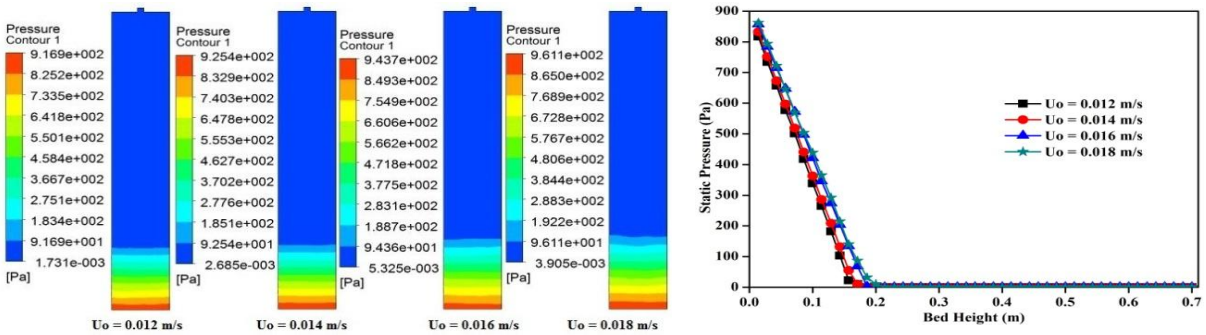

For Specularity Coefficient (Ø) of 0.75

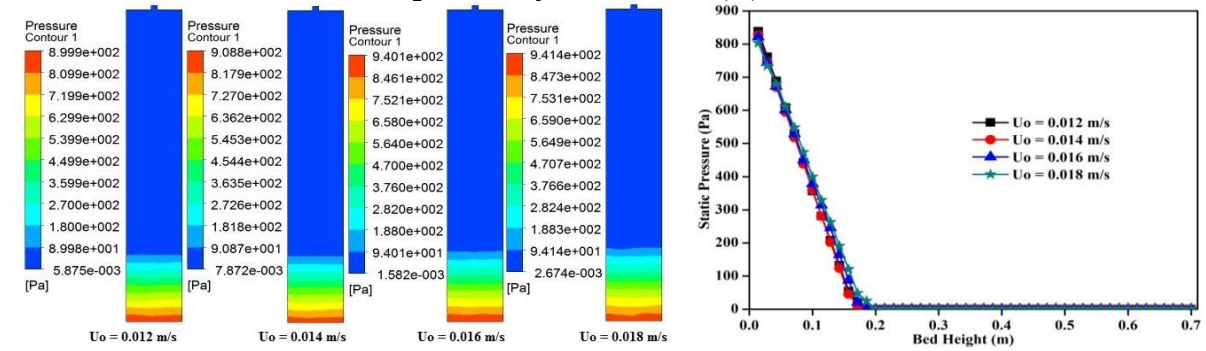

For Specularity Coefficient (Ø) of 1.0

Fig. – F.5: Comparison of contours of pressure drop and static pressure with air velocities for different specularity coefficients

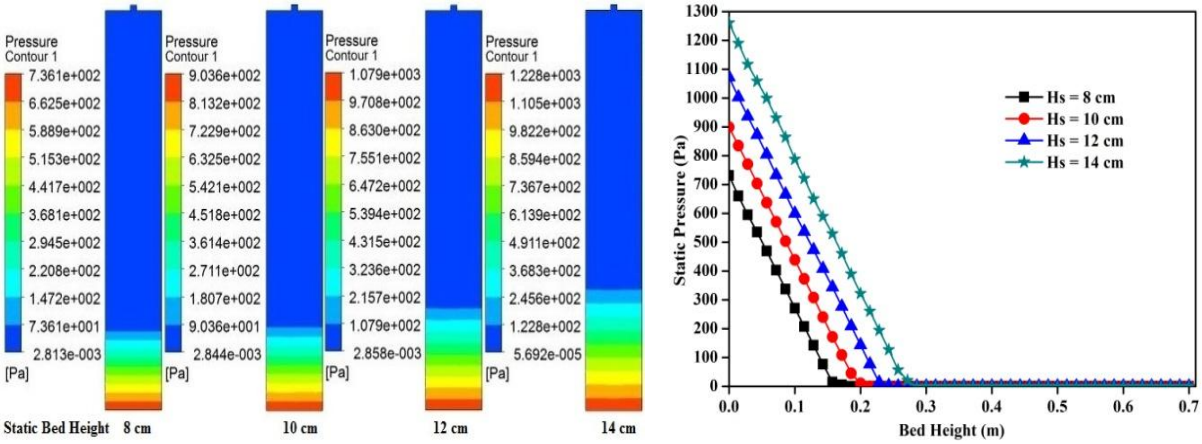

For Specularity Coefficient (Ø) of 0.0

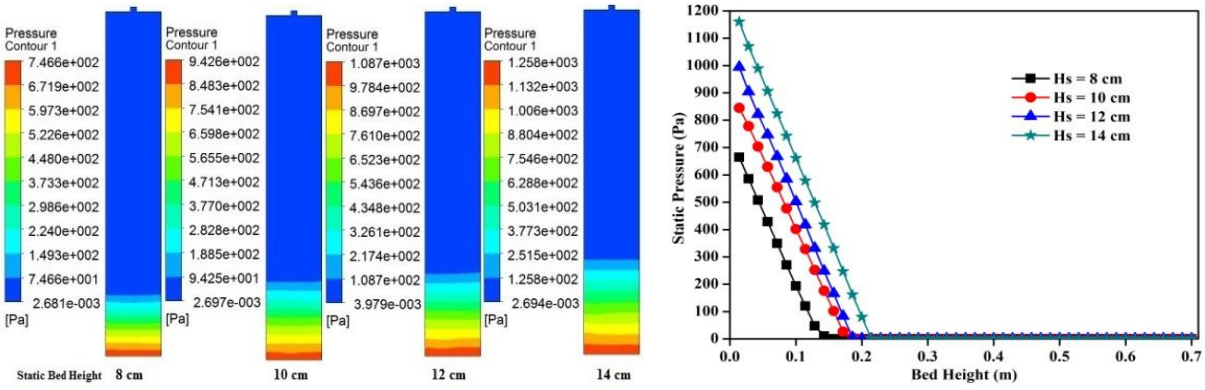

For Specularity Coefficient (Ø) of 0.25

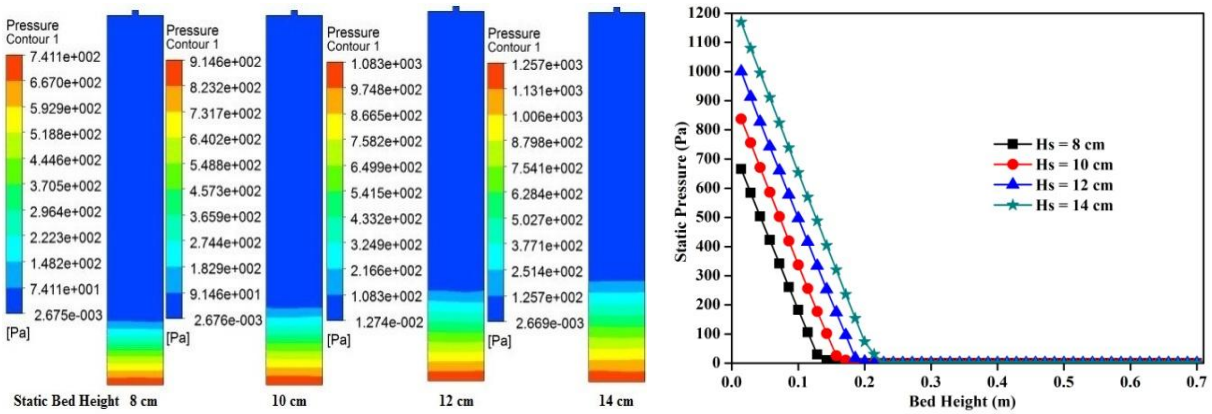

For Specularity Coefficient (Ø) of 0.50

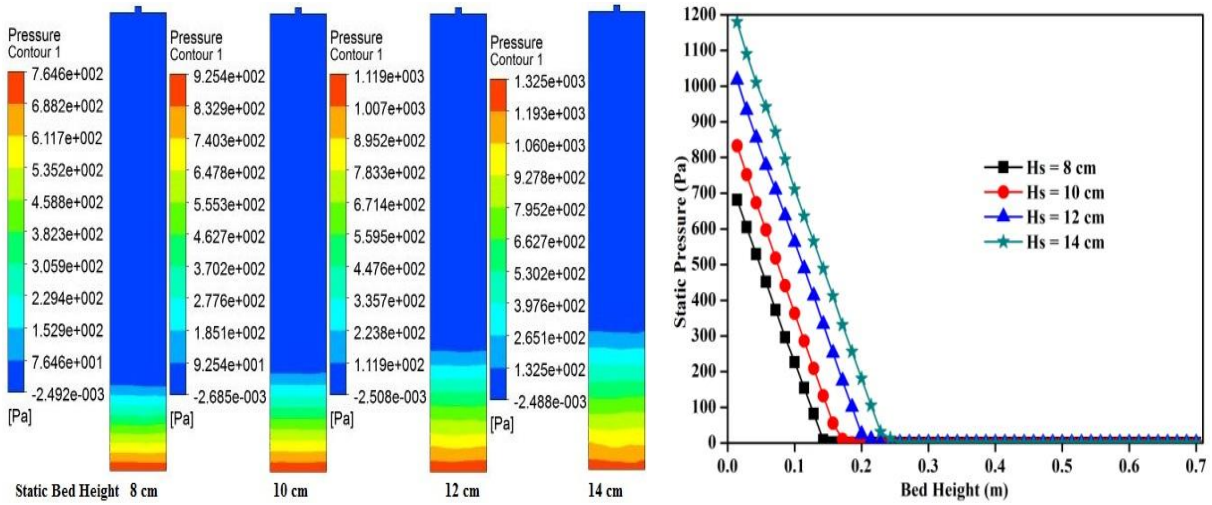

For Specularity Coefficient (Ø) of 0.75

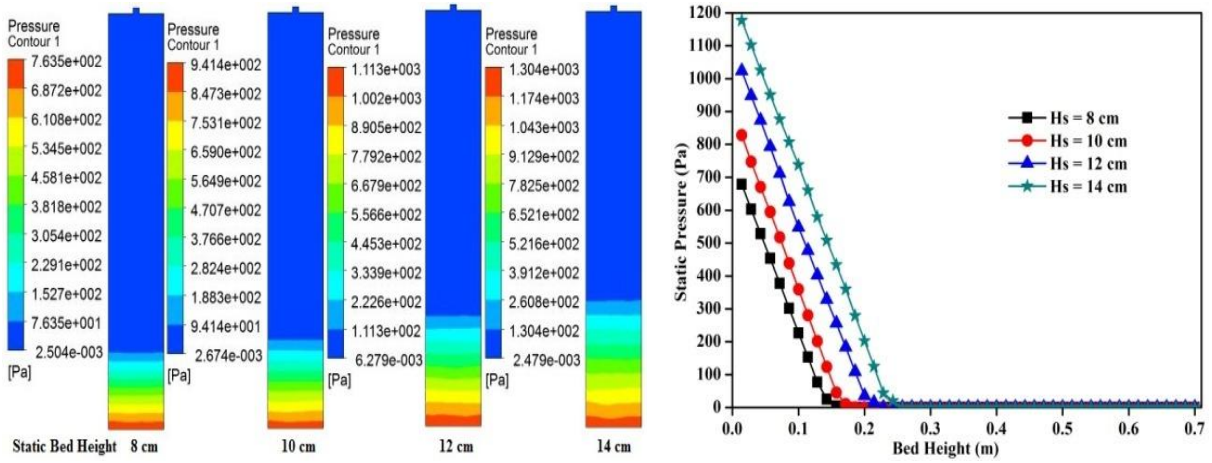

For Specularity Coefficient (Ø) of 1.0

Fig. – F.6: Comparison of contours of bed pressure drop and Static pressure for different static bed height for different specularity coefficient

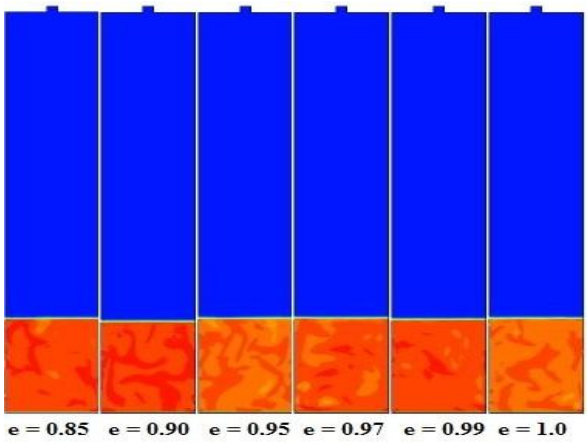

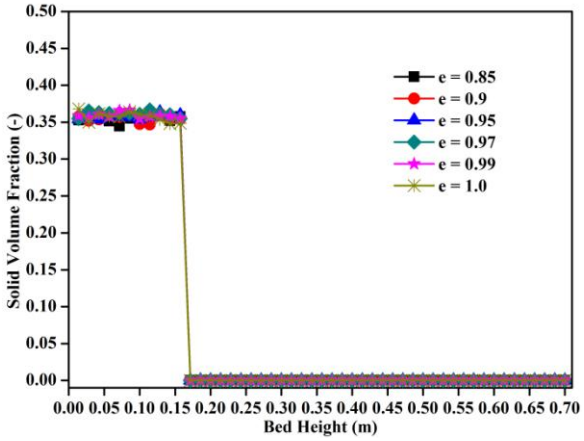

Static Bed Height for 8 cm

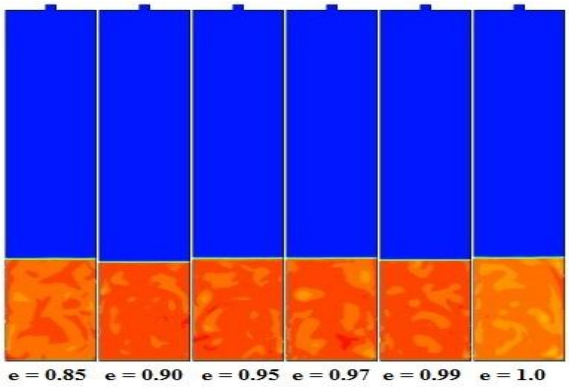

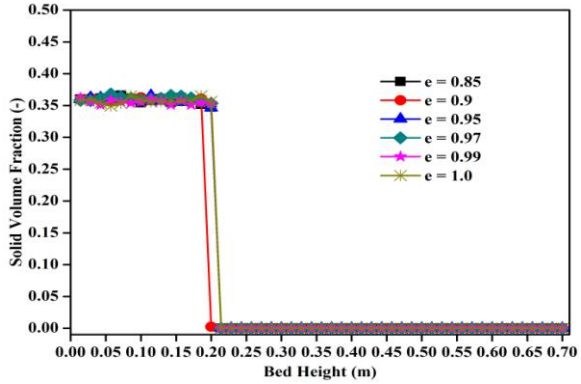

Static Bed Height for 10 cm

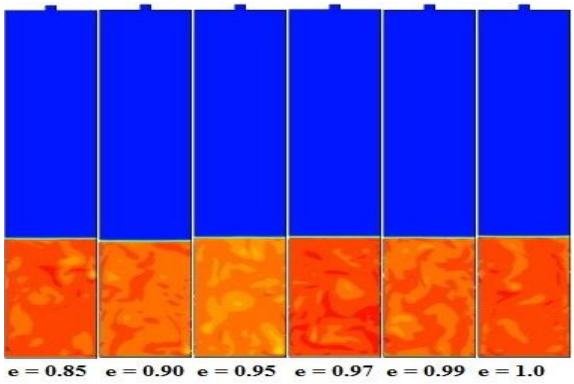

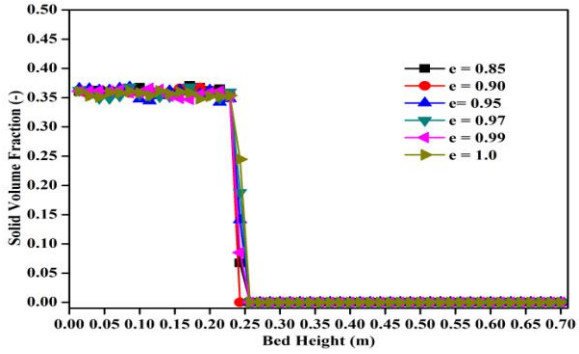

Static Bed Height for 12 cm

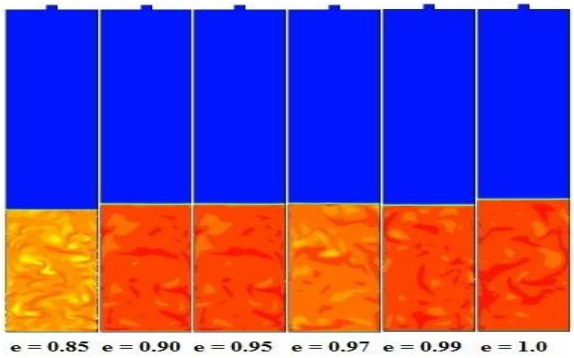

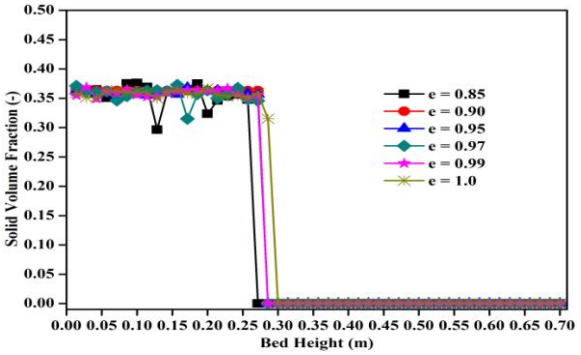

Static Bed Height for 14 cm

Fig. – G.1: Solid volume fractions with different static bed heights for different restitution coefficients

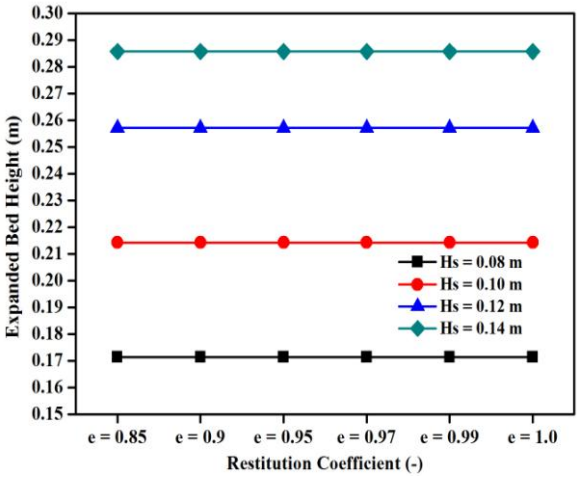

Fig. – G.2: Expanded bed height against restitution coefficient for different static bed heights

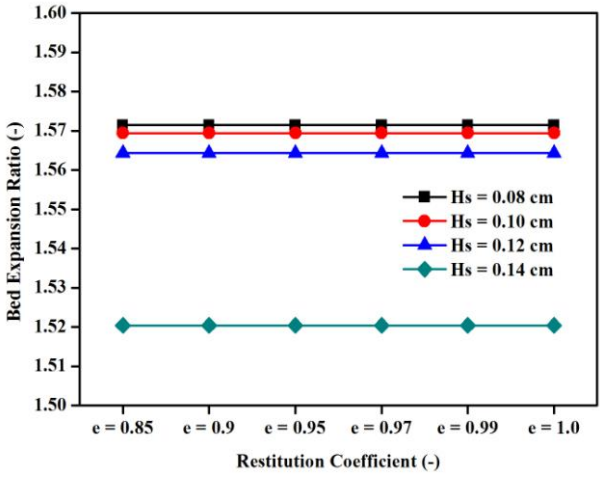

Fig. – G.3: Bed expansion ratio against restitution coefficient for different static bed heights

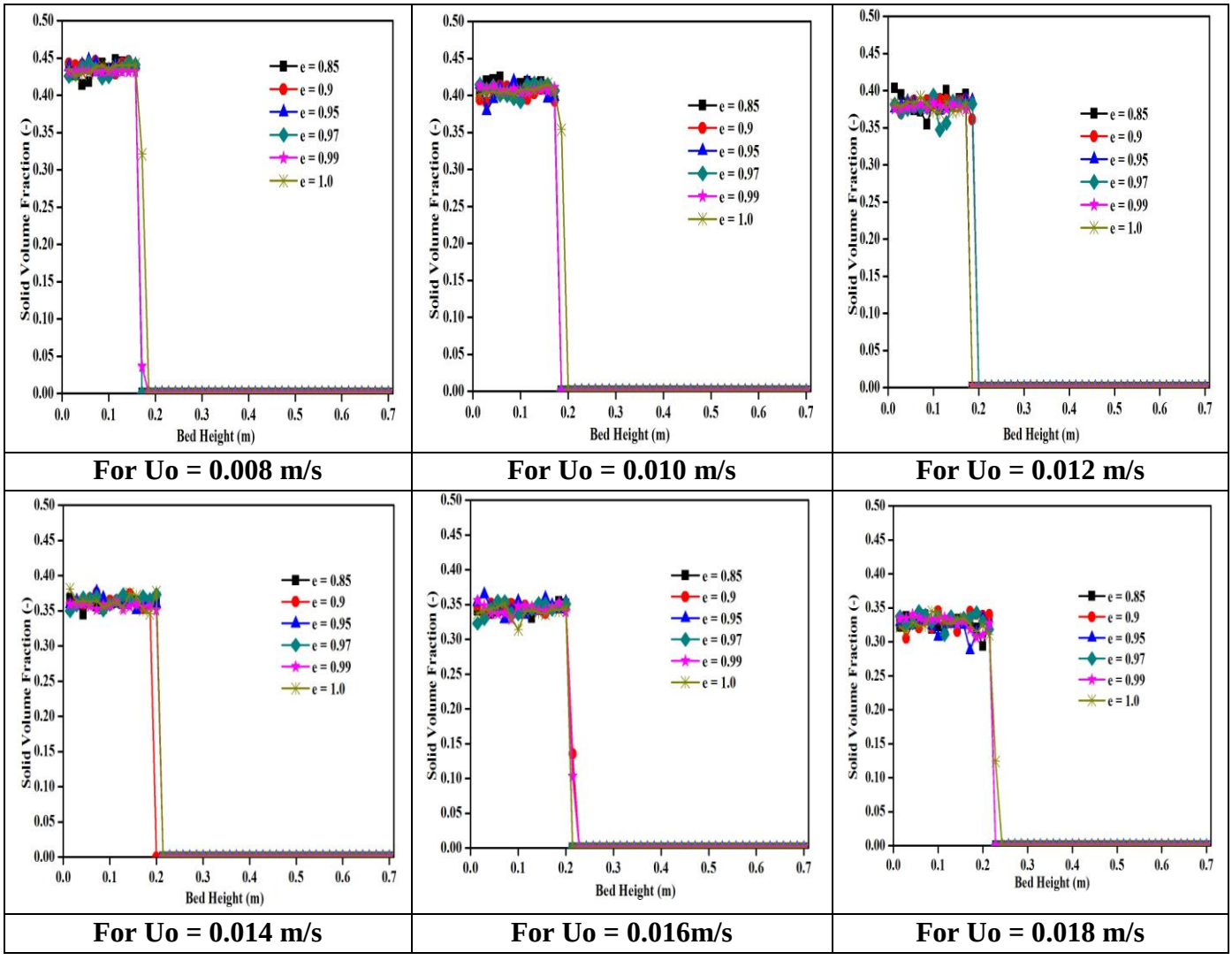

Fig. – G.4: Axial solid volume fractions with different air velocities for different restitution coefficients

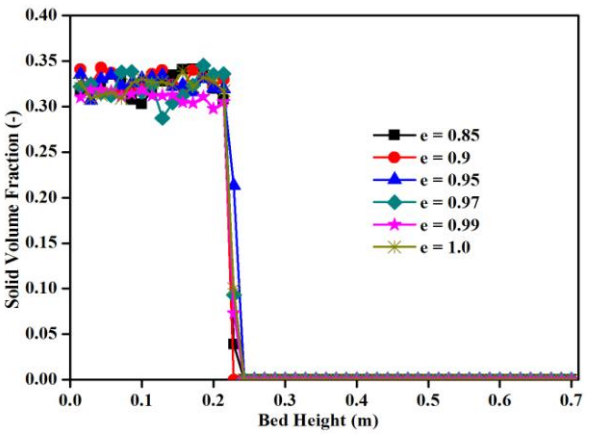

For Dp = 58 microns

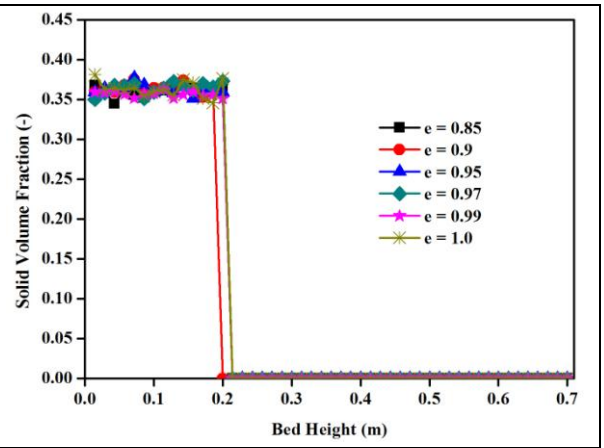

For Dp = 77 microns

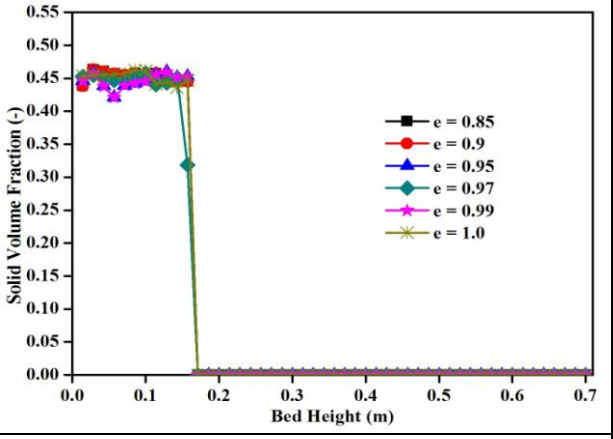

For Dp = 98 microns

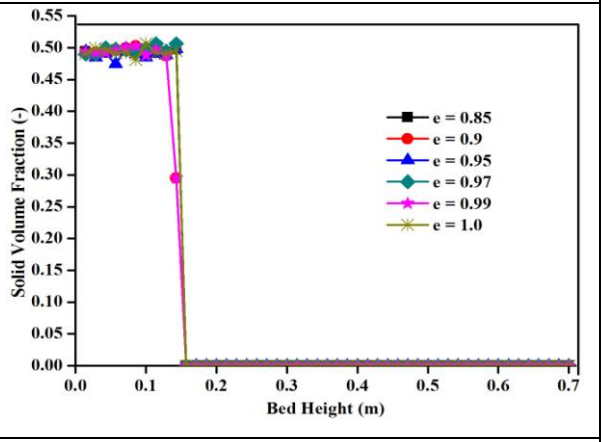

For Dp = 116 microns

Fig.- G.5: Axial solid volume fraction profile with particle size for different restitution coefficients

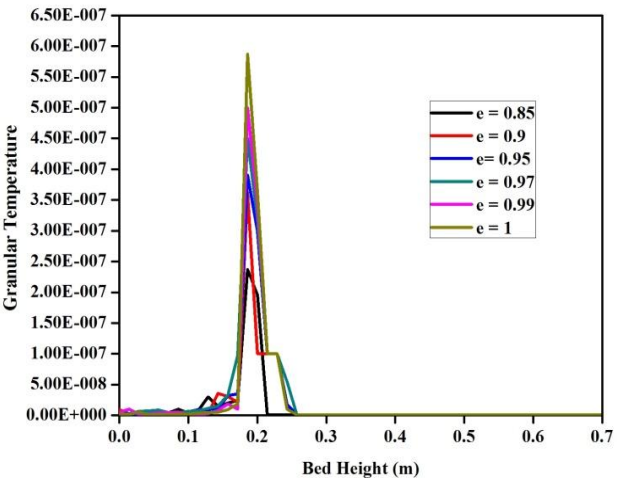

Fig. – G.6: Axial variation in granular temperature of particles for different restitution coefficients

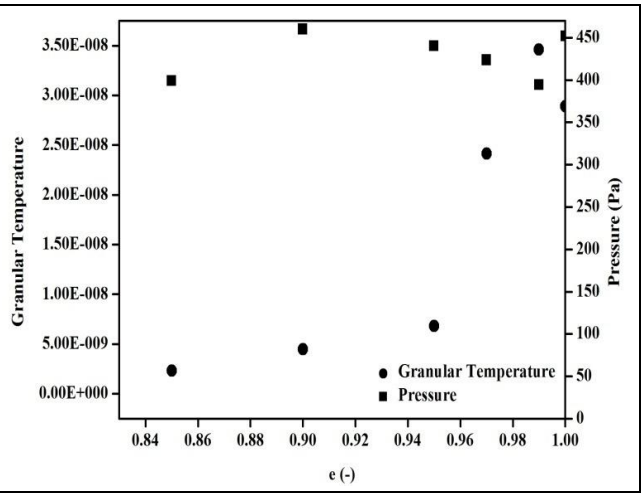

Fig. – G.7: Average solid phase variables as a function of the restitution coefficients

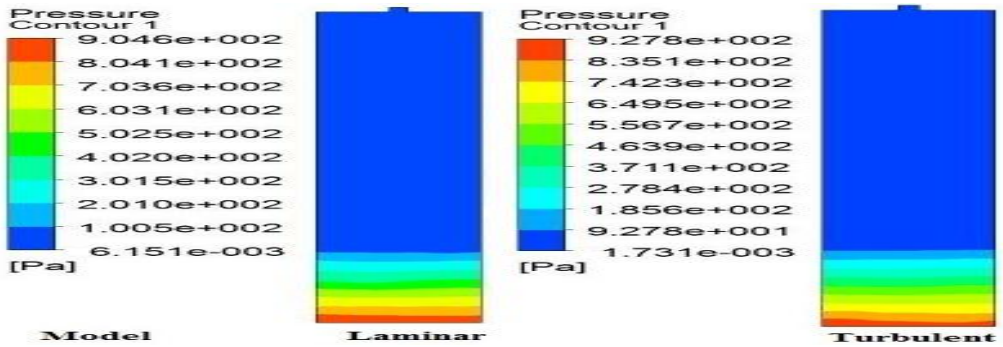

Fig. - H.1: Comparisons of pressure drops in laminar and turbulent models

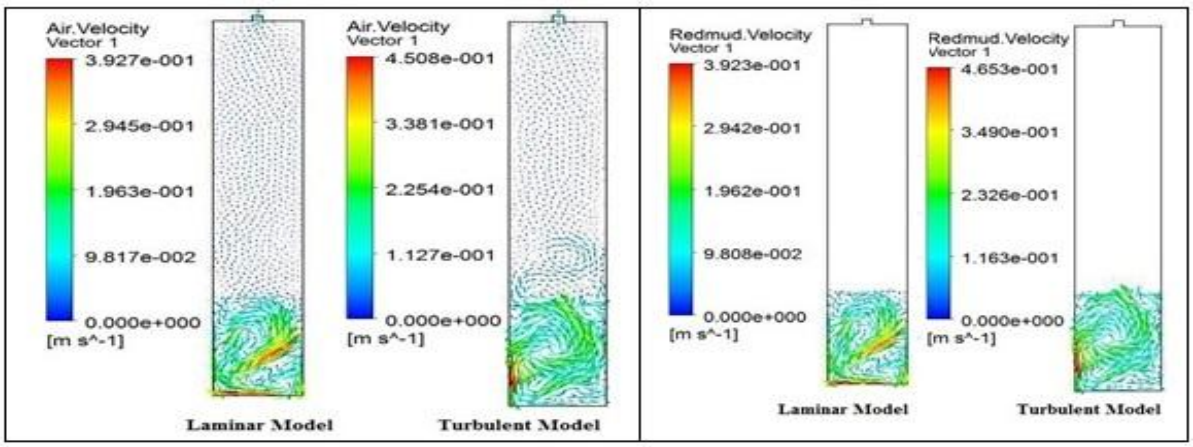

(a) Air velocity **(b) Particle velocity**

Fig. - H.2: Comparisons of velocity vector plots laminar and turbulent models

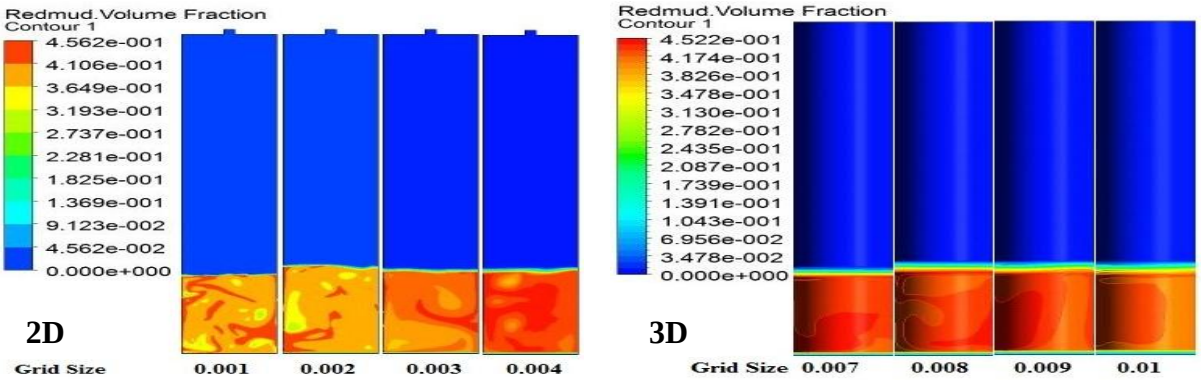

(a) Contours of Solid Volume Fraction

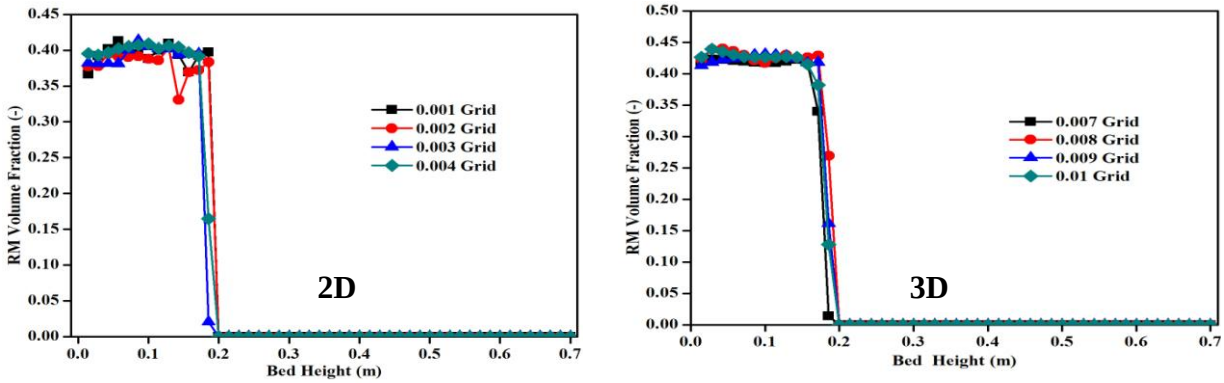

(b) Time Averaged Solid Volume Fraction against Bed Height

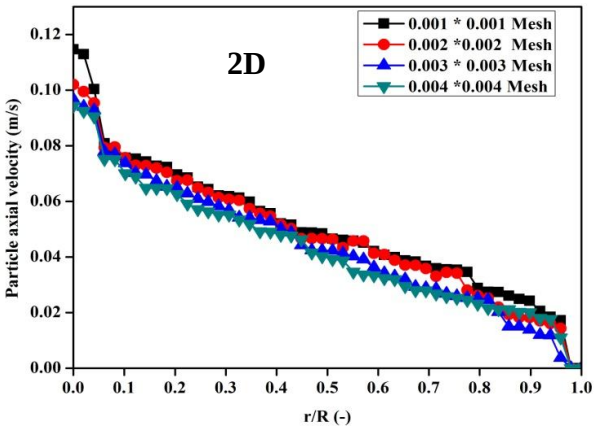

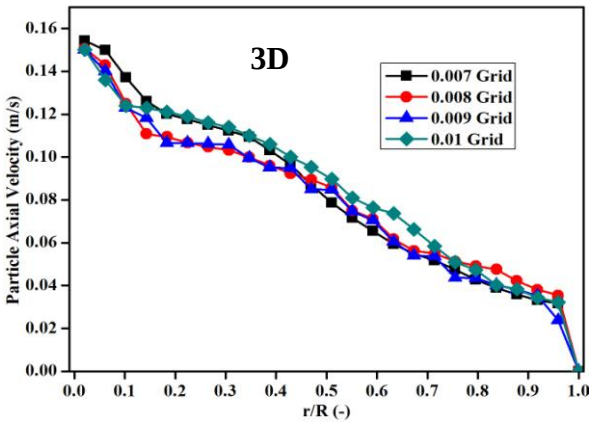

(c) Radially Simulated Particle Axial Velocity

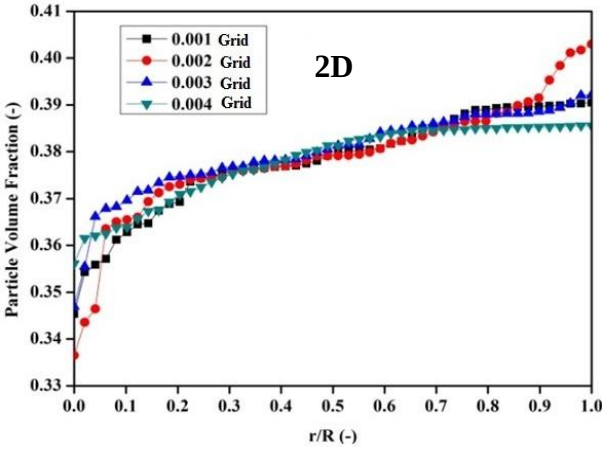

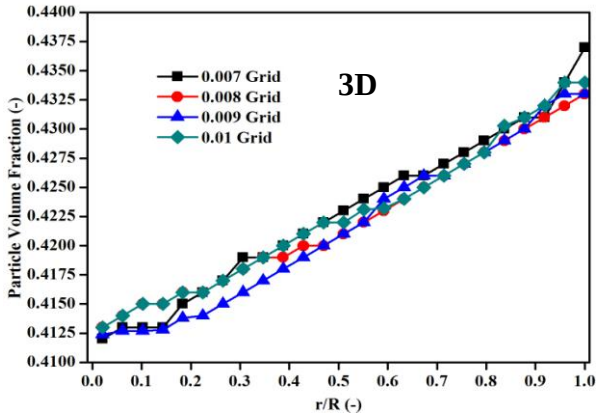

(d) Radially Simulated Particle Volume Fraction

Fig. – H.3: Grid independency for 2D and 3D simulations

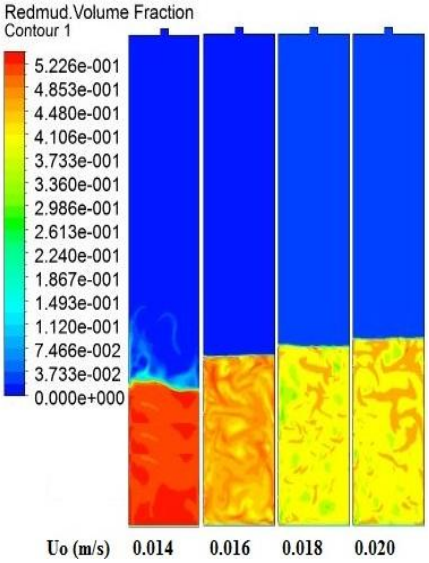

Gidaspow Drag Model

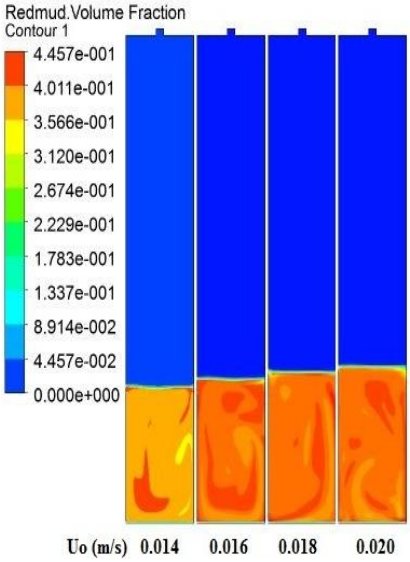

Syamlal – O'Brien Drag Model For Red Mud Particles

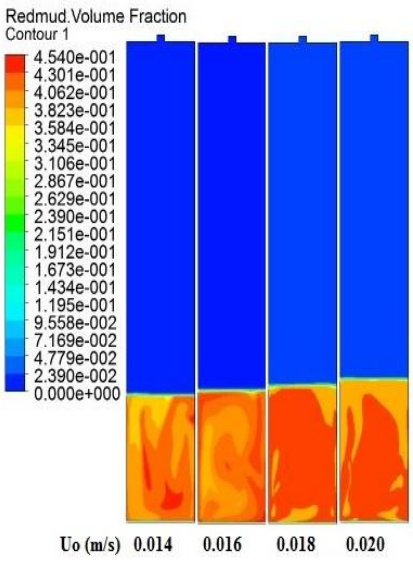

Wen & Yu Drag Model

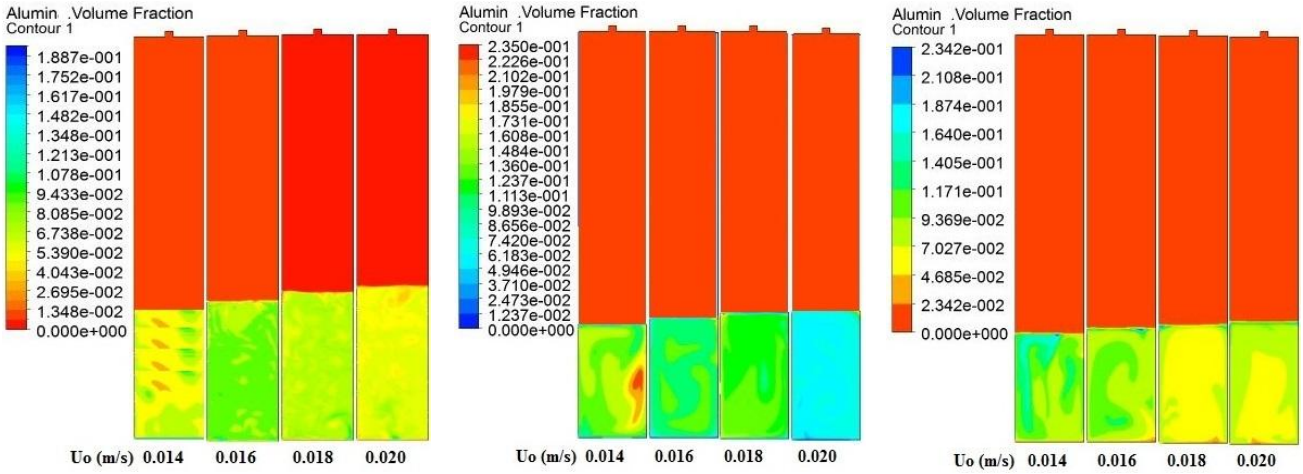

Gidaspow Drag Model **Syamlal – O'Brien Drag Model** **Wen & Yu Drag Model**

For Aluminium Particles

Fig. – I.1: Solid volume fractions with air velocities for different drag models

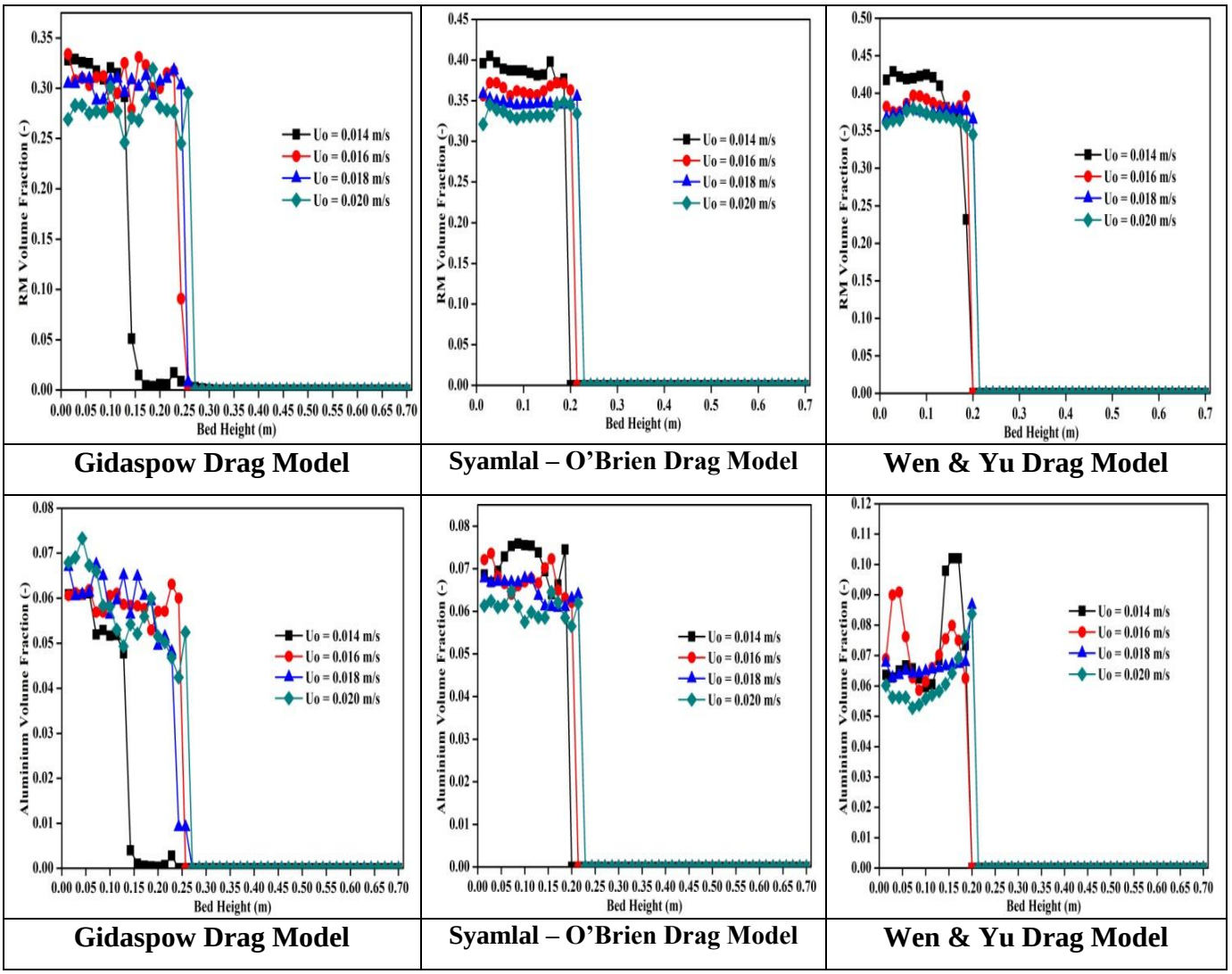

Gidaspow Drag Model **Syamlal – O'Brien Drag Model** **Wen & Yu Drag Model**

Gidaspow Drag Model **Syamlal – O'Brien Drag Model** **Wen & Yu Drag Model**

Fig. – I.2: Axial volume fraction of the solid phases with air velocities for different drag models

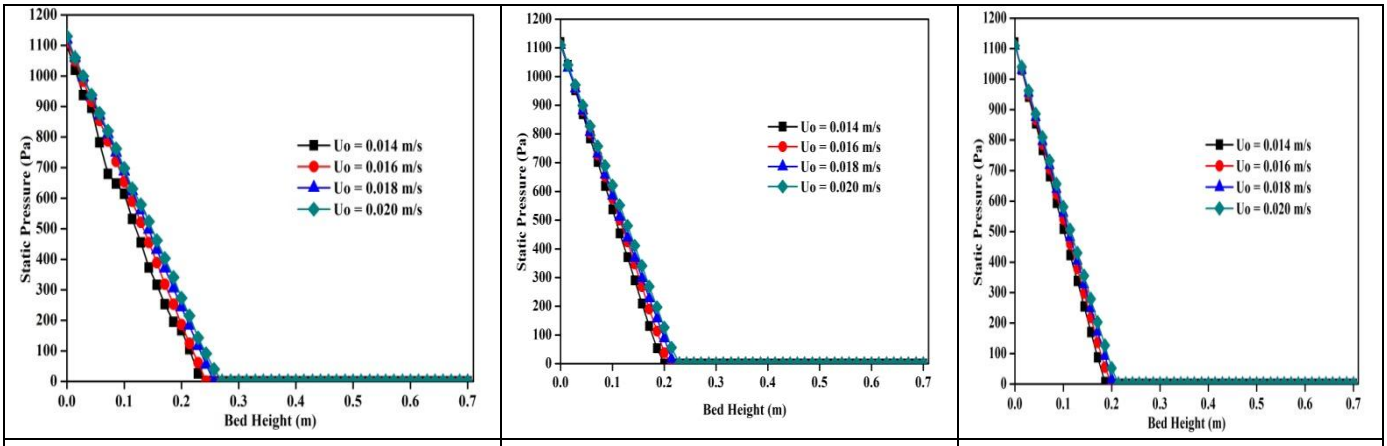

Gidaspow Drag Model	Syamlal – O'Brien Drag Model	Wen & Yu Drag Model

Fig. – I.3: Comparison of static pressures with air velocities for different drag models

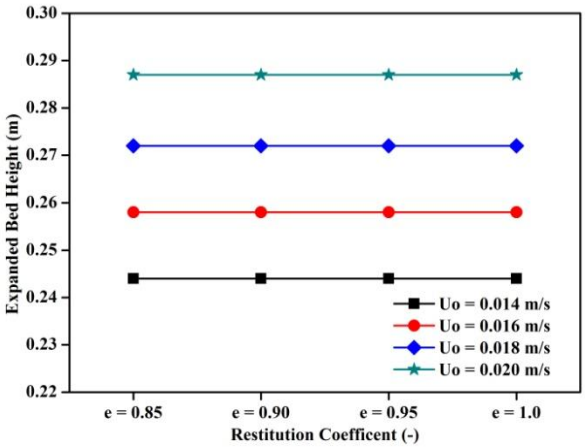

Fig. – I.4: Expanded bed height against restitution coefficient for different air velocities

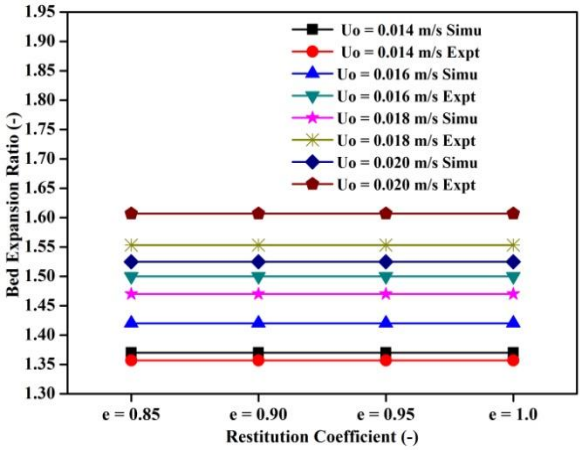

Fig. – I.5: Comparison among experimental and simulated values of bed expansion ratio against restitution coefficient for different air velocities

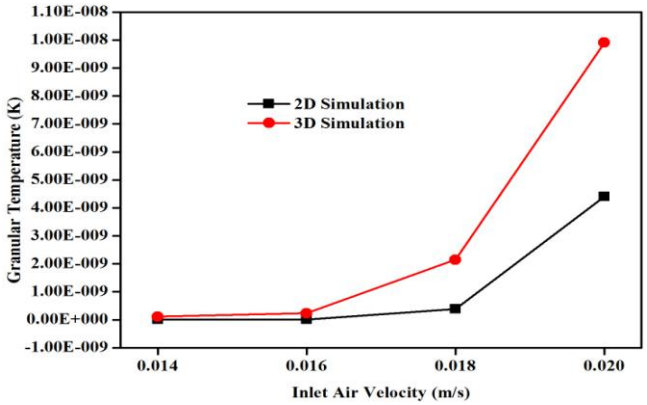

(a) Granular Temperature

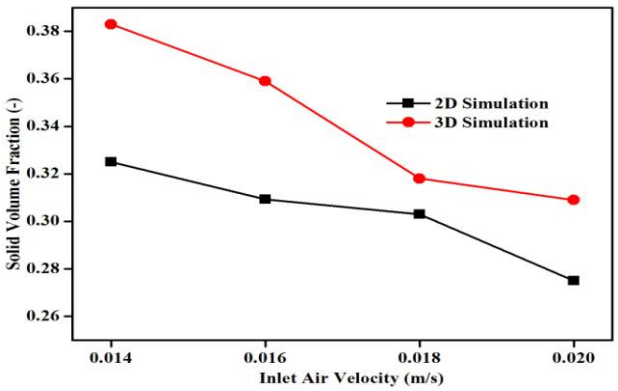

(b) Solid Volume Fraction

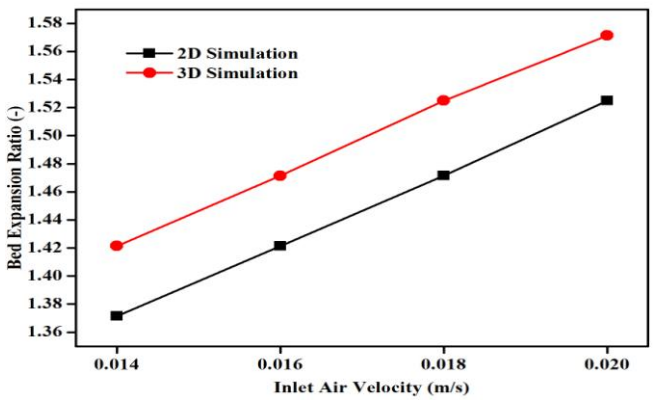

(c) Bed Expansion Ratio

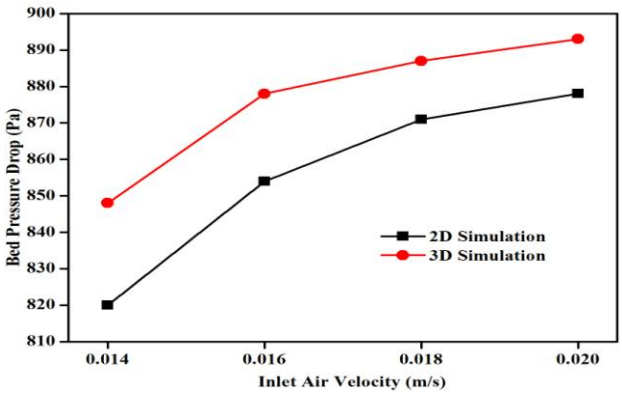

(d) Bed Pressure Drop

Fig. – I.6: Comparisons of bed dynamics with 2D and 3D simulations for different air velocities

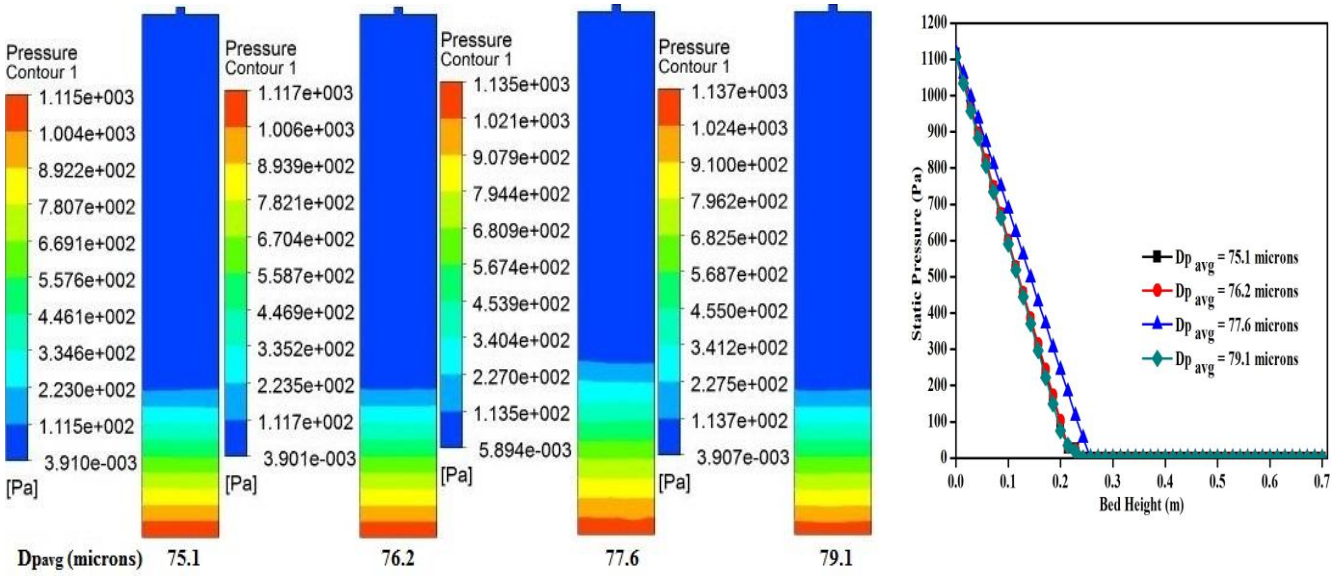

Gidaspow Drag Models

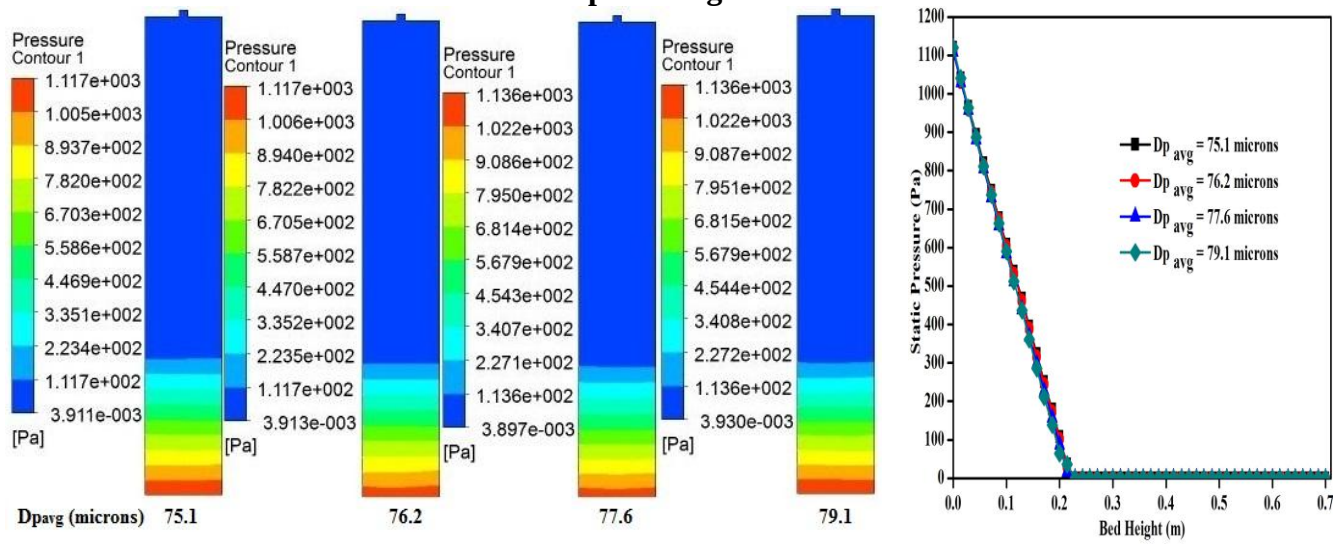

Syamlal – O'Brien Drag Models

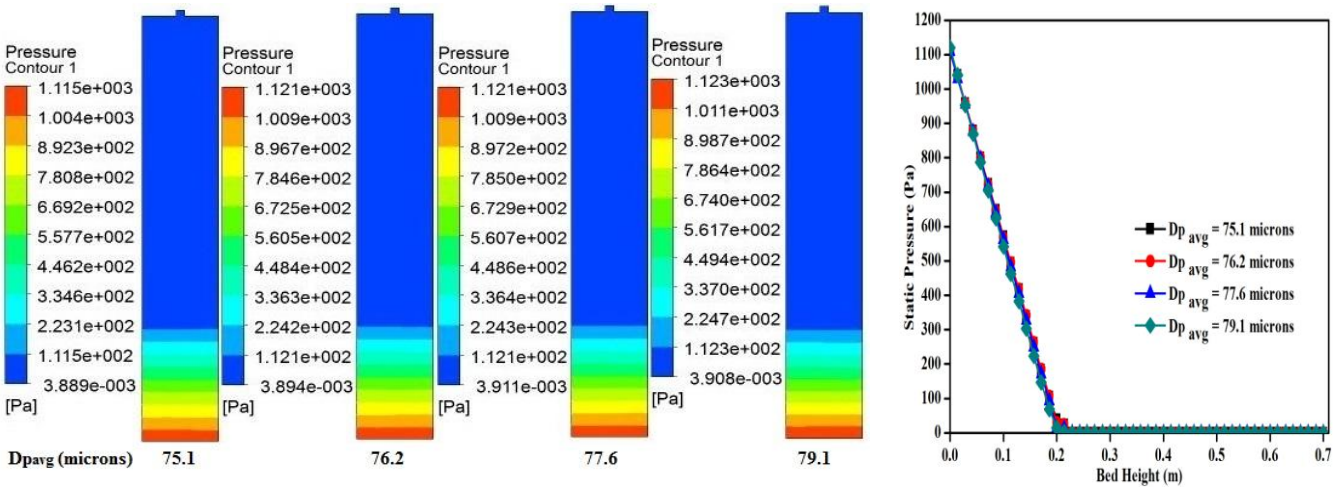

Wen & Yu Drag Models

Fig. – I.7: Comparison of contours of bed pressure drop and static pressure with different particle size of binary mixtures for different drag models

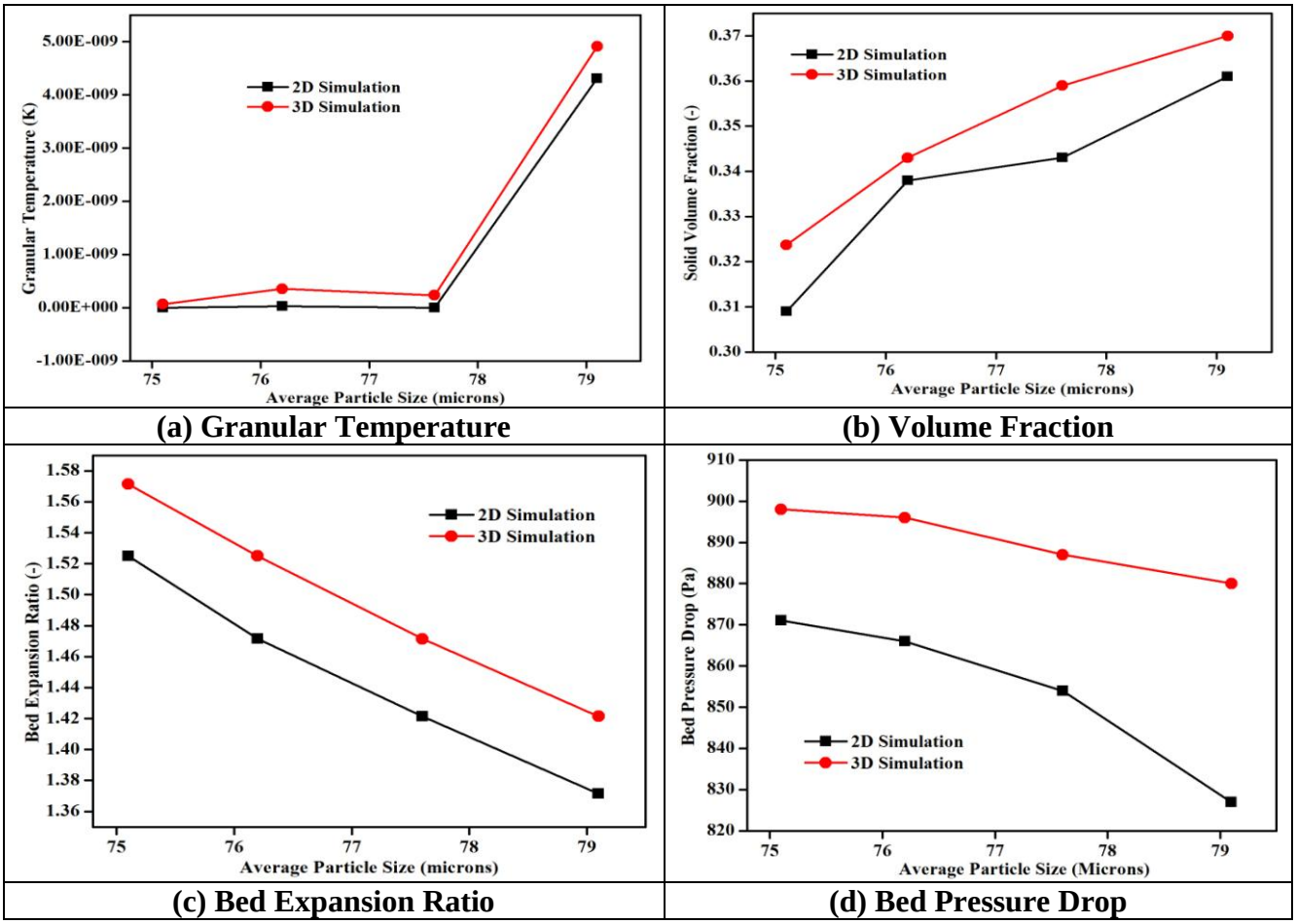

(a) Granular Temperature **(b) Volume Fraction**

(c) Bed Expansion Ratio **(d) Bed Pressure Drop**

Fig. – I.8: Comparisons of different particle sizes of binary mixtures for 2D and 3D simulated bed dynamics

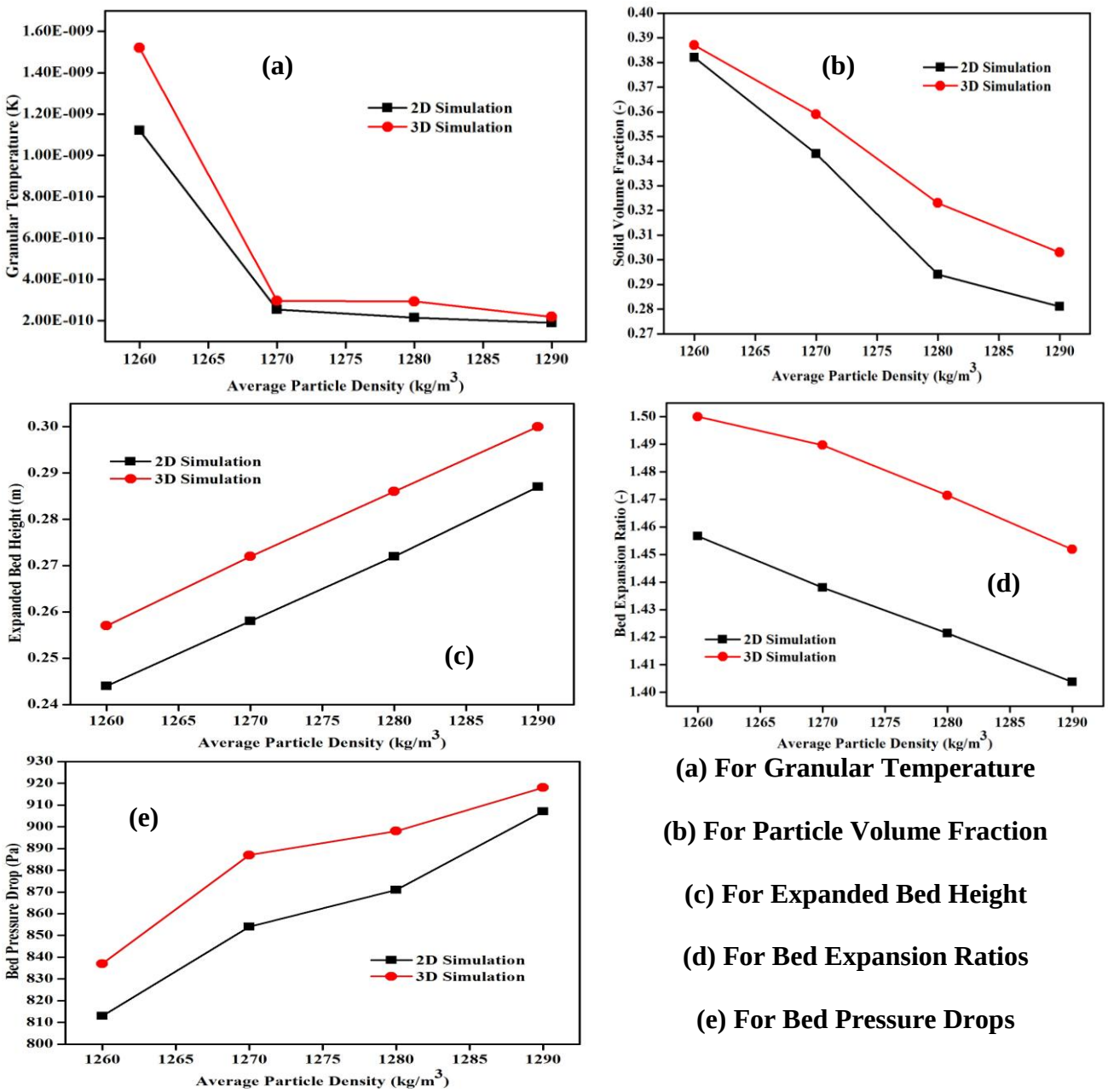

(a) For Granular Temperature

(b) For Particle Volume Fraction

(c) For Expanded Bed Height

(d) For Bed Expansion Ratios

(e) For Bed Pressure Drops

Fig. – I.9: Comparisons of bed dynamics between 2D and 3D simulations for different densities of binary mixtures

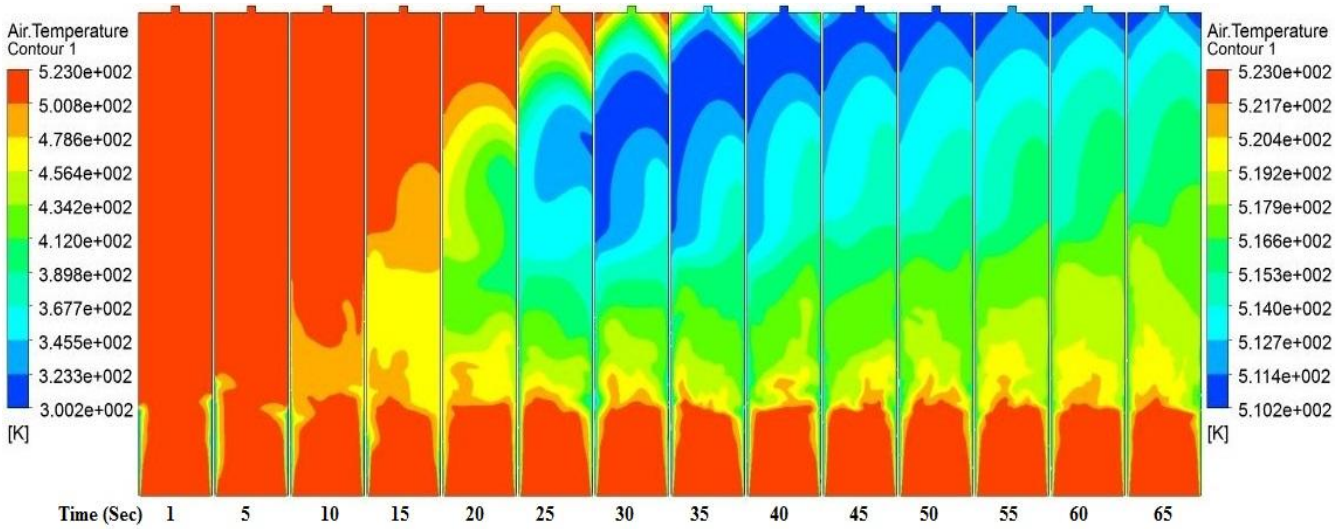

Fig. – J.1: Contours of gas temperature with simulation time

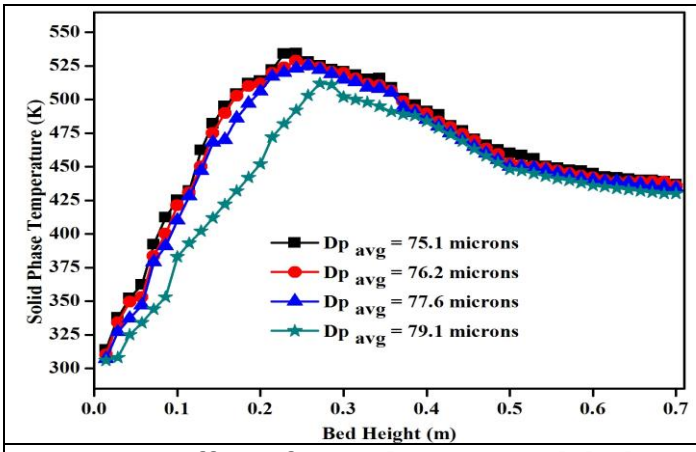

Fig. – J.2: Effect of particle size on solid phase temperature inside reactor

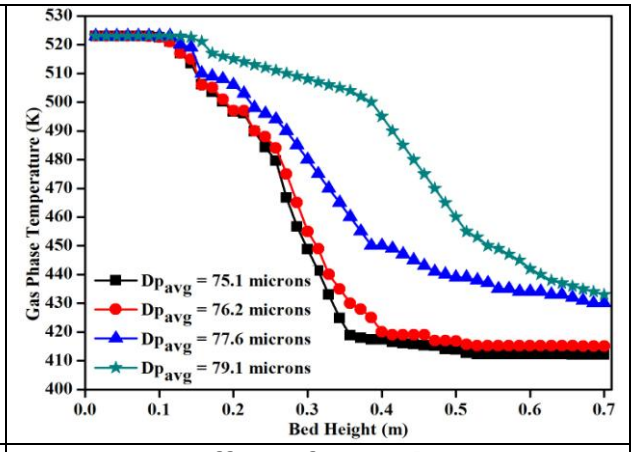

Fig. – J.3: Effect of particle size on gas phase temperature inside reactor

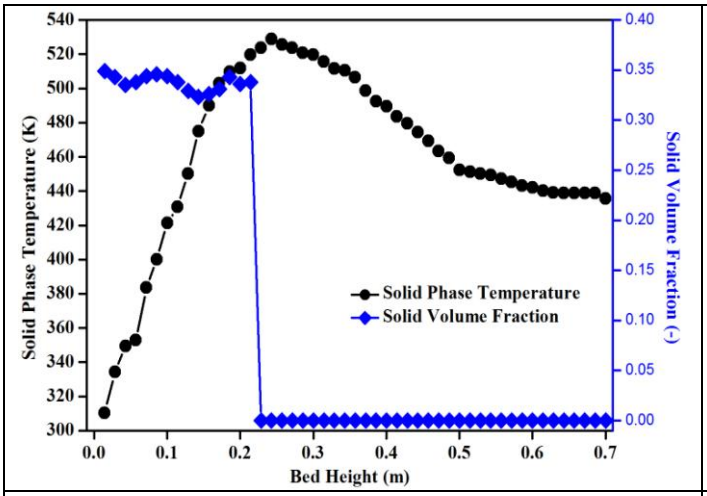

Fig. – J.4: Comparison between distributions of temperature and volume fraction for solid phase

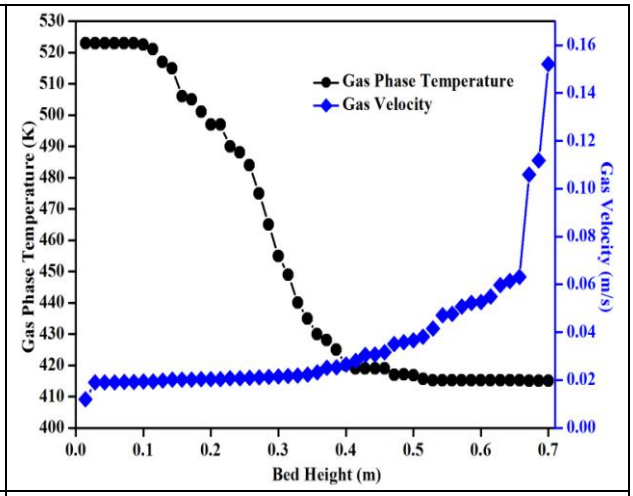

Fig. – J.5: Comparison between distribution of temperature and velocity for gas phase

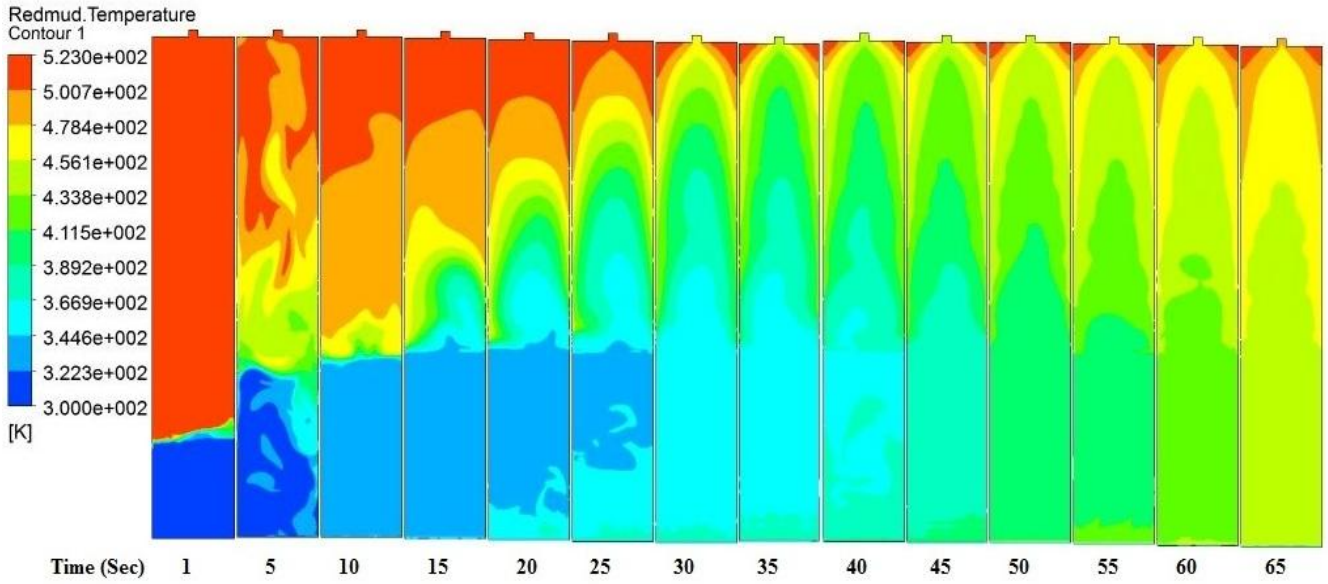

Fig. – J.6: Contours of solid phase temperature with simulation time

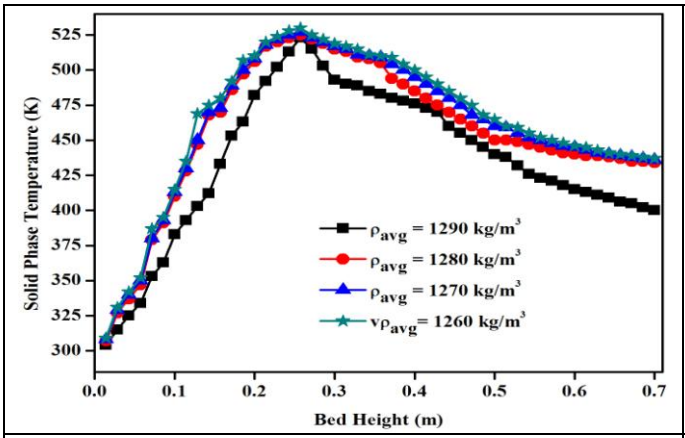

Fig. – J.7: Effect of particle density on solid phase temperature inside reactor

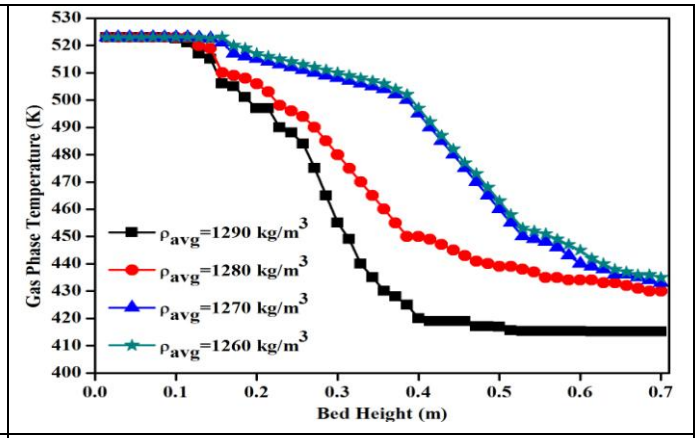

Fig. – J.8: Effect of particle density on gas phase temperature inside reactor

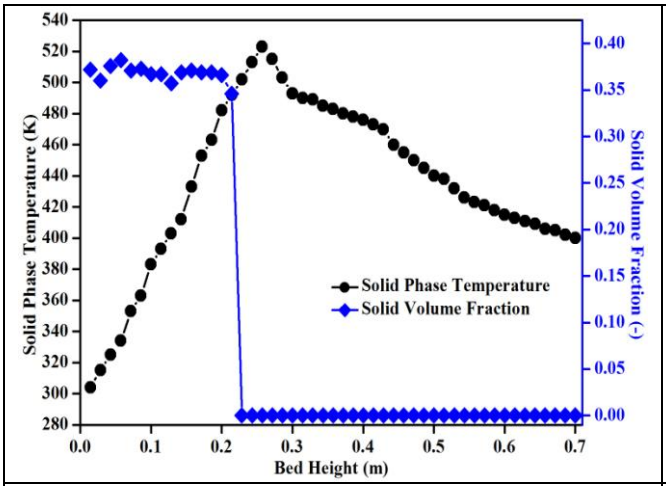

Fig. – J.9: Comparison of temperature and volume fraction distribution for solid phase

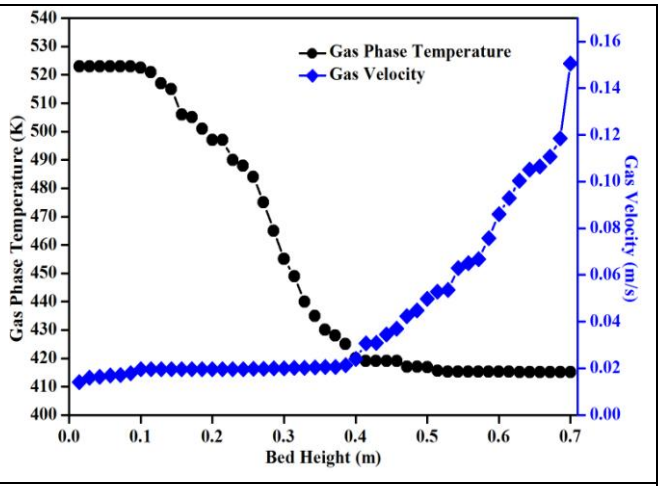

Fig. – J.10: Comparison of temperature and velocity distribution for gas phase

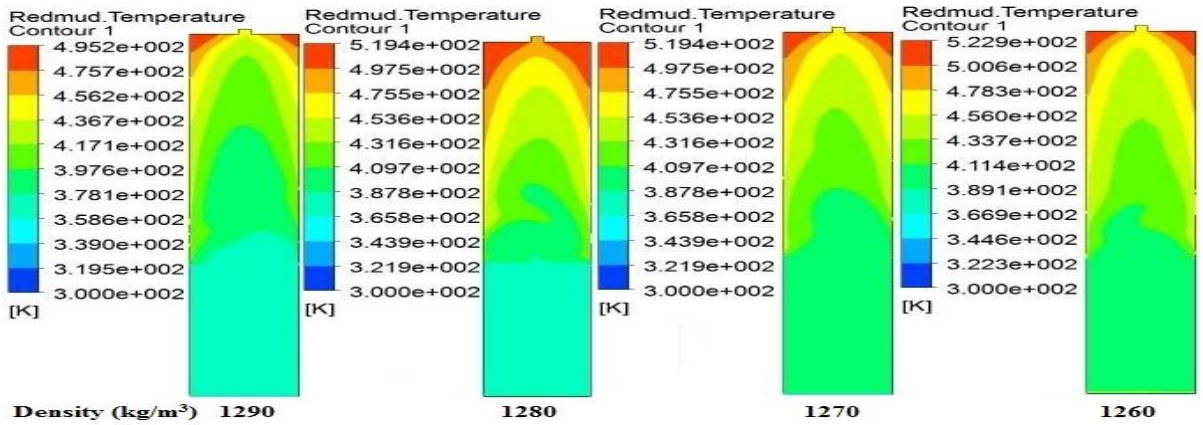

(a) For Solid Phase Temperature

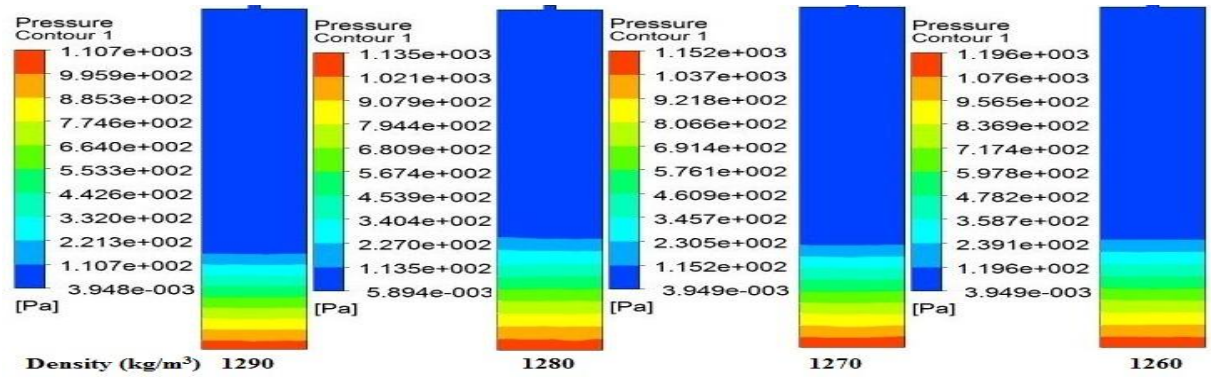

(b) Pressure Drop

Fig. – J.11: Contour plots for different densities of binary mixtures

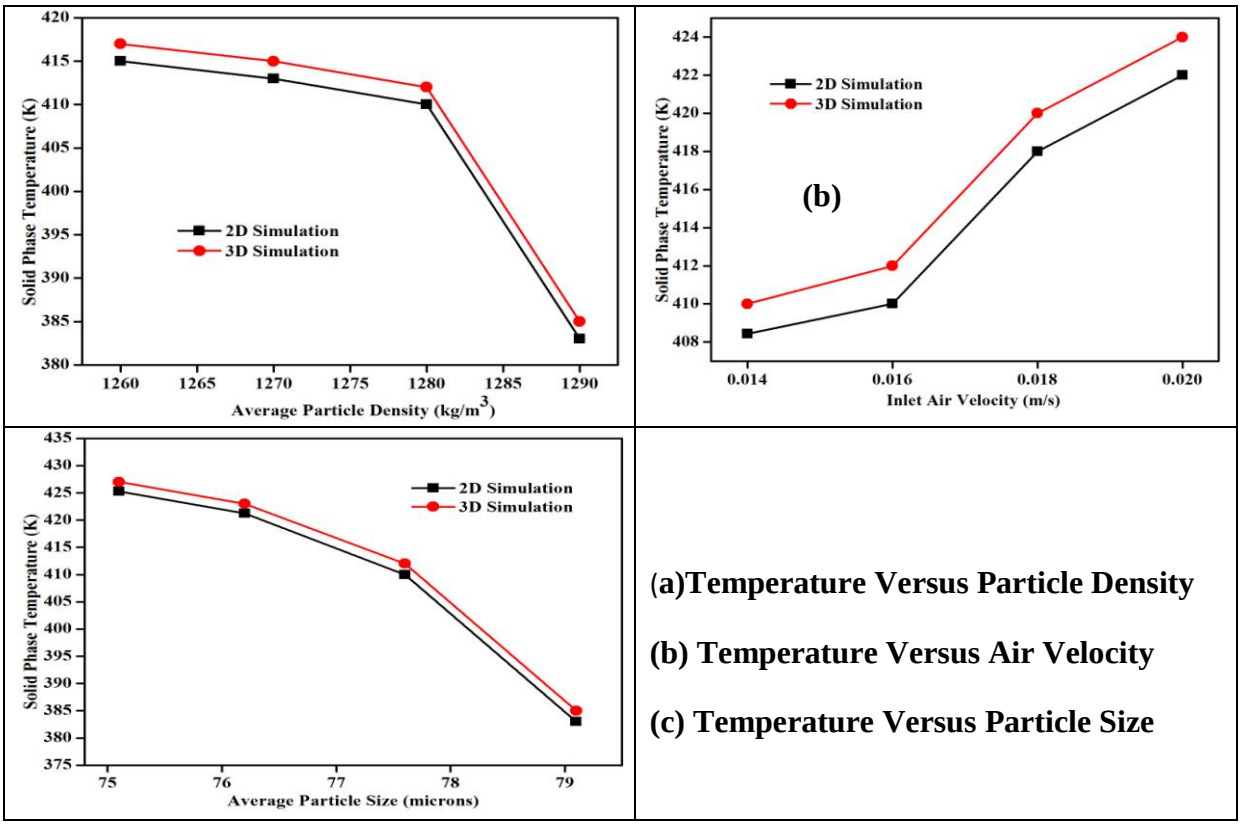

(a)Temperature Versus Particle Density

(b) Temperature Versus Air Velocity

(c) Temperature Versus Particle Size

Fig. – J.12: Comparison of solid phase temperature for 2D and 3D simulations

Table - 1: Under relaxation factors for different flow quantities

Variable	Relaxation Factor
Pressure	0.5
Density	1
Body Force	1
Momentum	0.2
Volume Fraction	0.5
Granular Temperature	0.2
Turbulent Kinetic Energy	0.8
Turbulent Dissipation Rate	0.8
Turbulent Viscosity	1

Table - 2: Comparison of bed expansion ratios for different bed materials

Superficial Air Velocity, m/s	Deviation in Expansion ratios, %					
	Sand		Red Mud		Aluminium	
	2D Simulation	3D Simulation	2D Simulation	3D Simulation	2D Simulation	3D Simulation
0.012	6.54	1.45	9.37	5.14	8.13	3.38
0.014	9.66	4.66	1.19	7.69	10.62	6.25
0.016	12	7.69	1.04	6.59	15.49	11.54
0.018	11.76	7.64	1.36	1.01	17.36	13.42

Table – 3: Comparison of expanded bed height and increase in bed expansion against particle size for different drag models

Particle Size, microns	Static Bed Height, m	Expanded Bed Height, m			Increase in Bed Expansion, %		
		Gidaspow	Syamlal - O'Brien	Wen & Yu	Gidaspow	Syamlal - O'Brien	Wen & Yu
58	0.10	0.228	0.214	0.2	128	114	100
77	0.10	0.214	0.2	0.185	114	100	85
98	0.10	0.171	0.157	0.142	71	57	42
116	0.10	0.157	0.142	0.142	57	42	42

Table – 4: Comparisons among expanded bed heights and increase in expansion with different static bed heights for different drag models

Static Bed Height, m	Expanded Bed Height, m			Increase in Bed Expansion, %		
	Gidaspow	Syamlal - O'Brien	Wen & Yu	Gidaspow	Syamlal - O'Brien	Wen & Yu
0.08	0.185	0.171	0.157	131	112	96
0.10	0.214	0.2	0.185	114	100	85
0.12	0.25	0.228	0.214	108	90	78
0.14	0.285	0.257	0.242	103	83	72

Table – 5: Comparison of maximum static pressure and static pressure bed height for different drag models with different particle sizes

Particle Size, Microns	Maximum Static Pressure, Pa			Static Pressure Bed Height, m		
	Gidaspow	Syamlal - O'Brien	Wen & Yu	Gidaspow	Syamlal - O'Brien	Wen & Yu
58	892.351	903.529	901.799	0.228	0.171	0.185
77	899.276	898.76	900.292	0.214	0.2	0.2
98	901.536	894.385	862.115	0.171	0.228	0.157
116	861.172	889.444	859.188	0.157	0.142	0.142

Table – 6: Comparison of expanded bed height and increase in bed expansion against particle size for different values of specularity coefficients

Particle Size, microns	Expanded Bed Height, cm					Increase in Bed Expansion, %				
	Ø=0	Ø=0.25	Ø=0.5	Ø=0.75	Ø=1.0	Ø=0	Ø=0.25	Ø=0.5	Ø=0.75	Ø=1.0
58	22.8	22.8	20	21.4	21.4	128	128	100	114	114
77	21.4	20	18.6	18.6	18.6	114	100	86	86	86
98	17.1	17.1	17.1	17.1	17.1	71	71	71	71	71
116	15.7	15.7	15.7	15.7	15.7	57	57	57	57	57

Table – 7: Comparisons of expanded bed height and percentage increase in bed expansion at different air velocities for different values of specularity coefficients

Inlet Air Velocity, m/s	Maximum Expanded Bed Height, cm					Increase in Bed Expansion, %				
	Ø=0	Ø=0.25	Ø=0.5	Ø=0.75	Ø=1.0	Ø=0	Ø=0.25	Ø=0.5	Ø=0.75	Ø=1.0
0.012	20	17.1	17.1	18.6	18.6	100	71	71	86	86
0.014	21.4	20	18.6	18.6	18.6	114	100	86	86	86
0.016	22.8	20	20	20	18.6	128	100	100	100	86
0.018	24.2	21.4	21.4	21.4	20	142	114	114	114	100

Table – 8: Comparisons of simulated expanded bed heights and increase in bed expansions with different static bed heights for different specularity coefficients

Static Bed Height, cm	Expanded Bed Height, cm					Increase in Bed Expansion, %				
	Ø=0	Ø=0.25	Ø=0.5	Ø=0.75	Ø=1.0	Ø=0	Ø=0.25	Ø=0.5	Ø=0.75	Ø=1.0
8	18.6	15.7	15.7	17.1	17.1	132	96	96	113	113
10	21.4	20	18.6	18.6	18.6	114	100	86	86	86
12	25	21.4	21.4	22.9	22.9	108	79	79	91	91
14	28.5	22.9	22.9	25.7	25.7	103	63	63	83	83

Table – 9: Comparison of static pressure bed heights with different particle sizes for different specularity coefficients

Particle Size, microns	Static Pressure Bed Height, cm				
	Ø=0	Ø=0.25	Ø=0.5	Ø=0.75	Ø=1.0
58	22.8	22.8	20	21.4	21.4
77	21.4	20	18.6	18.6	18.6
98	17.1	17.1	17.1	17.1	17.1
116	15.7	15.7	15.7	15.7	15.7

Table – 10: Comparison among static pressure bed heights with inlet air velocity for different specularity coefficients

Inlet Air Velocity, m/s	Static Pressure Bed Height, cm				
	Ø=0	Ø=0.25	Ø=0.5	Ø=0.75	Ø=1.0
0.012	20	17.1	17.1	18.6	18.6
0.014	21.4	20	18.6	18.6	18.6
0.016	22.8	20	20	20	18.6
0.018	24.2	21.4	21.4	21.4	20

Table – 11: Comparison of static pressure bed heights with different initial static bed heights for different specularity coefficients

Static Bed Height, cm	Static Pressure Bed Height, cm				
	Ø=0	Ø=0.25	Ø=0.5	Ø=0.75	Ø=1.0
8	18.6	15.7	15.7	17.1	17.1
10	21.4	20	18.6	18.6	18.6
12	25	21.4	21.4	22.9	22.9
14	28.5	22.9	22.9	25.7	25.7

Table – 12: Comparisons of expanded bed heights and percentage increase in bed heights with binary mixtures at different air velocities for different drag models

Superficial Air Velocity, m/s	Static Bed Height, m	Expanded Bed Height, m			Increase in Bed Expansion, %		
		Gidaspow	Syamlal - O'Brien	Wen & Yu	Gidaspow	Syamlal - O'Brien	Wen & Yu
0.014	0.14	0.244	0.214	0.2	74.3	52.9	42.9
0.016	0.14	0.258	0.229	0.214	84.3	63.6	52.9
0.018	0.14	0.272	0.244	0.229	94.3	74.3	63.6
0.020	0.14	0.287	0.258	0.244	105	84.3	74.3

Table – 13: Comparison of maximum static pressure and static pressure bed height against inlet air velocity of binary mixture for different drag models

Inlet Air Velocity, m/s	Maximum Static Pressure, Pa			Static Pressure Bed Height, m		
	Gidaspow	Syamlal - O'Brien	Wen & Yu	Gidaspow	Syamlal - O'Brien	Wen & Yu
0.014	937	952	942	0.244	0.214	0.2
0.016	950	963	960	0.258	0.229	0.214
0.018	962	978	955	0.272	0.244	0.229
0.020	971	999	982	0.287	0.258	0.244

Table – 14: Comparisons of expanded bed heights and increase in bed expansion with different particle sizes of binary mixture for different drag models

Average Particle Size, microns	Expanded Bed Height, cm			Increase in Bed Expansion, %		
	Gidaspow	Syamlal - O'Brien	Wen & Yu	Gidaspow	Syamlal - O'Brien	Wen & Yu
75.1	28.7	22.9	22.9	105	63.5	63.5
76.2	27.2	22.9	21.4	94.3	63.5	52.8
77.6	25.8	22.9	21.4	84.3	63.5	52.8
79.1	24.4	22.9	20	74.2	63.5	42.9

Table – 15: Comparisons of expanded bed height and increase in bed expansion with different particle density of binary mixture for different drag models

Average Particle Density, kg/m^3	Static Bed Height (RM + Al), cm	Expanded Bed Height, cm			Increase in Bed Expansion, %		
		Gidaspow Model	Syamlal - O'Brien Model	Wen & Yu Model	Gidaspow Model	Syamlal - O'Brien Model	Wen & Yu Model
1260	(12.5+1)	24.4	21.8	20	80.7	61.4	48.2
1270	(12+2)	25.8	23.6	22.9	84.3	68.5	63.5
1280	(11.5+3)	27.2	24.4	23.6	87.6	68.3	62.7
1290	(11+4)	28.7	25.8	25.8	91.4	72	72

Table – 16: Comparisons of expanded bed height and increase in bed expansion with different particle densities of binary mixture for different specularity coefficients

Average Particle Density, kg/m^3	Expanded Bed Height, cm					Increase in Bed Expansion, %				
	Ø=0	Ø=0.25	Ø=0.5	Ø=0.75	Ø=1.0	Ø=0	Ø=0.25	Ø=0.5	Ø=0.75	Ø=1.0
1260	24.4	22.9	23.5	21.9	21.9	80.7	69.7	74	62.3	62.3
1270	25.8	24.4	24.4	22.9	23.5	84.3	74.3	74.3	63.5	67.8
1280	27.2	25.8	26.4	24.4	24.4	87.6	77.9	82	68.3	68.3
1290	28.7	26.4	27.2	25.8	25.8	91.4	76	81.4	72	72

ADDENDUM

❖ Bed Pressure Drop

The commonly used correlation for bed pressure drop is Ergun Equation and is expressed below [Kunii and Levenspiel, Eq^{n} No. 6 (Page No. 64)].

$$\frac{\Delta P}{L_m} g = 150 \frac{(1-\varepsilon)^2}{\varepsilon^3} \frac{\mu u}{(\phi_s d_p)^2} + 1.75 \frac{1-\varepsilon}{\varepsilon^3} \frac{\rho_g u^2}{\phi_s d_p}$$

Using the system data (i.e. ρ = 1300 kg/m^3 and ε = 0.22], bed pressure drop is calculated theoretically and compared against experimentally observed values. Bed pressure drop decreases and increases with increase in particle size and static bed height respectively. This is shown in following Table.

Static Bed Height	Theoretical	Experimental	Particle Size	Theoretical	Experimental
8 cm	435.4 Pa	400 Pa	58 microns	578.03 Pa	600 Pa
10 cm	544.4 Pa	550 Pa	77 microns	544.4 Pa	550 Pa
12 cm	653.22 Pa	780 Pa	98 microns	513.24 Pa	530 Pa
14 cm	762.09 Pa	900 Pa	116 microns	505.8 Pa	520 Pa

❖ Minimum Fluidization Velocity

Similarly expression for minimum fluidization velocity available in literature is [Kunii and Levenspiel, Eq^{n} No. 18 (Page No. 69)] mentioned below.

$$u_{mf} = \frac{d_p^2 (\rho_s - \rho_g) g}{150 \mu} \frac{\varepsilon^3 \phi_s^2}{1-\varepsilon}$$

For 77 micron particle size, U_{mf} calculated theoretically and experimentally is 0.016 m/s and 0.012 m/s respectively. The U_{mf} value is almost same for different particle size as mentioned in the following Table.

Particle Size	Theoretical	Experimental
58 microns	0.009 m/s	0.012 m/s
77 microns	0.016 m/s	0.012 m/s
98 microns	0.026 m/s	0.018 m/s
116 microns	0.031 m/s	0.020 m/s